Improved models for predicting irradiation damage with uncertainty estimates from nuclear reactions

Shengli Chen

Université Grenoble Alpes

THÈSE

Pour obtenir le grade de

DOCTEUR DE L'UNIVERSITE GRENOBLE ALPES

Spécialité : **Mécanique des fluides, Energétique, Procédés**

Arrêté ministériel : 25 mai 2016

Présentée par

Shengli CHEN

Thèse dirigée par **Patrick BLAISE, CEA/DES/DSE**, et
codirigée par **David BERNARD, CEA/DES/IRESNE/DER/SPRC/LEPh**

préparée au sein du **CEA/DES/IRESNE/DER/SPRC/LEPh**
dans **l'École Doctorale I-MEP2 : Ingénierie – Matériaux, Mécanique, Environnemenlt, Energétique, Procédés, Production**

Improved models for predicting irradiation damage with uncertainty estimates from nuclear reactions

Thèse soutenue publiquement le **25 septembre 2020,**
devant le jury composé de :

M. Pablo RUBIOLO

Professeur, PHELMA – Grenoble INP, Président

M. Ulrich FISCHER

Chercheur, IRN – Karlsruhe Institute of Technology (KIT), Rapporteur

M. Joël ROSATO

Maître de conférences, Université Aix-Marseille, Rapporteur

M. Jose Manuel PERLADO MARTIN

Professeur, Universidad Politecnica de Madrid, Examinateur

M. Ian FARNAN

Professeur, Cambridge University, Examinateur

Mme. Emilie FERRIE

Maître de conférences, Université Grenoble Alpes, Examinatrice

M. Patrick BLAISE

Directeur de recherche, CEA, Directeur de thèse, Invité

M. David BERNARD

Ingénieur-chercheur, CEA Cadarache, Encadrant, Invité

Acknowledgements

It is a great opportunity to perform my PhD studies in CEA Cadarache with world-leading experts. I really enjoyed the relatively free work environment and all supports provided by CEA and our laboratory.

First of all, I would like to express my deepest gratitude to my main supervisor Dr. David Bernard for all his support and help. Especially, for his free-style advice and supervision that allow to explore various directions within the PhD framework. Thanks a lot for all the patience, time, guidance, and advice in the past three years. In most of the time, David is more like a kind colleague and friend to work with, so that I can finish this thesis with much less stress. Thanks also for his help during the telecommuting owing to Covid-19.

I would like to extend my sincere thanks to my PhD director Dr. Patrick Blaise. Thanks a lot for the enthusiastic supervision and helps as well as the organization of academic seminar with other divisions (even if it is strongly perturbed by Covid-19). Thanks a lot for the time and ideas with which you contributed to this thesis. Patrick also spent much time on reviewing this thesis.

Special thanks to my jury members, for their (remote) presence and suggestions on this thesis. It is my pleasure to defense my PhD before them, experts on different domains. Especially, I acknowledge my two thesis reviewers, Dr. Fischer and Dr. Rosato, they took much time to review the thesis and give their significant comments.

I gratefully acknowledge my colleagues of LEPh for all kinds of helps. Particularly, Dr. Gilles Noguère, my former supervisor when I was intern, for his significant advice and guidance on nuclear data. I am also grateful to Dr. Pierre Tamagno for his kind support, especially for the technical help on the use and development of the CONRAD code. Special thanks to Dr. Yannick Pénéliau for following my PhD studies during these three years and for all his helps and discussion.

Thanks to my colleagues, Dr. Jean Tommasi, Dr. Olivier Sérot, Dr. Laurent Buiron, Dr. Léonie Tamagno, Dr. Olivier Litaize, Dr. Maria Diakaki, Dr. Pascal Archier, and Mr. Elias Vandermeersch for helpful discussions and their contributions to this thesis. Thanks also to Dr. Pierre Leconte for tolerating my discussion with David for around hundred times.

I would like to recognize many helps received from our laboratory head, Dr. Véronique Bellanger-Villard. I also acknowledge Mrs. Claire Boucher and Mrs. Alexandra Herrenschmidt for their help on administrative formalities during my PhD studies. Certainly, thanks to Mrs. Agustina Alessio and Mrs. Rafaela Bueno-Clementi from doctoral school I-MEP2 for their nice supports during these three years.

Thanks to current and former PhD students and Postdoc of LEPh for the lunch time, jokes, and sometimes complaining in the past three years. It is also a good opportunity for me to supervise and work with my two interns, Mr. Dingbang Cai and Mr. Hao Li.

I am grateful to Cadarache Chinese PhD team (Hui, Fang, Jianwei, Ling, Shuqi, Weifeng, Chunhui, Congjin, Xiaoshu, Yuying, Jingtian, Linkai, etc.) for the afterwork time and delicious Chinese food. Thanks to all my friends, my former teachers and supervisors who directly or indirectly helped my former studies and my PhD works.

Last but not least, many thanks to my family and my girlfriend for their understanding and support, especially in the difficult period of Covid-19. Family is where life begins and love never ends.

Abstract

Because the irradiation damage is a major challenge of nuclear materials, it is of upmost importance to accurately calculate it with reliable uncertainty estimates. The main objective of this thesis is to develop and improve the methodologies for computing the neutron irradiation-induced displacement damages as well as their uncertainties. After a brief review on nuclear reaction models and primary radiation damage models, we propose a complete methodology for calculating damage cross sections from different nuclear reactions and the subsequent calculation of Displacement per Atom (DPA) rates.

The recoil energies from neutron-induced reactions are summarized with an estimation of the relativistic effect and the target thermal vibration. Particularly, a new method for computing the recoil energy from charged particle emission reactions is proposed by considering both the quantum tunneling and the Coulomb barrier. Some methods are developed to improve and verify numerical calculations. Damage cross section calculations from neutron radiative capture reaction and N-body reactions are also thoroughly analyzed and discussed. In addition to the neutron irradiation-induced displacement damage, the electron, positron, photon-induced DPA cross sections, as well as the beta decay and Fission Products (FPs)-induced damage are also investigated. Orders of magnitude of their relative contributions are given.

For the neutron irradiation-induced DPA rate calculation, attention should be paid when using infinite dilution cross sections. E.g., in the ASTRID inner core, the self-shielding correction on ECCO 33-group damage cross sections leads to a 10% reduction of DPA rate, whereas the multigroup correction is still not automatically treated for DPA rate calculation in neutronic codes nor for computing Primary Knock-on Atom (PKA) spectrum. Based on the presently proposed method for computing the FPs-induced DPA by atomistic simulations, the peak value of the FPs-induced DPA rate can be 4 to 5 times larger than the neutron-induced one in the cladding of the ASTRID inner core, even though the penetration of FPs in the Fe-14Cr cladding is less than 10 μm. Therefore, the question of whether the FPs-induced damage should be considered for determining fuel assembly lifetime in fast reactors needs to be discussed.

In the reactor vessel of a simplified pressurized water reactor, the covariance matrices of ^{235}U prompt fission neutron spectrum from ENDF/B-VII.1 and JENDL-4.0 respectively lead to 11% and 7% relative uncertainty of DPA rate. Neglecting the correlations of the neutron flux and PKA spectrum results in an underestimation by a factor of 21. The total uncertainties of damage energy rate are respectively 12% and 9%, whereas an underestimation by a factor of 3 is found if the correlations of damage cross section and neutron flux are not considered.

Keywords: DPA, Cross section, Uncertainty propagation

Maitrise des biais et incertitudes des sections efficaces et de la modélisation de la cinématique associées aux réactions nucléaires conduisant aux dommages dans les matériaux sous irradiation

Resumé

Étant donné que les dommages causés par l'irradiation constituent un défi majeur pour les matériaux nucléaires, il est nécessaire de calculer précisément ces dommages conjointement avec l'estimation de ses incertitudes. L'objectif principal de cette thèse est de développer et d'améliorer les méthodologies pour calculer les dommages induits par l'irradiation neutronique ainsi que de proposer une méthodologie pour l'estimation de l'incertitude. Après une brève revue des modèles de réactions nucléaires et des modèles de dommages d'irradiation primaires, on propose des méthodes complètes pour calculer la section efficace des dommages à partir de différentes réactions nucléaires pour calculer du taux de Déplacement par Atome (DPA).

Une interpolation améliorée est proposée pour produire la valeur de crête de la distribution d'énergie-angulaire à partir de données tabulées. Les énergies de recul des réactions induites par les neutrons sont résumées avec une estimation de l'effet relativiste et de la vibration thermique de la cible. En particulier, une nouvelle méthode de calcul de l'énergie de recul des réactions d'émission de particules chargées est proposée en considérant l'effet tunnel et la barrière Coulombienne. Certaines méthodes sont développées pour améliorer et vérifier les calculs numériques. Les calculs de la section de dommage provenant de la réaction de la capture et des réactions d'émission de N-corps sont également analysés et discutés en profondeur. En plus des dommages induits par l'irradiation neutronique, les sections DPA induites par les électrons, les positons et les photons et les dommages induits par la désintégration bêta sont également étudiées.

Pour le calcul du taux de DPA induit par l'irradiation neutronique, il convient de faire attention lors de l'utilisation de sections à dilution infinie. Par exemple, dans le cœur interne d'ASTRID, la correction d'autoprotection sur la section DPA de ECCO 33-groupe conduit à une réduction de 10% du taux de DPA, tandis que cette correction multi-groupe n'est pas toujours automatiquement traitée pour le calcul de DPA dans les codes neutroniques ni pour le calcul du spectre Primary Knock-on Atom (PKA). En plus des dommages par les neutrons, une méthode générale est proposée pour calculer les dommages de déplacement induits par les Produits de Fission (PFs) avec des

simulations de collisions atomistiques. Elle montre que la valeur de crête du taux de DPA induit par les PFs peut être 4 à 5 fois supérieure à celle induite par les neutrons dans la gaine du cœur interne d'ASTRID, même si la pénétration des PFs dans la gaine Fe-14Cr est inférieure à 10 μm. Par conséquent, la question si les dommages induits par les PFs doivent être pris en compte pour déterminer la durée de vie des assemblages combustibles dans les réacteurs rapides doit être discutée.

Dans la cuve d'un réacteur à eau pressurisée, les matrices de covariance du spectre de neutrons prompts de fission de ^{235}U venant de ENDF/B-VII.1 et JENDL-4.0 conduisent respectivement à une incertitude de 11% et 7% du taux de DPA. Négliger les corrélations du flux de neutrons et du spectre PKA entraîne une large sous-estimation d'un facteur de 21. Les incertitudes totales du taux de dommages sont respectivement de 12% et 9%, tandis que les nulles valeurs des corrélations de la section efficace de dommage et du flux de neutron conduisent à une réduction de l'incertitude par un facteur de 3.

Mots-clés : DPA, Section efficace, Propagation des incertitudes

Table of contents

List of figures

List of tables

Glossary

AD	Angular Distribution
ADC	Atomic Displacement Cascade
ARC	Athermal Recombination-Corrected (DPA model)
ASTRID	Advanced Sodium Technological Reactor for Industrial Demonstration
ATF	Accident Tolerant Fuel
BCA	Binary Collision Approximation
CB	Chen-Bernard (DPA model)
CM	Center of Mass
CONRAD	COde for Nuclear Reaction Analysis and Data assimilation
CS	Compton Scattering
CTM	Constant Temperature Model
DOM	Dispersive Optical Model
DPA	Displacement per Atom
DXS	Damage Cross Sections
ECIS	A nuclear reaction code for optical model calculation
ENDF	Evaluated Nuclear Data File
ENDF/B	American Evaluated Nuclear Data library
ENSDF	Evaluated Nuclear Structure Data File
EPDL	Evaluated Photon Data Library
FC	Full Cascade simulation (option in SRIM-like code)
FCCI	Fuel-Cladding Chemical Interaction
FP	Frenkel Pair(s)
FPs	Fission Products (only in Section 5.4)
FR	Fast neutron Reactor
GDR	Giant Dipole Resonance
GLQ	Gauss-Legendre Quadrature
GLQPI	Gauss-Legendre Quadrature-based Piecewise Integration
JEFF	(OECD/NEA) Joint Evaluated Fission and Fusion nuclear data library
JENDL	Japanese Evaluated Nuclear Data Library
JHR	Jules Horowitz Reactor
KFS	Konobeyev-Fischer-Simakov (efficiency function)
Lab	Laboratory
LHS	Latin Hypercube Sampling
LWRs	Light Water Reactors
MD	Molecular Dynamics
MF	McKinley-Feshbach (formula)

mNRT	modified Norgett-Robinson-Torrens (DPA model)
NEA	Nuclear Energy Agency
NJOY	A nuclear data processing code
NRT	Norgett-Robinson-Torrens (DPA model)
ODS	Oxide Dispersion-Strengthened (alloy)
OM	Optical Model
OMP	Optical Model Potential
PE	Photoelectric Effect
PENDF	Pointwise Evaluated Nuclear Data File
PFNS	Prompt Fission Neutron Spectra
PKA	Primary Knock-on Atom
PP	Pair Production
PUBI	Peak value-based Unit-Base Interpolation
PWR	Pressurized Water Reactor
RIPL	Reference Input Parameter Library
RPV	Reactor Pressure Vessel
QC	Quick Calculation (option in SRIM-like code)
RML	R-Matrix Limited (format)
RRR	Resolved Resonance Region
SA	Solution Annealed
SFR	Sodium-cooled Fast neutron Reactor
SM	Statistical Model
SRIM	A stochastic binary collision approximation code
TALYS	A nuclear reaction code
TDE	Threshold Displacement Energy
TENDL	TALYS-based Evaluated Nuclear Data Library
TMC	Total Monte Carlo
UBI	Unit-Base Interpolation
URR	Unresolved Resonance Region
XS	Cross Section

1 Introduction

1.1 Nuclear power

Because it is reliable, stable, and environmentally sustainable, nuclear power is one of the most important forms of decarbonized energy for reducing CO_2 emissions. Figure 1-1 shows the percentages of different sources of world electricity production in 2017 (25, 721 TWh) [1]. Currently, nuclear power accounts for approximately 10% of the total world electricity production. Figure 1-2 presents the percentages of different forms of primary energy supply by fuel in 2017 (162,483 TWh) [2]. Nuclear power consists of about 5% of the total primary energy supply. Nuclear energy is thus one of the most important energy resources for reducing global pollution and global warming without restraining the industrial development.

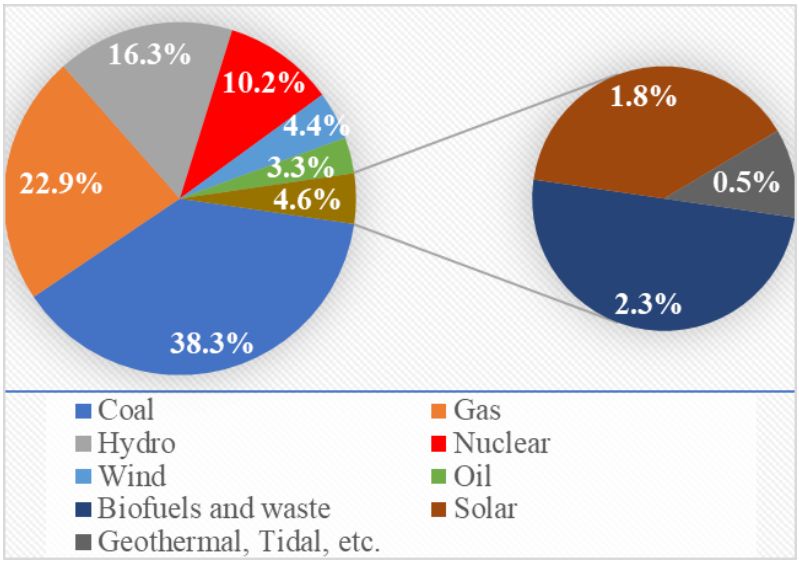

Figure 1-1. Sources of world electricity production in 2017 [1].

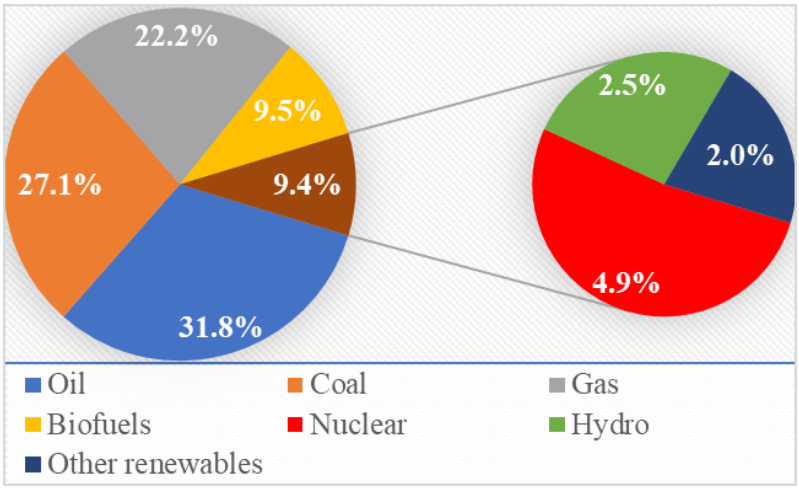

Figure 1-2. Total primary energy supply by fuel in 2017 [2].

Nuclear power is a good choice for the moment. However, current nuclear energy is not so economically competitive owing to the huge cost of building a nuclear power plant. One of the main reasons of the expensive building cost is due to the construction of extensive safety systems other than the three safety barriers (i.e. the fuel cladding, the envelope of the primary system (i.e. Reactor Pressure Vessel (RPV) and primary tubes), and the primary concrete containment). Since the strict requirements of safety systems are necessary for nuclear power plants, one strategy to improve the economic competitiveness of nuclear power is to produce more energy as possible for each reactor, such as the prolongation of the operating lifetime of nuclear reactors and the extension of fuel cycle length (thus reduction of the total time for refueling).

For current Gen II and Gen III commercial Light Water Reactors (LWRs), the recent development of Accident Tolerant Fuel (ATF) after the 2011 Fukushima Daiichi nuclear accident provides opportunities to improve the economic competition. For example, the use of high uranium density fuel can prolong the fuel cycle length [3–8]. The enhanced fuel cladding materials [5, 9–15] improve the mechanical strength of fuel rod, this may also allow prolonging the fuel cycle length with respect to the materials challenge. In addition, owing to their larger thermal neutron absorption cross sections than that of the current zircaloy [16], the enhanced ATF claddings may also reduce the neutron irradiation damage of RPV, so that the operating lifetime of LWRs could be prolonged (needs quantitative analyses).

For Gen IV Sodium-cooled Fast neutron Reactors (SFRs), the irradiation damage of the reactor vessel is not so important because the neutron irradiation of the vessel is much reduced by the shielding of fertile layer, reflector, and a large volume of sodium (and in-vessel neutron shielding in ASTRID [17]) between the inner core and the vessel. However, the lifetime of a fuel assembly (or the cycle length) mainly depends on the total irradiation damage of the fuel cladding. The critical measurement of irradiation damage of the cladding is the accumulated number of Displacement per Atom (DPA) [18, 19], which is a conventional quantity for quantifying the primary radiation damage [20]. The advanced Oxide Dispersion Strengthened (ODS) alloys [21] allow a long fuel lifetime for SFRs.

1.2 Irradiation damage of materials

The irradiation damage is one of the most important challenges for both LWRs and Fast neutron Reactors (FRs). The designed operating lifetime of an LWR and its possible prolongation is mainly based on the irradiation damage of the RPV. The neutron irradiation damage of cladding is also the main characteristic to determine the lifetime of the fuel assembly in SFRs. Here, we briefly explain why the irradiation damage is important for nuclear materials and the objectives of this thesis.

Figure 1-3 shows the typical stress-strain curves for the Solution Annealed (SA) 304L alloy irradiated in OSIRIS experimental reactor (CEA/Saclay) [22]. The chemical composition of the SA 304L steel is given in Table 1-1 [22]. It shows that the neutron irradiation damage obviously changes the characteristics of materials. In addition to the change of the stress-strain curve (including the yield stress and the rupture point) shown in Figure 1-3, radiation damage also leads to the swelling and hardening of materials [23]. A qualitative description of the irradiation dose-dependence of the swelling, hardening, and resistivity is illustrated in Figure 1-4 [23]. Due to the change of properties for irradiated materials, it is of great importance to accurately quantify the irradiation damage of materials for ensuring the operation and satisfying the safety criteria of nuclear reactors.

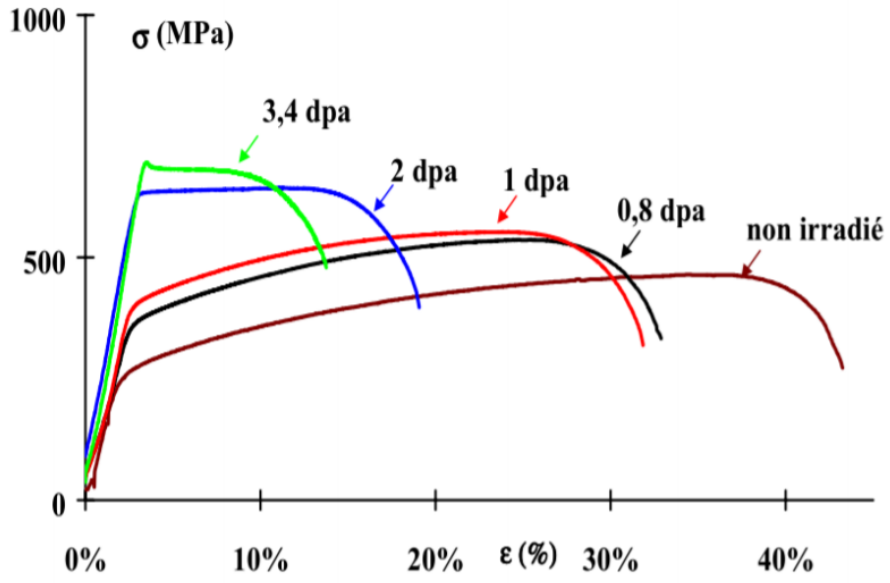

Figure 1-3. Stress-strain curves at 330 °C for the SA 304L alloy after different neutron irradiation doses (in DPA) (taken from Ref. [22, 24]).

Table 1-1. Chemical composition of the SA 304L alloy [22].

Element	C	S	P	Si	Mn	Ni	Cr	Cu	Co	N
wt%	0.022	0.007	0.032	0.36	1.79	9.86	18.16	0.25	0.064	0.061

Current experimental investigations on the irradiation effect of materials are mostly based on the ion or electron irradiation experiments. Because neutron and charged particles have different features, the emulation of neutron irradiation damage with charged particle-induced damage needs to be studied. DPA is a common quantity that intends to unify the irradiation damage induced by different particles, including neutron, light or heavy ions, electron, and photon.

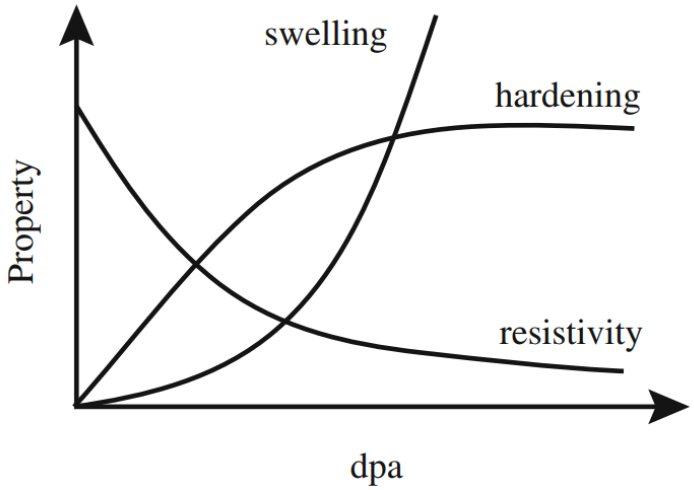

Figure 1-4. Qualitative plot of the dependence of swelling, resistivity, and hardening on irradiation damage (taken from Ref. [23]).

Nevertheless, even though the DPA is conventionally used to quantify the irradiation damage, the methods for calculating the number of DPA varies in different studies, or in a systematic study with different irradiation sources, such as proton and neutron shown in Ref. [25]. Consequently, a more detailed and rigor standard should be proposed to calculate the number of DPA from different irradiation sources, especially for polyatomic materials. A simple proposal is given in Section 4.7.

Nowadays, the so-called DPA can refer to the number of survived Frenkel pairs per atom, the total number of atomic displacements (excluding replacements) per atom, and the equivalent fast neutron dose (neutron energy > 0.1, > 0.5, or > 1 MeV depending on different researches). The second one is currently the standard for industrial applications and nuclear regulation. The first one is somewhat more realistic because it exactly counts the final point defects in irradiated materials. The last one is much further from the concept of DPA but it is still widely used. The main reason is that the current experimental measurement of neutron irradiation damage in reactors is only the measurement of neutron fluence (time-accumulated neutron flux) above a threshold energy (depending on dosimeter), e.g. 0.5 MeV or 1 MeV.

Because of the aforementioned problems for calculating the DPA, detailed methods are required for more accurate calculation of DPA. On the other hand, as previously explained that safety is one of the most important characteristics for nuclear reactor. Figure 1-5 illustrates the example of different margins for nuclear fuel. Similarly, an unique value of DPA without uncertainty is not enough for design, operation, and nuclear regulation. Therefore, in addition to the calculation of DPA, the present work also includes the uncertainty estimates of DPA by propagating the uncertainties of different domains, including nuclear data, DPA models, and neutronic calculations.

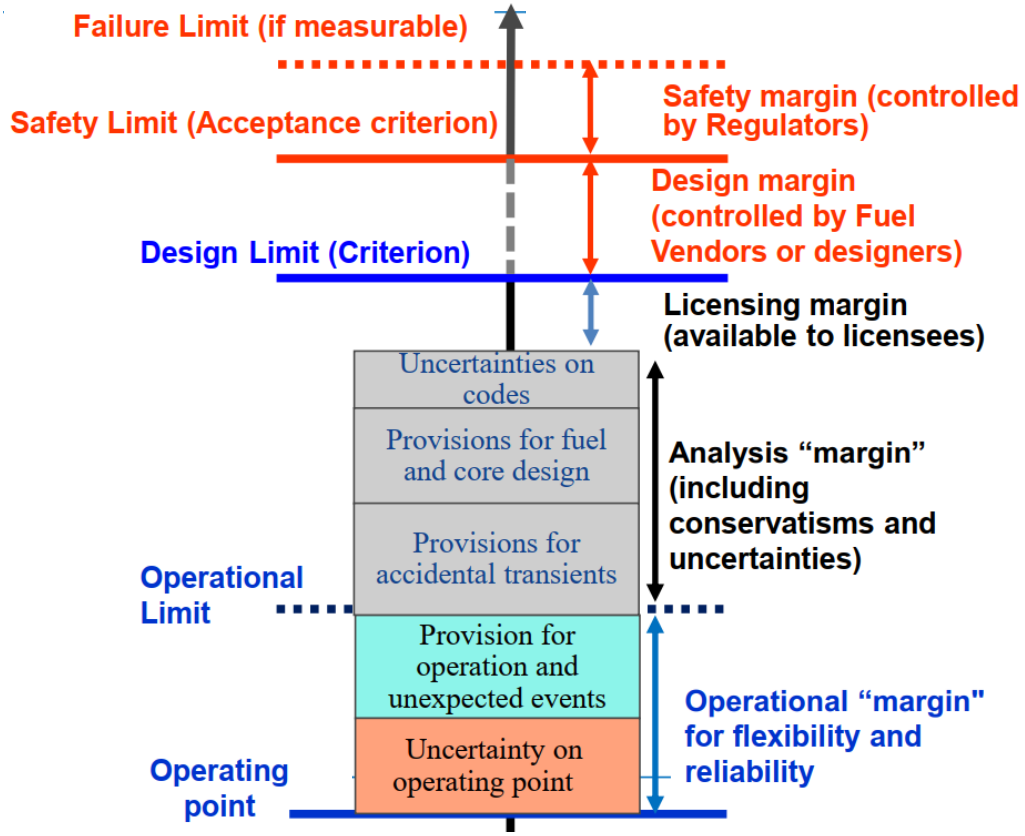

Figure 1-5. Schematic of safety margins (taken from Ref. [26]).

1.3 Objectives of this thesis

This thesis focuses on the proposition and investigation of methodologies for accurate calculation of DPA and the corresponding uncertainty for irradiated materials. The objectives include revisiting the models and methods for computing DPA from nuclear reactions. Then, the improvement of models and computation methodologies is proposed and studied. Our studies cover neutron-induced recoil energy, the subsequent damage cross section, damage rate calculation, and uncertainty quantification of DPA rate. In addition to neutron irradiation, other irradiation sources, such as electron, positron, photon, beta decay, and fission products for fuel cladding, are also considered. We intend to provide a complete schema and state potential problems for DPA calculation.

Some numerical results shown in this thesis are only examples of applications for specific cases, these results are not necessarily general for all cases. However, the methodologies presented in this thesis are applicable for any specific study. Using the same methodologies, one could obtain similar conclusions for most cases.

1.4 Overview of this thesis

The main structure of this thesis is ordered from micro to macro: Section 2 Nuclear reaction models and nuclear data (nuclear level), Section 3 Primary radiation damage models (atomic level), Section 4 Calculation of damage cross sections (from nuclear level to atomic level), Section 5 Calculation of DPA rates (applicable quantity for industrial needs), Section 6 Methods for uncertainty propagation (uncertainty estimates), Section 7 Uncertainty assessment of damage rate in a PWR vessel (a simplified example for industrial application), and Conclusions and prospects.

I would like to indicate that Sections 2, 3, and 6 are mainly the reviews of the current methods with some examples calculated in the present work for helping the understanding. The new contributions to the methodologies presented in these sections are: Section 2.5.2 on the interpolation of energy-angular distributions given in an Evaluated Nuclear Data File (ENDF), Section 3.6 describing a simple function for calculating the athermal recombination-corrected DPA, and Section 3.7.2 proposing the concept of residual energy transfer for analytically calculating the number of atomic displacements within binary collision approximation.

Section 4 presents the methodologies for computing the irradiation damage cross section for different reaction types. The methods (except basic knowledge such as two-body kinematics and the method already proposed in Ref. [27]) are originally proposed and/or verified in the present work. Works summarized in Section 5 are the originally proposed in this Ph.D thesis, certainly excluding some commonly known methods, such as the calculation of reaction rate. Section 7 shows the examples for uncertainty estimates in the RPV of a simplified Pressurized Water Reactor (PWR) mock-up using the methods presented in the above sections. Section 8 includes the main conclusion of this Ph.D thesis and the potential prospects for completing this work.

Owing to the numerous theories and definitions presented in this thesis, some symbols are redefined in different sections, especially in Sections 2 and 3. It is also possible that some quantities are expressed by different symbols according to different conventions in different disciplines. For readers, we keep in mind different theories (and the reasonings in several cases if necessary) and do not memorize the significance of each symbol.

2 Nuclear reaction models and nuclear data

Because most of the atomic displacements in nuclear reactors are initialized by nuclear reactions, this section briefly summarizes the nuclear reaction models used to compute damage cross sections. Figure 2-1 illustrates the total cross section of ^{56}Fe in JEFF-3.1.1 [28]. In the Resolved Resonance Region (RRR), the theoretical model is the R-matrix theory, which is presented in Section 2.1. In the high-energy region, owing to the lack of experimental resolution of resonance and the contribution of direct and/or pre-equilibrium reactions, the R-matrix is no longer pertinent. This region is called the continuum region, where the optical model for total cross section, potential elastic scattering cross section (c.f. Section 2.2) and the statistical model for nuclear reactions cross sections (c.f. Section 2.3) are applicable.

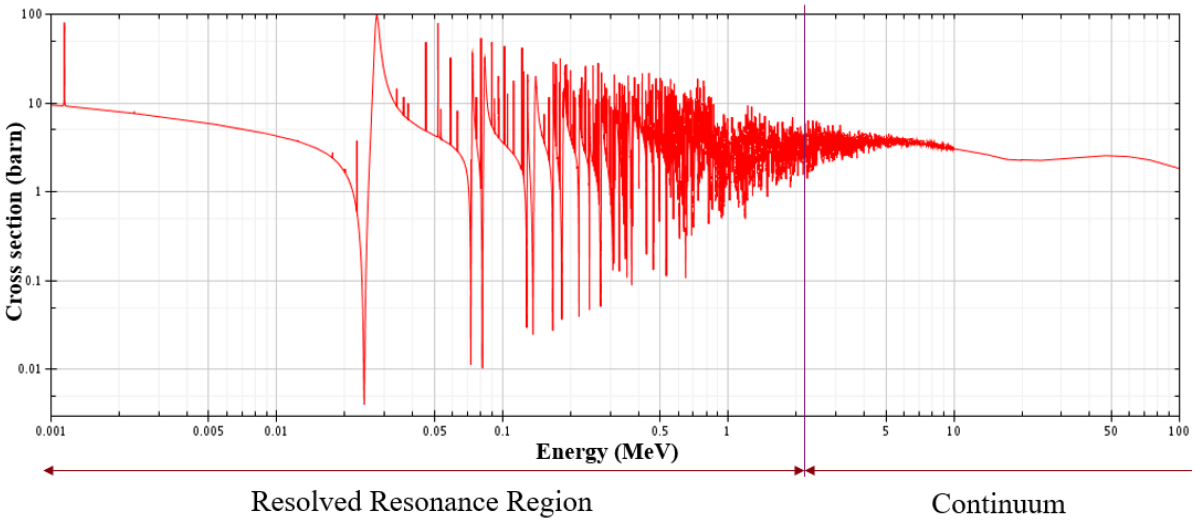

Figure 2-1. Total cross section of ^{56}Fe (JEFF-3.1.1).

In addition to nuclear cross sections, angular distribution and energy-angular distribution are necessary for computing radiation damage. Section 2.4 briefly shows the theory for calculating angular distribution. The calculation and conventional form of energy-angular distribution are presented in Section 2.5. Because of numerous parameters and symbols in nuclear models, some symbols may be redefined in some subsections. The redefinition of such symbols and their physical significance does not change the understanding of nuclear models in the corresponding subsections.

2.1 R-matrix theory

In the compound nucleus model (the time scale of compound nucleus reactions is of the order of 10^{-18} s - 10^{-15} s), the cross section from entrance channel c to exit channel c' with total angular momentum J is given by [29, 30]:

$$\sigma_{cc'}(E) = \frac{\pi}{k_\alpha^2} g_c \left| e^{2iw_C}\delta_{cc'} - U_{cc'} \right|^2 \delta_{JJ'} \quad (2\text{-}1)$$

where α represents the two particles making up the channel ($c = (\alpha, l, s, J)$), $k_\alpha = K_\alpha/\hbar$ where K_α is the momentum ($K_\alpha^2 = \frac{2mM^2}{(m+M)^2}E$) in the Center-of-Mass (CM) system, w_C is the Coulomb phase shift (zero for non-Coulomb channels), g_c is the statistical spin factor:

$$g_c = \frac{2J+1}{(2i+1)(2I+1)} \quad (2\text{-}2)$$

where *i* and *I* are the spins of the incident particle and the target, respectively. *U* is the scattering matrix, which can be expressed by:

$$U_{cc'} = \Omega_c W_{cc'} \Omega_{c'} \quad (2\text{-}3)$$

where $\Omega_c = e^{i(w_C - \varphi_c)}$ with φ_c being the potential scattering phase shift deduced from the Schrödinger equation. *W* is a matrix which can be calculated by:

$$W = P^{1/2}(\mathbf{1} - RL)^{-1}(\mathbf{1} - RL^*)P^{-1/2} \quad (2\text{-}4)$$

where **1** represents the identity matrix and

$$L = (S - B) + iP \quad (2\text{-}5)$$

where *P* and *S* are respectively the penetration factor and the shift factor deduced from the Schrödinger equation, *B* is the wave function boundary condition at the channel limit (i.e. channel radius) a_c. The elements of R-matrix are expressed as [29]:

$$R_{cc'}(E) = \sum_\lambda \frac{\gamma_{\lambda c}\gamma_{\lambda c'}}{E_\lambda - E} \quad (2\text{-}6)$$

where λ labels the discrete compound nucleus states, E_λ is the energy eigenvalue of state λ, $\gamma_{\lambda c}$ is the "reduced width amplitude" for state λ and channel *c* calculated by the width $\Gamma_{\lambda c}$ and the penetration factor P_c:

$$\Gamma_{\lambda c} = 2P_c\gamma_{\lambda c}^2 \quad (2\text{-}7)$$

Because the elements of the R-matrix describe the "internal" interaction in a nucleus, it is difficult (impossible for the time-being) to determine the elements $R_{cc'}$. Therefore, some simplified calculable R-matrix models are developed for the evaluation process. In current nuclear data libraries, the single-level/multilevel Breit-Wigner formula [31] and the Reich-Moore model [32] are widely used. It is noted that the inelastic scattering channels are not included in the current Reich-Moore format in ENDF. The calculation of inelastic scattering in the resonance region requires additional parameters stored in the recently proposed R-matrix Limited (RML) format. The resonance parameters are given in file 2 (conventionally called MF2) in ENDF-6 format.

In order to simply show the relationship between the cross section and resonance

parameters, Figure 2-2 illustrates the example of neutron elastic scattering cross section of ^{56}Fe around 46 keV with perturbed parameters with the CONRAD code [33]. The parameters from JEFF-3.1.1 are given in Table 2-1 [28]. The eigenvalue E_λ determines the energy peak of the resonance. The widths Γ_γ and Γ_n implicitly influence both the width and the peak value of the resonance.

Table 2-1. Resonance parameters of n+^{56}Fe of the resonance centered at 46.0535 keV in JEFF-3.1.1 [28].

Parameter	Model	E_λ (keV)	Γ_γ (meV)	Γ_n (meV)	J^π
Value	Reich-Moore	46.0535	265.125	5140	$3/2^-$

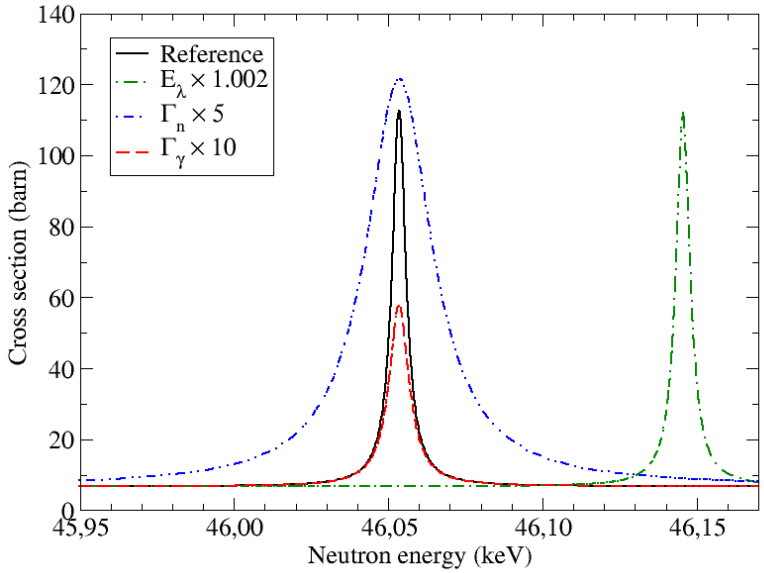

Figure 2-2. Neutron elastic scattering cross section of ^{56}Fe with perturbed parameters (calculated by CONRAD) [34].

2.2 Optical model

The R-matrix theory is the phenomenological model in the RRR and Unresolved Resonance Region (URR) when averaging over multiple compound states, but it is not applicable in the continuum region due to the lack of experimental resolution of resonance and because reactions are direct or pre-equilibrium. In the high-energy region, the Optical Model (OM) is usually used to calculate the total and shape elastic scattering cross sections. In the OM, one solves the Schrödinger equation by giving a potential, of which a usually used form is [35]:

$$\begin{aligned} \mathcal{U}(r,E) \quad = \quad & -\mathcal{V}_V(r,E) - i\mathcal{W}_V(r,E) - i\mathcal{W}_S(r,E) + \\ & [\mathcal{V}_{SO}(r,E) + i\mathcal{W}_{SO}(r,E)]\boldsymbol{l}\cdot\boldsymbol{\sigma} + \mathcal{V}_C(r) \end{aligned} \tag{2-8}$$

where E is the energy of the incident particle, r is the distance between the incident particle and the target nucleus. The subscript V, S, SO, and C respectively represent the Volume, Surface, Spin-Orbit, and Coulomb terms. $\mathcal{V}_i$ and $\mathcal{W}_i$ are the real and imaginary components of the potential for the term $i = V, S, SO, C$. $\boldsymbol{l}$ and $\boldsymbol{\sigma}$ are the orbital angular momentum vector and Pauli matrices vector, respectively.

In general, the position-dependence and the energy-dependence are separated into two individual functions:

$$\mathcal{X}_i(r, E) = X_i(E) f_i(r) \tag{2-9}$$

where $\mathcal{X} = \mathcal{V},\ \mathcal{W}$ and $i = V, S, SO$, X_i is the position-independent potential. The most widely used position-dependent functions are $f_V(r) = f(r, R_V, a_V)$ if $i = V$ and $f_i(r) = g(r, R_i, a_i)$ if $i = S, SO$ where f is a Woods-Saxon form [36] and g is proportional to the differential of f:

$$f(r, R_i, a_i) = \frac{1}{1+\exp\left[(r-R_i)/a_i\right]} \tag{2-10}$$

$$g(r, R_i, a_i) = -4a_i \frac{d}{dr} f(r, R_i, a_i) \tag{2-11}$$

Morillon and Romain proposed a potential based on the Dispersive Optical Model (DOM) for neutrons with incident energies from 1 keV to 200 MeV as [37]:

$$\begin{aligned} \mathcal{U}(r, E) = \quad & [V_V(E) + iW_V(E)] f(r, R, a) + [V_S(E) + iW_S(E)] g(r, R, a) \\ & + [V_{SO}(E) + iW_{SO}(E)] \frac{1}{r} \left(\frac{h}{m_\pi c}\right)^2 g(r, R, a) \boldsymbol{l} \cdot \boldsymbol{\sigma} \end{aligned} \tag{2-12}$$

In the DOM, the causality (a scattered wave cannot be emitted before the arrival of the incident wave) implies that the real part and imaginary part are connected by a dispersion term [38]:

$$\Delta V(E) = \frac{P}{\pi} \int_{-\infty}^{+\infty} \frac{W(E')}{E' - E} dE' \tag{2-13}$$

where P is the Cauchy principal value of the integral.

In the Morillon-Romain potential, the shape functions f and g are the same for different interactions, whereas different parameters are used for different parts in general OM potentials such as Koning-Delaroche [35]. Morillon and Romain obtained the systematics for the radius R and the diffuseness a for most spherical nuclei as [37]:

$$R = (1.295 - 2.7 \times 10^{-4} A) A^{1/3} \text{ (fm)} \tag{2-14}$$

$$a = 0.566 + 5 \times 10^{-9} A^3 \text{ (fm)} \tag{2-15}$$

where A is the mass number of the nucleus. It is noted that the best-fitted radius R is different from the systematics for light nuclei, such as $R = 1.268 A^{1/3}$ fm for ^{56}Fe [37]. Compared with the Koning-Delaroche OM Potential [35] (OMP), that of Morillon-Romain has less geometrical parameters and a better description of cross sections.

However, the angular distribution of elastic scattering calculated with the DOM agrees generally less with the experimental data than that of Koning-Delaroche, including for ^{56}Fe [37].

For a deformed nucleus, the prior value for the radius R in the Woods-Saxon form is given by [39]:

$$R = (1.295 - 2.7 \times 10^{-4} A) A^{1/3} [1 + \beta_2 Y_{20}(\Omega) + \beta_4 Y_{40}(\Omega)] \text{ (fm)} \qquad (2\text{-}16)$$

where β_2 and β_4 are quadrupole and hexadecapole deformation parameters, respectively. $Y_{20}(\Omega)$ and $Y_{40}(\Omega)$ are the corresponding spherical harmonics as a function of the body-fixed system Ω. In principle, if it is necessary, one can consider $Y_{60}(\Omega)$, $Y_{80}(\Omega)$, etc. and the corresponding deformation parameters.

All optimized prior parameters in the OMPs can be found in the Reference Input Parameter Library (RIPL) [40]. With a given OMP, ECIS [41] performs the optical calculations by solving the Schrödinger equation and the subsequent calculations using the wave functions. ECIS calculations provide cross sections and angular distributions for the shape elastic scattering (i.e. direct reaction) that is directly used in damage cross section calculations. Moreover, the optical calculation gives the neutron transmission coefficients that are mandatory for calculating other partial reactions.

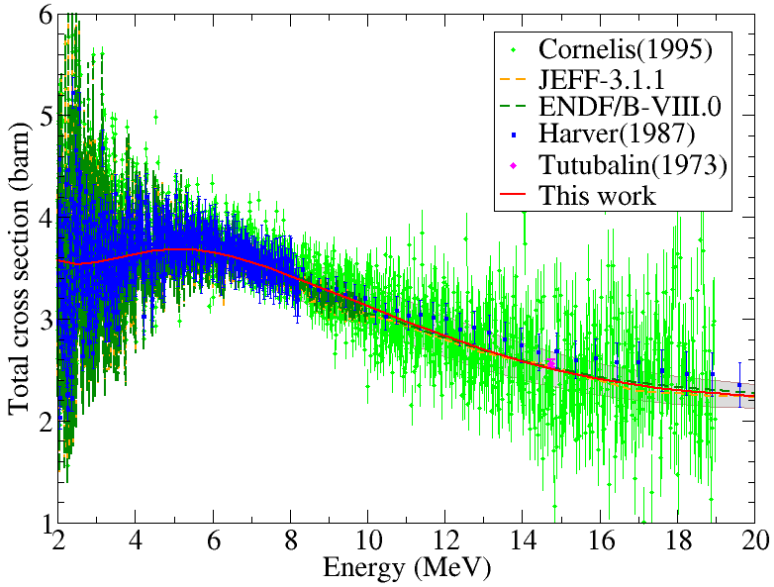

Figure 2-3. Total cross section of ^{56}Fe from ECIS calculation with optimized parameters [42].

Figure 2-3 shows the example of the total cross section on ^{56}Fe from ECIS calculation with optimized parameters in comparison with experimental data from EXFOR [43]. The OM calculations with optimized parameters are validated against experimental data in the high-energy region, where the cross section varies smoothly with neutron energy. However, the fluctuations below 5 MeV cannot be calculated with the OM. Moreover, it is hard to produce such fluctuations with the R-matrix formalism

because the forms generally do not correspond to resonances or interferences. The extension of the resonance parameters up to 2 MeV for ^{56}Fe is ongoing in our laboratory [44, 45], whereas the R-matrix is only limited below 850 keV in the current JEFF evaluations. Nevertheless, the model defects for predicting the fluctuation of cross section above the limit of R-matrix but below the OM region should be further investigated in future.

2.3 Statistical model

For the calculation of nuclear reactions cross sections, the Statistical Model (SM) is widely used. In the SM, the neutron cross sections are given by the Hauser-Feshbach formula [46]:

$$\sigma_{cc'} = \pi\tilde{\lambda}_c^2 g_c \frac{T_c T_{c'}}{\sum_i T_i} W_{cc'} \tag{2-17}$$

where T_i represents the average transmission coefficient of the reaction channel i, and $\tilde{\lambda}_c = \lambda_c/2\pi$ is the reduced De Broglie wavelength of the incident particle. $W_{cc'}$ is the width fluctuation correction factor between the entrance channel c and the exit channel c' (see also Refs. [47–49] for more details). Numerical comparisons between different approaches of $W_{cc'}$ can be found in Ref. [49].

In the Hauser-Feshbach formula, the neutron transmission coefficient T_n is calculated by using the OM in ECIS [41]. The transmission coefficients for other channels can be directly calculated by TALYS with a specific model. For example, the gamma-ray transmission coefficient T_γ for multipolarity ℓ of type X (where $X = M$ or E represent the magnetic or electric transition) can be calculated by:

$$T_{X\ell} = 2\pi f_{X\ell}(E_\gamma) E_\gamma^{X\ell} \tag{2-18}$$

where E_γ denotes the γ energy and $f_{X\ell}$ is the energy-dependent γ ray strength function, which is given by Kopecky and Uhl [50].

The generalized Lorentzian form is proposed for $E1$:

$$f_{E1}(E_\gamma) = K_{E1}\left[\frac{E_\gamma \tilde{\Gamma}_{E1}(E_\gamma)}{\left(E_\gamma^2 - E_{E1}^2\right)^2 + E_\gamma^2 \tilde{\Gamma}_{E1}^2(E_\gamma)} + \frac{0.7\Gamma_{E1}4\pi^2T^2}{E_{E1}^3}\right]\sigma_{E1}\Gamma_{E1} \tag{2-19}$$

The Giant Dipole Resonance (GDR) shape given by Brink and Axel [51, 52] is suggested for $M1$ and $E2$ radiation transition [50]:

$$f_{X\ell}(E_\gamma) = K_{X\ell}\frac{\sigma_{X\ell}E_\gamma\Gamma_{X\ell}^2}{\left(E_\gamma^2 - E_{X\ell}^2\right)^2 + E_\gamma^2\Gamma_{X\ell}^2} \tag{2-20}$$

The common coefficient in the above two forms of $f_{X\ell}$ is:

$$K_{X\ell} = \frac{1}{(2\ell+1)\pi^2\hbar^2c^2} \tag{2-21}$$

The energy-dependent damping width $\tilde{\Gamma}_{E1}(E_\gamma)$ and the nuclear "temperature" T are given by:

$$\tilde{\Gamma}_{E1}(E_\gamma) = \Gamma_{E1}\frac{E_\gamma^2+4\pi^2T^2}{E_{E1}^2} \tag{2-22}$$

$$T = \sqrt{\frac{E_n-S_n-\Delta-E_\gamma}{a(S_n)}} \tag{2-23}$$

where S_n is the neutron separation energy, E_n is the incident neutron energy, Δ is the pairing energy, and a is the level density parameter at S_n.

The normalized gamma-ray transmission coefficient is given by:

$$T_\gamma = \frac{2\pi\Gamma_\gamma}{D_0} \tag{2-24}$$

The Gilbert-Cameron formula [53] is widely used for computing the *s*-wave neutron average level spacing D_0 and other levels. In the Gilbert-Cameron formula, the Constant Temperature Model (CTM) is used to describe the cumulated excited level below S_n (Z, N+1):

$$N(E) = \exp\left(\frac{E-E_0}{T}\right) \tag{2-25}$$

Hence, the excited level density can be obtained as:

$$\rho(E) = \frac{dN(E)}{dE} = \frac{1}{T}\exp\left(\frac{E-E_0}{T}\right) \tag{2-26}$$

At high energy, the Fermi gas model [54] is used to describe the level density.

For statistical model calculations in the continuum region, the TALYS code [55] is widely used and was coupled into CONRAD [33]. It is notable that the OM code ECIS was also included in TALYS, so that both the OM calculations and the SM calculations can be performed with TALYS.

For calculating damage cross sections, since TALYS calculates the spectra of recoil nuclei from two-body kinematics, CONRAD provides the option for the damage calculation directly using the spectra computed by TALYS [34]. This option can reduce the computation time for total or partially total damage cross sections but is only available in the fast energy region for compound reactions. For scattering reaction, we combine the damage cross section computed with the recoil spectrum of TALYS and that computed with kinematics and angular distribution of the shape elastic scattering from ECIS calculation. However, it should be noted that the azimuthal angle and relativistic kinematics are not yet considered for computing recoil spectra in TALYS [55]. More details on the damage cross section calculation are with CONRAD are published in Refs. [34, 56].

Figure 2-4 shows the elastic and inelastic neutron scattering cross sections on ^{56}Fe from TALYS calculation with optimized parameters in comparison with experimental

data from EXFOR [43]. Elastic scattering includes the shape elastic scattering determined by OM calculations from ECIS and the nuclear reaction-induced elastic scattering from TALYS calculations. Both elastic scattering and inelastic scattering reactions use the incident neutron transmission coefficient T_n from OM calculations. Similar to the OM, the SM with optimized parameters corresponds well with experimental data in the high-energy region but it cannot describe the fluctuations below 5 MeV.

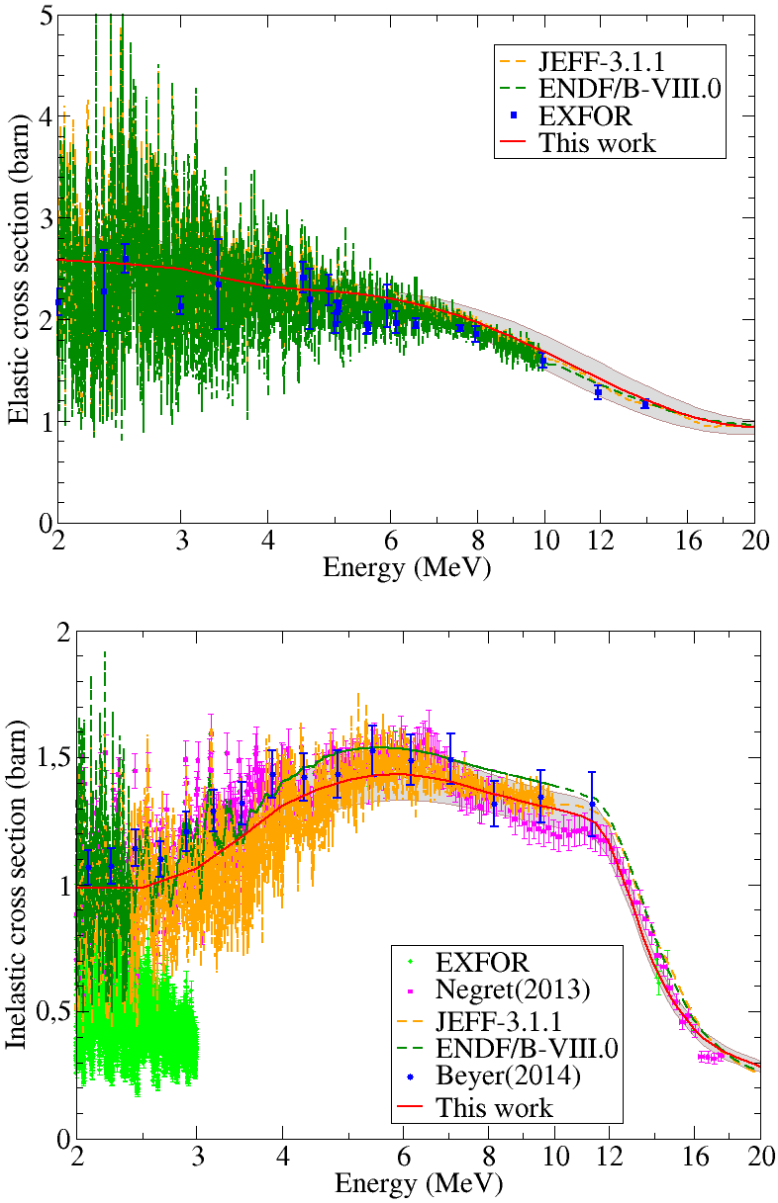

Figure 2-4. Elastic (upper) and inelastic (lower) neutron scattering cross sections of ^{56}Fe from TALYS calculation with optimized parameters [42].

2.4 Blatt-Biedenharn formula and angular distribution

The above three subsections describe models for calculating the angle-integrated

nuclear cross section, this subsection briefly presents the Blatt-Biedenharn formula [57] on the angular distribution. According to Blatt and Biedenharn, the angular distribution can be expressed as:

$$\frac{d\sigma_{cc'}}{d\Omega_{CM}} = \tilde{\lambda}_c^2 \sum_L B_{Lcc'}(E) P_L(\mu) \tag{2-27}$$

where P_L is the Legendre polynomial of degree L and μ is the cosine of neutron scattering angle in the CM system.

2.4.1 Elastic scattering of a spinless particle

For a spinless particle far from the scattering source, the angular distribution is simply calculated by:

$$\frac{d\sigma_{cc'}}{d\Omega_{CM}} = |f_w(\theta)|^2 \tag{2-28}$$

where $f_w(\theta)$ is the angle-dependent factor. Blatt and Biedenharn showed that:

$$f_w(\theta) = i\sqrt{\pi}\tilde{\lambda}_c \sum_{l=0}^{\infty} \sqrt{(2l+1)}\left(1 - e^{2i\varphi_l}\right) Y_{l,0}(\theta) \tag{2-29}$$

where φ_l is the phase-shift of l-wave and $Y_{l,0}(\theta)$ is the normalized spherical harmonics. Using the equality:

$$|f_w(\theta)|^2 = f_w(\theta) f_w^*(\theta) \tag{2-30}$$

where the symbol * represents the conjugate, the Legendre coefficient B_L is obtained as:

$$B_L = \sum_{l=0}^{\infty} \sum_{l'=|l-L|}^{l+L} (2l+1)(2l'+1)\,(ll'00|ll'L0)^2 \sin\varphi_l \sin\varphi_{l'} \cos(\varphi_l - \varphi_{l'}) \tag{2-31}$$

where $(ll'00|ll'L0)$ is the Clebsch-Gordan coefficient calculated by [58, 59]:

$$(ll'00|ll'L0) = l!\,l'!\,L!\sqrt{(2L+1)(l+l'-L)!\,(L+l-l')!\,(L+l'-l)!/(l+l'+L+1)!} \times \sum_n (-1)^n/[n!\,(l+l'-L-n)!\,(l-n)!\,(l'-n)!\,(L-l'+n)!\,(L-l+n)!] \tag{2-32}$$

The summation parameter n is constrained to ensure the number in each factorial to be positive.

In the case where $L = 0$, the only possible value of l' is $l' = l$. The corresponding Clebsch-Gordan coefficient is:

$$(ll00|ll00) = 1/\sqrt{(2l+1)} \tag{2-33}$$

The Legendre coefficient becomes:

$$B_0 = \sum_{l=0}^{\infty} (2l+1)\sin^2\varphi_l \tag{2-34}$$

Because a phase shift between the incident wave and the outgoing wave calculated from the Schrödinger equation depends on the incident energy, the Legendre

coefficients are energy-dependent, i.e.,

$$B_L(E) = \sum_{l=0}^{\infty} \sum_{l'=|l-L|}^{l+L} (2l+1)(2l'+1)\,(ll'00|ll'L0)^2 \sin\varphi_l(E)\sin\varphi_{l'}(E)\cos\left(\varphi_l(E) - \varphi_{l'}(E)\right) \tag{2-35}$$

For simplifying the notations, the variable E is not specifically noted in the section of the angular distribution.

2.4.2 General two-body reaction

Let $c = (\alpha,s)$ where α and s denote the incident channel index and channel spin in this subsection. The exit channel is similarly denoted by $c' = (\alpha',s')$. We define a function $\mathcal{H}(L,\alpha,s,l_1,J_1,l_2,J_2,\alpha',s',l_1',l_2')$ as:

$$\mathcal{H} \equiv Z(l_1J_1l_2J_2,sL)Z(l_1'J_1l_2'J_2,s'L) \times \Re[\Delta(1,\alpha s \to \alpha' s')^*\Delta(2,\alpha s \to \alpha' s')] \tag{2-36}$$

where $\Re$ represents the real part and Δ is defined as:

$$\Delta(x,\alpha s \to \alpha' s') \equiv \delta_{\alpha\alpha'}\delta_{ss'}\delta_{l_x l_x'} - U_{J_x}(\alpha s l_x \to \alpha' s' l_x') \tag{2-37}$$

where U is the scattering matrix. The Z function in $\mathcal{H}(L,\alpha,s,l_1,J_1,l_2,J_2,\alpha',s',l_1',l_2')$ is defined by:

$$\begin{aligned} Z(l_1J_1l_2J_2,sL) \equiv \quad & i^{L-l_1+l_2}\sqrt{(2l_1+1)(2l_2+1)(2J_1+1)(2J_2+1)} \\ & \times W(l_1J_1l_2J_2,sL)(l_1l_200|l_1l_2L0) \end{aligned} \tag{2-38}$$

where $W(l_1J_1l_2J_2,sL)$ is [60]:

$$W(l_1J_1l_2J_2,sL) = \Lambda(l_1J_1l_2J_2,sL)w(l_1J_1l_2J_2,sL) \tag{2-39}$$

where

$$\begin{aligned} w(l_1J_1l_2J_2,sL) \equiv \quad & \sum_n \left[\frac{(-1)^{n+l_1+J_1+l_2+J_2}(n+1)!}{(n-l_1-J_1-s)!(n-l_2-J_2-s)!(n-l_1-l_2-L)!(n-J_1-J_2-L)!}\right. \\ & \left. \times \frac{1}{(l_1+J_1+l_2+J_2-n)!(l_1+J_2+s+L-n)!(l_2+J_1+s+L-n)!}\right] \end{aligned} \tag{2-40}$$

and

$$\Lambda(l_1J_1l_2J_2,sL) = \Upsilon(l_1J_1s)\Upsilon(l_2J_2s)\Upsilon(l_1l_2L)\Upsilon(J_1J_2L) \tag{2-41}$$

with the definition of:

$$\Upsilon(abc) = \sqrt{\frac{(a+b-c)!(b+c-a)!(c+a-b)!}{(a+b+c+1)!}} \tag{2-42}$$

Using the notation of $\mathcal{H}(L,\alpha,s,l_1,J_1,l_2,J_2,\alpha',s',l_1',l_2')$, the Legendre coefficient for a general two-body reaction is calculated by [57]:

$$B_L = (-1)^{s'-s}\left\{\frac{1}{4}\sum_{J=0}^{\infty}\sum_{l=|J-s|}^{J+s}\sum_{l'=|J-s'|}^{J+s'}\mathcal{H}(L,\alpha,s,l,J,l,J,\alpha',s',l',l') + \frac{1}{2}\times \right.$$
$$\sum_{J_1=0}^{\infty}\sum_{l_1=|J_1-s|}^{J_1+s}\sum_{l_1'=|J_1-s'|}^{J_1+s'}\left[\sum_{J_2=J_1+1}^{\infty}\sum_{l_2=|J_2-s|}^{J_2+s}\sum_{l_2'=|J_2-s'|}^{J_2+s'}\mathcal{H}(L,\alpha,s,l_1,J_1,l_2,J_2,\alpha',s',l_1',l_2')\right.$$
$$+\sum_{l_2=l_1+1}^{J_1+s}\sum_{l_2'=|J_1-s'|}^{J_1+s'}\mathcal{H}(L,\alpha,s,l_1,J_1,l_2,J_2=J_1,\alpha',s',l_1',l_2')$$
$$\left.\left.+\sum_{l_2'=l_1'+1}^{J_1+s'}\mathcal{H}(L,\alpha,s,l_1,J_1,l_2=l_1,J_2=J_1,\alpha',s',l_1',l_2')\right]\right\} \quad (2\text{-}43)$$

2.4.3 Conventions of angular distribution

Since Blatt-Biedenharn formula shows that the angle-differential cross section is a combination of Legendre polynomials, the conventional differential cross section is expressed by:

$$\frac{d\sigma}{d\Omega} = \sum_L A_L(E)P_L(\mu) \quad (2\text{-}44)$$

where the Legendre coefficient is:

$$A_L = \tilde{\lambda}_c^2 B_L \quad (2\text{-}45)$$

This convention is used in CONRAD.

For two-body reactions, because the angular distribution on the azimuthal direction is always isotropic, the differential on the solid angle is simplified into $d\Omega = 2\pi d\mu$. Therefore, one can define the normalized angular distribution *f* as:

$$f \equiv \frac{d\sigma}{\sigma d\mu} \quad (2\text{-}46)$$

f is also the probability density function in [-1, 1], i.e.,

$$\int_{-1}^{1} f(\mu,E)d\mu = 1 \quad (2\text{-}47)$$

The definition of *f* and Eq. (2-44) imply that:

$$f(\mu,E) = \sum_L [2\pi A_L(E)/\sigma(E)]\, P_L(\mu) \quad (2\text{-}48)$$

On the other hand, Legendre polynomial satisfies:

$$\int_{-1}^{1} P_L(\mu)P_{L'}(\mu)d\mu = 2\delta_{LL'}/(2L+1) \quad (2\text{-}49)$$

where the Dirac function $\delta_{LL'}$ is:

$$\delta_{LL'} = \begin{cases} 1 & L' = L \\ 0 & L' \neq L \end{cases} \quad (2\text{-}50)$$

If one defines the Legendre coefficient a_L as the projection of *f* on P_L:

$$a_L(E) \equiv \int_{-1}^{1} f(\mu,E)P_L(\mu)d\mu \quad (2\text{-}51)$$

The energy angular distribution becomes:

$$f(\mu,E) = \sum_L \frac{2L+1}{2} a_L(E)P_L(\mu) \quad (2\text{-}52)$$

where

$$a_L = \frac{4\pi A_L}{(2L+1)\sigma} \tag{2-53}$$

This convention is used in ENDF format. The angular distribution is given in file 4 (conventionally called MF4) in ENDF.

Blatt-Biedenharn formula allows us to physically compute angular distributions. Figure 2-5 shows the examples of Legendre coefficients for neutron elastic scattering cross section of ^{56}Fe using the resonance parameters from JEFF-3.1.1. Nevertheless, it is not easy to determine the parameters in phenomenological nuclear reaction models satisfying all types of nuclear data, e.g., cross section, angular distribution, reaction Q-value, photon emission, etc. In most current evaluations, the resonance parameters are only optimized for cross sections. Because the angular distribution is very sensitive to the spin and parity, optimized parameters for cross section cannot necessarily be suitable for angular distributions. For the examples shown in Figure 2-5, resonances, interferences, and smooth variation of the absolute Legendre coefficients are found in Blatt-Biedenharn calculations using JEFF-3.1.1 resonance parameters, whereas the corresponding absolute Legendre coefficients $A_L \propto \sigma a_L$ for $L \in \{1,2,3,4\}$ deduced from JEFF-3.1.1 MF4 present only resonances as the cross section because the normalized Legendre coefficients a_L given in JEFF-3.1.1 MF4 are smooth (e.g. interpolation on two neighbor points of 46.309 keV and 52.475 keV).

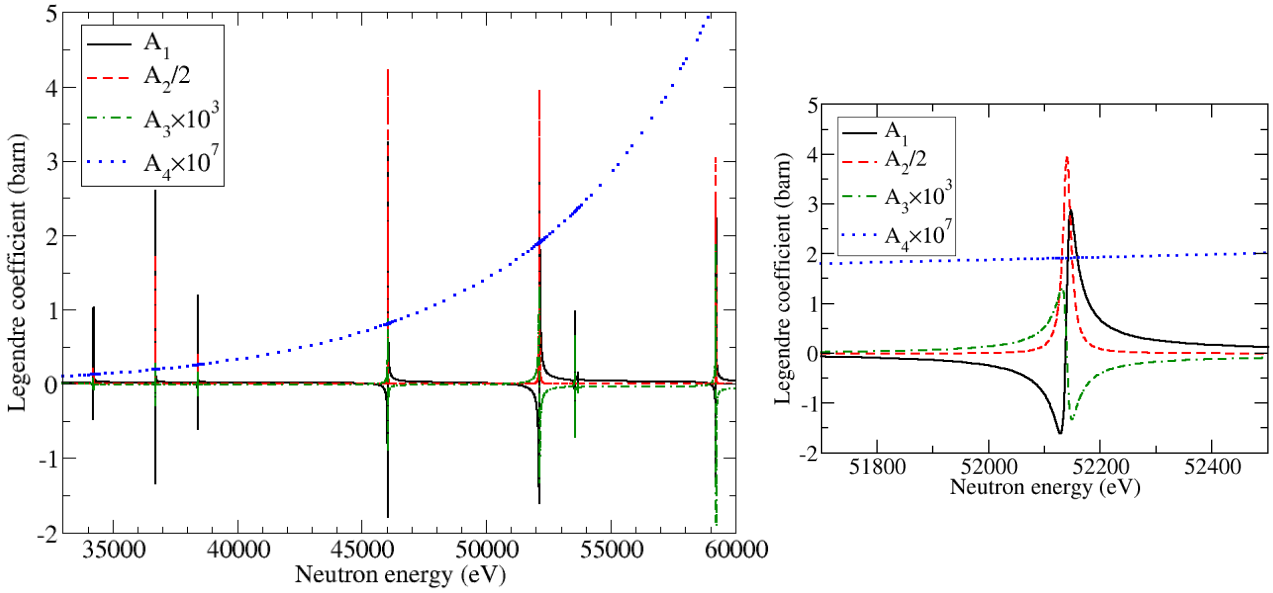

Figure 2-5. Legendre coefficients for neutron elastic scattering cross section of ^{56}Fe using resonance parameters from JEFF-3.1.1 and the zoom close to the resonance at 52.1397 keV (calculated by CONRAD).

In practice, angular distributions (especially for these in the RRR) are often

mathematical fittings based on experimental data rather than the calculations using Blatt-Biedenharn formula. The evaluators fit experimental data using a combination of Legendre polynomials, or directly tabulate the angular distribution on a specific grid of incident energy and emission angle (or its cosine). Therefore, cross sections and angular distributions are usually not correlated and physically incoherent in most of current ENDFs.

Recently, a set of resonance parameters well describing both cross sections and angular distributions was evaluated for ^{16}O [61]. This evaluation of n+^{16}O shows the possibility to evaluate physically coherent nuclear data with current phenomenological models (at least in the RRR).

2.5 Energy-angular distribution

For reactions of which the reaction *Q*-value is undetermined due to unresolved excitation levels, the distributions on secondary energy are also required. The energy-angular distribution is given in MF6 in ENDF format. Theoretically, the double-differential cross section can be calculated by:

$$\frac{d\sigma}{d\Omega dE'} = \sum_L A'_L(E,E')P_L(\mu) \tag{2-54}$$

where *E'* is the secondary energy and

$$A'_L(E,E') \equiv \frac{\partial A_L}{\partial E'}(E,E') \tag{2-55}$$

The normalized energy-angular distribution within the ENDF format is:

$$f(\mu,E,E') = \sum_L \frac{2L+1}{2} a_L(E,E')P_L(\mu) \tag{2-56}$$

Similar to angular distribution, the energy-angular distribution in ENDF is given by tabulated values of $a_L(E,E')$ or directly tabulated values of $f(\mu,E,E')$ on a specific grid in file 6 (called MF6).

2.5.1 Kalbach-Mann systematics

In addition to the combination of Legendre polynomials and tabulated values, Kalbach proposed an improved systematics for describing energy-angular distributions [62]:

$$\frac{f(\mu,E,E')}{a_0(E,E')} = \frac{a(E,E')}{2\sinh(a(E,E'))}\left[\cosh(a(E,E')\mu) + f_{MSD}(E,E')\sinh(a(E,E')\mu)\right] \tag{2-57}$$

where f_{MSD} is the fraction of multistep direct process (to be determined and tabulated along with a_0 in ENDF), $a(E,E')$ can be directly given by the evaluator or should be calculated with:

$$a(E,E') = C_1X_1 + C_2X_1^3 + C_3m'MX_3^4 \tag{2-58}$$

where the values of C_1, C_2, and C_3 are given in Table 2-2 and

$$\begin{cases} X_1 = \min\{(\varepsilon + S_b), E_1\} \times (\varepsilon' + S_b')/(\varepsilon + S_b) \\ X_3 = \min\{(\varepsilon + S_b), E_3\} \times (\varepsilon' + S_b')/(\varepsilon + S_b) \end{cases} \quad (2\text{-}59)$$

where S_b and S_b' are respectively the separation energies of the incident and emitted particles, E_1 and E_3 are given in Table 2-2, and

$$\begin{cases} \varepsilon = \frac{M}{m+M} E \\ \varepsilon' = \frac{M'}{m'+M'} E' \end{cases} \quad (2\text{-}60)$$

where m, M, m', and M' are respectively masses of incident, target, emitted, and residual particles with the unit of neutron mass.

Even if this systematics was proposed by Kalbach, it is conventionally called as the Kalbach-Mann systematics because the first version of this form was proposed by Kalbach and Mann [63]. The energy-angular distribution within the Kalbach-Mann systematics is tabulated values of $f_{MSD}(E, E')$ (and $a(E, E')$ in some evaluations) on a specific grid of (E, E') in ENDF MF6.

Table 2-2. Parameters in the Kalbach-Mann systematics [62].

Parameter	C_1	C_2	C_3	E_1	E_3
Unit	MeV^{-1}	MeV^{-3}	MeV^{-4}	MeV	MeV
Value	0.04	1.8E-6	6.7E-7	130	41

2.5.2 Interpolation of energy-angular distribution [64]

Because both secondary energy and emission angle are considered as variables in energy-angular distribution, the comparison between theoretical calculations and experimental measurements is more direct than cross section (excluding total cross section) and angular distribution. However, owing to the existence of two degrees of freedom for each incident energy, numerous validations against experimental data should be performed. In practice, one can only validate the double-differential cross sections with a limited number of experimental data. As a result, the accuracy of complete MF6 data depends on the sensitivities to model parameters.

Figure 2-6 shows the angle-integrated energy distributions, i.e. $\int_{-1}^{1} f(\mu, E, E')\, d\mu$, of continuum neutron inelastic scattering on ^{56}Fe in JEFF-3.1.1 [28] and ENDF/B-VIII.0 [65]. The most obvious difference is the threshold of reaction channel, the continuum inelastic scattering (i.e. MT91) opens at E_{thr} = 4.618 MeV and E_{thr} = 2.376 MeV in JEFF-3.1.1 and ENDF/B-VIII.0, respectively. Since the threshold energies where the cross sections are higher than 1 mbarn is 4.623 MeV and 4.803 MeV for JEFF-3.1.1 and ENDF/B-VIII.0, respectively, the difference of E_{thr} between the two

libraries is not so important for subsequent calculations.

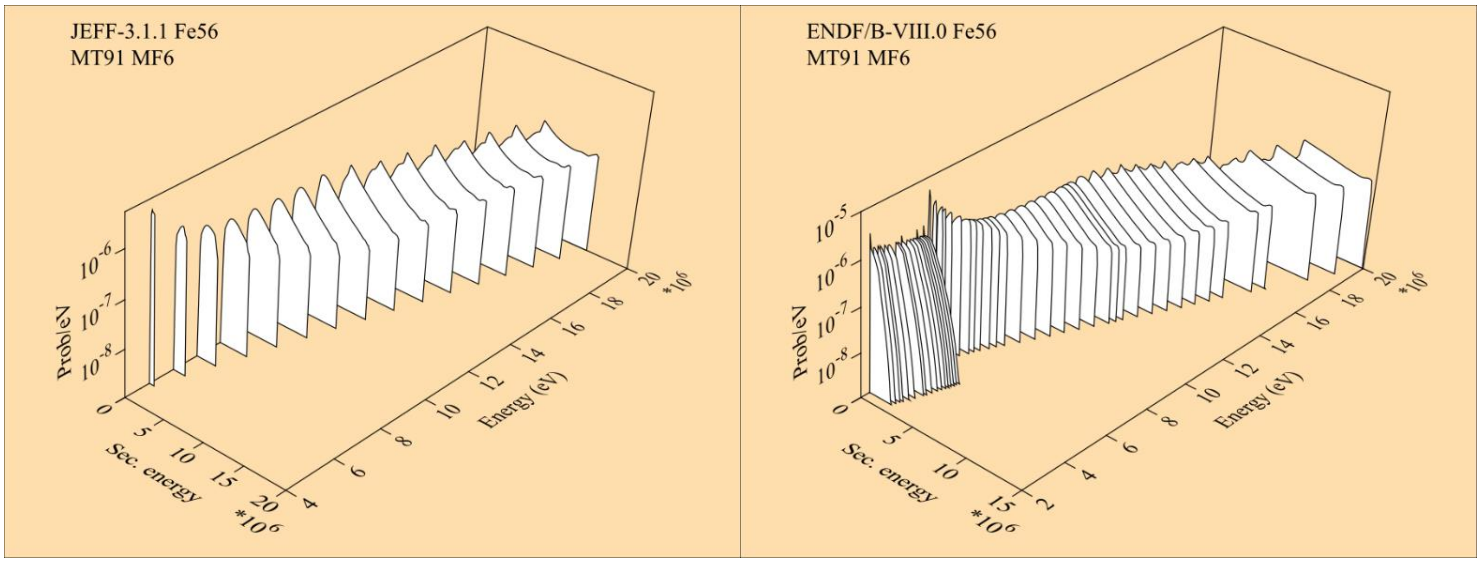

Figure 2-6. Angle-integrated energy distributions of continuum neutron inelastic scattering on ^{56}Fe in JEFF-3.1.1 (left, E_{thr} = 4.618 MeV) and ENDF/B-VIII.0 (right, E_{thr} = 2.376 MeV).

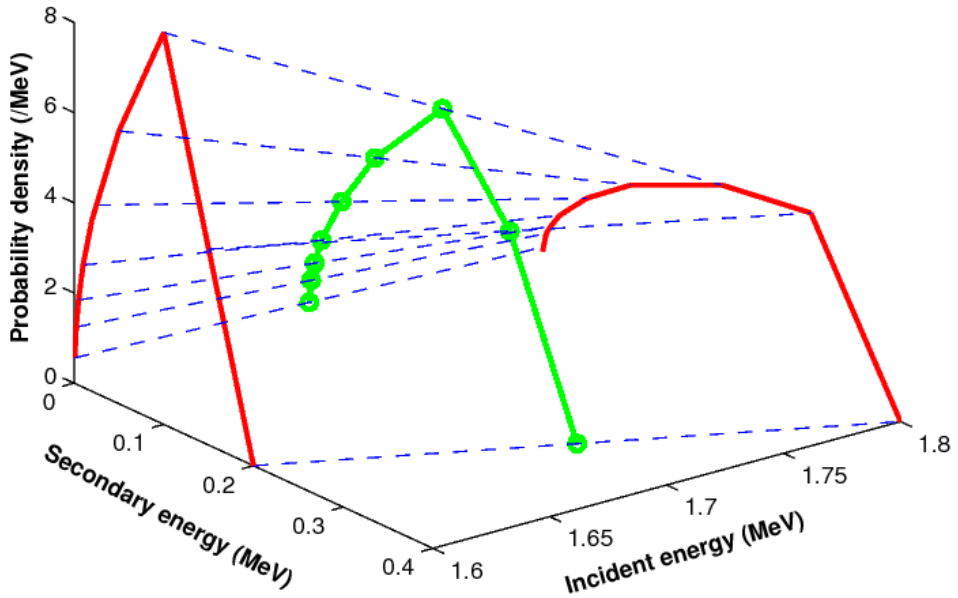

Figure 2-7. Scheme of the interpolation of energy-angular distributions. Red lines represent the data given in ENDF, the green points are interpolated data.

As shown in Figure 2-6, the energy-angular distribution is given in a specific grid on incident energy. Interpolation is thus required to determine the energy-angular distribution at each energy, as the example shown in Figure 2-7 with green points. The most common method for interpolating energy-angular distributions is the Unit-Base

Interpolation (UBI) [66, 67]. For linear-linear UBI, knowing the energy distribution at two incident energies $E_{n,0}$ and $E_{n,1}$, the probability for incident energy of E and secondary energy E' is given by [66, 67]:

$$P(E,E') = \frac{\tilde{P}(E,\widetilde{E'})}{E'_{\max,q} - E'_{\min,q}} \tag{2-61}$$

where

$$q = \frac{E - E_{n,0}}{E_{n,1} - E_{n,0}} \tag{2-62}$$

$$E'_{\max/\min,q} = (1-q)E'_{\max/\min,0} + qE'_{\max/\min,1} \tag{2-63}$$

$$\widetilde{E'} = \frac{E' - E'_{\min,q}}{E'_{\max,q} - E'_{\min,q}} \tag{2-64}$$

$$\tilde{P}(E,\widetilde{E'}) = (1-q)\tilde{P}(E_{n,0},\widetilde{E'}) + q\tilde{P}(E_{n,1},\widetilde{E'}) \tag{2-65}$$

$$\tilde{P}(E_{n,0/1},\widetilde{E'}) = (E'_{\max,0/1} - E'_{\min,0/1})P(E_{n,0/1},\widetilde{E'}(E'_{\max,0/1} - E'_{\min,0/1}) + E'_{\min,0/1}) \tag{2-66}$$

where $P(E_{n,0/1},\widetilde{E'}(E'_{\max,0/1} - E'_{\min,0/1}) + E'_{\min,0/1})$ is given in ENDF. Figure 2-8 shows the energy distribution for incident energies between 19 MeV and 20 MeV for continuum inelastic scattering of ^{56}Fe. The right figure is plotted with the normalized secondary energy $\widetilde{E'}$ and the corresponding probability density $\tilde{P}(E,\widetilde{E'})$ for a more intuitive view.

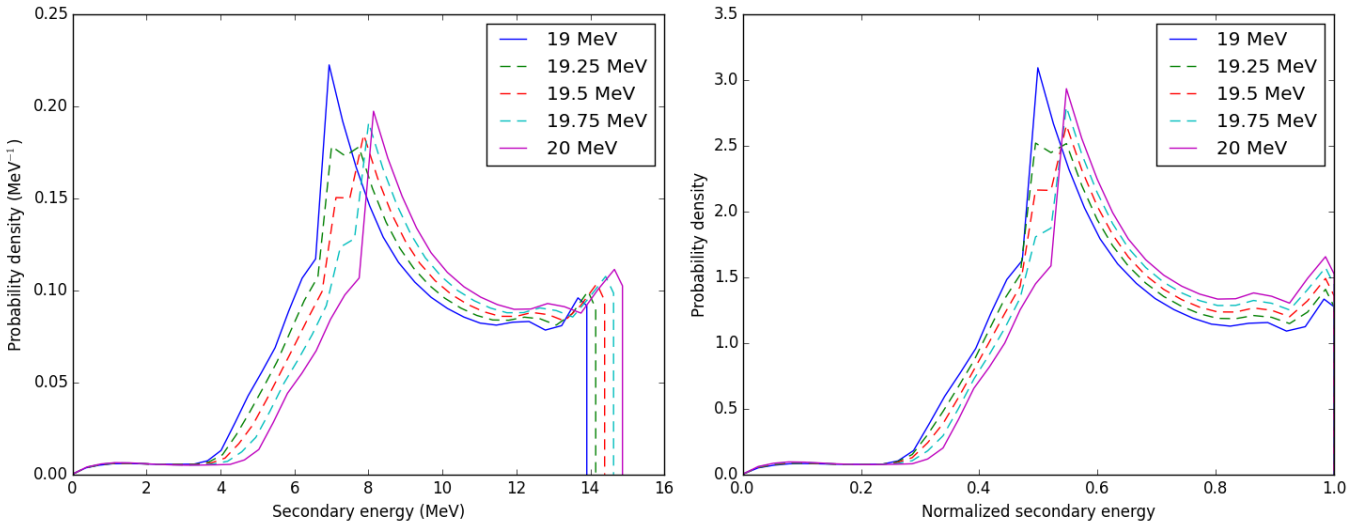

Figure 2-8. UBI of angle-integrated energy distributions of incident energy between 19 and 20 MeV neutron continuum inelastic scattering with ^{56}Fe. The right figure uses the normalized secondary energy to intuitively show the peak values.

As shown in Figure 2-8, the UBI cannot give reasonable peak value of the energy

distribution between two given points. To obtain more physically realistic energy-angular distributions from interpolation, the present work proposes a Peak value-based UBI (PUBI) for interpolating the energy distributions. In the PUBI, we divide the secondary energies into two intervals according to the peak values. Then the UBI is used to each interval. Assuming the probability density has an unique global maximum, $E_{m,0/1}$ represents the secondary energy corresponding to the maximum probability density of energy distribution:

$$P\left(E_{n,0/1}, E_{m,0/1}\right) = \max_{E'_{0/1}}\left\{P\left(E_{n,0/1}, E'_{0/1}\right)\right\} \tag{2-67}$$

We suppose that the maximum probability for incident energy E is determined by:

$$E_{m,q}/\left(E'_{\max,q} - E'_{\min,q}\right) = (1-q)E_{m,0}/\left(E'_{\max,0} - E'_{\min,0}\right) + qE_{m,1}/\left(E'_{\max,1} - E'_{\min,1}\right) \tag{2-68}$$

Let denote:

$$\hat{E} = \begin{cases} \frac{E' - E'_{\min,q}}{E_{m,q} - E'_{\min,q}} & E' \le E_{m,q} \\ \frac{E' - E_{m,q}}{E'_{\max,q} - E_{m,q}} & E' > E_{m,q} \end{cases} \tag{2-69}$$

The energy distribution is expressed by:

$$P(E, E') = \begin{cases} \frac{\hat{P}_{\mathrm{I}}(E,\hat{E})}{E_{m,q} - E'_{\min,q}} & E' \le E_{m,q} \\ \frac{\hat{P}_{\mathrm{II}}(E,\hat{E})}{E'_{\max,q} - E_{m,q}} & E' > E_{m,q} \end{cases} \tag{2-70}$$

where

$$\hat{P}_{\mathrm{I/II}}\left(E, \hat{E}\right) = (1-q)\hat{P}_{0,\mathrm{I/II}}\left(E_{n,0}, \hat{E}\right) + q\hat{P}_{1,\mathrm{I/II}}\left(E_{n,1}, \hat{E}\right) \tag{2-71}$$

where

$$\begin{cases} \hat{P}_{0/1,\mathrm{I}}\left(E_{n,0/1}, \hat{E}\right) = \left(E_{m,0/1} - E'_{\min,0/1}\right)P\left(E_{n,0/1}, \hat{E}\left(E_{m,0/1} - E'_{\min,0/1}\right) + E'_{\min,0/1}\right) \\ \hat{P}_{0/1,\mathrm{II}}\left(E_{n,0/1}, \hat{E}\right) = \left(E'_{\max,0/1} - E_{m,0/1}\right)P\left(E_{n,0/1}, \hat{E}\left(E'_{\max,0/1} - E_{m,0/1}\right) + E_{m,0/1}\right) \end{cases} \tag{2-72}$$

The results corresponding to Figure 2-8 but with the PUBI method are shown in Figure 2-9. The peak values and the corresponding secondary energies are monotonic for the data obtained by the PUBI method. Figure 2-9 shows physically reasonable energy distributions for incident energies between the two given neighbor energies.

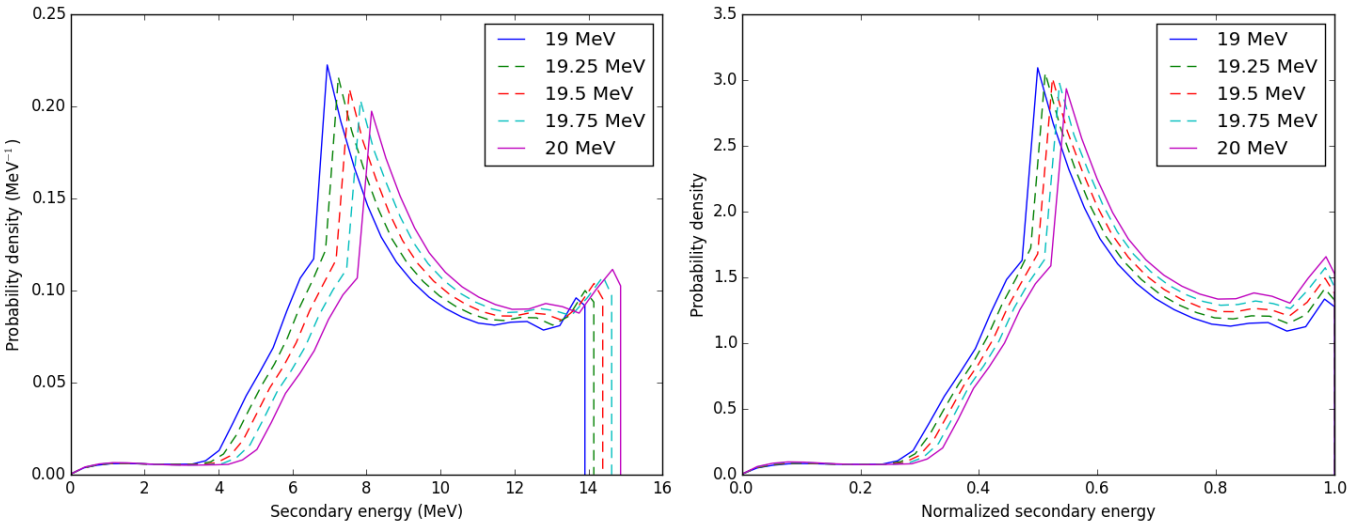

Figure 2-9. Same results as Figure 2-8 but with the PUBI method.

3 Primary radiation damage models

This section briefly presents the theory and main common models for calculating primary radiation damage. Section 3.1 presents the threshold energy for atomic displacement. Sections 3.2 - 3.5 shortly describe the current analytical or semi-empirical models for computing the number of atomic vacancies from a given Primary Knock-on Atom (PKA) energy. Section 3.6 is a simple correction proposed in the context of this Ph.D work by analyzing experimental data. Section 3.7 is a short introduction of advanced modeling methods to compute the irradiation-induced primary damage. This subsection also includes the discussion on the "full cascade simulation" and "quick calculation" options in the widely used code SRIM. At the end of this section, I list the experimental methods for measuring the number of atomic vacancies after irradiation.

3.1 Threshold atomic displacement energy

The Threshold Displacement Energy (TDE) defines the minimum recoil energy to create stable defects. Due to the anisotropic structure of crystalline materials, the TDE is direction-dependent in crystalline structures. Figure 3-1 shows the example of direction-independence of TDE for iron [68]. Because of limited experimental measurements, the TDEs are mainly determined by Molecular Dynamics (MD) simulations for the time-being.

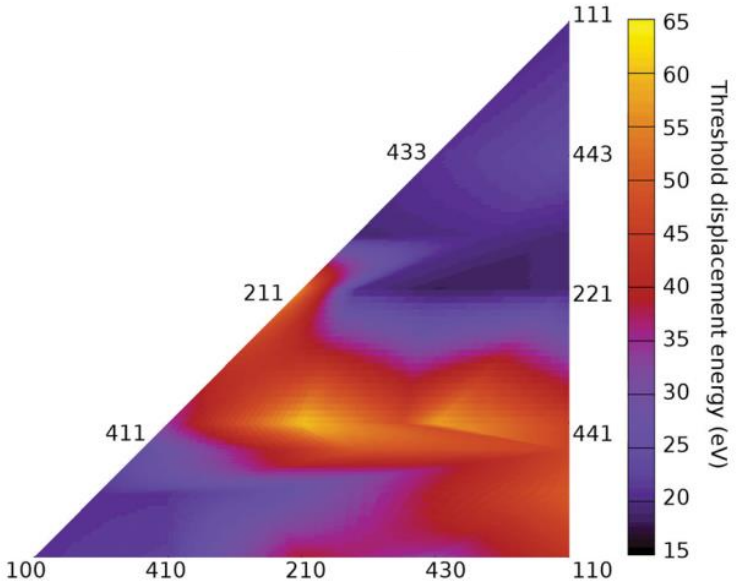

Figure 3-1. Direction-dependent threshold displacement energy for bcc iron [68]. The data are projected in the triangle of which the vertices are (1,0,0), (1,1,0), and (1,1,1).

Because of the direction-dependence of TDE, the probability of stable atomic

displacement P_d increases from 0 to 1 with the kinetic energy of the knock-on atom increasing from 0 to the maximum TDE. Figure 3-2 shows the example of the average number of atomic displacements with respect to PKA energy in Cu from experimental measurements [69]. No atom is displaced if the PKA energy is below the minimum TDE. From the minimum TDE to the maximum TDE, because the increase in PKA energy leads to possible displacements in more directions, P_d increases with PKA energy.

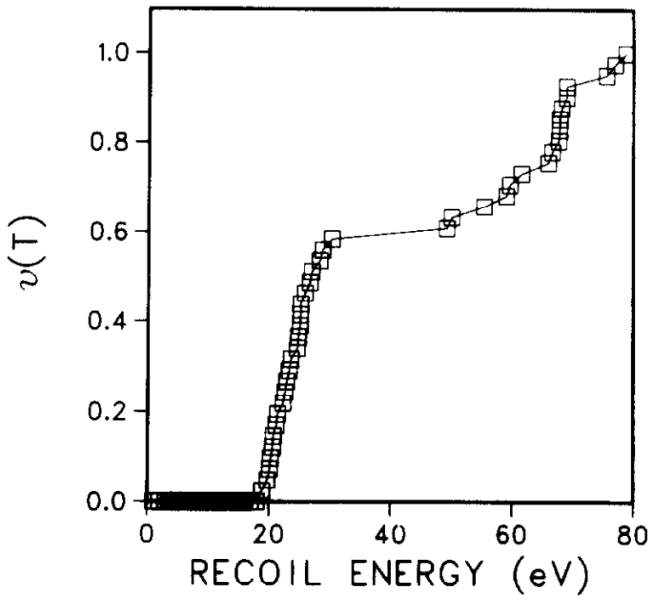

Figure 3-2. Experimental data of the average number of displacements with respect to PKA energy in Cu [69].

In industry, most structural materials are polycrystalline (i.e. arbitrary combinations of crystallites). Moreover, in nuclear reactors, the incident direction of the energetic particle is almost isotropic in the scale of atomic displacement. It is thus possible to use the average TDE, simply noted by E_d hereinafter. The direction-averaged TDE is calculated by:

$$E_d = \frac{1}{4\pi}\int_0^{2\pi}\int_{-\pi}^{\pi} E_d(\theta,\varphi)\sin\theta d\theta d\varphi \tag{3-1}$$

where θ is the colatitude and φ is the longitude. For iron, the average MD results using 10 potentials show $E_d = 40$ eV [70].

For simplification, it is conventionally assumed that P_d is described by a step function of the average TDE, as the dashed curve shown in Figure 3-3:

$$P_d(E) = \begin{cases} 0, & E < E_d \\ 1, & E \geq E_d \end{cases} \tag{3-2}$$

This simplification is widely used in different analytical formulae for computing the number of atomic displacements.

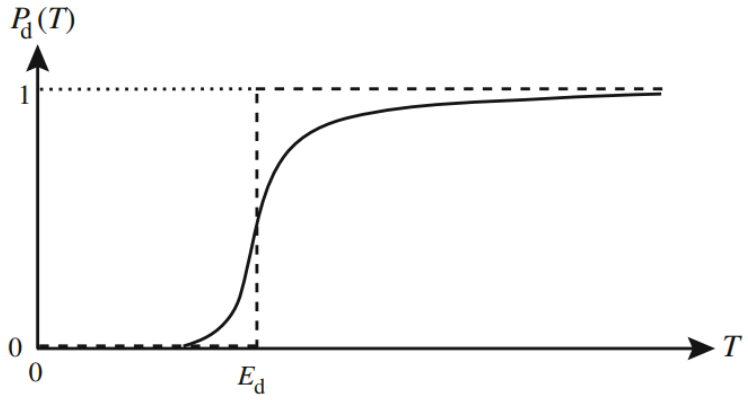

Figure 3-3. Probability of stable atomic displacement versus recoil energy [23]. The dashed curve represents the step function approximation.

In this manuscript, the mentioned TDE or E_d refers to the average TDE hereinafter if no additional precision. The corresponding displacement probability is the step function given by Eq. (3-2) and shown in Figure 3-3.

3.2 Kinchin-Pease formula

Let note $v(E)$ the number of displaced atoms induced by an energetic atom with kinetic energy of E. Figure 3-4 illustrates the two-body atomic collision between the PKA and an atom in the lattice. The number of atomic vacancies induced by the two free atoms after a collision is $v(E-T)+v(T-E_d)$. Because the final number of stable atomic displacements is not changed by such a collision, one has:

$$v(E) = v(E-T) + v(T-E_d) \tag{3-3}$$

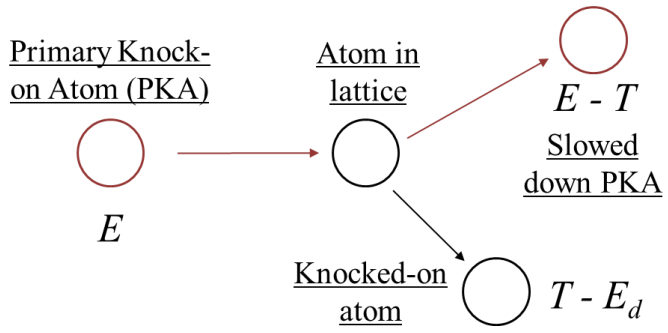

Figure 3-4. Schematic of two-body atomic collision between PKA and an atom in lattice.

To develop a simple formula for computing the number of atomic displacements induced by a PKA with kinetic energy E, Kinchin and Pease assumed that [71]:

(i) All collisions are two-body elastic atomic collisions between atoms;

(ii) Atoms are hard spheres;

(iii) The materials are amorphic;

(iv) The probability of stable atomic displacement P_d is Eq. (3-2);

(v) Energy lost to the lattice is negligible, i.e. $T - E_d \approx T$;

(vi) If the PKA energy is larger than its ionization energy E_I, PKA losses kinetic energy without inducing atomic displacements until PKA energy reduces to E_I.

Assumptions (i) and (ii) imply that the energy-differential collision is:

$$\frac{d\sigma}{dT}(E,T) = \frac{\sigma(E)}{E}, \forall T \in [0,E] \tag{3-4}$$

where $\sigma(E)$ is the total atomic collision cross section. This differential cross section can be easily obtained using the probability density of the impact parameter (c.f. Appendix A1). On the other hand, assumption (v) leads Eq. (3-3) to:

$$v(E) = v(E-T) + v(T) \tag{3-5}$$

Because the material is amorphic, i.e. assumption (iii), for $E < E_I$, one has:

$$v(E) = \frac{1}{E}\int_0^E [v(E-T) + v(T)]\, dT \tag{3-6}$$

On the other hand,

$$\int_0^E v(E-T)\, dT = \int_0^E v(T)\, dT \tag{3-7}$$

Therefore, the equation governing $v(E)$ becomes:

$$v(E) = \frac{2}{E}\int_0^E v(T)\, dT \tag{3-8}$$

If $E < E_d$, assumption (iv) implies $v(E) = 0$. If $E_d < E < 2E_d$, the PKA induces at least 1 displacement, itself or a replacement of another atom. The kinetic energy of the displaced atom $E - E_d < E_d$, it cannot lead to a second displacement. Therefore, $v(E) = 1$ for $E_d < E < 2E_d$. Using the two boundary conditions for $E < 2E_d$, one can find the solution of the integral equation:

$$v(E) = \frac{2E}{E_d}, 2E_d < E < E_I \tag{3-9}$$

Assumption (vi) is equivalent to:

$$v(E) = v(E_I), E > E_I \tag{3-10}$$

Accordingly, the mathematical expression of the Kinchin-Pease (KP) formula is [71]:

$$v_{KP}(E_{PKA}) = \begin{cases} 0, & 0 < E_{PKA} < E_d \\ 1, & E_d < E_{PKA} < 2E_d \\ \frac{E_{PKA}}{2E_d}, & 2E_d < E_{PKA} < E_I \\ \frac{E_I}{2E_d}, & E_I < E_{PKA} \end{cases} \tag{3-11}$$

3.3 Lindhard's theory of damage energy

Kinchin-Pease model assumes that all atomic collisions are all elastic collisions. Taking the inelastic collision effect into account, Lindhard *et al.* developed integral equations to compute the so-called damage energy [72], noted by E_a hereinafter. Damage energy is the effective energy lost to atomic motion, the difference between kinetic energy and damage energy is the energy lost to electronic excitation and ionization. In a monatomic material having a same type of PKA (i.e. same atomic number and mass), the damage energy is computed by the integrodifferential equation [72]:

$$k_L \varepsilon^{1/2} \cdot E_a{}'(\varepsilon) = \int_0^{\varepsilon^2} \frac{dt}{2t^{3/2}} \tilde{f}\left(t^{1/2}\right) \left[E_a\left(\varepsilon - \frac{t}{\varepsilon}\right) - E_a(\varepsilon) + E_a\left(\frac{t}{\varepsilon}\right)\right] \quad (3\text{-}12)$$

where $\varepsilon = E_{PKA}/E_L$, $t = \varepsilon^2 T/T_m$ with T the transferred energy, $T_m = E$ if the incident and target atoms are the same (i.e. same mass and same charge), and

$$E_L = \frac{k_C e}{0.8853 a_0} Z_R Z \left(Z_R^{2/3} + Z^{2/3}\right)^{1/2} (A_R + A)/A \text{ [eV]} \quad (3\text{-}13)$$

$$k_L = \left(11.53 \frac{m_e}{m_N}\right)^{1/2} \frac{Z_R^{2/3} Z^{1/2} (A_R + A)^{3/2}}{\left(Z_R^{2/3} + Z^{2/3}\right)^{3/4} A_R^{3/2} A^{1/2}} \quad (3\text{-}14)$$

where Z and A ($Z_R = Z - z$ and $A_R = A + 1 - a_z$, respectively) are the atomic number and the atomic mass number for lattice atom (PKA, respectively). The corresponding physical constants are given in Table 3-1. $k_L \varepsilon^{1/2}$ is the electronic stopping power. The scattering function $\tilde{f}\left(t^{1/2}\right)$ is from the universal Thomas-Fermi differential cross section $\pi a^2 \frac{dt}{2t^{3/2}} \tilde{f}\left(t^{1/2}\right)$, where $a = (9\pi^2/128)^{1/3} a_0 \left(Z_R^{2/3} + Z^{2/3}\right)^{-1/2}$ and a_0 is the Bohr radius.

Table 3-1. Physical constants [73].

Symbol	k_C	e	a_0	m_e	m_N	$\frac{k_C e}{0.8853 a_0}$	$\left(11.53 \frac{m_e}{m_N}\right)^{1/2}$
Name	Coulomb constant	Elementary charge	Bohr radius	Mass of electron	Mass of nucleon	Coefficient in E_L	Coefficient in k_L
Unit	N m^{2}C^{-2}	C	pm	MeV/c^2	MeV/c^2	-	-
Value	8.988×10^9	1.602×10^{-19}	52.92	0.5110	931.5	30.734	0.07953

Based on the numerical solution of integral equations by using the universal Thomas-Fermi interaction potential [74–76], Lindhard *et al.* found that the damage energy $E_a(\varepsilon)$ is nearly inversely proportional to k_L at high energy. On the other hand, at low energy, due to negligible loss to electrons, $E_a(\varepsilon) \approx \varepsilon$. By consequence, they gave

a partition function of the shape as [72]:

$$P(\varepsilon) = \frac{1}{1+k_L g(\varepsilon)} \tag{3-15}$$

By interpreting Lindhard's numerical results of the partition function [72], Robinson presented the numerical approximation by an analytical expression for the function $g(\varepsilon)$ [77]:

$$g(\varepsilon) = 3.4008\varepsilon^{1/6} + 0.40244\varepsilon^{3/4} + \varepsilon \tag{3-16}$$

The damage energy $E_a(E_{PKA}) = E_{PKA} \times P(E_{PKA}/E_L)$ can be thus analytically calculated for each PKA energy. It is noteworthy that the damage energy calculated with the *assumption (E)* in Ref. [72] is several percent too high, this is consistent with the results calculated by Coulter [78].

Lindhard's equation is deduced in the regions I (where the nuclear stopping is dominating and relatively little energy goes into electronic motion) & II (where the nuclear stopping falls off, while the electronic stopping goes on increasing as $E^{1/2}$), i.e. $v < v_1 = v_0 Z^{2/3}$ [72]. The last condition conducts that $E_{PKA} < 24.9AZ^{4/3}$ keV or $\varepsilon < 286A/Z$. So, the upper bound of the validity domain is $\varepsilon = 572$ ($E_{PKA} = 23.5$ MeV) for ^{28}Si and $\varepsilon = 617$ ($E_{PKA} = 107$ MeV) for ^{56}Fe. The calculation for $\varepsilon > 1000$ is thus unphysical.

We remark that the upper bound of the validity domain of PKA energy increases with atomic mass number A and the maximum energy of PKA given by neutron elastic scattering (which is $T_{max} = \frac{4A}{(A+1)^2} E_n$) decreases with A. Under the approximation of neutron elastic scattering, the upper bound of incident neutron energy in the Lindhard's numerical results is:

$$E_n < 6.225Z^{4/3}(A+1)^2 \text{ keV} \tag{3-17}$$

The upper limit of neutron energy is thus 1.6 GeV for ^{56}Fe. However, for ^{7}Li, this limit is 1.3 MeV, which is included in the neutron spectrum for both fission and fusion reactors.

3.4 Norgett-Robinson-Torrens formula

Since the damage energy is the effective kinetic energy lost to atomic motion, the PKA kinetic energy in the Kinchin-Pease formula should be replaced by the damage energy for computing the number of atomic displacements. Based on the more than 40-years Binary Collision Approximation (BCA) simulations of ion collisions in solids [79], Norgett, Robinson, and Torrens proposed a new formula (conventionally called as NRT, or modified Kinchin-Please) in 1975 [80] using Lindhard's damage energy [72, 77]:

$$\nu_{NRT}(E_a) = \begin{cases} 0, & 0 < E_a < E_d \\ 1, & E_d < E_a < \frac{2E_d}{0.8} \\ \frac{0.8E_a}{2E_d}, & \frac{2E_d}{0.8} < E_a \end{cases} \quad (3\text{-}18)$$

where the constant 0.8 is the correction of the hard-sphere collision cross section obtained by BCA simulation (the original approximate value of the correction is 0.86) [79].

NRT-DPA formula is considered as the current international standard for quantifying the irradiation damage [20]. It is again noted that Lindhard's damage energy and the subsequent NRT formula is valid only for $E_{PKA} < 24.9AZ^{4/3}$ keV. Most numerical results shown in this thesis are based on NRT formula if no special instruction is given.

3.4.1 A modification of NRT

On the other hand, according to the definition of the average threshold displacement energy, at least an atom is displaced if $E_{PKA} > E_d$. One can understand that the inelastic collision-induced energy loss of a displaced PKA does not change the number of total atomic displacements for $E_d < E_{PKA} < 2E_d$ because the excess or remaining energy (i.e. the kinetic energy after the displacement of PKA) $E_{PKA} - E_d$ is not sufficient to induce a second displacement. This definition implies a modified NRT (mNRT) formula [81]:

$$\nu_{mNRT}(E_a) = \begin{cases} 0, & 0 < \boldsymbol{E_{PKA}} < E_d \\ 1, & (\boldsymbol{E_d < E_{PKA}}) \& \left(E_a < \frac{2E_d}{0.8}\right) \\ \frac{0.8E_a}{2E_d}, & \frac{2E_d}{0.8} < E_a \end{cases} \quad (3\text{-}19)$$

This mNRT is almost the same as the standard NRT formula for neutron-induced damage. However, the mNRT may lead to a larger number of vacancies for damage induced by light particles, such as electron and photon (examples shown in Sections 4.5 and 4.6), because the contribution of $(E_d < E_{PKA}) \& (E_a(E_{PKA}) < E_d)$ is not negligible.

3.5 Athermal Recombination-Corrected formula

Even if NRT-DPA formula is used as the standard, the overestimation of DPA by the NRT model is found in 1977 with the electrical resistance measurements of the irradiated thin-fold specimens of copper and silver [82]. One of the issues in the NRT model is that the in-cascade recombination of displaced atoms is neglected. Taking this effect into account, the Athermal Recombination-Corrected DPA (ARC-DPA) formula is proposed by Nordlund *et al.* [83–85].

The relative damage efficiency ξ is defined as the ratio of the "true" number of Frenkel Pairs (FP) to the number of FP calculated with the NRT formula. Its expression

is based on the fact that the number of FP N_{FP} tends to $a'E_a$ when E_a tends to infinity and N_{FP} tends to $c'{E_a}^k$ ($k \approx 0.8$) (where *a'* and *c'* are constants) at low energy but higher than the threshold energy [83, 84]. Therefore, the following simple function is proposed:

$$N_{FP} = a'{E_a}^{b+1} + c'E_a \tag{3-20}$$

Accordingly, the efficiency becomes:

$$\xi_{ARC}(E) = \frac{N_{FP}}{N_{NRT}} = \frac{a'{E_a}^{b+1} + c'E_a}{0.8E_a/2E_d} = a{E_a}^b + c \tag{3-21}$$

By continuity of DPA, one imposes an additional condition $\xi(2E_d/0.8) = 1$ that leads to:

$$\xi_{ARC}(E_a) = (1 - c_{ARC}) \times \left[0.8\frac{E_a}{2E_d}\right]^{b_{ARC}} + c_{ARC} \tag{3-22}$$

The coefficients b_{ARC} and c_{ARC} are fitted through the results of MD simulations or possible experimental data for each material. Within this adjustment, the effective and empiric ARC-DPA formula is given by:

$$\nu_{ARC}(E_a) = \begin{cases} 0, & 0 < E_a < E_d \\ 1, & E_d < E_a < \frac{2E_d}{0.8} \\ \frac{0.8E_a}{2E_d}\xi_{ARC}(E_a), & \frac{2E_d}{0.8} < E_a \end{cases} \tag{3-23}$$

Konobeyev and coworkers have calculated and suggested the threshold energy, the coefficients b_{ARC} and c_{ARC} in ARC-DPA for elements from Li to U [86]. The data are used to implement the ARC-DPA into NJOY [87] from Be to U [88]. The corresponding results are delivered for the JEFF-3.3 nuclear data library [89]. In the work of Konobeyev, the threshold energies seem to be accurate, but the deviations of the coefficient c_{ARC} (which is defined as $c_{ARC} = E_d/E_{deff}$, where E_{deff} is the effective threshold energy that is defined by $N_{NRT} = N_{FP}$ at the end of cascade [90]) to those from the MD simulations are observed (e.g., Cu, W, Pt shown in Table 3-2). Another conclusion of Konobeyev's work is that the coefficient b_{ARC} has a weak influence on the efficiency calculation.

Table 3-2. c_{ARC} from Konobeyev's systematics and MD simulations [86].

Element	Fe	Ni	Cu	Pd	Ag	W	Pt	Au
MD	0.286	0.227	0.118	0.152	0.257	0.119	0.112	0.130
Konobeyev	0.31±0.09	0.23±0.08	0.30±0.09	0.32±0.09	0.31±0.17	0.60±0.17	0.36±0.10	0.43±0.12

One of the drawbacks of fitting MD results using the ARC-DPA formula is that the

fitted parameters are strongly dependent on E_d, which is actually not well determined. For example, for the same MD results, (i.e. the total number of atomic displacements are given) if one changes E_d by $E_d^* = xE_d$ $(x \neq 1)$, the corresponding efficiency function is $\xi_{ARC}^*(E_a) = x\xi_{ARC}(E_a)$ for having the same number of displacements. Therefore, the corresponding coefficients obey:

$$(1 - c_{ARC}^*) \times \left[0.8\frac{E_a}{2xE_d}\right]^{b_{ARC}^*} + c_{ARC}^* = x\left[(1 - c_{ARC}) \times \left[0.8\frac{E_a}{2E_d}\right]^{b_{ARC}} + c_{ARC}\right] \quad (3\text{-}24)$$

for any damage $E_a \gg E_d$. This condition is equivalent to:

$$\begin{cases} b_{ARC}^* & = & b_{ARC} \\ (1 - c_{ARC}^*)x^{-b_{ARC}^*} & = & x(1 - c_{ARC}) \\ c_{ARC}^* & = & xc_{ARC} \end{cases} \quad (3\text{-}25)$$

There are three independent constraints for determining two variables b_{ARC}^* and c_{ARC}^*. Consequently, $\xi_{ARC}^*(E_a) = x\xi_{ARC}(E_a)$ is mathematically impossible! Therefore, if the value of E_d is changed, one has to refit the coefficients in ARC-DPA model rather than a direct deduction from the previous fitting based on another E_d. Moreover, the refitted efficiency $\xi_{ARC}^*(E_a)$ must have a different shape from the original one $\xi_{ARC}(E_a)$.

3.6 A simple proposition [91]

Owing to the utilization of MD simulations, the ARC-DPA can generally much better describe DPA than the NRT formula. One of the drawbacks of the ARC model is that MD simulation results are required for each isotope. Therefore, we propose a simple efficiency function without introducing parameters excluded in the NRT-DPA metric or requiring MD simulations.

Here, we simply recall the reasoning of Robinson and Torrens on the calculation of the number of point defects [79]. The annihilation equation of point defects is [79]:

$$\frac{dn}{dt} = -kn^2 \quad (3\text{-}26)$$

where *n* represents the concentration of point defects of either kind. By integrating, the solution of Eq. (3-26) can be calculated:

$$n(t) = \frac{n_0}{1+kn_0t} \quad (3\text{-}27)$$

where $n_0 \equiv n(t = 0)$. Therefore,

$$\frac{n(t)}{n_0} = \frac{1}{1+kn_0t} \quad (3\text{-}28)$$

Inspiring from the equation of annihilation, Robinson and Torrens proposed that

$$\frac{N_{FP}}{N_{NRT}} = \frac{1}{1+\alpha N_{NRT}} \quad (3\text{-}29)$$

where α is a fitted coefficient (equivalent to kt in the annihilation equation). The average energy dissipated to each displaced atom is thus [79]:

$$\frac{E_a}{N_{FP}} = \frac{2E_d}{0.8} + \alpha E_a \tag{3-30}$$

The efficiency function based on the NRT formula is defined as:

$$\xi(E_a) = \frac{N_{FP}}{N_{NRT}(E_a)} = \frac{N_{FP}}{0.8E_a/2E_d} \tag{3-31}$$

Therefore, one obtains:

$$\xi(E_a) = \frac{2E_d/0.8}{2E_d/0.8+\alpha E_a} \tag{3-32}$$

The above efficiency function tends to 0 by increasing the damage energy. However, the defect production is almost a linear function of the damage energy after the formation of displacement sub-cascade at high energy collisions [92–94]. The efficiency should thus be a constant after the subthreshold energy, which defines the threshold of sub-cascade formation. Both MD simulations and experimental data show the asymptotic value of the efficiency is about 0.3 for most isotopes. Consequently, the asymptotic value of the efficiency (β) should be taken into account:

$$\xi_{CB}(E_a) = \frac{2E_d/0.8}{2E_d/0.8+\beta E_a} + \beta \tag{3-33}$$

where $\beta = Z/(1.5A)$ is an additive parameter that accounts for the asymptotic value of $\xi(E_a)$. $\beta \propto Z/A$ because a stronger Coulomb force or a lighter mass leads to a longer path that induces "more" sub-cascades. The advantage of this improved efficiency function is that we correlate the atomic displacement efficiency with the atomic number and the atomic mass of the irradiated material without requiring fitting parameters as needed in the ARC-DPA model. In addition, the same β is used for the coefficient in the denominator of the first term to simplify the expression. This improved correction is referred to Chen-Bernard (CB) in this subsection.

The ratios of ARC and CB to the NRT metric for the Fe, Ni, and Cu are shown in Figure 3-5. Fe and Ni are the two most important elements in the RPV for radiation damage investigations. All the three elements are of importance in fusion reactors. The values of b_{ARC} and c_{ARC} in ARC-DPA formula and the threshold energy E_d for these elements are compiled by Nordlund [85] and listed in Table 3-3. The original results of MD simulations can be found in Ref. [95] and Ref. [96] for Fe and Ni, respectively. The experimental data are extracted from the report of the Nuclear Energy Agency (NEA) [84], which accounts for the experimental measurements of Jung [97]. The DPA

is proportional to the Resistivity of Frenkel pairs per unit concentration (RF) (c.f. Eq. 1 in Ref. [82]). The experimental uncertainties are deduced from the RF values compiled in Tables 5 and 16 in Ref. [97]. It can be found that the CB corresponds well with the experimental data. The discrepancies between the CB model and the experimental values are even less than the ARC-DPA model for Fe, Ni, and Cu.

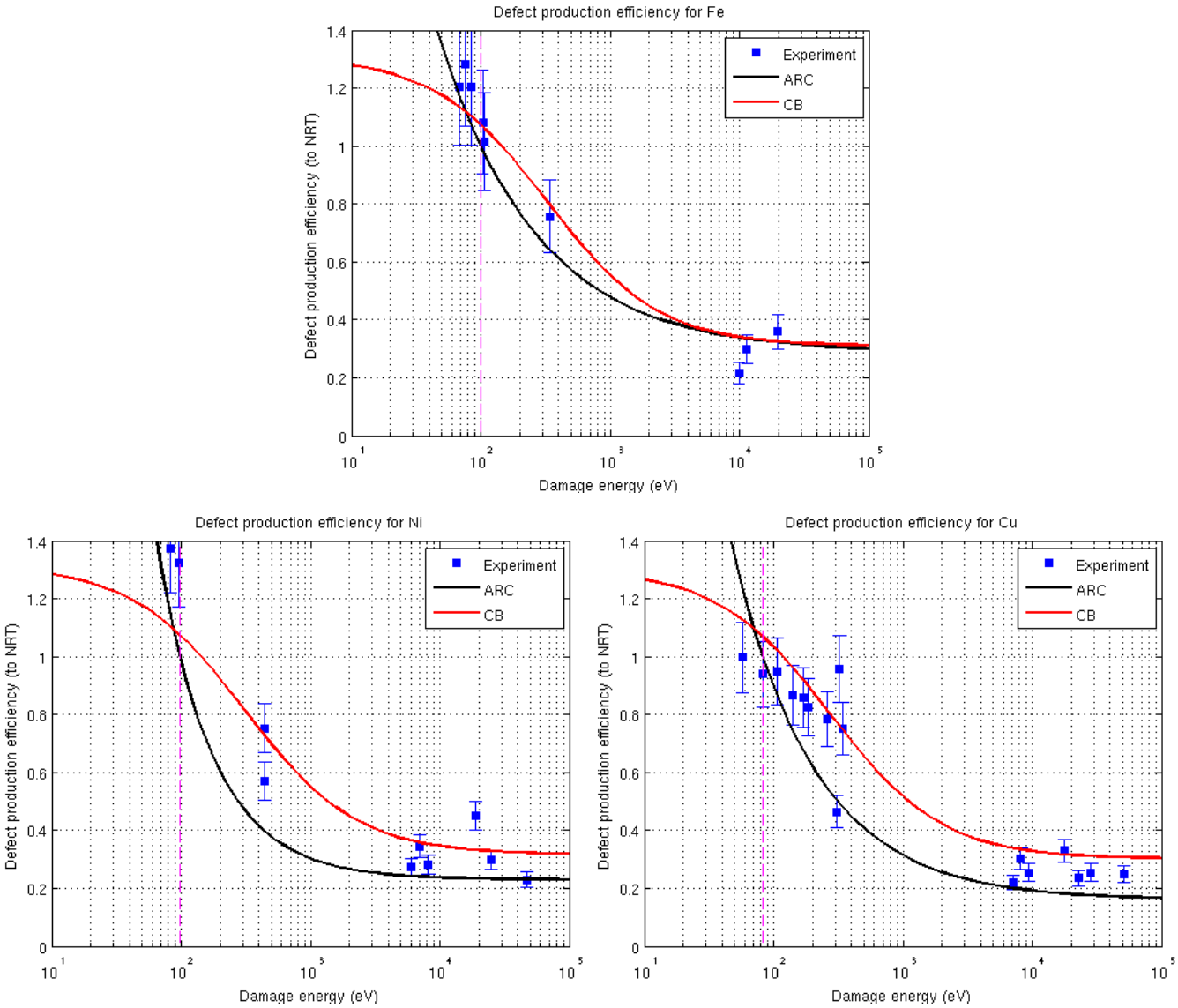

Figure 3-5. Ratios of experimental data, ARC-DPA, and CB-DPA to the NRT formula for Fe, Ni, and Cu versus damage energy E_a. The experimental data extracted from NEA report [84]. The experimental uncertainties are deduced from Tables 5 and 16 in Ref. [97] through the Resistivity of Frenkel pairs per unit concentration. The dashed pink lines indicate E_a=2E_d/0.8.

Averback deduced experimental DPA numbers of copper and silver according to the measurement of electrical resistivity [82]. The data of Averback are given as a function of DPA-averaged PKA energy (i.e. the weighting function for computing the average PKA energy is the number of DPA), which is larger than the average PKA

energy. However, these data can reveal the asymptotic values of displacement efficiency. The total uncertainty of Averback's DPA comes from the uncertainties of the thickness of samples (5% for samples number 2 & 3 and 10% for other ones) and the correction to convert measured thin film resistivities (10%). The ratios of ARC and CB to the NRT metric for the Cu and Ag are shown in Figure 3-6 with Averback's experimental data. The ratios of experimental data to NRT value for Cu are corrected because Averback adopted Lucasson's threshold energy of 29 eV [98]. The ARC-DPA parameters of Ag are listed in the last row in Table 3-3 [86].

Table 3-3. Parameters for DPA calculation.

Material	E_d (eV)	b_{ARC}	c_{ARC}
Fe [85]	40	-0.568	0.286
Ni [85]	39	-1.01	0.23
Cu [85]	33	-0.68	0.16
Ag [86]	39	-1.06	0.257

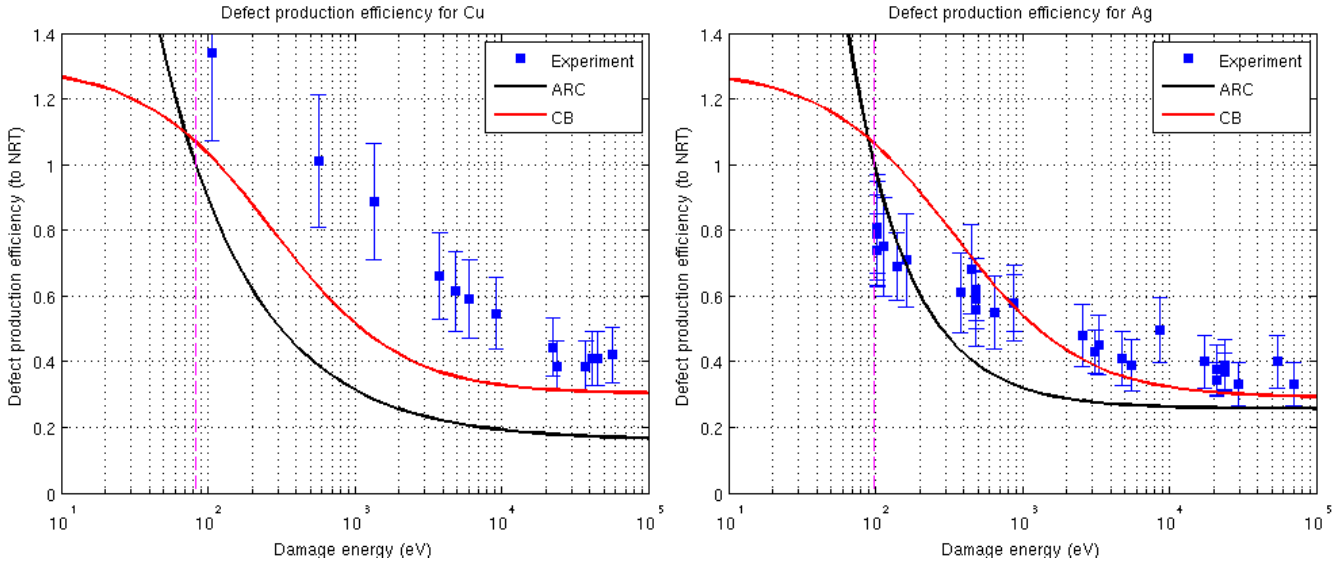

Figure 3-6. Ratios of Averback's experimental data [82], ARC-DPA, and CB-DPA to NRT for Cu and Ag versus damage energy computed with the DPA-weighted average PKA energy. The uncertainties are from the uncertainties of sample thickness and electronic resistivity.

Figure 3-5 shows that the CB formula corresponds well to experimental data for Fe, Ni, and Cu. Results in Figure 3-6 show the good agreement of the asymptotic value of the CB-DPA for Ag. The asymptotic value of Averback's experimental measurement is higher than both ARC-DPA and CB-DPA, while the asymptotic experimental data shown in Figure 3-5 are between ARC-DPA and CB-DPA. Comparing with the NRT metric, no additional parameter is used in the CB formula. The simpler form of the CB

than that of the ARC directly results in fewer calculations for the propagation of uncertainties from nuclear parameters to DPA rates. In addition, MD simulations are required for each isotope to fit the parameters b_{ARC} and c_{ARC} in the ARC-DPA metric. Konobeyev and coworkers have tried to find a systematics to determine the parameter c_{ARC} in ARC-DPA, but the discrepancies between the systematics and the molecular dynamics simulations are evident [86].

3.7 BCA and MD simulations

The aforementioned formulae for calculating the number of atomic displacements are based on various assumptions and/or empirical observations. Moreover, the lattice binding energy is often neglected in such analytical formulae. The crystalline structure is considered only in the determination of the angle-averaged TDE. Even in the modern ARC-DPA model, it is impossible to fit all MD results as the examples shown in Figure 3-7. Accurate calculations by following all knocked-on atoms are thus required for computing the "exact" number of atomic displacements.

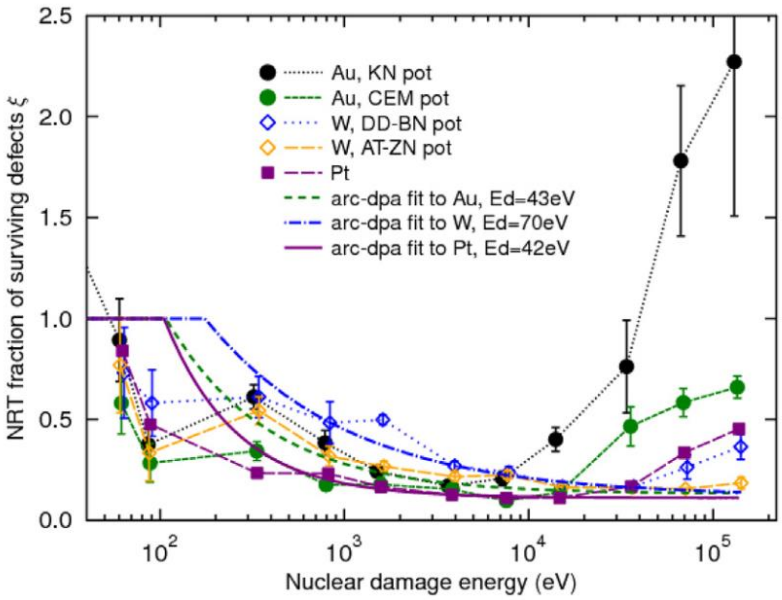

Figure 3-7. Ratios MD simulations-based number of atomic displacements to the NRT formula for Au, W, and Pt along with the corresponding ARC-DPA fittings [99].

3.7.1 Brief introduction of BCA and MD simulations

BCA simulation follows each two-body collision to estimate the number of displaced atoms [79]. The two widely used BCA codes are SRIM [100] and MARLOWE [79]. The former performs Monte Carlo simulations for amorphous materials, while the latter considers the crystalline structure. MARLOWE is more complex but SRIM is easier to use thanks to its graphical user interface. Another shortcoming of SRIM is its very time-consuming Monte Carlo simulations. A SRIM-

like open-source code Iradina [101], which is about two orders of magnitude faster than SRIM [102], was recently developed.

While BCA considers only two-body collisions, MD treats collective interatomic interactions. MD simulation is thus more complex and more realistic than BCA. Because MD simulates together all considered atoms, it permits not only to calculate the number of atomic displacements but also the time evolution of vacancy, interstitial, size of cascade clustering, etc.

Since MD simulates many-body interactions, it is much more time-consuming than BCA. The heavy computation burden is an important issue that limits the application of MD for high energy particles. Figure 3-8 shows the time evolution of point defects obtained by MD simulations [103]. Higher PKA energy implies larger displacement cascade and longer time to form stable point defects. To overcome this shortcoming of heavy computation burden, the Cell Molecular Dynamics for Cascades (CMDC) [104] code has been developed to accelerate the MD simulations by treating only the "active box" rather than the whole domain of the simulation. Ortiz proposed another solution that the MD is used at low energy while the BCA is used at high energy [105].

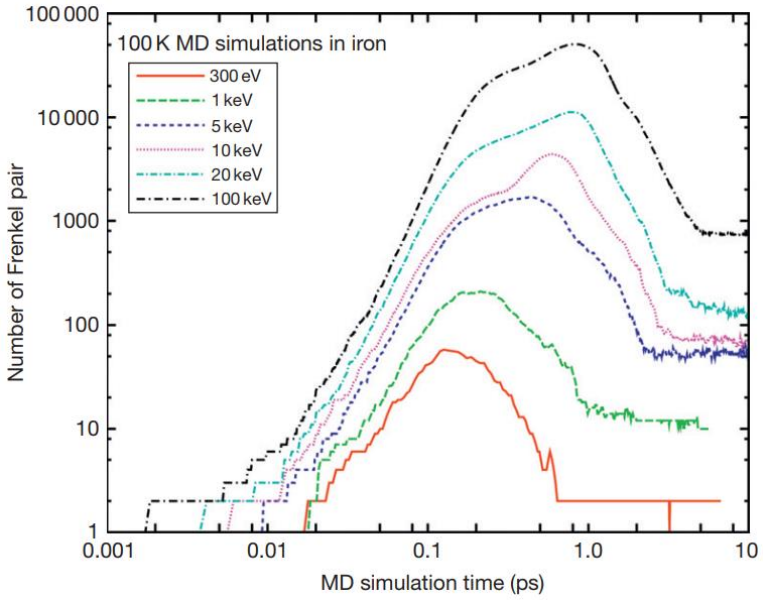

Figure 3-8. Evolution of the number of Frenkel pairs formed during displacement cascades using MD simulations [103].

BCA and MD are more realistic than the semi-empirical analytical formulae for computing the number of atomic displacements. However, BCA and MD results depend on the chosen semi-empirical interatomic potential (in BCA, stopping power is more referred). As a consequence, BCA and MD calculations rest also as references before their validation against experimental data.

3.7.2 Recent discussion on SRIM-like BCA codes [106]

As mentioned in Section 3.7.1, SRIM is widely used to determine the number of atomic displacements. However, different options in SRIM give inconsistent values of the number of atomic vacancies [107, 108]. Stoller *et al.* recommended the use of Quick Calculation (QC) option (i.e. using Lindhard's damage energy for PKA distribution obtained by BCA-based Monte Carlo simulations [109]) with the proposed methods to obtain the results comparable with the standard NRT formula [107]. Recently, Crocombette and Van Wambeke [102] and Weber and Zhang [109] recommended to use Full Cascade (FC) simulations in SRIM-like codes because of its physical significance.

To explain the discrepancy between QC (or comparable results with NRT-DPA) and FC in SRIM-like BCA codes, we revisit the reasoning of KP model [106]. The following of this subsection is a brief summary of our published paper in *Results in Physics* [106]. Firstly, it is noteworthy that the number of vacancies in lattice induced *by an incident ion* is different to that induced by a PKA. Because we distinguish the atomic displacement induced by ion and PKA only in this subsection, the notations $v(E)$ for ion-induced number of vacancies and $\bar{v}(E)$ for PKA-induced one used in Ref. [106] are kept in this subsection. Moreover, for PKA energy that $E \gg E_d$, $\bar{v}(E) \approx v(E)$ [106], it is thus not necessary to distinguish $v(E)$ and $\bar{v}(E)$ at high energy.

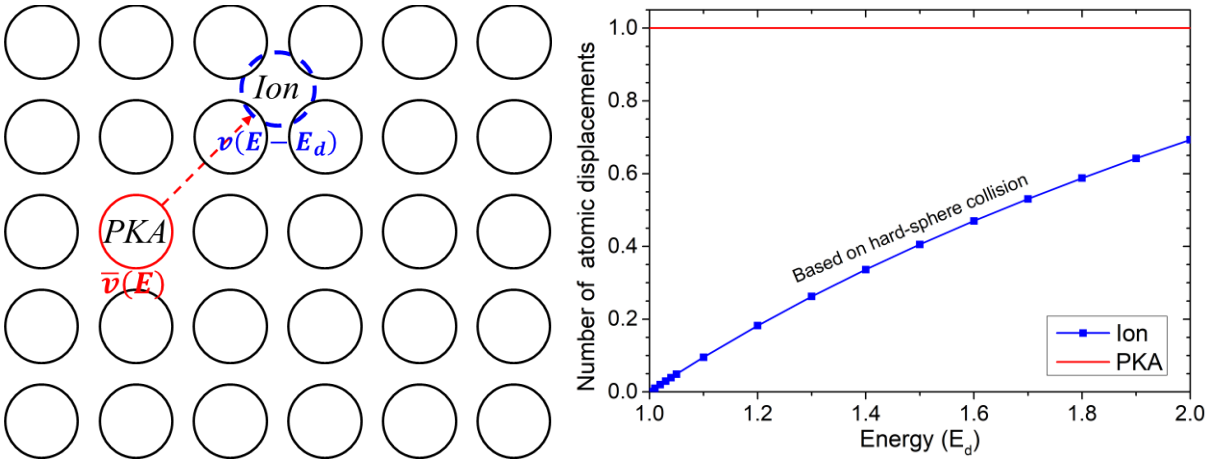

(a) (b)

Figure 3-9. Difference between the ion-induced and PKA-induced number of atomic displacements. (a) Schematic of the displacement of a PKA with energy E. Once this PKA is displaced by consuming E_d energy, it is a free ion with (E - E_d) kinetic energy. (b) Number of atomic displacements induced by an incident ion and a PKA at energy from E_d up to $2E_d$.

As illustrated in Figure 3-9(a), the difference between $v(E)$ and $\bar{v}(E)$ is that the former does not count the incident ion as a vacancy, while the latter includes the knocked-on PKA as one vacancy. The number of atomic displacements induced by an

incident ion and a PKA shown Figure 3-9(b) are quite different in $[E_d, 2E_d]$. For high energy PKA, as the schematic illustrated in Figure 3-9(a), the number of displacements induced by a PKA with energy E (i.e. $\bar{\nu}(E)$) is approximately equal to the sum of 1 displacement for itself and the number of displacements induced by the displaced free ion with $(E - E_d)$ kinetic energy, (i.e. $\nu(E - E_d)$):

$$\bar{\nu}(E) \approx \nu(E - E_d) + 1 \tag{3-34}$$

For the elastic collision of two identical atoms as shown in Figure 3-10, the number of vacancies induced by the two free atoms after such collision is $\nu(E - T) + \nu(T - E_d)$. Since the knocked-on atom is accounted as one displacement, one has:

$$\nu(E) = \nu(E - T) + \nu(T - E_d) + 1 \tag{3-35}$$

Supposing the atoms as hard spheres, the differential collision cross section is (c.f. Appendix A1):

$$\sigma(E, T) = 1/E, \quad \forall T \in [0, E] \tag{3-36}$$

Therefore, the integral equation governing $\nu(E)$ is simplified to:

$$\nu(E) = \frac{1}{E}\int_0^E [\nu(E - T) + \nu(T - E_d)]dT + 1 \tag{3-37}$$

An evident mathematical solution of Eq. (3-37) is:

$$\nu(E) = E/E_d \tag{3-38}$$

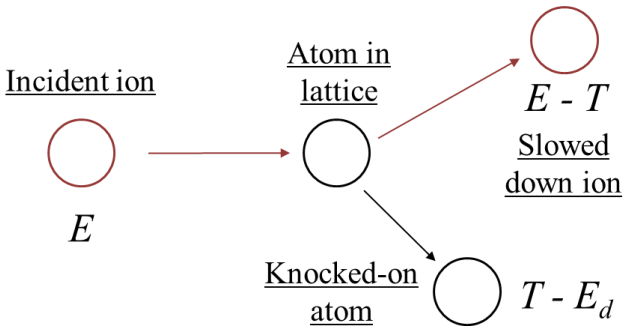

Figure 3-10. Schematic of energy transfer via elastic atomic collision.

Eq. (3-38) is an exact mathematical solution of Eq. (3-37). The physical issue of Eq. (3-38) is that $\nu(T - E_d) < 0$ when $T < E_d$ and $\nu(T - E_d) > 0$ when $E_d < T < 2E_d$, whereas $T < E_d$ is physically impossible and the definition of E_d implies $\nu(T - E_d) = 0$ for $T - E_d < E_d$. However, Eq. (3-38) satisfies $\int_0^{2E_d} \nu(T - E_d)dT = 0$, which implies $\int_0^E \nu(T - E_d)dT = \int_{2E_d}^E \nu(T - E_d)dT$ for $E > 2E_d$. Consequently, for ion energy $E > 2E_d$, Eq. (3-38) still satisfies Eq. (3-37) with the physical constraint

$v(T) = 0$ for $T < E_d$ using the approach of the first term in Eq. (3-37): $\int_0^E v(E - T)dT \approx \int_0^{E-E_d} v(E - T)dT$. An intuitive understanding of Eq. (3-38) is that each atomic displacement consumes E_d kinetic energy. Therefore, the total energy lost to the lattice by atomic displacements is $v(E)E_d$.

In fact, as explained by Kinchin and Pease [71], if there is only one kinematic atom and its kinetic energy is below E_d (above E_d but below $2E_d$ resp.), it can displace only 0 (1 resp.) atom in lattice. However, as shown in Figure 3-11, atoms in displacement cascades having kinetic energy below E_d or $2E_d$ can transfer energy with other kinematic atoms during the displacement cascade, so that more atomic displacements are formed than the Kinchin-Pease displacements. For example, $E_1 = 0.8E_d$ and $E_2 = 0.5E_d$ can induce an atom with a maximum energy of $1.3E_d$ that is possible for a kinematic atom to displace 1 atom (shown in Figure 3-11(a)) and is more than enough to induce 1 displacement for an atom in lattice (shown in Figure 3-11(b)), while atomic displacement is not possible for this case according to Kinchin-Pease. This kind of energy transfer is noted by **residual energy transfer** hereinafter.

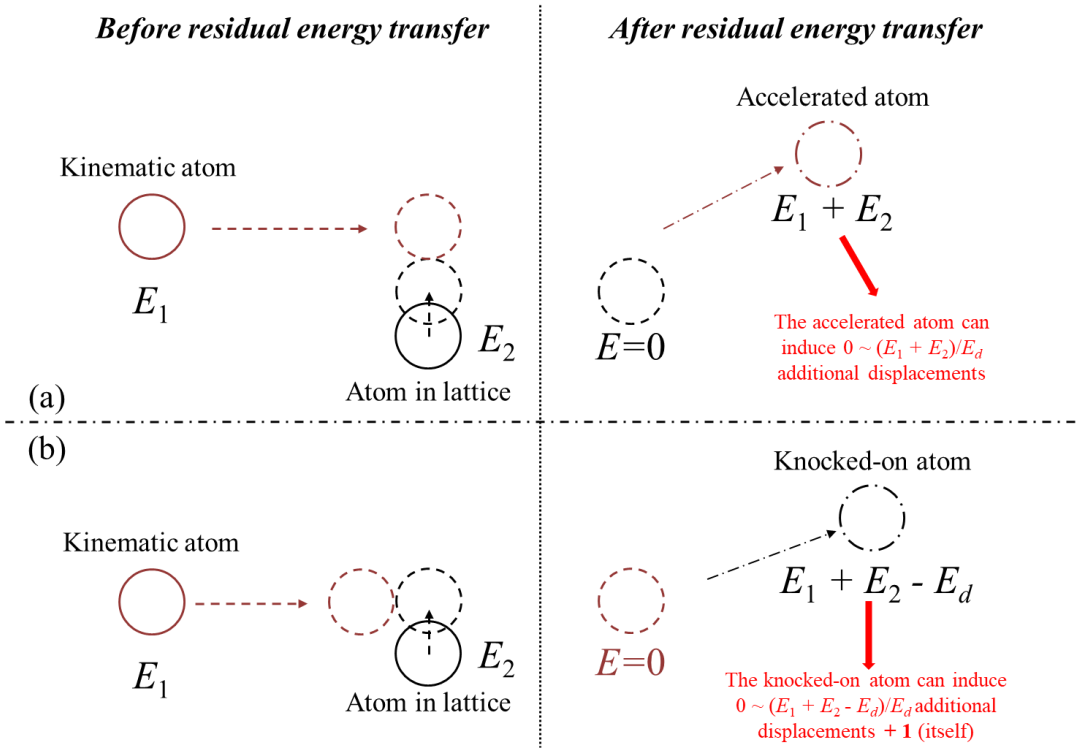

Figure 3-11. Schematic of the maximum residual energy transfers from an atom in lattice to a kinematic atom (upper) and from a kinematic atom to an atom in lattice (lower).

Nevertheless, it is impossible that all available energies are used in atomic displacements. In fact, if the below E_d residual energy of an atom cannot be transferred

to other kinematic atoms, or this residual atom cannot receive enough energy from other atoms, this part of residual energy would be lost. Therefore, an efficiency of available energy (denoted by κ_α, referred to the efficiency of residual energy transfer hereinafter) is introduced. The definition of κ_α implies that one effective atomic displacement consumes E_d/κ_α available energy. By taking the electronic effects and correction on atomic collision into account, the corrected number of vacancies is:

$$\nu(E) = \kappa E_a(E)/E_d, \quad \text{for } E_a(E) > E_d \tag{3-39}$$

where $E_a(E)$ is the damage energy [72], $\kappa = \kappa_\alpha \kappa_\beta$ where κ_β (= 0.8 in NRT formula) is the correction on atomic collision.

The energy dependence of κ_α is qualitatively illustrated in Figure 3-12. The main properties are:

- κ_α increases with ion energy. Higher ion energy leads to more atoms with damage energy around E_d after several atomic collisions. The probability of residual energy transfer (as the example shown in Figure 3-11) is thus higher.
- $\kappa_\alpha(2E_d) < 0.5$. An incident ion with kinetic energy $E = 2E_d$ is able to displace one atom. However, it cannot displace two atoms (possible but the probability is quasi-null). For the hard-sphere elastic scattering of identical atoms, Figure 3-9(b) shows $\kappa_\alpha(2E_d) = 0.35$.
- κ_α is quasi-constant for $E \gg E_d$. Except for the residual energy transfer that enhances the atomic displacement, there is also available energy ($> E_d$) transfer but without inducing displacement. At high energy, there should be an equilibrium between the two energy transfers.

Since Ref. [79] shows that κ_β is almost energy-independent, κ increases with the incident ion energy and becomes quasi-constant above a threshold.

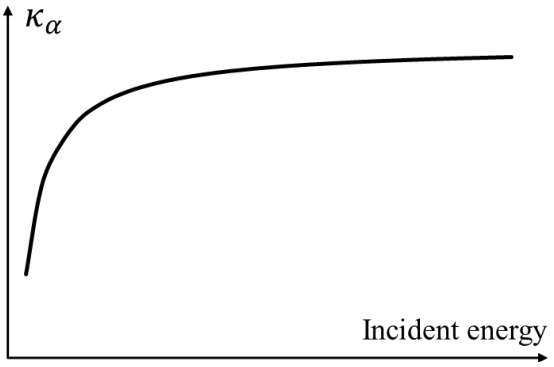

Figure 3-12. Qualitative description of energy dependence of κ_α.

According to Eq. (3-39), the ratio of atomic displacements to the current international standard metric NRT is:

$$\nu/\bar{\nu}_{NRT} = 2.5\kappa \tag{3-40}$$

It is emphasized that κ is energy-dependent. If one assumes $\kappa = 0.8$, which is used in the NRT formula to correct atomic collision, Eq. (3-39) doubles the number of atomic displacements computed by the NRT model. Taking the athermal recombination effect into account, the corresponding correction function (also called as the efficiency) of Eq. (3-39) can be directly determined by:

$$\xi = \xi_{ARC}/2.5\kappa \tag{3-41}$$

where ξ_{ARC} is the efficiency of the recently ARC-DPA formula that is based on the NRT model [84, 85]. Nevertheless, it should be noted that κ or mainly κ_α is energy-dependent.

Since QC is deduced by following the trajectory of ion while the FC follows all collided atoms, the damage energies calculated with these two options are not strictly the same. Assuming the damage energy computed in the QC is the same as that simulated with FC (although they are a little different), the ratio of FC (approximately Eq. (3-39)) to QC is:

$$\mathrm{FC/QC} = \nu/\bar{\nu}_{NRT} = 2.5\kappa \tag{3-42}$$

Therefore, $\mathrm{FC/QC} = 2.5$ if $\kappa = 1$. Using $\kappa = \kappa_0 \equiv 0.86$ which is in fact the value of κ_β from BCA [79], one has $(\mathrm{FC/QC})_0 = 2.15$. The values of FC/QC for all cases shown in Ref. [106] are included in [0.9, 1.2]$\times (\mathrm{FC/QC})_0$.

3.8 Measurements of number of atomic displacements

Because no model is perfect, experimental measurements are fundamental to accurately quantify the number of atomic vacancies in irradiated materials. In order to avoid the influence of thermal recombination, experiments for measuring the number of atomic displacements should be performed in cryogenic temperature (< 10 K). Three methods can be used to count the number of point defects in irradiated materials, including direct counting using Transmission Electron Microscopy (TEM) [110], Positron Annihilation Spectroscopy (PAS) [111], and Change of Electronic Resistivity (CER) [82].

PAS can be used for measuring the number of vacancies because atomic vacancies in lattice lead to low electron density [112]. If point defects are presented, positrons will reside in vacancies so that they annihilate less rapidly than the annihilation in the bulk of the material.

CER is a common method to quantify the number of Frenkel pairs in metals. For a specific metal, the number of Frenkel pairs is deduced by:

$$N_{FP} = \Delta\rho/\rho_{FP} \tag{3-43}$$

where $\Delta\rho$ is the CER and ρ_{FP} is the resistivity per Frenkel pair. The values of ρ_{FP} with

uncertainties and possible ranges are summarized in Table 3-4. The number of atomic vacancies can be thus directly calculated by the difference of CER before and after irradiation. The uncertainty of ρ_{FP} is directly propagated to the measured number of atomic vacancies. For iron, ρ_{FP} results in 20% uncertainty of experimental data via the CER measures.

Table 3-4. Resistivity per Frenkel pair (in μΩm) for monatomic materials [90, 97].

Element	Min	Max	Max2[a]	Jung [97]	Unc. [97]	Broeders [90]	Unc.[b] [90]
Al	1.32	4.3	6.8	4		3.7	
Ni	3.2	7.1	11.2	7.1	0.8	7.1	0.8
Cu	1.15	3		2.5	0.3	2.2	0.5
Pd	9		10.5	9	1	9	1
Ag	1.4	2.1	2.5	2.1		2.1	0.4
Ir[c]				6.7	0.5	6.7	0.5
Pt	6	9.5		9.5	0.5	9.5	0.5
Au	0.89	3.2	5.1	2.5		2.6	
Pb	1		20	-		-	
Th	15	19		-		19	
V	6		40	22	7	21	
Cr	37	40		-		37	2
Fe	12.5	30		30	5	24.6	
Nb	14	16		16		14	3
Mo	4.5	15		15	4	13.4	
Ta	16	17		16	3	16.5	3
W	7.5	28		27	6	27	6
Mg	0.8	9	21.5	9		9	
Sc				-		50	
Ti	18	42		-		24.9	
Co	14	35		16	5	15.5	5
Zn	4.2	20		15	5	17.9	
Y	50			-		50	20
Zr	35	40		35	8	37.5	8
Cd	5	10	19	-		14.5	8
Pr				-		135	5
Nd				-		135	5
Eu	100			-		-	
Gd				-		160	30

Tb				-	155	30
Dy				-	145	30
Ho				-	145	30
Er				-	180	35
Tm					140	30
Yb					75	25
Lu	75	145			145	30
Re	20				20	
Ga					5.4	0.5
U					22	
In					2.6	
βSn	1.1		4.2		1.13	0.2
Sm					140	30
Bi	7500					

[a] Maximum value adopted by Jung or Broeders or by the systematics given in Ref. [90].

[b] Uncertainty estimated by author from Ref. [90].

[c] Elements in red are those with only one available value.

4 Calculation of damage cross sections

Both DPA formulae and BCA and MD simulations use PKA energy as a major parameter. In applications, the given quantities from particle transport calculations are the spectra of incident energetic particles, such as neutron spectra in nuclear reactors, rather than PKA spectra. For a given neutron spectrum, the corresponding PKA spectrum can be calculated by the standard code SPECTER [113] and two recently developed codes DART [114] and SPECTRA-PKA [115]. The typical method of primary DPA calculation applied in nuclear reactors is the generation of Damage Cross Sections (DXS) through the nuclear data processing code NJOY [87]. The DPA rates can be calculated with the DPA cross sections and the spectra of incident particles computed by particle transport codes. This section presents the methods for calculating damage cross sections.

4.1 Thermal vibration of the target atom [116]

4.1.1 Two-body elastic collision kinematics

The recoil energy of PKA is fundamental for DPA calculations. Figure 4-1 shows the scheme of the collision in the Laboratory (Lab) frame. The incident and emitted kinetic energies are referred to E and E', respectively. E_R stands for the recoil energy of the target nucleus. m and v (m' and v') are respectively the mass and velocity of the incident (outgoing) particle. M and M' denote the mass of target and residual nuclei, respectively. The kinetic energy of the target is set to $1.5kT$, which is the average kinetic energy for particles with temperature T. $k = 8.617 \times 10^{-5}$ eV/K is the Boltzmann constant. θ denotes the angle of the target due to thermal vibration. The angle between the velocity of CM and the incident direction is denoted by φ. The emission angle is referred to α. The emission angle in the CM frame is noted as α_c.

The conservation of energy conducts to:

$$E + 1.5kT = E' + E_R + Q \tag{4-1}$$

where Q is the reaction energy. The conservation of momentum before and after collision shows:

$$mv + Mv_T \cos\theta = m'v' \cos\alpha + M'v_R \cos\beta \tag{4-2}$$

$$Mv_T \sin\theta = m'v' \sin\alpha + M'v_R \sin\beta \tag{4-3}$$

At low incident energies, the emission angle in the CM frame, i.e. α_c, is supposed to be isotropic. At high energies, the angular distribution can be found in ENDF, which often gives the distribution of α_c. The angular distribution of α can be determined by that of α_c and φ because $\alpha = \alpha_c + \varphi$. The conservation of momentum before collision

leads to:

$$mv + Mv_T \cos\theta = (m+M)v_{CM} \cos\varphi \tag{4-4}$$

$$Mv_T \sin\theta = (m+M)v_{CM} \sin\varphi \tag{4-5}$$

φ satisfies thus:

$$\tan\varphi = \frac{Mv_T \sin\theta}{mv + Mv_T \cos\theta} \tag{4-6}$$

Due to the symmetry, one can further suppose that $\theta \in [0, \pi]$. Consequently, for $mv > Mv_T$, i.e. $mE > 1.5MkT$,

$$\varphi = \tan^{-1}\left(\frac{Mv_T \sin\theta}{mv + Mv_T \cos\theta}\right) \tag{4-7}$$

The corresponding recoil energy $E_R(E, T, \alpha_c, \theta)$ can be thus determined as a function of (E, T, α_c, θ).

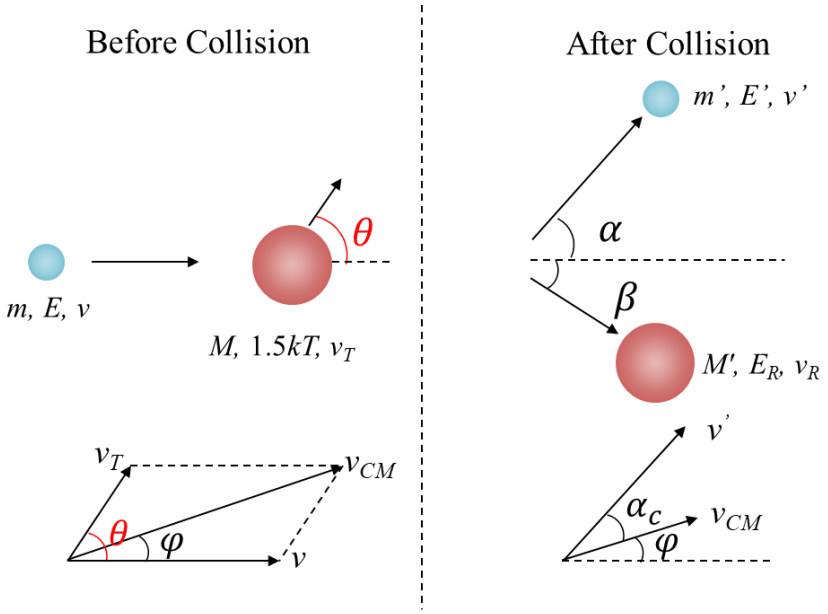

Figure 4-1. Schematic of the collision in the Lab frame.

The recoil energy depends on the angle of the thermal vibration θ. However, it is not so important to study the dependence of recoil energy on θ because the latter has to be random. The random value of θ leads to the isotropic angular distribution. Therefore, the recoil energy averaged over θ is investigated. The isotropic angular distribution of θ conducts to:

$$E_R(E, T, \alpha_c) = \frac{1}{2}\int_{-1}^{1} E_R(E, T, \alpha_c, \theta) d(\cos\theta) \tag{4-8}$$

where $E_R(E, T, \alpha_c, \theta)$ is determined by the aforementioned kinematics.

4.1.2 Numerical results

Figure 4-2 shows the average recoil energy calculated with Eq. (4-8) of ^{56}Fe for 100 eV, 500 eV, 1 keV, and 5 keV energy neutron elastic scattering with different temperatures as a function of α_c. The influence of temperature is more important at lower incident energy. However, due to the threshold energy of atomic displacement, the temperature effect on recoil energy has no influence on DPA computation when the recoil energy is lower than E_d or $2.5E_d$ ($2E_d/0.8$), which is equal to 40 eV or 100 eV for iron [20, 70].

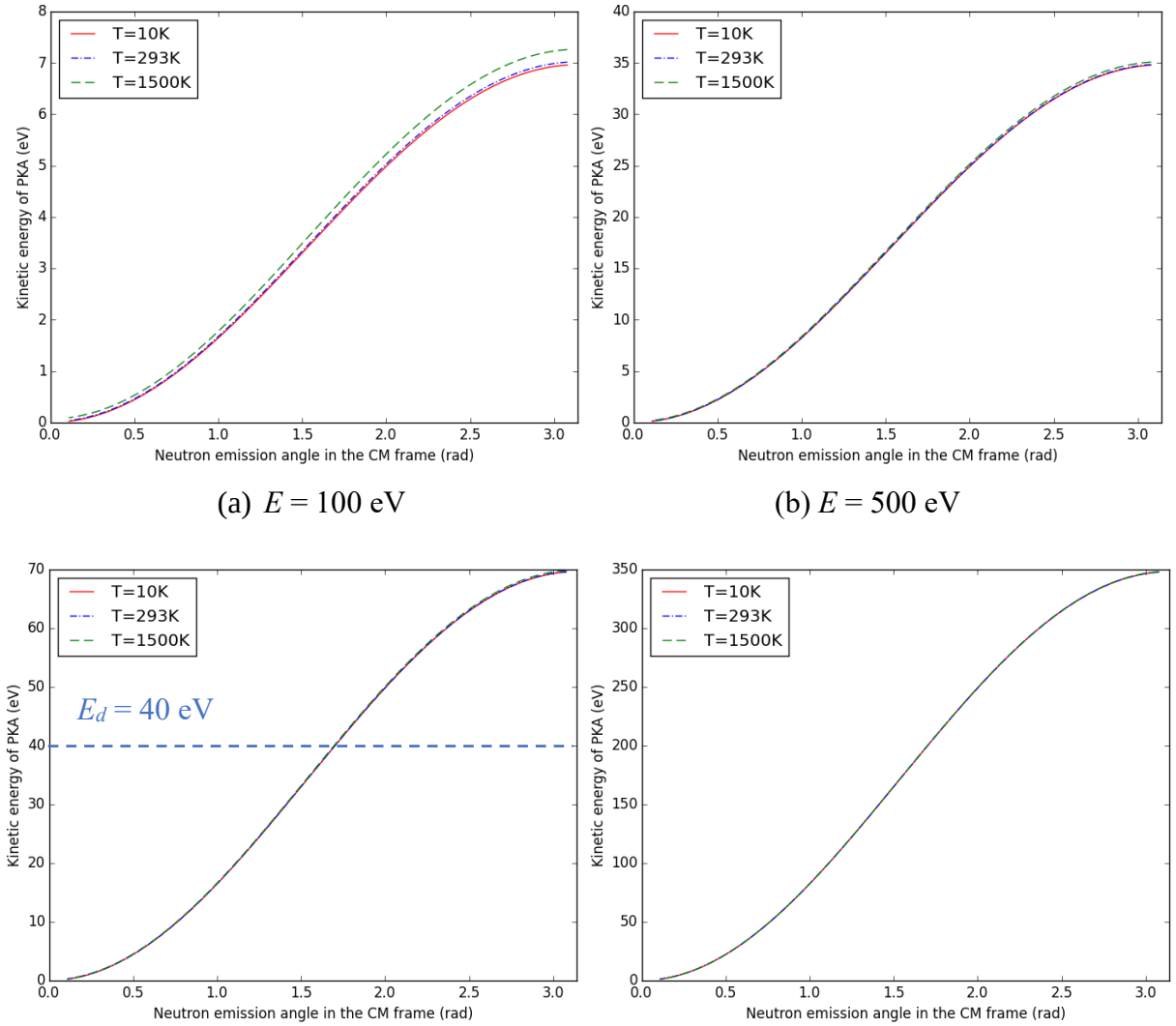

(a) E = 100 eV (b) E = 500 eV

(c) E = 1 keV (d) E = 5 keV (3 curves coincide)

Figure 4-2. Average PKA energy of ^{56}Fe for 100 eV, 500 eV, 1 keV, and 5 keV incident neutrons with different target temperatures.

For neutron elastic scattering shown in Figure 4-2, different temperatures of ^{56}Fe have the same DPA number (0 DPA) for incident energy lower than 500 eV. For 1 keV

neutron, the maximum recoil energy is higher than E_d but lower than $2.5E_d$. Therefore, the DPA number does not change with the temperature. For high incident neutron that the recoil energy of ^{56}Fe can be higher than $2.5E_d$. However, the temperature effect on recoil energy is negligible because of the quite small contribution of the kinetic energy of target ($1.5kT$ = 0.2 eV when T = 1500 K) before the collision, as shown in Figure 4-2(d). The average recoil energies with different incident energies and different temperatures are given in Table 4-1. Both Figure 4-2 and Table 4-1 show that the consideration of the thermal vibration of the target has a negligible influence on DPA computations. As a consequence, the DPA cross sections computed by NJOY without considering the thermal vibration of the target can be directly used.

Table 4-1. Average recoil energy (in eV) of ^{56}Fe for 100 eV, 500 eV, 1 keV, 5 keV, and 10 keV incident neutron elastic scattering with different temperatures.

E	100 eV	500 eV	1 keV	5 keV	10 keV
10 K	3.52	17.61	35.22	176.09	352.11
293 K	3.56	17.65	35.25	176.12	352.15
1500 K	3.71	17.80	35.41	176.25	352.37

4.2 Relativistic effect on the calculation of recoil energy [117]

4.2.1 Relativistic kinematics

Figure 4-3 illustrates the schematic of a general two-body collision kinematics in the laboratory frame. The kinetic energies of the incident and the emission particles are respectively denoted by *E* and *E'*. The corresponding momenta are denoted by *p* and *p'*. Due to the negligible influence of the thermal vibration of the target particle [116], the kinetic energy of the target is supposed to be 0. The recoil energy and momentum of the residual particle are denoted by E_R and p_R, respectively. *m*, *M*, *m'*, and *M'* represent the rest masses of the incident, target, emission, and residual particles in the ground state, respectively. The emission angle and the recoil angle are respectively denoted by φ and α.

The special relativity can be used in a laboratory framework that is approximatively an inertial reference. For the system illustrated in Figure 4-3, the conservation of momentum shows:

$$p' \sin\varphi = p_R \sin\alpha \tag{4-9}$$

$$p = p' \cos\varphi + p_R \cos\alpha \tag{4-10}$$

Eliminating α and denoting $\mu = \cos\varphi$, one obtains:

$$p_R^2 = p^2 - 2pp'\mu + p'^2 \tag{4-11}$$

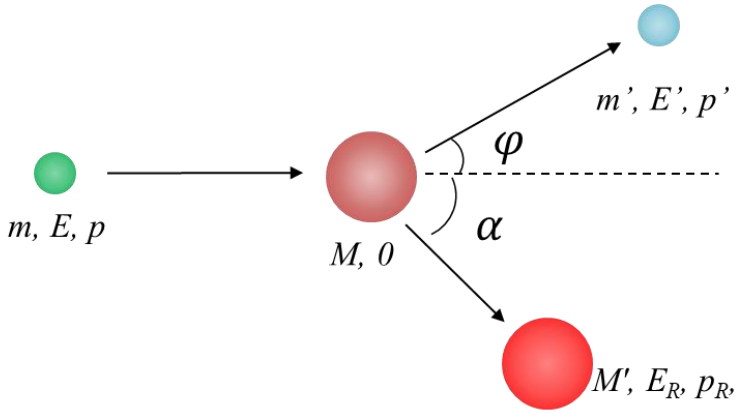

Figure 4-3. Schematic of the collision in a laboratory framework.

On the other hand, the relationship between relativistic momentum and energy shows:

$$p^2c^2 + m^2c^4 = (E + mc^2)^2 \tag{4-12}$$

$$p'^2c^2 + m'^2c^4 = (E' + m'c^2)^2 \tag{4-13}$$

$$p_R^2c^2 + M'^2c^4 = (E_R + M'c^2)^2 \tag{4-14}$$

For the sake of convenience, the rest energy is simply noted by the corresponding rest mass in the following equations. Replacing momenta by kinetic energies, the conservation of momentum before and after the reaction leads to:

$$E_R(E_R + 2M') = E(E + 2m) + E'(E' + 2m') - 2\sqrt{EE'(E + 2m)(E' + 2m')}\mu \tag{4-15}$$

Because both the recoil energy and the right-hand side of Eq. (4-15) are always positive, the physical solution of Eq. (4-15) is:

$$E_R = \sqrt{M'^2 + E(E + 2m) + E'(E' + 2m') - 2\sqrt{EE'(E + 2m)(E' + 2m')}\mu} - M' \tag{4-16}$$

The first order approximation is:

$$E_R = \frac{1}{2M'}\left[E(E + 2m) + E'(E' + 2m') - 2\sqrt{EE'(E + 2m)(E' + 2m')}\mu\right] \tag{4-17}$$

This approximation is valid for $E_R \ll M'c^2 \approx A_R$ GeV where A_R is the mass number of the recoil particle. For incident energy that $E/m \ll 1$, one can further obtain the recoil energy within classic mechanical assumption as:

$$E_{R,c} = \frac{1}{M'}\left[mE + m'E' - 2\sqrt{mm'EE'}\mu\right] \tag{4-18}$$

According to Eqs. (4-17) and (4-18), it is noticeable that for a specific reaction type and a given (E', μ), the recoil energy is inversely proportional to the mass of the residual

nucleus. Therefore, the 2-D plots of recoil energies for the ^{56}Fe target are general for all the nuclei by a factor of the ratio of residual masses. Moreover, the ratio of relativistic recoil energy to the classic mechanical one $E_R/E_{R,c}$ depends only on reaction type. In other words, for a specific reaction type, the 2-D plots of $E_R/E_{R,c}$ are exactly the same for all nuclei.

Due to the conservation of energy, the allowed range of the secondary energy E' in Eqs. (4-17) and (4-18) is determined by the energy loss and the recoil energy (E_R and $E_{R,c}$). In the present work, the maximum secondary energies are taken from JEFF-3.1.1 [28] for 20 MeV incident neutron-induced continuum reactions. For 200 MeV neutron-induced reactions, roughly assuming that the recoil energy is proportional to the incident energy (which is the case for classical elastic scattering), the reasonable maximum secondary energy becomes:

$$E'_{max}(200\ \text{MeV}) = E - 10(20 - E'_{max}(20\ \text{MeV}) - Q_t) - Q_t \qquad (4\text{-}19)$$

where Q_t (in MeV) is the threshold energy of the continuum reaction.

For a discrete reaction having a determined excitation energy -Q' (by convention, Q' represents the increase in kinetic energy of the system due to the excitation of the nucleus), the conservation of energy before and after the reaction implies:

$$E' = E + Q - E_R \qquad (4\text{-}20)$$

where

$$Q = Q' + [m + M - (m' + M')] \qquad (4\text{-}21)$$

An equation governing E_R can be determined by inserting Eq. (4-20) into Eq. (4-17). Due to the square root term in Eq. (4-17), one puts the square root term in one side and then takes the square to eliminate the square root for solving E_R. Because the equation involving E_R is a quartic equation, numerical methods are more feasible for a determined reaction Q-value.

For a specific Q-value at given incident energy, the relationship between E_R and E' given in Eq. (4-20) does not depend on reaction type nor on masses of particles. On the other hand, Eq. (4-17) points out that E_R strongly depends on the residual mass. Therefore, the recoil energy calculated by combining Eqs. (4-17) and (4-20) with a selected Q-value and a selected target nucleus is not as general as the 2-D plots of $E_R(E', \mu)$, which are representative of the corresponding reaction types by a factor of the ratio of residual masses (except that the maximum secondary energy depends on nucleus).

4.2.2 Numerical results

In this section, the numerical results are shown only for neutron-induced nuclear reactions. Nevertheless, due to the quasi-identical masses of proton and neutron, the

results on the recoil energy are almost the same for proton-induced reactions. For the same reason, the results for the (n,n') reactions are quite similar to those of the (n,p) reaction.

Figure 4-4 and Figure 4-5 respectively show the recoil energy within special relativity (in MeV) versus E' and μ for 20 MeV and 200 MeV neutron-induced proton production reaction (n,p) and α production reaction (n,α). Figure 4-6 illustrates the same results for 200 MeV α induced (α,n) reaction of ^{56}Fe. We remark again that these 2-D plots of the recoil energy are general for the corresponding reaction types by a factor of the ratio of residual masses (except that the maximum secondary energy depends on nucleus).

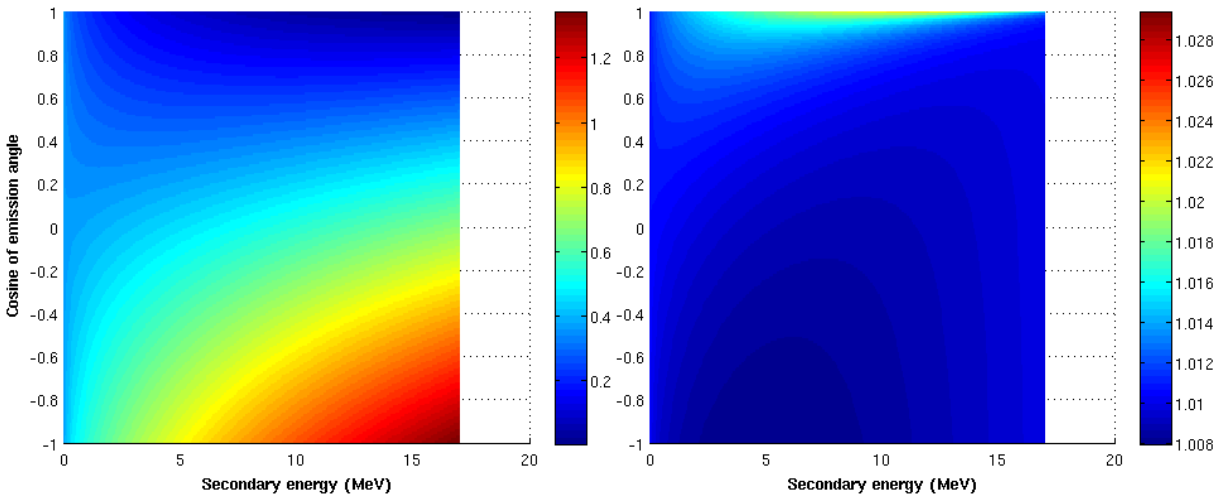

(a) (n,p)

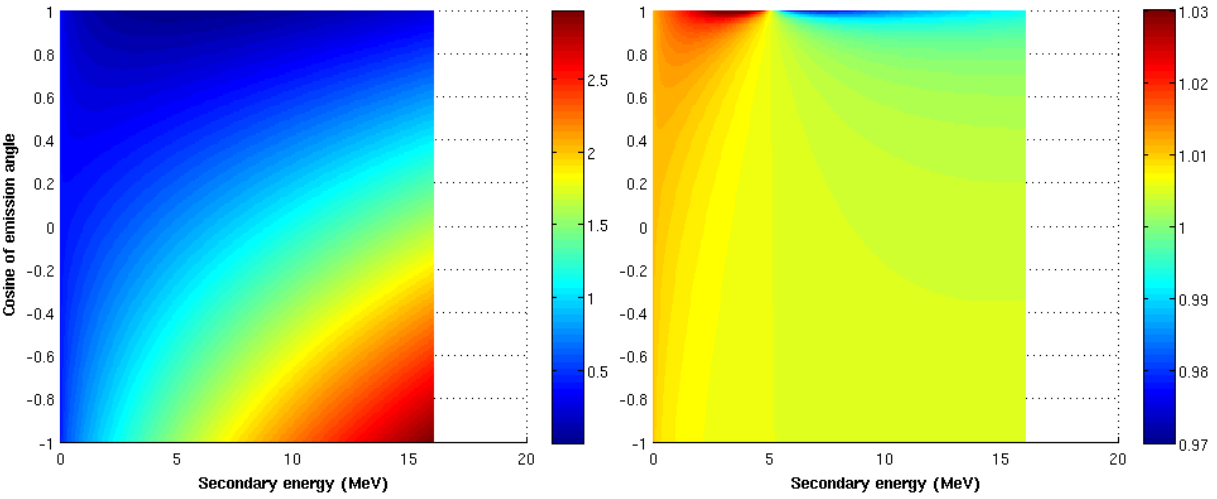

(b) (n,α)

Figure 4-4. Recoil energy within special relativity (left, in MeV) for 20 MeV neutron-induced proton emission reaction (a) and α emission reaction (b) of ^{56}Fe and the ratio of relativistic to classic mechanical results for all nuclei (right).

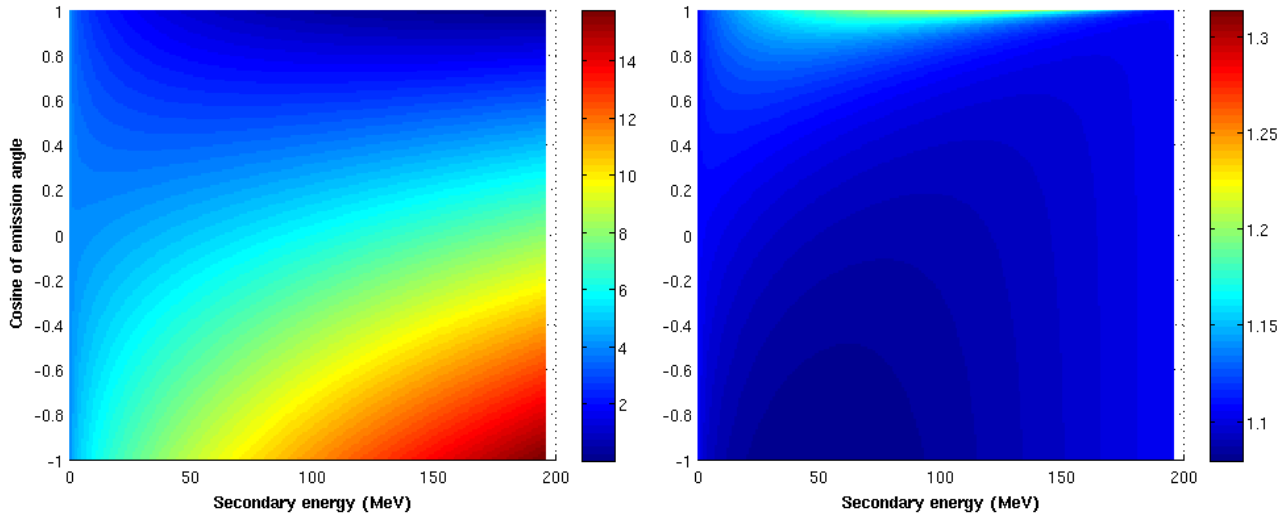

(a) (n,p)

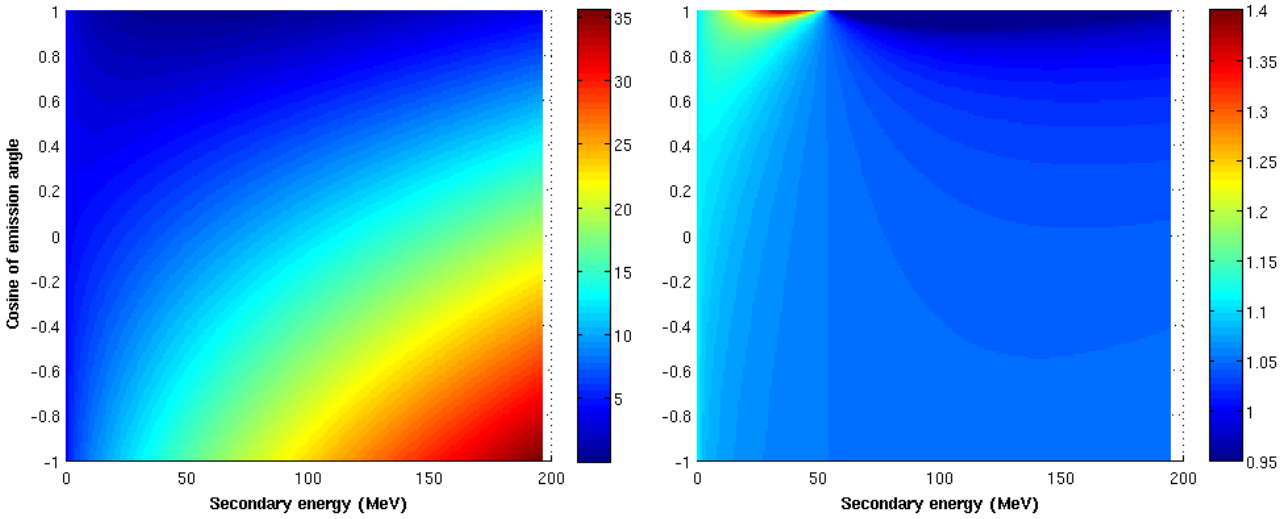

(b) (n,α)

Figure 4-5. Recoil energy within special relativity (left, in MeV) for a 200 MeV neutron-induced proton emission reaction (a), and α emission reaction (b) of ^{56}Fe and the ratio of relativistic to classic mechanical results for all nuclei (right).

As shown in Figure 4-4 and Figure 4-5, the global maximum (minimum resp.) recoil energies are always at $\mu = -1$ ($\mu = 1$ resp.) because Eq. (4-17) points out the decrease of E_R with μ. For $\mu = -1$, E_R increases with E', so that the global maxima are at $E' = E'_{max}$. In fact, according to Eq. (4-17), E_R increases with E' when $\mu \leq 0$. For a given $\mu > 0$, E_R is not a monotone function of E'. An example of a 200 MeV neutron-induced (n,α) reaction with $\mu = 1$ is shown in Figure 4-7.

The corresponding ratios of recoil energies with relativistic calculations to the classic mechanical ones $E_R/E_{R,c}$ are illustrated in the corresponding right figures of Figure 4-4, Figure 4-5, and Figure 4-6. Since $E_R/E_{R,c}$ is neither independent on target

particles nor recoil particles, the 2-D plots of $E_R/E_{R,c}$ are the same for the corresponding reactions of all nuclei (except that the maximum secondary energy depends on nucleus). For the (n,n') and (n,p) reactions, the relativistic corrections on recoil energy are always positive, while both positive and negative relativistic corrections are possible for (n,α) and (α,n) reactions. The maximum and minimum ratios for the (n,α) reaction are respectively infinite and null.

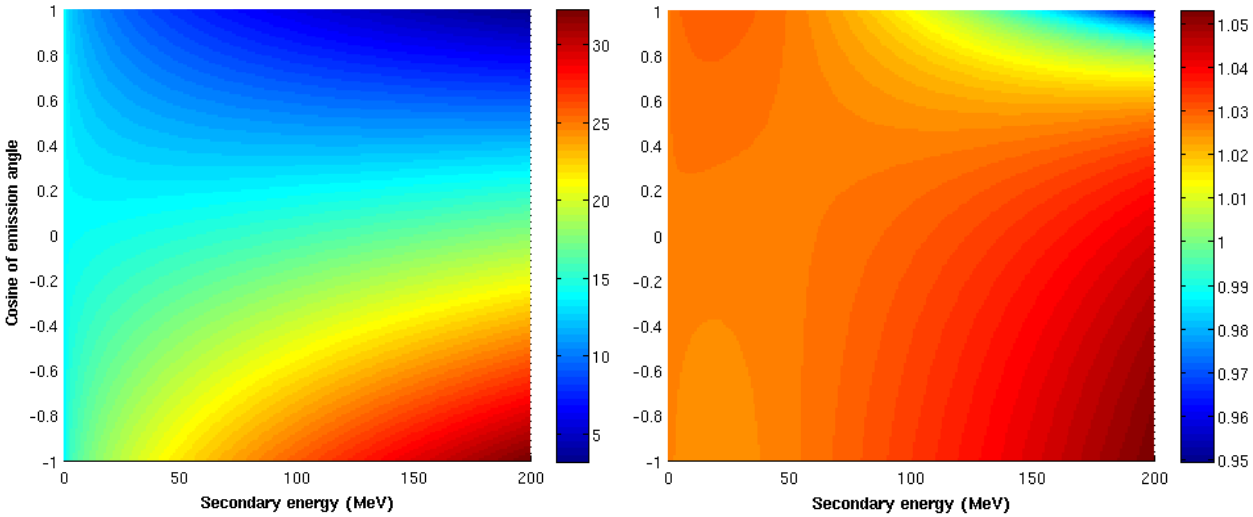

Figure 4-6. Recoil energy within special relativity (left, in MeV) and 200 MeV α-induced ^{56}Fe (α,n) reaction the ratio of relativistic to classic mechanical results for all nuclei (right).

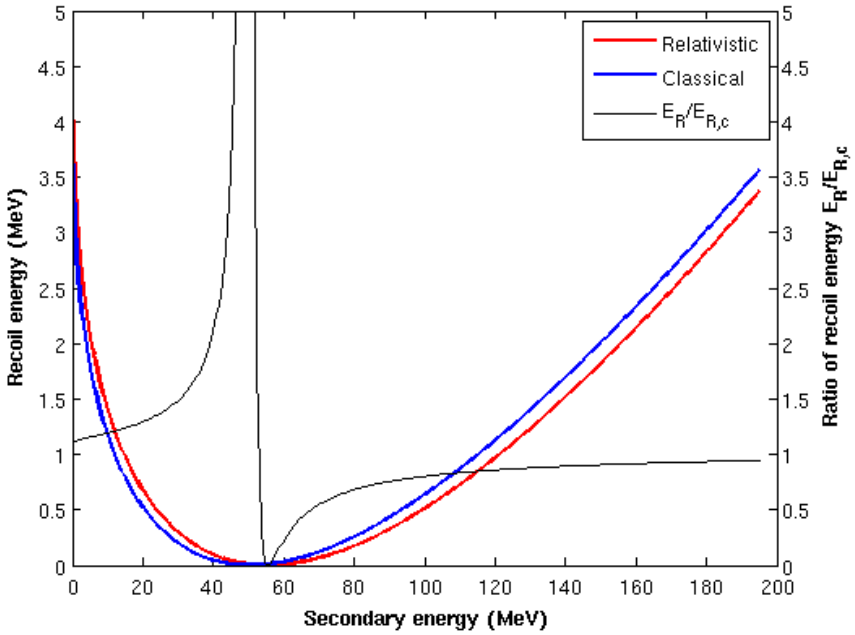

Figure 4-7. Recoil energies within special relativity and classical mechanics versus secondary energy for the 200 MeV neutron-induced (n,α) reaction with ^{56}Fe at $\mu = 1$.

As a matter of fact, as the example shown in Figure 4-7, the recoil energy at $\mu = 1$ is null at $E' = mE/m'$ for classic mechanical collision and at $E' = \sqrt{E(E+2m)+m'^2} - m'$ (larger than mE/m' because $E(E+2m)+m'^2 = (mE/m'+m')^2 + [1-(m/m')^2]E^2$ and $m' > m$) for relativistic collision. Different secondary energies at which the recoil energies are null lead to the values of infinity (i.e. $E_{R,c} = 0$) and zero (i.e. $E_R = 0$) for the relativistic to classic mechanical ratio. For reactions such as (n,n'), (n,p), and (α,n), because $m' \leq m$ and $E' < E$, the recoil energy cannot be null, such extreme values of infinity and zero are not possible. More precisely, when $E' < m'E/m$ or $\mu \leq 0$, the relativistic correction is always positive.

For incident neutron energy below 20 MeV, the relativistic treatment has less than 3% correction on recoil energy. However, the relativistic effect should be taken into account for high incident energy, whereas it is rarely considered for computing damage cross section (including the widely used code NJOY). Taking the examples of 200 MeV incident neutron, the relativistic recoil energies can be more than 30% higher than the classic mechanical ones. Moreover, large relativistic corrections on recoil energy lead to the broadening of PKA spectra. Table 4-2 gives the ranges of PKA energies for 20 MeV and 200 MeV neutron-induced (n,n'), (n,p), and (n,α) reactions of ^{56}Fe. The maximum recoil energy is about 10 keV and 1500 keV higher by considering the relativistic effect for 20 MeV and 200 MeV incident neutron, respectively. Such a considerable increase in maximum PKA energy implies that the range of energies for MD or BCA simulations should be extended when the relativistic effect is taken into account in PKA energy calculations.

Table 4-2. Recoil energy ranges of 20 MeV and 200 MeV incident neutron with ^{56}Fe target within classic mechanical ($E_{R,c}$) and relativistic (E_R) assumptions.

E (MeV)	Reaction	$E_{R,c}$ (keV)		E_R (keV)	
		Min	Max	Min	Max
20	(n,n')	6.9	1250	7.1	1262
	(n,p)	2.2	1332	2.3	1345
	(n,α)	0.0	2955	0.0	2970
200	(n,n')	0.6	14245	0.8	15743
	(n,p)	0.4	14275	0.5	15780
	(n,α)	0.0	33544	0.0	35318

Because the minimum PKA energies are much smaller than the maximum ones, the ranges of PKA spectra are approximatively equal to the corresponding maximum recoil energies. In addition, Eqs. (4-17) and (4-18) point out that E_R and $E_{R,c}$ are inversely

proportional to the residual mass. Consequently, for a specific reaction type at a given incident energy, the broadening of the ranges of PKA spectra due to the relativistic effect is almost inversely proportional to the PKA mass.

For a determined reaction Q-value, the recoil energy has only one degree of freedom on μ. Nevertheless, as previously mentioned, the equation governing E_R is a quartic equation. The numerical method is more feasible for calculating recoil energy. Figure 4-8 shows the relationship between E_R and E' according to both the conservation of momentum (i.e. Eq. (4-17)) and the conservation of energy (i.e. Eq. (4-20)) for the ground state ($Q = -2.91$ MeV), the fifth excitation state ($Q = -3.25$ MeV), and the thirteenth (and the last in the JEFF-3.1.1 nuclear data library [28], $Q = -3.75$ MeV) excitation state of neutron-induced proton production reactions on ^{56}Fe. Because the recoil energy obeys both Eq. (4-17) and Eq. (4-20), the recoil energy for a given μ and a given Q is found at the intersection of the two corresponding curves in Figure 4-8.

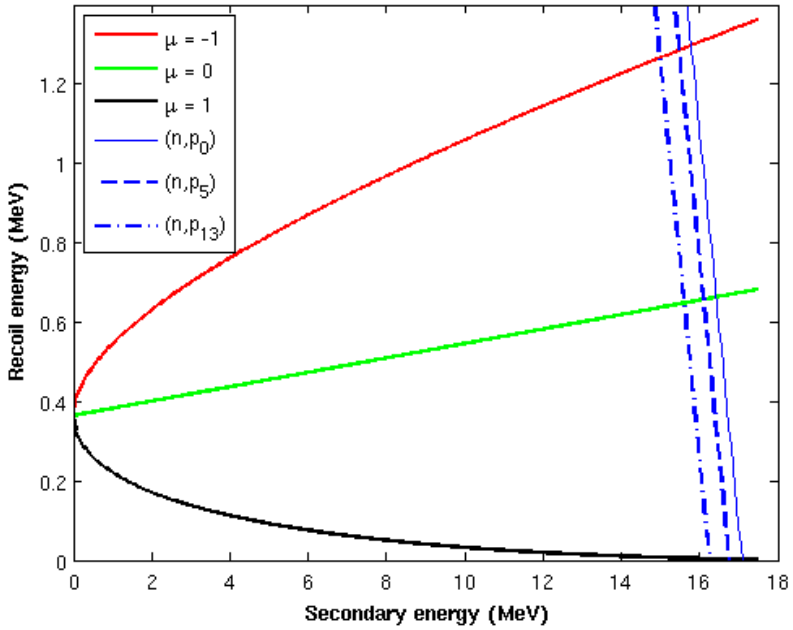

Figure 4-8. Recoil energy within special relativity versus secondary energy obtained with Eq. (4-17) ($\mu = -1, 0, 1$) and Eq. (4-20) (blue lines) for 20 MeV neutron (n,p$_i$) reactions of ^{56}Fe.

The numerical results for the relativistic recoil energies of (n,p$_0$), (n,p$_5$), and (n,p$_{13}$) reactions versus μ and the corresponding relativistic corrections are plotted in Figure 4-9 for 20 MeV and 200 MeV incident neutrons. The same results for (n,α_0) and (n, α_{10}) reactions (ground state $Q = 0.326$ MeV and the last excitation level in JEFF-3.1.1 with $Q = -2.13$ MeV) are also shown in Figure 4-9. Because the recoil energies of discrete reactions are special cases included in the general case $E_R(\mu, E')$, the relativistic

corrections are within the range determined by Eqs. (4-17) and (4-18) and illustrated in Figure 4-4 and Figure 4-5 (probably with a higher maximum secondary energy $E'_{max,d}$ to cover the range of E' for all discrete reactions).

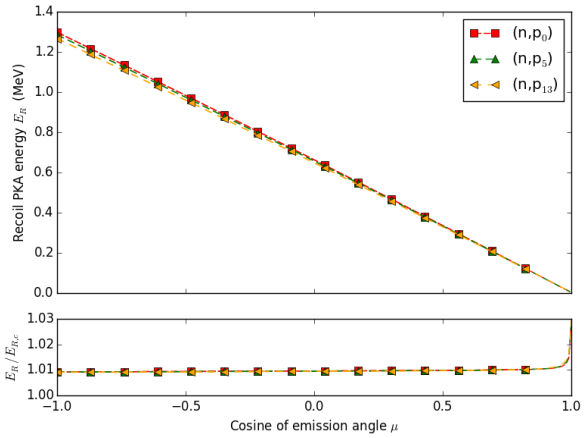

(1a) 20 MeV (n,p) reactions

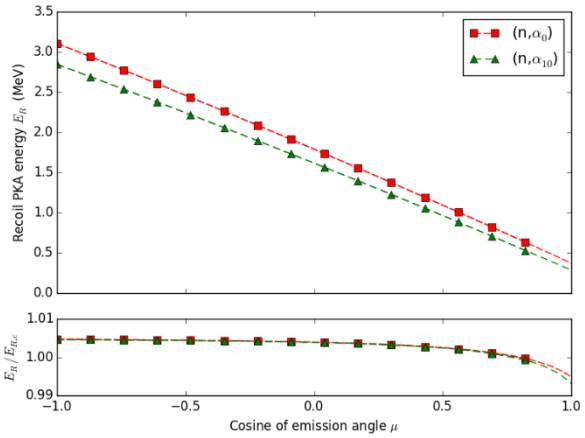

(1b) 20 MeV (n,α) reactions

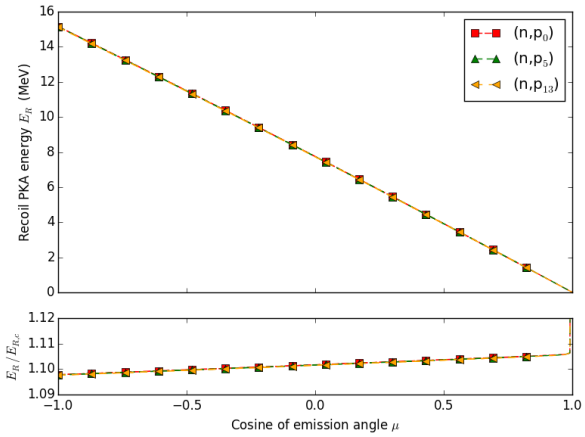

(2a) 200 MeV (n,p) reactions

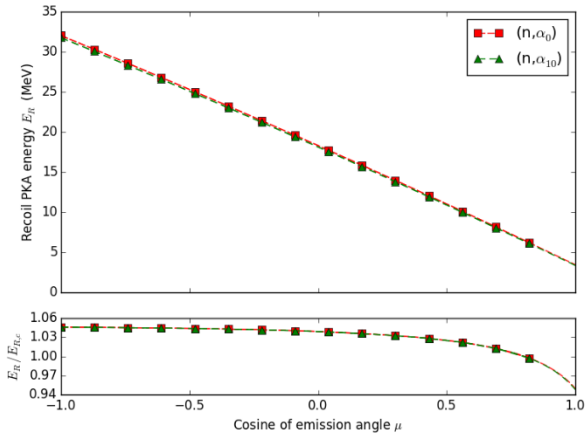

(2b) 200 MeV (n,α) reactions

Figure 4-9. Recoil energy versus μ for relativistic kinematics and the corresponding relativistic corrections for 20 MeV and 200 MeV neutron-induced discrete p and α emissions of ^{56}Fe.

4.2.3 Summary of relativistic corrections

The relativistic correction is almost 1% (10% resp.) for 20 MeV (200 MeV resp.) neutron-induced (n,n') and (n,p) reactions, while that of (n,α) reactions is from -0.6% to 0.5% (from -6% to 5% resp.). It has been observed that for a specific discrete reaction type, the relativistic correction is not sensitive to the excitation energy. In fact, at low incident energy, the relativistic correction is quite small. At high incident energy where the relativistic correction is significant, compared with the total energy, the Q-value is negligible. Again, we notice that the relativistic corrections for discrete reactions depend on target nuclei, while the 2-D plots are representative of the corresponding

reaction types by a factor of the ratio of residual masses (except that the maximum secondary energy depends on nucleus).

Table 4-3. Maximum ratio of relativistic quantities to the classical ones.

E (MeV)	Reaction	Recoil energy	Damage energy[b]	NRT-DPA[b]
20 MeV	(n,n')	1.028	1.027	1.027
	(n,p)	1.029	1.028	1.028
	(n,α)	∞	∞	∞
	(α,n)[a]	1.005	1.002	1.002
200 MeV	(n,n')	1.325	1.314	1.314
	(n,p)	1.314	1.301	1.301
	(n,α)	∞	∞	∞
	(α,n)[a]	1.053	1.006	1.006

[a] $E'_{max} = E$ is used to compute the maximum and minimum difference of DPA

[b] For ^{56}Fe target

To globally evaluate the relativistic effect on atomic displacement, Table 4-3 summarizes the maximum ratios of relativistic quantities to the classic mechanical ones for recoil energy, damage energy, and the NRT metric-based DPA number. It is noticeable that the ratios of NRT-DPA given in Table 4-3 are exactly the same as the ratios based on ARC-DPA because the high PKA energies lead to the constant efficiency $\xi_{ARC} = c_{ARC}$. As explained in Section 4.2.2, the infinity for recoil energy and the corresponding damage energy of the (n,α) reaction is due to the null classic mechanical recoil energy. As for DPA, if there is one point at which the classic mechanical damage energy is below the threshold energy while the relativistic one is above, the ratio is infinite.

For incident neutron energy lower than 20 MeV, the relativistic corrections are within 3%. Except for the small region in which the relativistic effect is obviously more important than other regions (e.g. Figure 4-4), the relativistic corrections are about 1% in the damage calculation for the (n,n') and (n,p) reactions. For 200 MeV neutron, the maximum corrections are more than 30% (and about 10% on average). For elastic scattering, one can use a +0.05%E/MeV correction on the PKA energy from classical kinematics [118]. Consequently, the computation of PKA spectra and damage cross sections for neutron or proton energy up to 200 MeV (and higher for spallation neutron sources) should be based on the relativistic kinematics. **For the time-being, such relativistic effects are not yet considered in NJOY** (or a recently developed code NECP-Atlas [119]) **for computing damage cross section.**

For a given incident energy, the relativistic effect is less important for incident

particles with higher masses. As summarized in Table 4-3, the maximum relativistic correction of 200 MeV α-induced neutron emission reaction is only 5% on PKA energy and lower on damage energy. For neutron in fission (~ 2 MeV) and fusion (~ 14 MeV) reactors, the classic mechanical kinematics should be a good approximation for computing PKA energy from nuclear reactions.

4.3 Calculation of recoil energy in different frames

Detailed derivations of two-body reaction inducing recoil energy in the Lab and the CM frame are presented in our published paper NIMB456(2019)120 [64]. Here the main equations concerning the calculation of recoil energy as a function of emission angle (and the secondary energy for continuum reaction in both Lab and CM frame) are summarized. As shown in Section 4.2, the relativistic effect is within 1% for neutron energy below 20 MeV, which is the case for both fission and fusion reactors. The classic mechanical kinematics is assumed in this section. In the case of high neutron energy, it suffices to replace the recoil energy by the relativistic one.

4.3.1 Discrete reactions [64]

Figure 4-10 shows the schematics of the collision in the Lab and CM frames. The incident and emitted kinetic energies are referred to E and E' in the Lab frame, respectively. E_R stands for the recoil energy of the PKA in the Lab frame. m and v_1 (m' and u_1) are the mass and velocity of the incident (outgoing) particle in the CM frame, respectively. M and v_2 (M' and u_2) are the mass and velocity of recoil particle before (after) the collision in the CM frame, respectively.

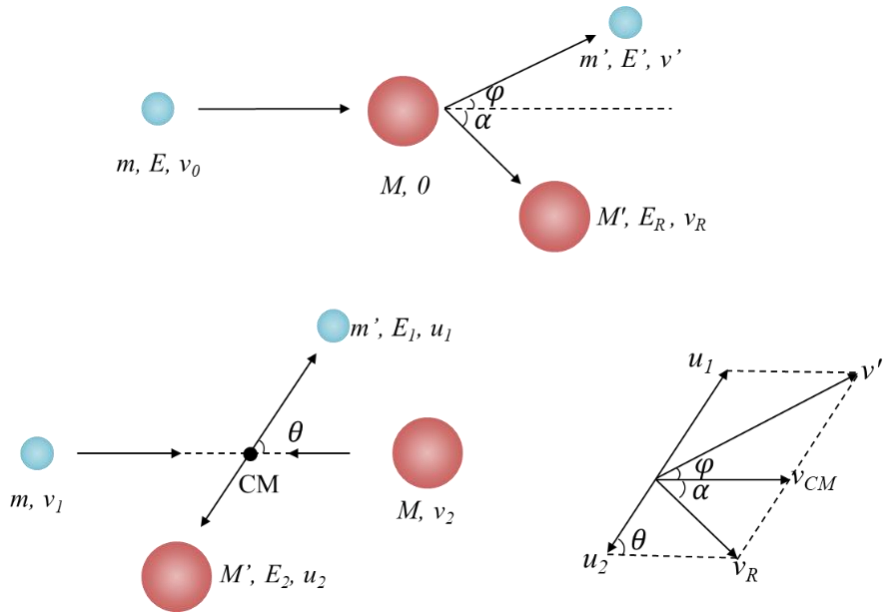

Figure 4-10. Schematics of the collision in the Lab (upper) and the CM (lower) frames.

In nuclear reactions, $(m' + M') = (m + M)$ is not necessarily correct because of the energy and mass transfer. Nevertheless, $(m' + M')/(m + M) = 1$ is numerically valid even though a quite small percentage of the mass is reduced during the nuclear reactions. One can define the "effective mass" $R(E)$ as:

$$R(E) = \sqrt{1 + \frac{(m+M)Q}{ME}} \tag{4-22}$$

where Q is the total energy change during the collision:

$$Q = Q' - [(m' + M') - (m + M)]c^2 \tag{4-23}$$

where Q' is the reaction energy. For elastic scattering, $R(E) = 1$. One can obtain the recoil energy according to the conservation of momentum and energy after and before reaction as:

$$E_R(E, \mu) = \frac{m'ME}{(m+M)^2}\left[\frac{mM'}{m'M} - 2R(E)\sqrt{\frac{mM'}{m'M}}\mu + R(E)^2\right] \tag{4-24}$$

where $\mu = \cos\theta$.

4.3.2 Continuum reactions [64]

In the continuum reactions, because the reaction energy cannot be specifically determined, the conservation of energy cannot be used to reduce one degree of freedom of unknowns. In most of the current ENDFs, the double-differential cross sections are energy-angular distributions of the emitted particle. Therefore, we should calculate the recoil energy as a function of emission angle and secondary energy. The double-differential cross sections are recommended to be given in the Lab frame (because of the appearance of secondary energy). However, many double-differential data are still in the CM frame. It is always possible to change the data in the CM frame into the Lab frame or directly use the change of variables during the calculation of damage cross sections, but the best method as explained in Ref. [64] is the direct calculation using double-differential data in the CM frame. This subsection briefly presents the explicit equation of recoil energy versus emission angle and secondary in both the Lab frame and the CM frame.

4.3.2.1 Recoil energy vs emission angle and secondary energy in the Lab frame

For the schematic shown in Figure 4-3, the recoil energy as a function of emission angle and secondary energy in the Lab frame can be calculated by:

$$E_R(E, E', \tilde{\mu}) = \frac{1}{M'}[mE - 2\sqrt{mm'EE'}\tilde{\mu} + m'E'] \tag{4-25}$$

where $\tilde{\mu} = \cos\varphi$ with φ the emission angle in the Lab frame.

4.3.2.2 Recoil energy vs emission angle and secondary energy in the CM frame

For the schematic shown in Figure 4-3, the recoil energy as a function of emission angle and secondary energy in the CM frame can be calculated by:

$$E_R(E, E_1, \mu) = \frac{mM'}{(m+M)^2}E - 2\frac{\sqrt{mm'EE_1}}{m+M}\mu + \frac{m'}{M'}E_1 \tag{4-26}$$

where $\mu = \cos\theta$ and E_1 is the secondary energy in the CM frame.

4.3.3 Charged particle emission reactions [73]

For neutral particle emission, the recoil energy of PKA can be formed as:

$$E_R(\mu, E) = \frac{1}{A+1}\left(E^* - 2\sqrt{aE^*E_s}\mu + aE_s\right) \tag{4-27}$$

where

$$E^* = \frac{A+1-a}{A+1}E \tag{4-28}$$

$$E_s = E_a \equiv Q + \frac{A}{A+1}E \tag{4-29}$$

It is noticeable that E_s is the total kinetic energy of the system in the CM frame after the collision.

Figure 4-11 points out the rest energy of the system at different status. For two-body charged particle emission nuclear reactions, the system after the collision has the minimum energy that is equal to the Coulomb barrier energy:

$$V_C = k_C\frac{z(Z-z)}{R_0}e^2 \tag{4-30}$$

where z (Z, respectively) is the atomic number of the emitted (target, respectively) nucleus, and the minimum distance among two particles after the collision is

$$R_0 = r_0 a^{1/3} + r_0(1 + A - a)^{1/3} \tag{4-31}$$

where r_0 is about 1.2 to 1.4 fm. From the point of view of the classic mechanism, if the incident neutron has not enough energy to overcome the Coulomb barrier, i.e. $Q + \frac{A}{A+1}E < V_C$, the reaction cannot happen. However, due to the quantum tunneling, the collision is possible even though $Q + \frac{A}{A+1}E < V_C$. The probability of quantum tunneling is included in the corresponding nuclear reaction cross section. Once the reaction happens, the system has at least the energy of V_C. Therefore, at the end of the acceleration of emission particle due to the Coulomb force, the recoil energy of PKA can be calculated using Eq. (4-27) with

$$E_s = \max(Q + \frac{A}{A+1}E, V_c) \tag{4-32}$$

For conservative consideration, $r_0 = 1.2$ fm is used to compute the Coulomb barrier. The Coulomb barrier energy is thus calculated by:

$$V_C = \frac{1.198z(Z-z)}{a^{1/3}+(1+A-a)^{1/3}} \text{ MeV} \quad (4\text{-}33)$$

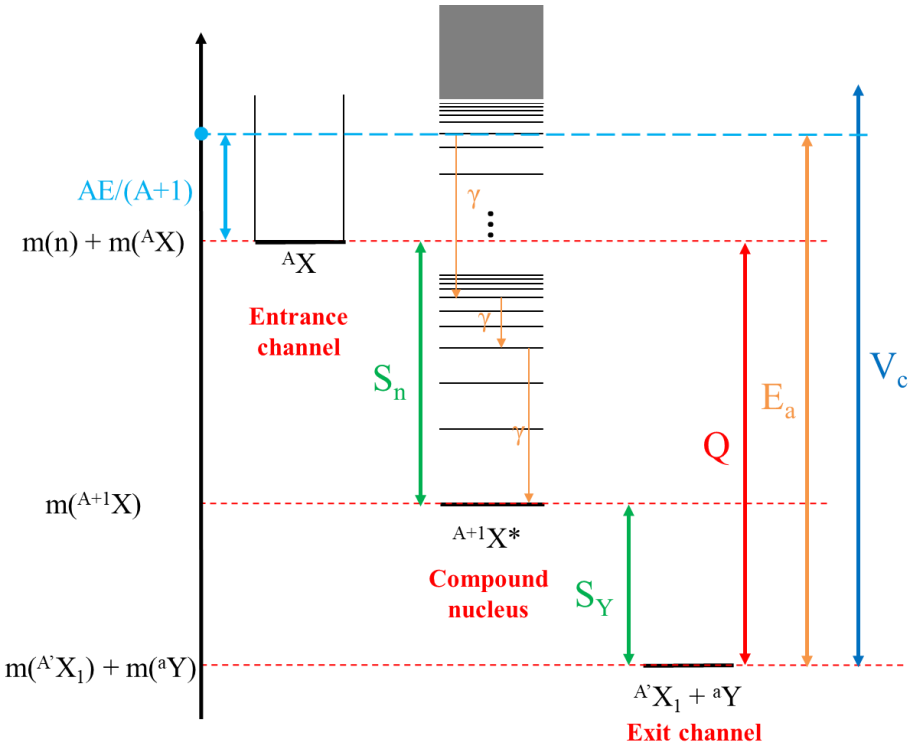

Figure 4-11. Rest energy of the system: before reaction, in compound nucleus form, and after the collision. S_x (in green) illustrates the separation energies of particle x, Q is the sum of S_x, V_C is the Coulomb barrier energy.

It is noticeable that the widely used nuclear data processing code NJOY takes the minimum of $Q + \frac{A}{A+1}E$ and V_C [27]. In the case of $Q + \frac{A}{A+1}E > V_C$, NJOY may consider the energy loss via deexcitation of the compound nucleus. Nevetheless, the formula proposed in the present work can directly imply the formula for neutron scattering [27, 64] using $z = 0$. The Coulomb barrier energy used in NJOY is [27]:

$$V_{C,\text{NJOY}} = \frac{1.029zZ}{a^{1/3}+A^{1/3}} \text{ MeV} \quad (4\text{-}34)$$

The constant 1.029 is the result of using $r_0 = 1.4$ fm.

Figure 4-12 shows the maximum PKA energies for ^{56}Fe, ^{58}Ni, and ^{59}Ni. 1 MeV is chosen because the conventional measurements of DPA are actually the measurements of neutron fluence above 1 MeV. 14.1 MeV is the energy of D+T fusion produced neutron [120]. 20 MeV is the upper limit of fission reactors. The maximum PKA energies of neutron elastic scatterings are shown in green lines for comparison. The 0

maximum PKA energy of 1 MeV neutron (n,p)-NJOY for ^{56}Fe is due to the negative value of $Q + \frac{A}{A+1}E$. For these three isotopes widely used in steel (^{59}Ni is the product of neutron capture reaction of ^{58}Ni), the increase in PKA energies also leads to the extension of energy range for simulations.

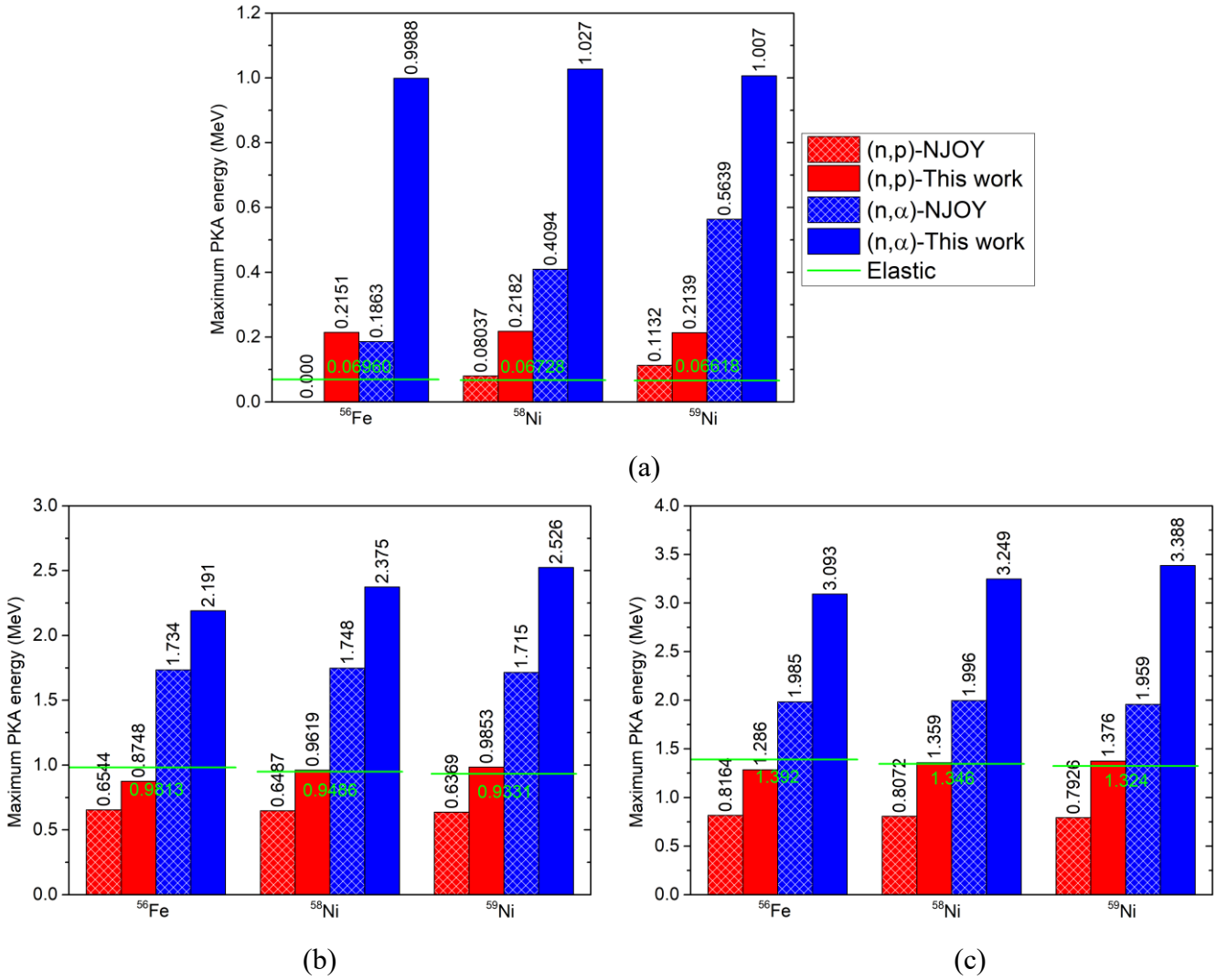

Figure 4-12. Maximum PKA energies for 1 MeV (a), 14.1 MeV (b), and 20 MeV (c) neutron-induced reactions for ^{56}Fe, ^{58}Ni, and ^{59}Ni. The green lines are maximum PKA energies of neutron elastic scattering.

4.3.4 Radiative capture reaction [34]

This section details the calculation of recoil energy from (z,γ_i) reaction. The velocity of the CM is determined by the total momentum before the reaction, i.e.:

$$(m + M)v_{CM} = \sqrt{2mE} \tag{4-35}$$

where E is the incident energy of the z particle. On the other hand, since the total momentum in the CM frame is null, one has:

$$p_{R,CM} = p_{\gamma,i,CM} \tag{4-36}$$

where the subscript R and γ represents the residual particle and emitted photon, respectively. The relationship between relativistic momentum and energy shows:

$$p_{\gamma,i,CM}^2 c^2 = E_{\gamma,i}^2 \tag{4-37}$$

where c is the light speed. Since the velocity of recoil particle v_R (or $v_{R,CM}$) of (z,γ_i) reaction is negligible when compared with light speed, one has the simple relationship:

$$p_{R,CM} = (m + M)v_{R,CM} \tag{4-38}$$

Consequently,

$$(m + M)v_{R,CM} = E_{\gamma,i}/c \tag{4-39}$$

Using the geometrical relationship (c.f. Figure 4-10 with the notation $v_{R,CM} \equiv u_2$) [34]:

$$v_R^2 = v_{CM}^2 - 2v_{CM}v_{R,CM}\cos\theta + v_{R,CM}^2 \tag{4-40}$$

One can obtain the recoil energy as:

$$E_{R,\gamma,i}(E) = \frac{mE}{M+m} - 2\sqrt{\frac{mE}{M+m}}\sqrt{\frac{E_{\gamma,i}^2}{2(M+m)c^2}}\cos\theta + \frac{E_{\gamma,i}^2}{2(M+m)c^2} \tag{4-41}$$

4.4 Neutron-induced damage cross sections

Section 3 presents several formulae for calculating the number of atomic displacements using the threshold displacement energy and damage energy as two major parameters. If one defines a generalized damage energy as:

$$\widetilde{E_a}(E) = \begin{cases} 0, & 0 < E_a < E_d \\ 2E_d/0.8\,, & E_d < E_a < 2E_d/0.8 \\ E_a(E)\xi(E_a), & 2E_d/0.8 < E_a \end{cases} \tag{4-42}$$

Different formulae can be expressed by an unique formula:

$$v = 0.8\widetilde{E_a}(E)/2E_d \tag{4-43}$$

Therefore, this generalized damage energy is used to compute damage cross section so that the damage rate R_D can be calculated by:

$$R_D = \frac{0.8}{2E_d} < \sigma_D, \phi > \tag{4-44}$$

where σ_D and ϕ respectively represent the damage cross section and the incident flux, E_d is the average threshold displacement energy. E_d is not included in the damage cross section because σ_D is not sensitive to E_d (c.f. Ref. [121]). This definition of σ_D permits to approximately calculate primary damage rate using any value of E_d (because E_d is not so well-known for the time-being and some researchers do not pay attention to the value of E_d used in the calculation of damage cross section).

In order to simplify the notations, the generalized damage energy $\widetilde{E_a}$ is simply referred to damage energy and noted by E_a in this section. Since the NRT formula is still the current international standard, the generalized damage energy is almost identical to the Lindhard damage energy in most cases.

4.4.1 Two-body reactions [64]

For discrete reactions, the damage energy is a function of incident energy E and the cosine of emission angle μ:

$$E_a(\mu, E) \tag{4-45}$$

The emission angular-integrated damage cross section is obtained by:

$$\sigma_D(E) = \sigma(E) \int_{-1}^{1} f(\mu, E)\, E_a(\mu, E) d\mu \tag{4-46}$$

where $\sigma(E)$ is the corresponding nuclear cross section. $f(\mu, E)$ is the probability density of angular distribution for the incident energy E versus the cosine of the emission angle μ in the CM frame (c.f. Section 2.4).

For continuum reactions, an additional degree of freedom on secondary energy is required: $E_R(E, E', \tilde{\mu})$ or $E_R(E, E_1, \mu)$. Since both $E_R(E, E', \tilde{\mu})$ and $E_R(E, E_1, \mu)$ are explicit functions of secondary energy and the cosine of emission angle, we do not specify the notation double-differential data in the Lab frame and the CM frame anymore in this paper (certainly, it should be specified in calculations). Let simply denote (E', μ) for secondary energy and the cosine of emission angle for continuum reactions. The corresponding Lindhard damage energy can be thus simply noted by $E_a(E, E', \mu)$.

The energy-angle-integrated damage cross section related to a given continuum reaction is calculated by:

$$\sigma_D(E) = \sigma(E) \int_0^{\infty} \int_{-1}^{1} f(E, E', \mu)\, E_a(E, E', \mu) d\mu dE' \tag{4-47}$$

where $f(E, E', \mu)$ is the probability density of energy-angular distribution in the Lab frame or the CM frame for the incident energy E versus the secondary energy E' and the cosine of the emission angle μ. The corresponding recoil energy is given in Section 4.3.2.1 and Section 4.3.2.2 if $f(E, E', \mu)$ is given in the Lab frame and in the CM frame, respectively. Details of $f(\mu, E, E')$ are given in Section 2.5.

Numerical methods used to calculate integrals are Gauss-Legendre Quadrature (GLQ) over the cosine of emission angle and trapezoidal integration over the secondary energy. Because the generalized damage energy is not a continuous function versus PKA energy (c.f. Eq. (4-42)), it is not a continuous function of μ (and E' in principle). Therefore, numerical convergence is difficult to ensure if the GLQ is used to compute integration from -1 to 1. Figure 4-13 indicates the neutron elastic DPA cross sections of

^{56}Fe computed with different numbers of points in the GLQ. The damage cross section does not converge for the 150-point GLQ at neutron energy below 10 keV because of the large contribution of damage energy in the $[0, 2E_d/0.8]$ range. The integral converges at high incident energy because the damage energy lower than $2E_d/0.8$ is less important.

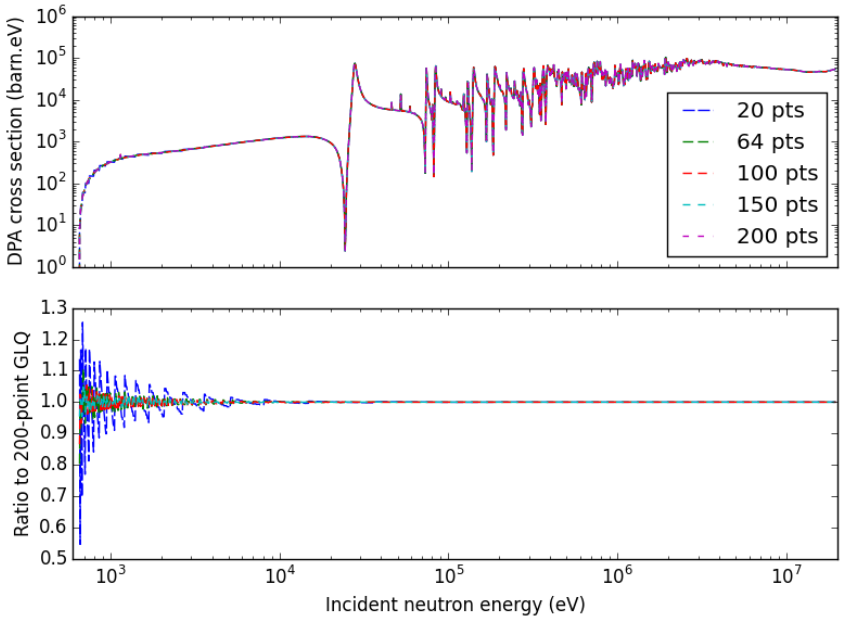

Figure 4-13. Neutron elastic scattering DPA cross sections of ^{56}Fe performed with different points Gauss-Legendre quadrature (upper) and the corresponding ratios to the 200-point Gauss-Legendre quadrature calculation (lower).

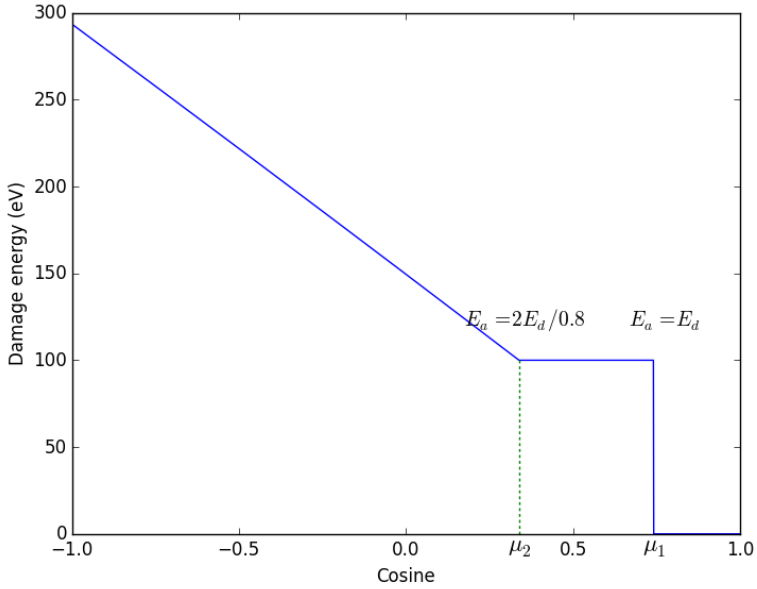

Figure 4-14. Generalized damage energy of ^{56}Fe versus μ for 5 keV neutron elastic scattering. The two critical points are determined by Lindhard damage energy equal to E_d and $2.5E_d$.

Because the issue of numerical convergence is a result of the discontinuity of the generalized damage cross section, a GLQ-based Piecewise Integration (GLQPI) over μ from -1 to 1 is proposed to ensure the numerical convergence of integration [64]. As the example shown in Figure 4-14, the two critical points to connect the three intervals are obtained with:

$$\begin{cases} E_a(\mu_1, E) = E_d \\ E_a(\mu_2, E) = 2E_d/0.8 \end{cases} \tag{4-48}$$

where E_a represent Lindhard damage energy. With the notations of μ_1 and μ_2, $E_a > 2E_d/0.8$ for μ in the interval [-1, μ_2]; μ in [μ_2, μ_1] is equivalent to damage energy in $[E_d, 2E_d/0.8]$, so the damage energy is $2E_d/0.8$; for $\mu > \mu_1$, the damage energy is zero. Hence, the damage cross section is computed by:

$$\sigma_D(E) = \sigma(E)\left[\int_{-1}^{\mu_2} f(\mu, E)\, E_a(\mu, E) d\mu + \frac{2E_d}{0.8}\int_{\mu_2}^{\mu_1} f(\mu, E)\, d\mu\right] \tag{4-49}$$

Figure 4-15 illustrates the damage cross sections with 20 points and 200 points GLQPI and the corresponding ratio. The excellent agreement between the DPA cross sections calculated with 20-point GLQPI and 200-point GLQPI points out the convergence of the integral. It is noticeable that the maximum order can be up to 64 in ENDF-6 [66], that signifies more than 33 points are required. For the purpose of verification, more than 33 points should be used as a reference to verify the convergence of numerical integration. However, due to the negligible contribution of high-order Legendre polynomials on damage cross sections (c.f. Ref. [64]), fewer points are in general required for efficient integration.

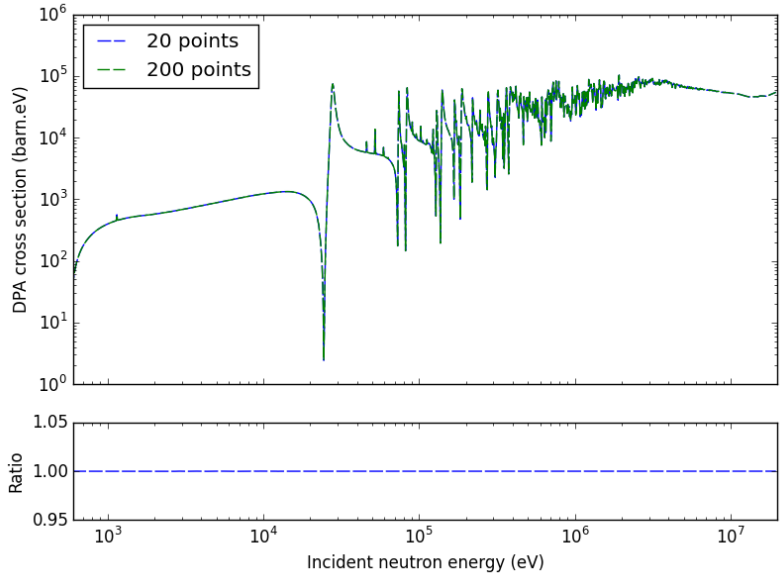

Figure 4-15. Neutron elastic scattering DPA cross sections of ^{56}Fe performed with 20 and 200 points Gauss-Legendre Quadrature based Piecewise Integration (GLQPI).

For continuum reactions, the additional integration over secondary energy is required for damage cross sections. Because the integrand of the integration over the secondary energy is not a linear function, the method of computations with additional points excluded in ENDF is proposed to verify the convergence of integration [64]. We also proposed an improved method to interpolate double-differential cross sections between two neighbor incident energies for performing more accurate calculation and verification of damage cross section [64].

4.4.2 Radiative capture reactions

For radiative capture reactions, because of the gamma cascade of deexcitation, photons are successively emitted. This successive emission of photon complicates the calculation of radiation damage: secondary photons are emitted before, during, or after the atomic displacement cascade?

For the first case, i.e. all photons are emitted before the atomic displacement cascade, one should calculate the recoil energy after successive emissions of photon. Since there are several deexcitation schemes for a nucleus with excitation energy higher than the first excited level, various combinations of deexcitation down to the ground state should be considered. In addition, because the angular distributions of successive gamma emissions are independent, one should treat a series of successive kinematics to compute the expectation of recoil energy. Therefore, in this case, Monte Carlo sampling is recommended for calculating the recoil energy or the damage energy.

In the case where successive photon emission happens during the atomic displacement cascade, one has to couple the deexcitation of the compound nucleus and the atomic displacement simulation. On one hand, the deexcitation half-life depends on the nucleus and its excitation energy. On the other hand, atomic displacement cascade depends on the energy of recoil nucleus. Therefore, I think that no method excluding Monte Carlo simulation can predict the radiation damage in this case.

Assuming that each photon is emitted after the equilibrium of displacement cascade, i.e. the last case, the corresponding damage cross section is calculated via:

$$\sigma_D(E) = \sigma(E) \sum_i I_i(E) \int_{-1}^{1} f_i(\mu, E)\, E_a\left(E_{R,\gamma,i}(\mu, E)\right) d\mu \qquad (4\text{-}50)$$

where $I_i(E)$ is the intensity (or probability) of emitting photon with $E_{\gamma,i}$, $f_i(\mu, E)$ is the corresponding angular distribution, and the recoil energy $E_{R,\gamma,i}(\mu, E)$ is given in Section 4.3.4. It is noteworthy that Eq. (4-50) can include continuum (z,γ) reaction-induced damage cross section if one defines:

$$I_i(E) \int_{-1}^{1} f_i(\mu, E)\, E_a\left(E_{R,\gamma,i}(\mu, E)\right) d\mu \equiv \int_{E_{\gamma,i}^{-}}^{E_{\gamma,i}^{+}} \int_{-1}^{1} f_\gamma(\mu, E, E_\gamma)\, E_a\left(E_{R,\gamma}(\mu, E)\right) d\mu dE_\gamma \qquad (4\text{-}51)$$

where $f_\gamma(\mu, E, E_\gamma)$ is the angular distribution for incident energy E and emitted gamma energy of E_γ; $E_{\gamma,i}^-$ and $E_{\gamma,i}^+$ are respectively the minimum and maximum gamma energies in the considered range $[E_{\gamma,i}^-, E_{\gamma,i}^+]$. If a fine energy structure of photon energy that the first-order approximation $E_\gamma = E_{\gamma,i}$ can be used for E_γ in $[E_{\gamma,i}^-, E_{\gamma,i}^+]$, Eq. (4-50) directly includes both discrete and continuum gamma emissions with the definition of:

$$I_i(E) = \int_{E_{\gamma,i}^-}^{E_{\gamma,i}^+} \int_{-1}^{1} f_\gamma(\mu, E, E_\gamma)\, d\mu dE_\gamma \tag{4-52}$$

for continuum reactions.

Since the compound nucleus reaction leads to isotropic angular distribution and it is predominant in capture reactions, one may use the approximation of isotropic angular distribution for (z,γ) reactions. Therefore, the calculation can be simplified as:

$$\sigma_D(E) = \sigma(E)\frac{1}{2}\sum_i I_i(E) \int_{-1}^{1} E_a\left(E_{R,\gamma,i}(\mu, E)\right) d\mu \tag{4-53}$$

Because the Lindhard damage energy is a concave function (i.e. second-order derivation is negative) versus PKA energy and recoil energy is a linear function of μ for (z,γ) reactions, assuming isotropic angular distribution, one can use a conservative estimate of damage cross section of (z,γ_i) reaction by maximizing the integrand of Eq. (4-50):

$$\begin{aligned} \int_{-1}^{1} f_i(\mu, E) E_a\left(E_{R,\gamma,i}(\mu, E)\right) d\mu &\leq \int_{-1}^{1} f_i(\mu, E) E_a\left(E_{R,\gamma,i}(\mu = 0, E)\right) d\mu \\ &\leq E_a\left(\frac{mE}{M+m}\right) + E_a\left(\frac{E_{\gamma,i}^2}{2(M+m)c^2}\right) \end{aligned} \tag{4-54}$$

In fact, for any generalized damage energy, physical analysis implies that the number of atomic displacements increases with PKA energy but the increment decreases with PKA energy. Accordingly, a specific generalized damage (not limited to the Lindhard damage energy) should also behave as a concave shape. Consequently, one has the following inequality for each damage energy:

$$\sigma_D(E) \leq \sigma(E)\left[E_a\left(\frac{mE}{M+m}\right) + \sum_i I_i E_a\left(\frac{E_{\gamma,i}^2}{2(M+m)c^2}\right)\right] \tag{4-55}$$

In fact, since the maximum recoil energy from elastic scattering is:

$$E_{R,max}(E) = \frac{4mE}{M+m} \tag{4-56}$$

$E_a(mE/(M+m)) = 0$ for energy lower than the cut-off energy, E_c, where the contribution of elastic scattering begins, i.e. $4mE_c/(M+m) = E_d$. In this region (or extended up to $4E_c$), the radiative capture reaction-induced damage comes only from photon kick.

NJOY divides the above maximization into two parts according to different nuclear

data: the neutron data section and photon data section as [27]:

$$\sigma_D(E) \leq \sigma(E)\left\{\underbrace{\left[E_a\left(\frac{mE}{M+m}\right)+E_a\left(\frac{\left(\frac{ME}{m+M}+Q\right)^2}{2(M+m)c^2}\right)\right]}_{\text{neutron}}+\underbrace{\left[\sum_i I_i E_a\left(\frac{E_{\gamma,i}^2}{2(M+m)c^2}\right)-E_a\left(\frac{\left(\frac{ME}{m+M}+Q\right)^2}{2(M+m)c^2}\right)\right]}_{\text{photon}}\right\} \quad (4\text{-}57)$$

In the case where no data is available for photons production, the use of neutron data can give a reasonable conservative estimate of damage cross section.

It should be noted, whether photon data are available or not, NJOY conservatively calculates the radiative capture reaction-induced damage cross section. In other words, the radiative capture reaction-induced damage cross section is always overestimated by NJOY calculation. However, it is noticeable that radiative capture reaction-induced DPA rate is negligible when compared with the total DPA rate.

4.4.3 N-body reactions

This subsection discusses the reactions with various emitted particles, such as (n,np) reaction. This kind of reaction is simply referred to N-body reactions hereinafter. Because N (> 2) particles appear after such nuclear reactions, the conservation of momenta leads to 1 vector equation and thus 3 algebraic equations for 3D momenta projections. If the reaction *Q*-value is determined, one has an additional equation governing the conservation of energy. The total unknown numbers are 3N: N norms and 2N angles of momenta. The degree of freedom is thus 3N - 4. For two-body reactions, because the two particles after the reaction and the incident particle are always in the same plan, the projections of momenta in the perpendicular direction are null. This condition implies two equations concerning the projections of momenta in one direction: projections of momenta in the perpendicular direction are null for both particles. Therefore, for two-body reactions, there is only 1 degree of freedom for a determined *Q*-value and 2 degrees of freedom for continuum reactions.

Similar to the radiative capture reactions discussed in Section 4.4.2, N-body reaction-induced number of DPA depends on the order of successive particle emissions and Atomic Displacement Cascade (ADC). Taking ^{56}Fe(n,np)^{55}Mn as an example, one should identify the order of reactions among: ^{56}Fe(n,n)^{56}Fe → ^{56}Fe(,p)^{55}Mn → ADC, ^{56}Fe(n,n)^{56}Fe → ADC → ^{56}Fe(,p)^{55}Mn, ^{56}Fe(n,p)^{56}Mn → ^{56}Mn(,n)^{55}Mn → ADC, or ^{56}Fe(n,p)^{56}Mn → ADC → ^{56}Mn(,n)^{55}Mn. Furthermore, there are some possible cases where the second light particle is emitted during the ADC. The order of nuclear reactions should mainly depend on the separation energy of the emitted particle. The

order of successive nuclear reactions and ADC depends on the kinetic energy of PKA and the half-lives of the residual nuclei. No information is given on the order of N-body nuclear reactions in the current ENDFs, we suppose that all particles are simultaneously emitted before the ADC for the moment.

In an ENDF, 3N - 4 (or 3N - 3 if the reaction *Q*-value is undetermined) independent energy or angular distributions should be provided for accurate calculation of damage cross section for a N-body reaction, except that the recoil energy distribution is already given. However, because current ENDFs are mainly provided for particle transport calculations, almost only energy and/or angular distribution of the light particle identical to the incident particle is given. In this case, it is impossible to perform accurate calculations of damage cross sections. To obtain an estimate of damage cross section for a N-body reaction, MacFarlane proposed a two-body reaction approximation as: "… The same procedure is used for (n,2n), (n,nα), etc., with no account being taken of any extra charged particles emitted" [27] and "… for reactions like (n,n'p) or (n,n'α) … HEATR treats these reactions in the same way as (n,p) or (n,α)" [122].

In order to clarify the methods used in the NJOY for computing the damage cross sections for N-body reactions, I do the test and verification of ^{56}Fe (n,2n), (n,nα), and (n,np) reactions with TENDL-2017 [123], which includes the recoil energy distributions in MF6. For (n,2n), (n,nα), and (n,np) reactions of ^{56}Fe, the angular distributions of the residual nuclei in TENDL-2017 are isotropic in the Lab frame. However, in the compound nucleus theory, the angular distribution of the residual nucleus is isotropic in the CM frame, thus anisotropic in the Lab frame. It should be noted that the azimuthal angle is not considered for computing recoil spectra in TALYS [55]. This approximation is not realistic for reactions with more than two ejectiles. Furthermore, relativistic kinematics is not considered in TALYS, whereas as the relativistic effect is not negligible for high incident neutron energies. E.g., 20 MeV and 200 MeV neutron-induced (n,n') (or (n,p)) reactions respectively leads to around +1% and +10% corrections on recoil energy [117]. Nevertheless, TENDL is the only library that includes the differential cross sections of residual nuclei.

Figure 4-16 illustrates damage cross sections of ^{56}Fe (n,2n), (n,nα), and (n,np) reactions calculated by NJOY-2016 with double-differential cross sections of different particles from TENDL-2017 and the ratios to the calculations based on complete double-differential cross sections. From Figure 4-16, one can find that if the recoil energy distribution is available, NJOY directly takes the recoil energy distribution for computing damage cross section. If there are only data for the emitted neutron or charged particle, NJOY uses these data by assuming two-body kinematics. In the case where both neutron and charged particle data are given, NJOY prefers differential cross

section of charged particle and neglects the data of neutron during the approximate treatment of two-body kinematics.

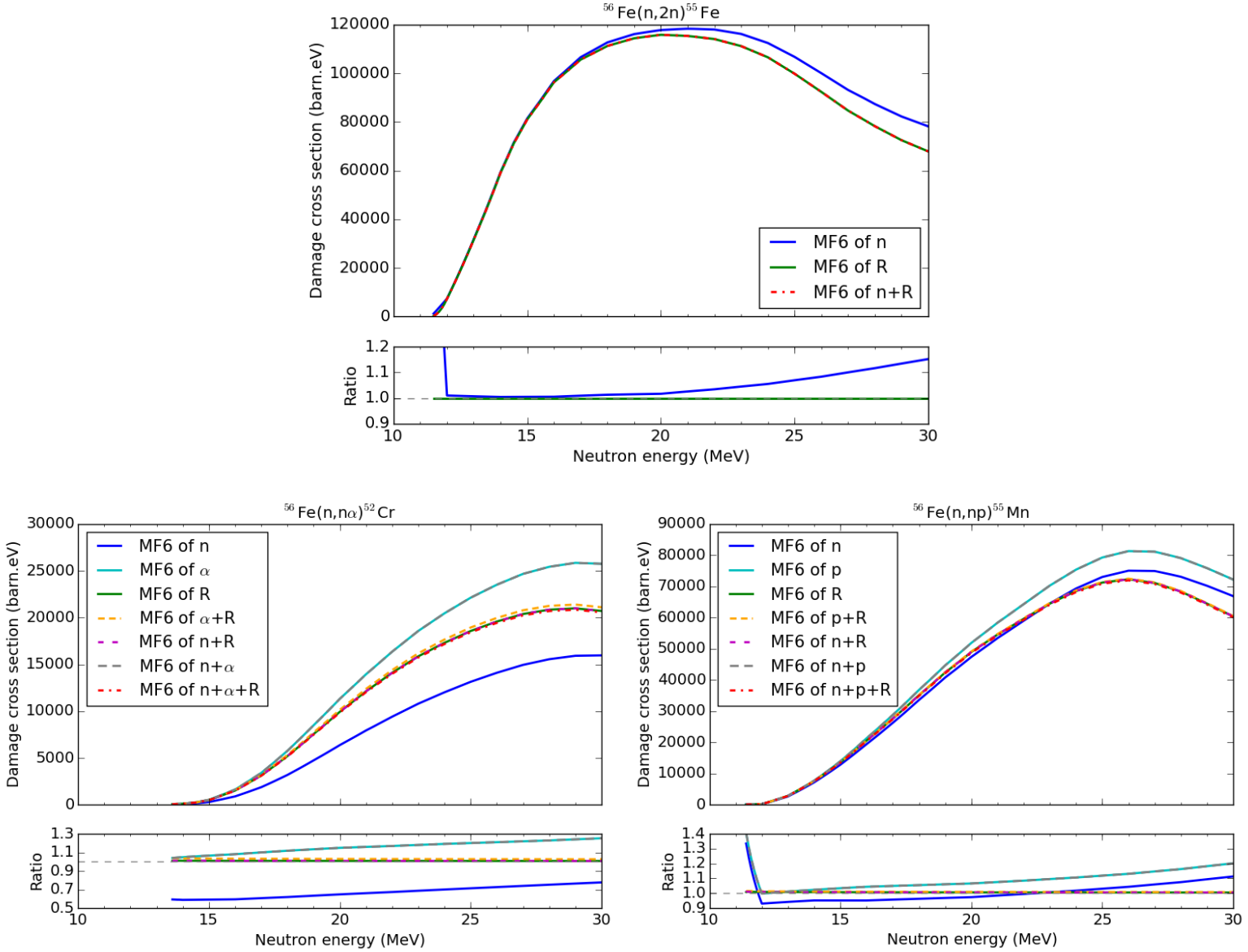

Figure 4-16. Damage cross sections of ^{56}Fe (n,2n), (n,nα), and (n,np) reactions calculated by NJOY-2016 with double-differential cross sections of different particles from TENDL-2017 and the ratios to the calculations based on complete double-differential cross sections.

In addition to NJOY calculation, we calculate the damage cross sections of the aforementioned three reactions using recoil energy distributions in TENDL-2017 by:

$$\sigma_D(E) = \sigma(E) \int_0^{E_{R,max}} f(E, E_R)\, E_a(E_R) E_R \qquad (4\text{-}58)$$

where $f(E, E_R)$ is the energy-distribution of recoil energy E_R given in TENDL-2017. Since the double-differential cross sections are tabulated, one should interpolate the data between two neighbor tabulated points. The original interpolation mode proposed

in TENDL-2017 is histogram interpolation for these reactions.

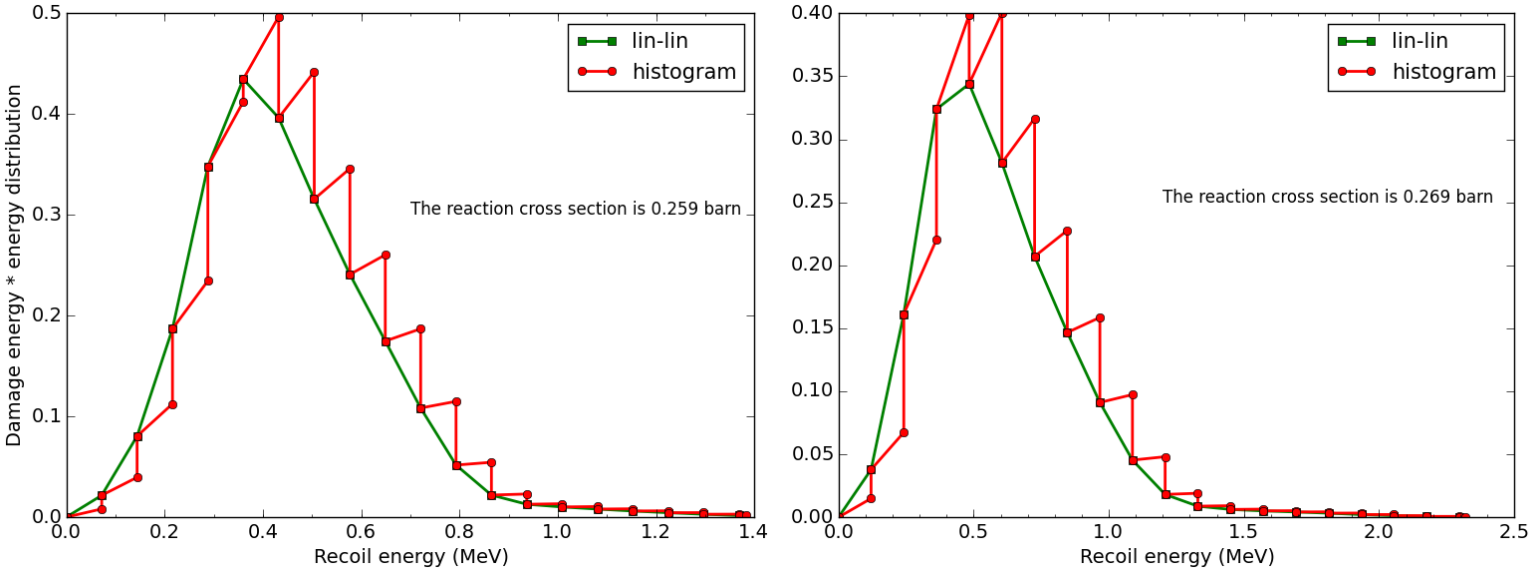

Figure 4-17. Product of damage energy and recoil energy distribution (i.e. $f(E,E_R)E_d(E_R)$) of 20 MeV (left) and 30 MeV (right) incident neutron ^{56}Fe (n,np) reactions with linear-linear and histogram interpolations of energy distribution. Original interpolation mode in TENDL-2017 is histogram. The damage cross section is the integration of the curves from 0 to the maximum recoil energy. The damage cross section is the integration of the curves from 0 to the maximum recoil energy.

Figure 4-17 compares the product of damage energy and recoil energy distribution of ^{56}Fe (n,np) reactions with linear-linear and histogram interpolations of energy distribution at 20 MeV and 30 MeV incident energies. Because the damage energy is an increasing function of PKA energy, histogram recoil energy distribution leads to an increasing production of damage energy and energy distribution in each interval. Therefore, the damage cross sections calculated using linear-linear and histogram interpolations are different.

Figure 4-18 illustrates the damage cross sections calculated by NJOY and those calculated in the present work with linear-linear and histogram interpolations of recoil energy distribution. In general, linear-linear interpolation leads to about 5% reduction of damage cross section when compared with histogram interpolation. NJOY calculations and the damage calculated in the present work are globally in good agreement. For (n,nα) reaction, the agreement with NJOY is better if it is treated as a (n,α) reaction (i.e. PKA is ^{53}Cr rather than ^{52}Cr). The quite small deviations between NJOY and the present calculations should be mainly from numerical issues. From the above comparisons, one can conclude that the methods used in NJOY for computing N-body reactions-induced damage cross sections are quite reliable.

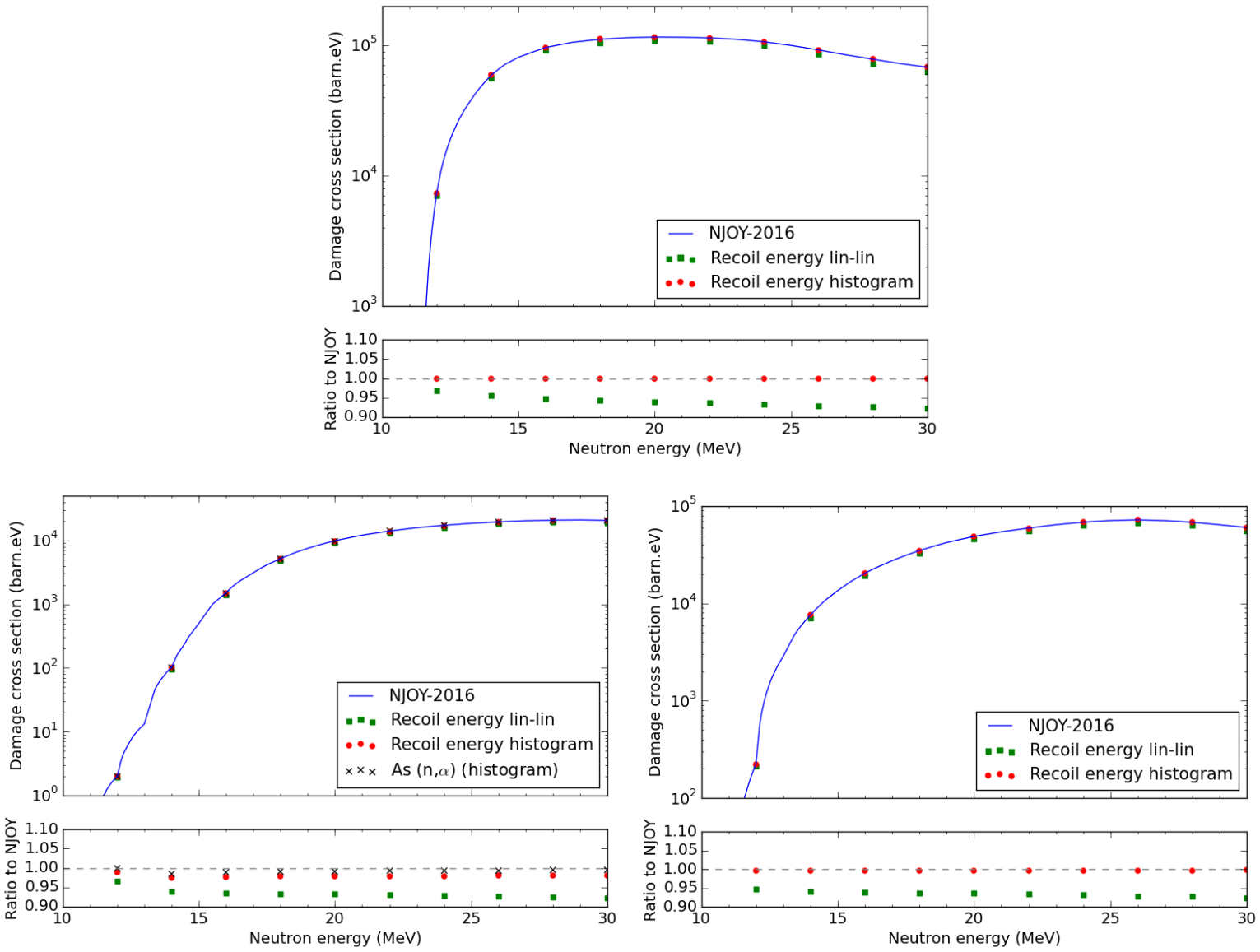

Figure 4-18. Comparison of damage cross sections of ^{56}Fe (n,2n), (n,nα), and (n,np) reactions calculated by NJOY-2016 and the present work with different double-differential cross sections from TENDL-2017.

4.5 Photon-induced damage cross sections [124]

This subsection presents the photon-induced DPA cross sections published in Ref. [124]. The main photon-matter interactions for photon energy below several tens MeV are: Photoelectric Effect (PE), Compton Scattering (CS), and Pair Production (PP). These reactions have a common emitted particle, electron. In PP, a positron is also produced. Therefore, for computing the photon-induced damage cross sections, one should firstly calculate the electron and positron-induced ones.

4.5.1 Electron and positron-induced damage cross section

The total DPA cross section by an incident electron or positron of energy E is

calculated by:

$$\sigma_{DPA}^{e}(E) = \int_0^{T_{max}} \upsilon(T) \frac{d\sigma}{dT} dT \tag{4-59}$$

where $d\sigma/dT$ is the differential scattering cross section, T_{max} is the maximum energy that can be transferred to atom, $\upsilon(T)$ is the number of atomic displacements induced by an atom with energy T. Oen computed tabulated values of electronic $d\sigma/dT$ for various elements with Mott differential scattering cross section [125]. McKinley and Feshbach [126] deduced an approximation with a simpler expression for the differential scattering cross section:

$$\frac{d\sigma}{dT}(E,T) = \frac{\pi Z^2 e^4 (1-\beta^2) T_{max}}{(mc^2)^2 \beta^4 T^2} \left\{ 1 - \beta^2 \frac{T}{T_m} \pm \frac{\pi}{137} \beta Z \left[\left(\frac{T}{T_m} \right)^{1/2} - \frac{T}{T_m} \right] \right\} \tag{4-60}$$

where $\beta^2 = E(E + 2mc^2)/(E + mc^2)^2$ with mc^2 is the rest energy of electron or positron, Z is the atomic number, the term involving $\pi\beta Z/137$ is positive for electron and negative for positron. Accordingly, the differential scattering cross section of electron is larger than that of positron. The maximum transferred energy is:

$$T_{max}(E) = \frac{2E}{Mc^2}(E + 2mc^2) \tag{4-61}$$

where Mc^2 is the rest mass energy of the atom. The threshold energy of electrons or positrons for displacing atoms is thus:

$$T_d^{e,p} = \sqrt{(mc^2)^2 + Mc^2 E_d/2} - mc^2 \tag{4-62}$$

Using the typical value of 40 eV for E_d of iron [70], one can obtain $T_d^{e,p} = 0.63$ MeV.

It is noteworthy that the McKinley-Feshbach (MF) analytical formula is a first-order approximation of Mott cross section and is valid for $Z/137 < 0.2$, i.e. $Z < 27$ [126]. Therefore, iron is almost the heaviest atom, for which MF approach can be used. For atoms with atomic number above 27, Mott cross section should be used for computing electron and positron-induced damage cross sections.

4.5.2 From electron and positron to photon-induced damage cross sections

Total photon-induced DPA cross section is the sum of three partial damage cross sections:

$$\sigma_t(E_\gamma) = \sigma_{DPA}^{CS}(E_\gamma) + \sigma_{DPA}^{PE}(E_\gamma) + \sigma_{DPA}^{PP}(E_\gamma) \tag{4-63}$$

4.5.2.1 Compton Scattering

The DPA cross section for CS is given by [127]:

$$\sigma_{DPA}^{CS}(E_\gamma) = \int_0^{E_{max}} \frac{d\sigma^{CS}(E_\gamma, E)}{dE} n(E) dE \tag{4-64}$$

where $d\sigma^{CS}(E_\gamma, E)/dE$ is the CS cross section for producing an electron of energy E. The Klein-Nishina formula [128] shows:

$$\frac{d\sigma^{CS}(E_\gamma,E)}{dE} = \frac{\pi(9\times10^3 e)^2 Z}{mc^2(E_\gamma - E)^2}\left\{\left(\frac{mc^2 E}{E_\gamma^2}\right)^2 + 2\left(\frac{E_\gamma - E}{E_\gamma}\right)^2 + \frac{E_\gamma - E}{E_\gamma^3}[(E-mc^2)^2 - (mc^2)^2]\right\} \quad (4\text{-}65)$$

where e is the charge of electron, all energies are in MeV and $d\sigma^{CS}(E_\gamma, E)/dE$ is in $\mathrm{m}^2/\mathrm{MeV} = 10^{28}$ barn/MeV. The upper limit of integration represents the maximum kinetic energy of electrons induced by a gamma ray of energy E_γ and is given by:

$$E_{max}(E_\gamma) = \frac{2E_\gamma}{2+mc^2/E_\gamma} \quad (4\text{-}66)$$

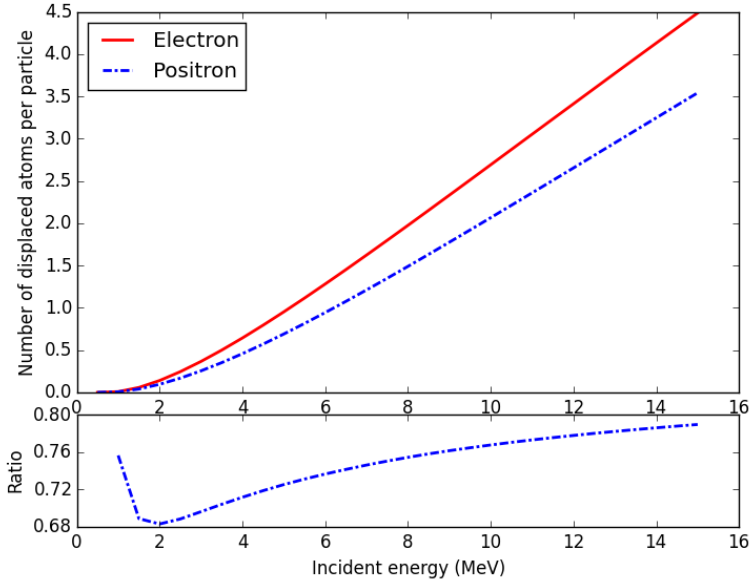

Figure 4-19. Total displaced atoms per incident electron or positron. The lower figure shows the ratio of atomic displacement number induced by positron to that induced by electron.

$n(E)$ in Eq. (4-64) represents the average number of displaced atoms induced by an electron with kinetic energy E. It is computed with:

$$n(E) = N_V \int_0^E \frac{\sigma_{DPA}^e(T)}{S(T)} dT \quad (4\text{-}67)$$

where N_V is the atomic density of the material, S is the electronic stopping power [129], and σ_{DPA}^e refers to the electron-induced DPA cross section studied in Section 4.5.1. $n(E)$ is shown in Figure 4-19 with the red solid line.

4.5.2.2 Photoelectric Effect

The kinetic energy of electrons produced by PE is:

$$E = E_\gamma - B_e \quad (4\text{-}68)$$

where B_e is the binding energy of electrons. B_e is generally of the order of magnitude of several hundred eV, which is very small compared with E_γ. $B_e = 7.11$ keV for K-shell electrons of iron [130], while most studies neglect the electronic binding energy. Due to the determined energy of electrons for a given energy photon, the damage cross section for PE is:

$$\sigma_{DPA}^{PE}(E_\gamma) = \sigma^{PE}(E)n(E) \tag{4-69}$$

In the energy region of damage calculation, the cross section for PE is given by Hall's formula [131]:

$$\begin{aligned}\sigma^{PE}(E) \quad = \quad & \frac{5}{4}\frac{4\pi Z\left(9\times10^3 e\right)^2\alpha^4}{(mc^2)^2}\exp[-\pi\alpha + 2\alpha^2(1-\ln\alpha)] \times \frac{(\gamma+1)^{3/2}}{(\gamma-1)^{7/2}} \\ & \times\left\{\frac{4}{3}+\frac{\gamma(\gamma-2)}{\gamma+1}\left[1-\frac{1}{2\gamma\sqrt{\gamma^2-1}}\ln\left(\frac{\gamma+\sqrt{\gamma^2-1}}{\gamma-\sqrt{\gamma^2-1}}\right)\right]\right\}\times 10^{28}\ \text{barn}\end{aligned} \tag{4-70}$$

where the factor 5/4 accounts the PE for electrons of K-shell and other shells (1/4 of K-shell), $\alpha = Z/137$, γ is the Lorentzian factor:

$$\gamma = \frac{E+mc^2}{mc^2} \tag{4-71}$$

4.5.2.3 Pair Production

For the PP, because both electrons and positrons are produced for a photon with energy higher than $2mc^2 = 1.022$ MeV, one should treat both electron-induced and positron-induced displacement damage. Alexander doubled the electron-induced damage for the PP [132]. Kwon and Motta neglected the positron-induced DPA because the positron annihilates by combining with an electron [133]. Fukuya and Kimura used the most reasonable method that computing the positron-induced damage with the same method applied in the calculation of electron-induced DPA by using the corresponding stopping power for positrons [134]. This work recommends the utilization of the method proposed by Fukuya and Kimura.

Similar to the computation of DPA cross sections for CS given in Eq. (4-64), the PP damage cross section is calculated by:

$$\sigma_{DPA}^{PP}(E_\gamma) = \int_0^{E_\gamma-2mc^2}\frac{d\sigma^{PP}(E_\gamma,E)}{dE}\left[n\left(E_\gamma-2mc^2-E\right)+\bar{n}(E)\right]dE \tag{4-72}$$

where $\bar{n}(E)$ represents the average number of displaced atoms induced by a positron with kinetic energy E. $\bar{n}(E)$ is illustrated in Figure 4-19 with the blue dotted line. The ratio $\bar{n}(E)/n(E)$ shown Figure 4-19 points out that $\bar{n}(E)$ is 68%-80% of $n(E)$. The differential cross section for the PP $d\sigma^{PP}(E_\gamma,E)/dE$ has been determined by Bethe [135, 136] and different models were summarized by Davisson and Evans [131]. Evans calculated the integration over the whole energy domain [137]. Due to the complexity

of differential cross section for PP, Kwon and Motta used Evans' integrated data by assuming the equiprobable energy distribution. Fukuya and Kimura used a numeric approach as:

$$\frac{d\sigma^{PP}(E_\gamma,E)}{dE} = \sigma_{co} Z^2 F(s)/(E_\gamma - 2mc^2) \quad (4\text{-}73)$$

where $\sigma_{co} = 5.8 \times 10^{-4}$ barn and for iron,

$$F(s) = g(u)\left\{h(u)\left[1 - 2^n\left(s - \frac{1}{2}\right)^n\right] + [1 - h(u)]\left[1 - 2^m\left(s - \frac{1}{2}\right)^m\right]\right\} \quad (4\text{-}74)$$

where $s = E/(E_\gamma - 2mc^2)$, $u = \ln(E_\gamma/mc^2)$, $m = 2$, $n = 8$, and

$$g(u) = -0.1835u^3 + 1.653u^2 - 2.1543u + 0.7614 \quad (4\text{-}75)$$

$$h(u) = 0.2193u + 0.1825 \quad (4\text{-}76)$$

If only the electrons are considered, the damage cross sections for PP computed with Evans' integrated formula and Fukuya-Kimura approximation have a few percent difference. The numerical results shown in Section 4.5.2.4 are based on the Fukuya-Kimura approximation for the energy distribution of electrons and positrons.

4.5.2.4 Monte Carlo simulations

The approximate analytic expressions of gamma-matter interaction cross sections are proposed to compute the gamma-induced DPA cross sections. To verify the above-mentioned gamma-matter interaction cross sections, the present work compares the analytic expression with Monte Carlo simulated data. The simulations of photon transport are performed with Tripoli-4.10® [138] using the Evaluated Photon Data Library (EPDL)-97 [139].

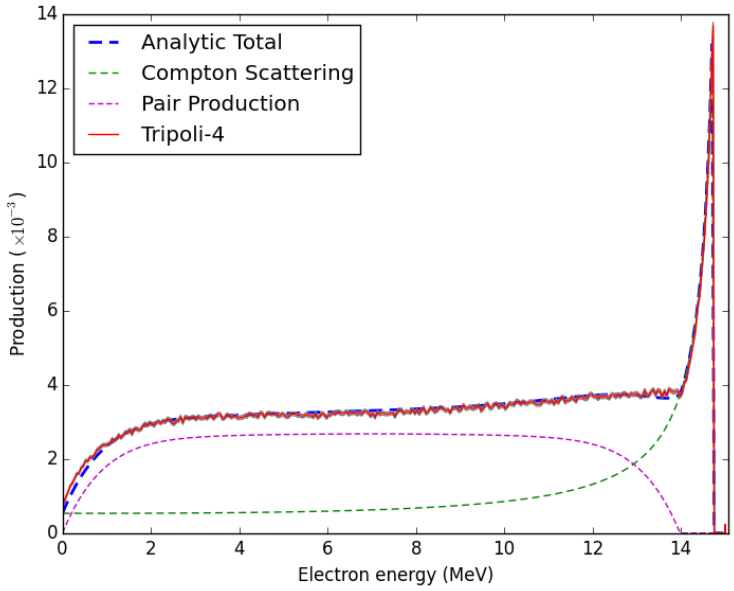

Figure 4-20. Electron production of 15 MeV incident gamma in ^{56}Fe

Figure 4-20 illustrates the example of electrons production in ^{56}Fe for incident gamma energies of 15 MeV. The statistical uncertainties of Monte Carlo simulations are plotted in grey (not evident due to the small uncertainties), while the simulated data are illustrated by the red lines. The small peak near to the incident energy is the electron production for PE. Good agreement between the analytic expression and Monte Carlo simulations is found through the production of electrons.

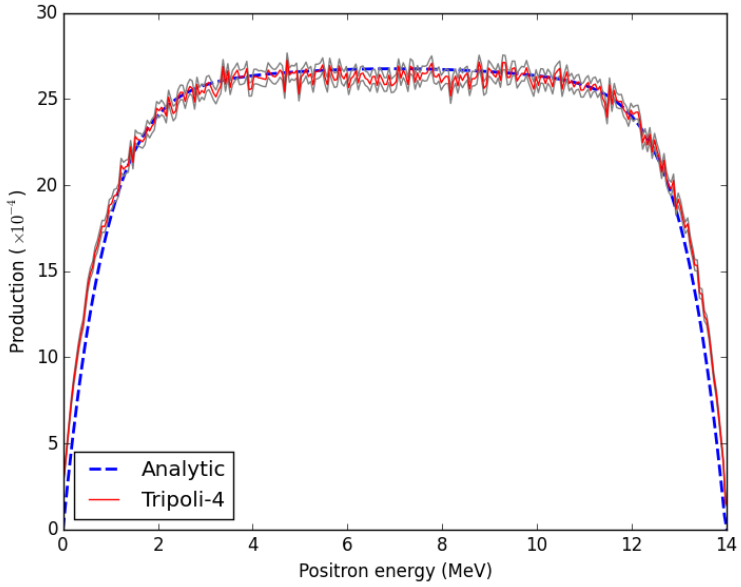

Figure 4-21. Positron production of 15 MeV incident gamma in ^{56}Fe.

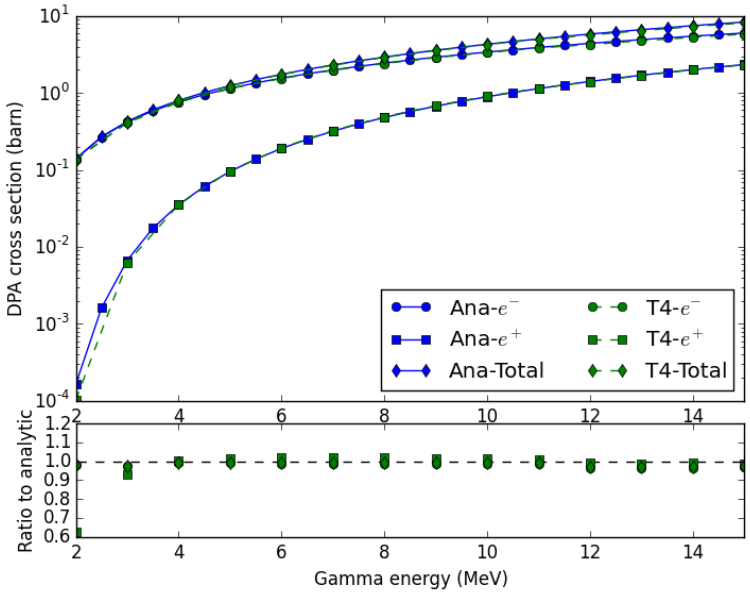

Figure 4-22. Photon-induced DPA cross sections for iron based on McKinley-Feshbach analytical approximation (blue, noted as Ana) and Tripoli-4 simulations (green, noted as T4).

Figure 4-21 shows the production of positrons for 15 MeV incident gamma in ^{56}Fe. Due to the small number of positrons produced by gamma-ray, the statistical

uncertainties are larger than those of electron production. The analytic expression has a similar form as the Monte Carlo simulated results. Around 14% difference is observed at the peak of positron production for 3 MeV gamma [124], whereas the dispersion of simulated data is also about 3%. The tendency shows that the energy distribution of positrons computed with EPDL-97 through Monte Carlo simulations is sharper than that of Fukuya-Kimura. The analytic formula has a globally good agreement with Monte Carlo simulated result for 15 MeV gamma. EPDL-97 has little flatter energy distribution of positrons for gamma-ray with high incident energy. The DPA cross sections computed with the two methods are illustrated in Figure 4-22. Excellent agreement is found between analytic results and Monte Carlo simulation-based calculations.

4.5.3 Electron, positron, and photon-induced DPA cross sections for iron

Figure 4-22 shows the total electron, positron, and photon-induced DPA cross section for iron based on the Mott scattering cross sections for electron and positron. The exact Bethe formula [135, 136] is used for calculating differential reaction cross section of PP. Because the photon-induced DPA cross section is much smaller than the other ones, it is multiplied by a factor of 5 for illustrating its variation along with photon energy.

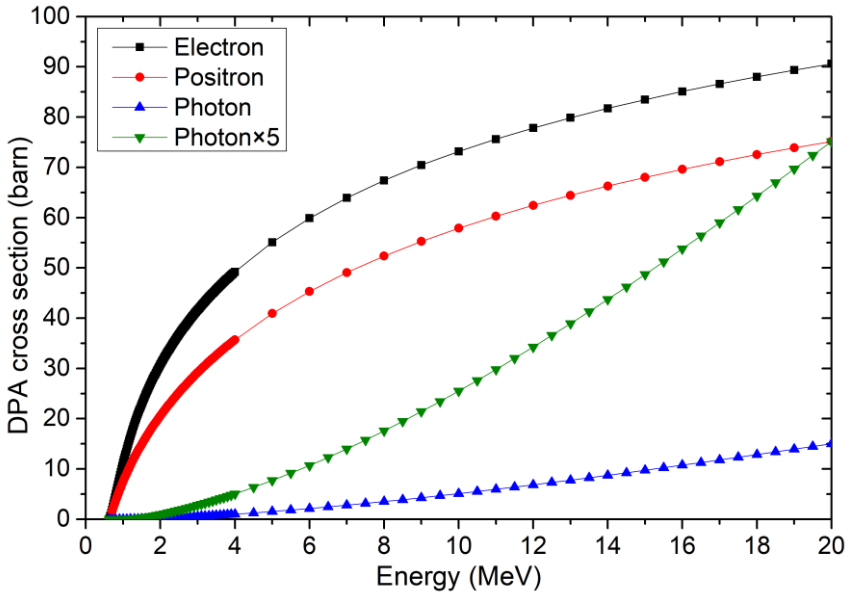

Figure 4-23. Electron, positron, and photon-induced NRT-DPA cross sections for iron based on the Mott cross sections.

For particle energy below 10 MeV, which is the case for most fission reactors, photon-induced DPA cross section is more than 10 times smaller than the electron and positron-induced one. However, it is notable that the smaller DPA cross section does not imply less DPA induced by photon than electron or positron in a specific case

because the DPA rate is the product of DPA cross section and the corresponding flux.

Here, a photon induces atomic displacements only through its subsequent products electron and/or positron. For photon energy larger than around 10 MeV, photon is able to displace atoms via photo-nuclear reaction. However, the photo-nuclear reaction-induced DPA cross section is negligible when compared with that induced by photon-matter reactions [140].

4.6 Beta decay-induced damage cross sections [81]

Nuclear disintegrations, which are normally slower than atomic displacement cascade (~ 10 ps [99]), are rarely individually studied for atomic displacement calculation. The three nuclear transitions are alpha decay, beta decay (β^- and β^+/ε), and gamma transition. The gamma transition is found in all nuclear reactions other than elastic scattering due to the deexcitation of recoil nuclei. The emitted gamma is considered in the gamma spectrum and its contribution can be thus included in gamma-induced DPA [124]. The recoil of residual nucleus during the gamma emission is calculated by the same reasoning given in Section 4.4.2 (but this part is still not considered in all current studies). Alpha decay is a two-body reaction and is conservatively considered in Ref. [141]. For most neutron-induced reactions other than (n,2n), nuclei generally loose more protons than neutrons, such as (n,p), (n,d), (n,^{3}He), (n,α), and (n,np). Therefore, the unstable recoil nuclei are mostly in the "south-east" of the line of stability on the N-Z plot. The most possible nuclear transition is the beta decay which emits an electron. Moreover, due to the emission of (anti)neutrino, the beta decay is a three-body reaction, which complicates the calculation of irradiation damage from kinematics. This section presents the atomic displacement induced by beta decay. All results were published in Ref. [81].

4.6.1 Beta decay

The beta decay of a nucleus ${}^A_Z\mathrm{X}$ can be expressed by:

$$ {}^A_Z\mathrm{X} \rightarrow {}^A_{Z+1}\mathrm{X} + e^- + \upsilon \tag{4-77} $$

where υ represents antineutrino. The electronic antineutrino is conventionally denoted by $\bar{\upsilon}_e$. For the sake of convenience, the present work uses the simple notation υ. Figure 4-24 illustrates the corresponding schema of the beta decay for the nucleus ${}^A_Z\mathrm{X}$. After the beta decay, the excited nucleus will deexcite via a cascade of gamma emissions except for pure beta isotopes. The probability of different branch of beta decay can be determined by Fermi's Golden Rule [142]:

$$ P = \frac{2\pi}{\hbar}\left|H_{fi}\right|^2 \rho\left(E_f\right) \tag{4-78} $$

where $\rho\left(E_f\right)$ is the density of final state, H_{fi} is the Hamiltonian describing the

interaction between the initial state and the final state. Figure 4-25 shows (in red) the intensity (or relative probability) of beta decay of ^{56}Mn with data from the latest Evaluated Nuclear Structure Data File (ENSDF) evaluation [143].

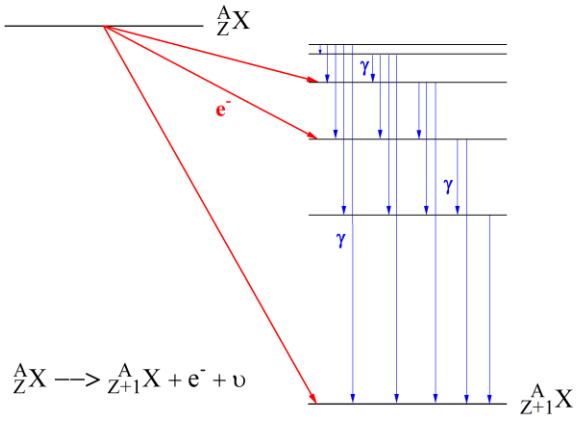

Figure 4-24. General energy level schema of a beta decay.

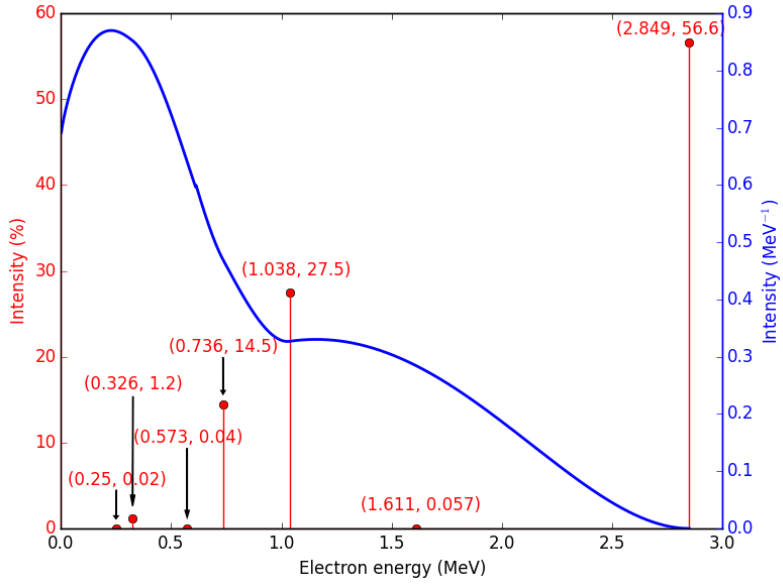

Figure 4-25. Intensity of ^{56}Mn beta emission (from ENSDF [143]) and the corresponding energy distribution of the emitted electrons.

Since the beta decay is always accompanied by an antineutrino, the kinetic energy of the emitted electron is not the total energy release of the beta decay. For each level i beta decay, the electron spectrum can be approximately calculated by [142]:

$$\chi_i(p) \propto p^2(Q_i - E_e)^2 F(Z+1,p)\left|M_{fi}\right|^2 S(p,q) \qquad (4\text{-}79)$$

where p and q respectively represent the momenta of the electron and the antineutrino, Q_i is the Q-value of transition i, E_e is the kinetic energy of the electron, $F(Z+1,p)$ is Fermi's function accounting the Coulomb field, $\left|M_{fi}\right|^2$ is the nuclear matrix element

[144], and $S(p,q)$ is an additional electron and antineutrino momentum dependence.

Taking all transition channels into account, the electron spectrum of a beta decay is:

$$\chi(p) = \sum_i \tilde{P}_i \chi_i(p) \tag{4-80}$$

where $\tilde{P}_i$ is the intensity (or relative probability) of the i-level beta decay. Figure 4-25 illustrates (in blue) the energy distribution of the emitted electron from the beta decay of ^{56}Mn [143]. The form of the electron spectrum shown in Figure 4-25 is in good agreement with those produced by JANIS [145]. The electron spectrum can be used to determine the number of DPA using the corresponding electron-induced DPA cross section.

4.6.2 Electron-induced displacement damage

The calculation of electron-induced DPA cross section is given in Section 4.5.1. As indicated in Section 3.4, for the study of electron-induced damage, the use of NRT or mNRT leads to large differences. Figure 4-26 shows the electron-induced DPA cross sections of iron for NRT and mNRT formulae using the MF approach and Mott series. Figure 4-27 illustrates the examples of $n(E)$ (i.e. average number of atomic displacements induced by a kinematic electron) calculated with the DPA cross sections shown in Figure 4-26. Using the spectrum of the electron and $n(E)$, the number of DPA can be determined by:

$$DPA = \int_0^\infty n(E)\phi(E)dE \tag{4-81}$$

where ϕ refers to the electron spectrum (such as the blue curve shown in Figure 4-25).

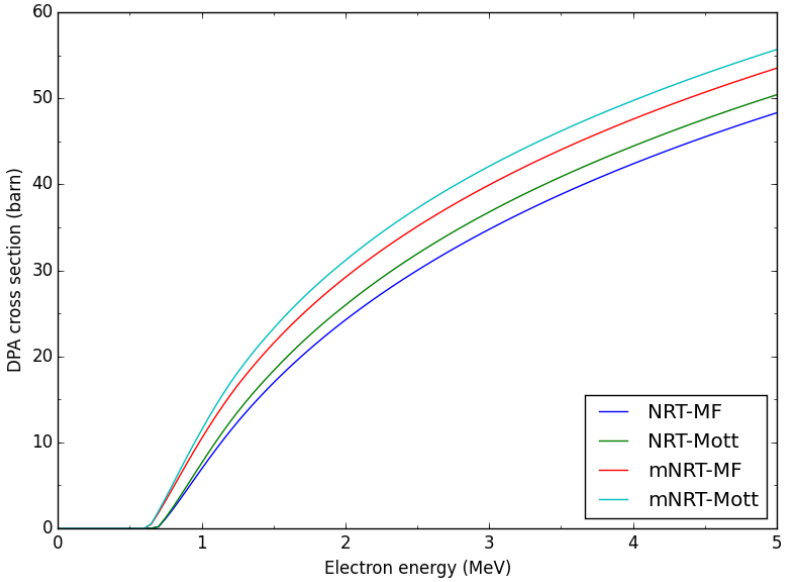

Figure 4-26. Electron-induced DPA cross sections for iron.

Table 4-4 summarizes the number of displaced atoms, i.e. N_{FP}, induced by an electron from ^{56}Mn beta decay in pure ^{56}Fe. Taking the widely used MF approach of electron scattering cross section as the reference, the use of Mott's series leads to additional 8% DPA. This value is in good agreement with the data shown in Ref. [124]. Compared with the standard NRT formula, the mNRT-based DPA shows an increase of 36%. It is observed that the mNRT and Mott's series can yield 47% more DPA than the standard NRT and the widely used MF approach for ^{56}Mn beta decay electron-induced atomic displacement in pure ^{56}Fe. Therefore, the use of Mott's series and the mNRT is of importance for computing the atomic displacement induced by beta decay electrons.

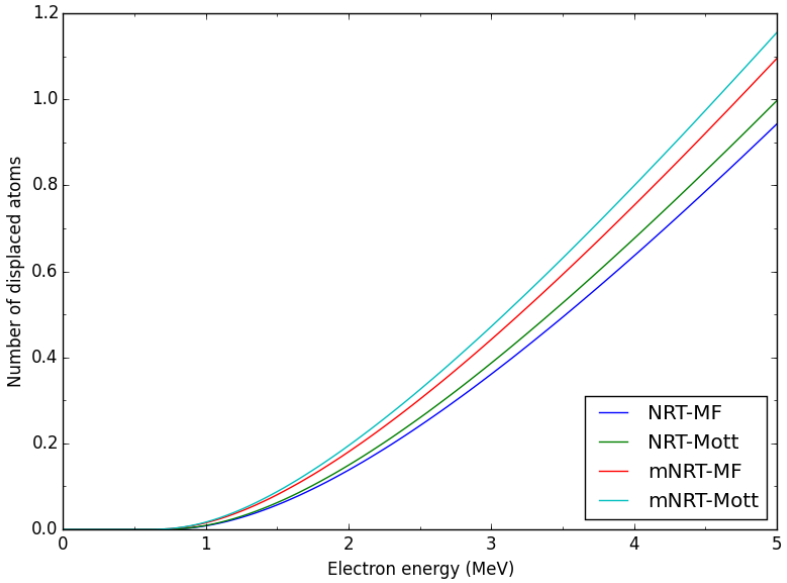

Figure 4-27. Total number of displaced atoms per incident electron.

Table 4-4. N_{FP} of ^{56}Fe induced by an electron from ^{56}Mn beta decay.

	NRT_MF	NRT_Mott	mNRT_MF	mNRT_Mott
$N_{FP} \times 10^{-3}$	27.97	30.39	38.03	41.21
Ratio to NRT_MF	1.000	1.086	1.359	1.472

4.6.3 Atomic displacement induced by residual atom

For general studies of beta decay, the recoil kinetic energy of the residual nucleus is negligible in comparison with the energies of electrons and antineutrinos [146]. However, since the threshold energy of atomic displacement is generally below 100 eV, the residual nucleus of a beta decay is also able to induce atomic displacement.

Figure 4-28 illustrates the kinematics of the three particles after a beta decay. The conservation of momenta implies:

$$\vec{p}_R + \vec{p}_e + \vec{p}_\upsilon = \vec{0} \tag{4-82}$$

where the subscripts R, e, and υ represent the residual atom, emitted electron, and the antineutrino, respectively. The norm of the momentum of the residual nucleus is thus:

$$\|\vec{p}_R\| = \|\vec{p}_e + \vec{p}_\upsilon\| \tag{4-83}$$

For the sake of convenience, one denotes the norm of a vector by the same notation without an arrow. Accordingly,

$$p_R^2 = p_e^2 + p_\upsilon^2 + 2\vec{p}_e \cdot \vec{p}_\upsilon \tag{4-84}$$

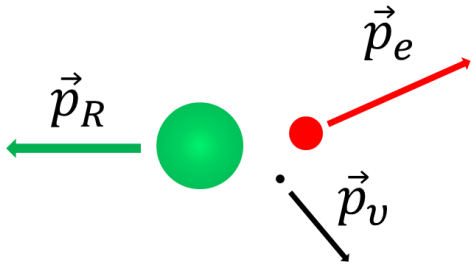

Figure 4-28. Schematic of kinematics of a beta decay. R, e, and υ represent the residual atom, the emitted electron, and the antineutrino, respectively.

Supposing isotropic distribution of the angle between the directions of electron emission and antineutrino emission, one has:

$$\int \vec{p}_e \cdot \vec{p}_\upsilon d\Omega = 0 \tag{4-85}$$

where Ω is the solid angle. Therefore, averaging over the angular distribution, one has:

$$p_R^2 = p_e^2 + p_\upsilon^2 \tag{4-86}$$

According to the relationship between momentum and energy, the kinetic energy of the residual nucleus is:

$$E_R = \sqrt{p_R^2 c^2 + M^2 c^4} - Mc^2 \tag{4-87}$$

where c is the speed of light and M is the rest mass of the residual nucleus:

$$M = M_0 + E^*/c^2 \tag{4-88}$$

where M_0 is the mass in the ground state, E^* is the excitation energy. In general, the excitation energy is negligible in comparison with the rest mass. The approximation $M \cong M_0$ can be thus used in most cases, including the beta decay. It is noteworthy that nonrelativistic treatment can be directly used for the residual nucleus because $E_R \ll Mc^2$ [117]. On the other hand, Eq. (4-86) shows that $p_R \geq p_e$. Consequently,

$$E_R \geq E_R^- \equiv \sqrt{E_e(E_e + 2mc^2) + M^2 c^4} - Mc^2 \tag{4-89}$$

where E_e represents the kinetic energy of the emitted electron. This lower boundary is emphasized because the spectrum of E_R^- can be directly determined using the spectrum

of E_e as the example shown in Figure 4-25.

Since the kinetic energy of the residual nucleus is generally much smaller than those of emitted electron and antineutrino, the energy of antineutrino is approximately:

$$E_\upsilon = Q - E_e \tag{4-90}$$

where Q is the total energy release in the beta decay. On the other hand, due to the negligible mass of antineutrino, one has directly:

$$p_\upsilon = E_\upsilon / c \tag{4-91}$$

Therefore, for each level of the beta decay, the recoil energy of the residual nucleus is:

$$E_R = \sqrt{E_e(E_e + 2mc^2) + (Q - E_e)^2 + M^2c^4} - Mc^2 \tag{4-92}$$

The spectrum of E_R is calculated during the calculation of the one of E_e.

Similar to E_R^-, one can have an upper limit of recoil energy:

$$\begin{aligned} E_R &\leq E_R^+ \equiv \sqrt{E_e(E_e + 2mc^2) + (Q_{max} - E_e)^2 + M^2c^4} - Mc^2 \\ &\leq E_R^{+b} \equiv \sqrt{E_e(E_e + 2mc^2) + Q_{max}^2 + M^2c^4} - Mc^2 \end{aligned} \tag{4-93}$$

where Q_{max} is the maximum energy release (e.g. 2.85 MeV for the beta decay of ^{56}Mn). E_R^+ (or E_R^{+b}) can also be directly determined via the spectrum of E_e. Using E_R^- and E_R^+, one can obtain the range of DPA numbers induced by the residual nucleus without calculating the spectrum of E_R. It is noteworthy that $E_R \leq E_R^{+b}$ shows that the two-body treatment in Ref. [141] can give a conservative value for the residual nucleus-induced DPA of a beta decay.

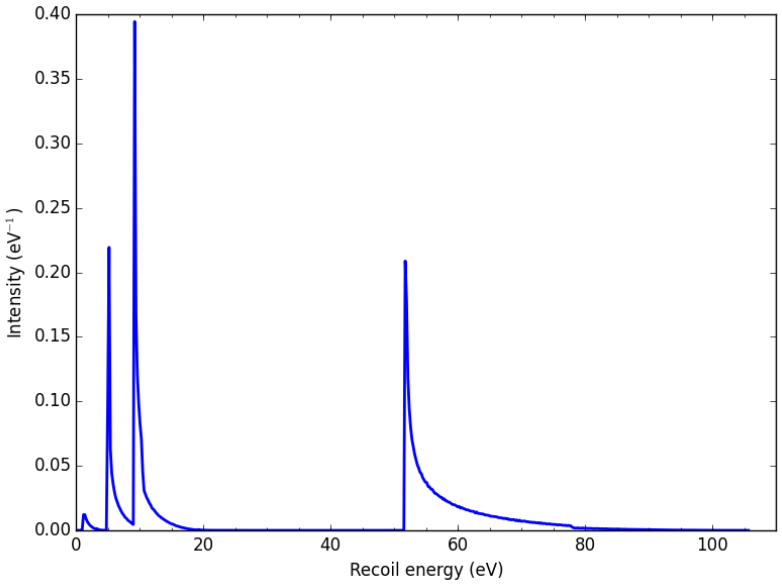

Figure 4-29. Recoil energy spectrum from ^{56}Mn beta decay.

Table 4-5 gives the N_{FP} induced by the kinetic energy of the residual nucleus from

^{56}Mn beta decay in pure ^{56}Fe. The data in Table 4-5 are calculated by the lower boundary E_R^-, two upper boundaries E_R^+ and E_R^{+b}, and the spectrum of recoil energy illustrated in Figure 4-29. As expected, using E_R^- and E_R^+ (or E_R^{+b}) and the emitted electron spectrum can give the range of correct DPA. Therefore, in the case where the beta decay-induced DPA is not so important, one can directly use E_R^+ to obtain a conservative value. On the other hand, one can take the average of two values calculated with E_R^- and E_R^+ for a reasonably approximative value. In the case of ^{56}Mn beta decay, the average DPA calculated based on E_R^- and E_R^+ is 0.5798, which is quite close to the exact calculation 0.5665.

Table 4-5. N_{FP} of ^{56}Fe induced by the residual nucleus from ^{56}Mn beta decay.

E_R^-	E_R^+	E_R^{+b}	Average	E_R spectrum	Ref. [141]
0.1596	1.0000	1.0251	0.5798	0.5665	1.4313

Using the method in Ref. [141], the residual nucleus-induced DPA in ^{56}Mn beta decay is 1.43. Therefore, compared with the methods proposed in the present work, Ref. [141] overestimates the residual kinetic energy-induced atomic displacement by a factor of 2.5 in ^{56}Mn beta decay. It is noteworthy that Ref. [141] proposes the use of the mass difference, which is 3695.64 keV for ^{56}Mn beta decay. However, $Q_{max} =$ 2848.86 keV because the β^- emission of ^{56}Mn leads to ^{56}Fe at excited level with excitation energy higher than 846.776 keV [143]. If we replace the mass difference by Q_{max}, the recoil energy proposed by Ref. [141] becomes 83.8 eV, which implies 1 DPA if the NRT or the mNRT formula is applied.

Comparing data from Table 4-4 and Table 4-5, the number of DPA induced by the recoil energy of the residual nucleus is larger than that induced by the emitted electron by a factor of 13.5 (20 if the standard NRT formula and the MF approach are used). Consequently, for the calculation of beta decay-induced atomic displacement, the kinetic energy of the residual nucleus has to be taken into account. In other words, the consideration of electron-induced DPA only is not sufficient to compute the beta decay-induced atomic displacements.

4.7 Discussion on damage cross sections of polyatomic materials

For a specific PKA energy, the number of DPA can be determined with the methods presented in Section 3. Assuming an explicit relationship between PKA energy and the number of atomic displacements, one can determine the DPA cross section for a given nuclear reaction *i* of the target *j* through:

$$\sigma_{DPA,i,j}(E) = \sigma_{i,j}(E) \int_{-1}^{1} f_{i,j}(\mu, E)\, \nu\big(E_{R,i,j}(\mu, E), i, j\big) d\mu \qquad (4\text{-}94)$$

where $\nu\left(E_{R,i,j}(\mu,E),i,j\right)$ denotes the number of atomic displacements for a PKA energy of $E_{R,i,j}(\mu,E)$, $f_{i,j}(\mu,E)$ is the angular distribution in the CM frame, and $\sigma_{i,j}(E)$ is the nuclear cross section. $\nu\left(E_{R,i,j}(\mu,E),i,j\right)$ can be determined with the methods presented in Section 3 (e.g., MD and BCA) or by solving Lindhard equation [72] (e.g., Refs. [78, 114]).

As explained in Section 3, the TDE of atomic displacement is direction-dependent. Due to the use of average TDE in explicit DPA formulae, additional uncertainty of $E_{d,j}$ (E_d for the target *j*) is introduced in DPA calculations. In order to decrease the influence of $E_{d,j}$ in DPA cross sections calculations, one defines the damage energy cross sections by:

$$\sigma_{D,i,j}(E)=\sigma_{i,j}(E)\int_{-1}^{1}f_{i,j}(\mu,E)\left[2.5E_{d,j}\nu\left(E_{R,i,j}(\mu,E),i,j\right)\right]d\mu \qquad (4\text{-}95)$$

The total damage cross section of atom *j* is computed by summing all possible reaction channels *i*:

$$\sigma_{D,j}(E)=\sum_i\sigma_{i,j}(E)\int_{-1}^{1}f_{i,j}(\mu,E)\left[2.5E_{d,j}\nu\left(E_{R,i,j}(\mu,E),i,j\right)\right]d\mu \qquad (4\text{-}96)$$

The DPA cross sections can be directly deduced by:

$$\sigma_{DPA,j}(E)=\sigma_{D,j}(E)/\left(2.5E_{d,j}\right) \qquad (4\text{-}97)$$

For convenience, let *J* denote polyatomic materials. The damage energy for the polyatomic material *J* is computed by:

$$\sigma_{DPA,J}(E)=\sum_{j\in J}c_j\sum_i\sigma_{i,j}(E)\int_{-1}^{1}f_{i,j}(\mu,E)\left[\nu\left(E_{R,i,j}(\mu,E),i,j,J\right)\right]d\mu \qquad (4\text{-}98)$$

where c_j represents the fraction of atom *j* in the compound material *J*, $\nu\left(E_{R,i,j}(\mu,E),i,j,J\right)$ refers to the number of atomic displacements in *J* by the PKA produced from the reaction *i* on the target *j*. Because the NRT-DPA formula or other formulae is valid only for monatomic materials, one should calculate displacements in polyatomic materials using MD simulations or BCA calculations. The equation concerning damage cross section can be rewritten as:

$$\sigma_{DPA,J}(E)=\sum_{j\in J}c_j\sum_i\sigma_{i,j}(E)\int_{-1}^{1}f_{i,j}(\mu,E)\left[\nu\left(E_{R,i,j}(\mu,E),i,j\right)\eta(E_R,i,j,J)\right]d\mu \qquad (4\text{-}99)$$

where $\eta(E_R,i,j,J)$ represents the ratio of displacement number in *J* to that in monatomic *j* for the reaction *i* of atom *j* produced PKA. The PKA kinetic energy E_R depends on μ. In the case where $\eta(E_R,i,j,J)$ does not depend on E_R nor reaction *i*, with the notation $\eta(j,J)\equiv\eta(E_R,i,j,J)$, the DPA cross section in compound materials can be expressed by the DPA cross sections in monatomic materials:

$$\begin{aligned}\sigma_{DPA,J}(E) &= \sum_{j\in J} c_j \eta(j,J) \sum_i \sigma_{i,j}(E) \int_{-1}^{1} f_{i,j}(\mu,E)\, \nu\big(E_{R,i,j}(\mu,E),i,j\big) d\mu \\ &= \sum_{j\in J} c_j \eta(j,J) \sigma_{DPA,j}(E)\end{aligned} \quad (4\text{-}100)$$

Therefore, for $\eta(E_R,i,j,J)$ independent on E_R nor i, the DPA cross sections of polyatomic materials can be directly deduced from the damage energy calculated by NJOY with:

$$\sigma_{DPA,J}(E) = \sum_{j\in J} c_j \eta(j,J) \sigma_{D,j}(E) / \big(2.5 E_{d,j}\big) \quad (4\text{-}101)$$

For compound materials, one may use an equivalent TDE defined as [147]:

$$E_{d,eq} = \big(\sum_j c_j / E_{d,j}\big)^{-1} \quad (4\text{-}102)$$

where c_j and $E_{d,j}$ are respectively the concentration and threshold energy of atom j. This equation is validated by $MgA1_2O_4$ via binary collision Monte Carlo simulations [147]. Using the equivalent TDE, the DPA cross section of the compound material J is further simplified as:

$$\sigma_{DPA,J}(E) = \frac{0.8}{2E_{d,eq}} \sum_{j\in J} c_j \eta(j,J) \sigma_{D,j}(E) \quad (4\text{-}103)$$

An important remark is that owing to the different numbers of displacement in j and J, the computation of total DPA cross section of compound materials with those of elementary atoms is different from the computation for nuclear cross sections, which is:

$$\sigma_J(E) = \sum_{j\in J} c_j \sigma_j(E) \quad (4\text{-}104)$$

5 Calculation of DPA rates

5.1 DPA rate calculation using damage cross sections

Here, the notations defined in Section 4.7 are used. For a specific incident particle, the total DPA rate induced by this particle in material *J* is computed by:

$$\tau_{DPA,J} = \int_0^\infty \sigma_{DPA,J}(E)\phi(E)dE \tag{5-1}$$

where $\phi(E)$ represents the spectrum of the incident particle. In practice, the spectra are always given in specific energy grids rather than continuous functions versus energy, two methods are proposed to compute the integral.

In order to directly use the multigroup spectra without introducing additional uncertainties from pointwise interpolation, one can compute the multigroup DPA cross sections. Therefore, the DPA rate is given by:

$$\tau_{DPA,J} = \sum_k \sigma_{DPA,J,k}\phi_k \tag{5-2}$$

where the index *k* stands for the group number, the multigroup DPA cross sections are:

$$\sigma_{DPA,J,k} = \int_{E_{inf,k}}^{E_{sup,k}} \sigma_{DPA,J}(E)\varphi(E)dE \,/\, \int_{E_{inf,k}}^{E_{sup,k}} \varphi(E)dE \tag{5-3}$$

where the weighting function $\varphi(E)$ should be equal to the real continuous spectrum $\phi(E)$ in principle. However, because the real continuous spectrum is unknown, some general functions are proposed. Therefore, additional bias is introduced by multigroup DPA cross sections. An example of reducing this kind of additional uncertainties is shown in our previous work [116].

To avoid the additional bias from multigroup DPA cross sections (especially for highly fluctuating reactions cross sections such as the neutron-induced ones), one can use continuous DPA cross sections. However, in this case, the interpolation of incident spectra is required. The advantage of this method is to avoid the calculation of multigroup cross sections.

In monatomic materials, the calculation of DPA rate can be simplified to:

$$\tau_{DPA} = \frac{0.8}{2E_d}\int_0^\infty \sigma_D(E)\phi(E)dE \tag{5-4}$$

where σ_D is the damage cross section discussed in Section 4. In multigroup approximation, the DPA rate is calculated by:

$$\tau_{DPA} = \frac{0.8}{2E_d}\sum_k \sigma_{D,k}\phi_k \tag{5-5}$$

where the index *k* stands for the group number, the multigroup damage cross sections being given by the expression:

$$\sigma_{D,k} = \int_{E_{inf,k}}^{E_{sup,k}} \sigma_D(E)\varphi(E)dE \,/\, \int_{E_{inf,k}}^{E_{sup,k}} \varphi(E)dE \tag{5-6}$$

where $\varphi(E)$ is a weighting function identical to the one used in Eq. (5-3).

5.2 Self-shielding correction on DPA rate calculation [116]

From the calculations shown in Section 4.4, the damage cross section can be separated into two terms:

$$\sigma_D(E) = \sigma(E)\bar{E}_a(E) \tag{5-7}$$

where $\bar{E}_{a,i}(E)$ is the averaged damage energy. The DPA rate induced by a particle other than atoms in a material can be thus reformulated as:

$$\tau_{DPA} = \int_0^\infty \sum_i \frac{0.8}{2E_d} \times \left[\bar{E}_{a,i}(E)\sigma_i(E)\right] \phi(E)dE \tag{5-8}$$

where the index i reveals the reaction types, such as elastic scattering and inelastic scatterings. $\sigma_i(E)$ is the cross section of the reaction i at energy E, $\phi(E)$ refers to the flux of the incident particle, and $\bar{E}_{a,i}(E)$ is the corresponding averaged damage energy.

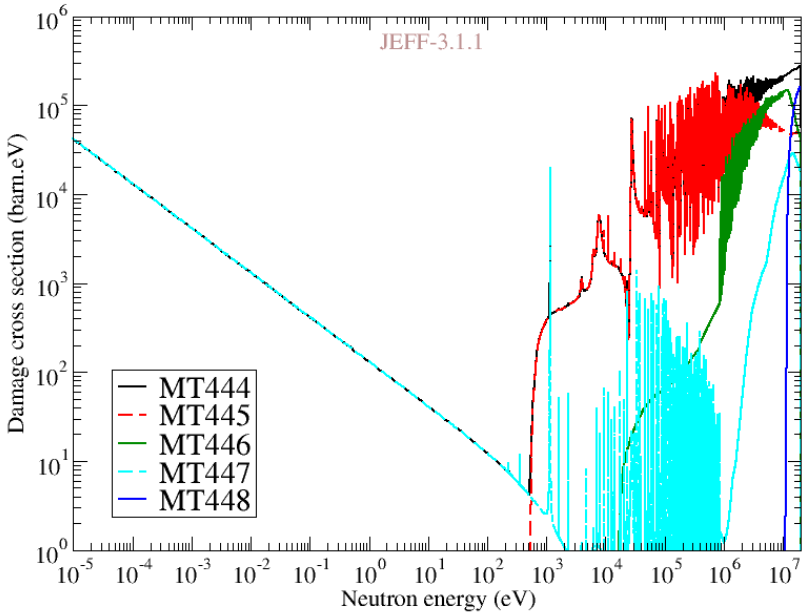

Figure 5-1. Total, elastic, inelastic, disappearance, and other n+^{Nat}Fe reaction-induced damage cross sections at room temperature.

In a reactor core, the upper limit of the integral in Eq. (5-8) is 20 MeV for neutrons. $\sigma_{D,i}(E) = \bar{E}_{a,i}(E)\sigma_i(E)$ is the damage cross section (in barn.eV) induced by the reaction type i at incident energy E as shown in Figure 5-1, which illustrates the total, elastic scattering, total inelastic scattering, disappearance, and other neutron reactions-induced damage cross sections (MT444, MT445, MT446, MT447, and MT448 respectively) for natural Fe at room temperature. The disappearance damage cross

section is the sum of damages caused by reactions without neutron emission, i.e. reactions from MT102 to MT120. For ^{56}Fe in JEFF-3.1.1, only the cross sections from MT102 to MT107 are evaluated. The disappearance signifies no neutron emission after the reaction, such as (n,γ), (n,p), and (n,α) reactions. It is noticeable that the DPA rates induced by reactions excluded in MT445-MT447, e.g. (n,2n) and (n,np), are quite negligible in fission reactors.

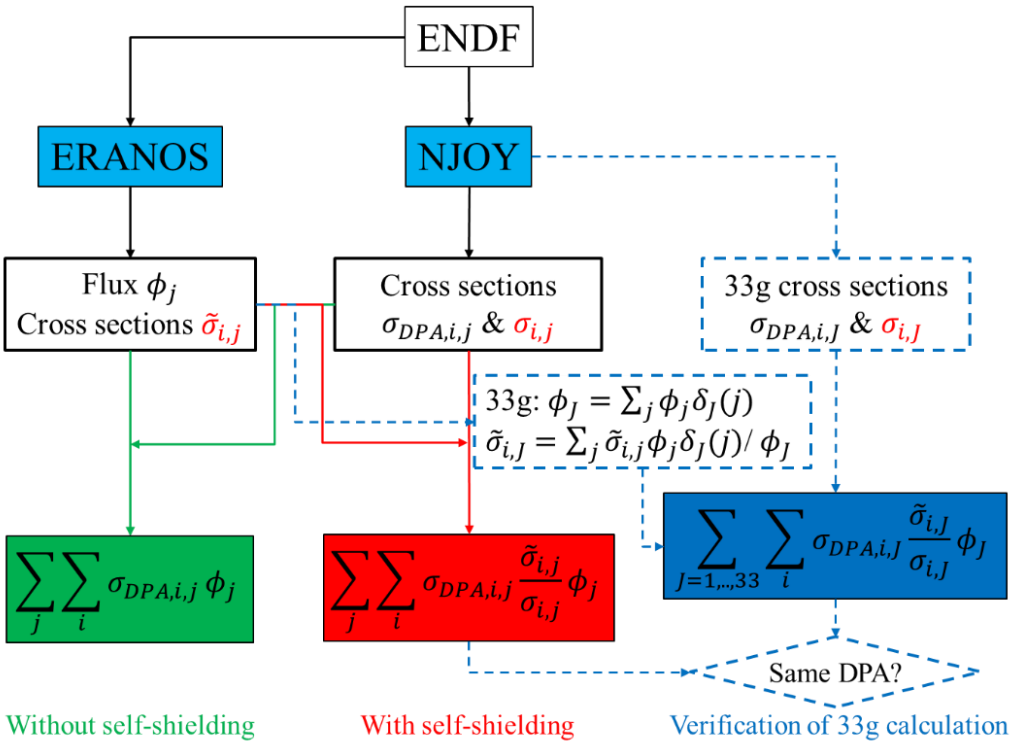

Figure 5-2. Flowchart of DPA calculations without (green) and with (red) self-shielding corrections. The dashed scheme is only for the verification of ECCO 33-group calculations by using multi-group cross sections and flux computed with transport code with finer energy structure (ECCO 1968-group in our studies).

Figure 5-2 illustrates the different routines of DPA calculations. Eq. (5-8) is the method of DPA calculation without considering the self-shielding correction (green scheme in Figure 5-2). However, both cross sections and neutron flux are modified in deterministic codes due to the self-shielding treatment. The DPA rate after the correction of self-shielding should be calculated by:

$$\tau_{DPA} = \int_0^{20MeV} \sum_i \frac{0.8}{2E_d} \times \left[\bar{E}_{a,i}(E)\tilde{\sigma}_i(E)\right] \tilde{\phi}(E) dE \qquad (5\text{-}9)$$

where $\tilde{\sigma}$ and $\tilde{\phi}$ represent cross sections and neutron flux with the self-shielding correction. The neutron flux mentioned in the following description is the self-shielded neutron flux, ϕ will be thus used rather than $\tilde{\phi}$ to simplify the notation. Hence, the DPA

rate can be calculated by:

$$\tau_{DPA} = \frac{0.8}{2E_d} \times \int_0^{20MeV} \sum_i \sigma_{DPA,i}(E) \frac{\tilde{\sigma}_i(E)}{\sigma_i(E)} \phi(E) dE \quad (5\text{-}10)$$

Discretizing the integral to the sum of multi-group structure:

$$\tau_{DPA} = \frac{0.8}{2E_d} \times \sum_{j=1}^{G} \sum_i \sigma_{DPA,i,j} \frac{\tilde{\sigma}_{i,j}}{\sigma_{i,j}} \phi_j \quad (5\text{-}11)$$

where G is the number of groups, $\tilde{\sigma}_{i,j}$ denotes the self-shielded multi-group reaction cross section. This method corresponds to the red routine illustrated in Figure 5-2.

In order to evaluate the accuracy of self-shielding corrections based on 33-group structure, an additional scheme shown in Figure 5-2 by blue dashed symbols is used in the present work. Using the multi-group neutron flux ϕ_j and self-shielding corrected cross sections $\tilde{\sigma}_{i,j}$ calculated by transport code in a finer structure (ECCO 1968-group in our studies), we compute 33-group neutron flux by summing neutron flux of which the group j in the finer structure is included in group J of 33-group. The deduced 33-group cross sections are obtained by conserving the same reaction rates.

In the following studies, the infinite dilution multigroup cross sections $\sigma_{i,j}$ and $\sigma_{DPA,i,j}$ are computed by the GROUPR module in NJOY2016.20 with the weighting function iwt8 (i.e. thermal -- 1/E -- fast reactor -- fission & fusion) shown in Figure 5-3. The self-shielding corrected multi-group cross sections $\tilde{\sigma}_{i,j}$ are calculated by ECCO, of which the methods of self-shielding calculations are presented in Ref. [148].

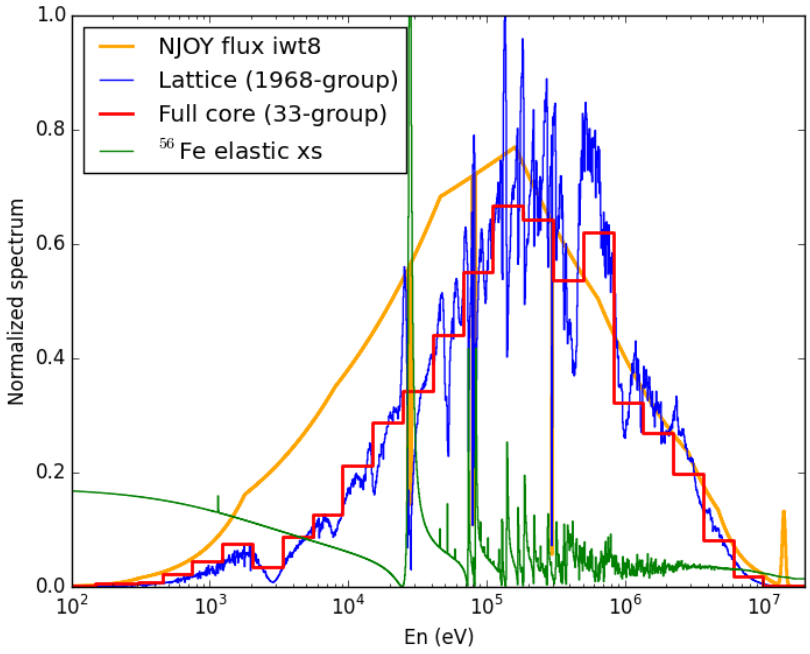

Figure 5-3. Normalized neutron spectra for NJOY-iwt8, 1968-group lattice calculation (blue) and 33-group full core calculation (red) flux in ASTRID inner core, and the relative elastic scattering cross section of ^{56}Fe.

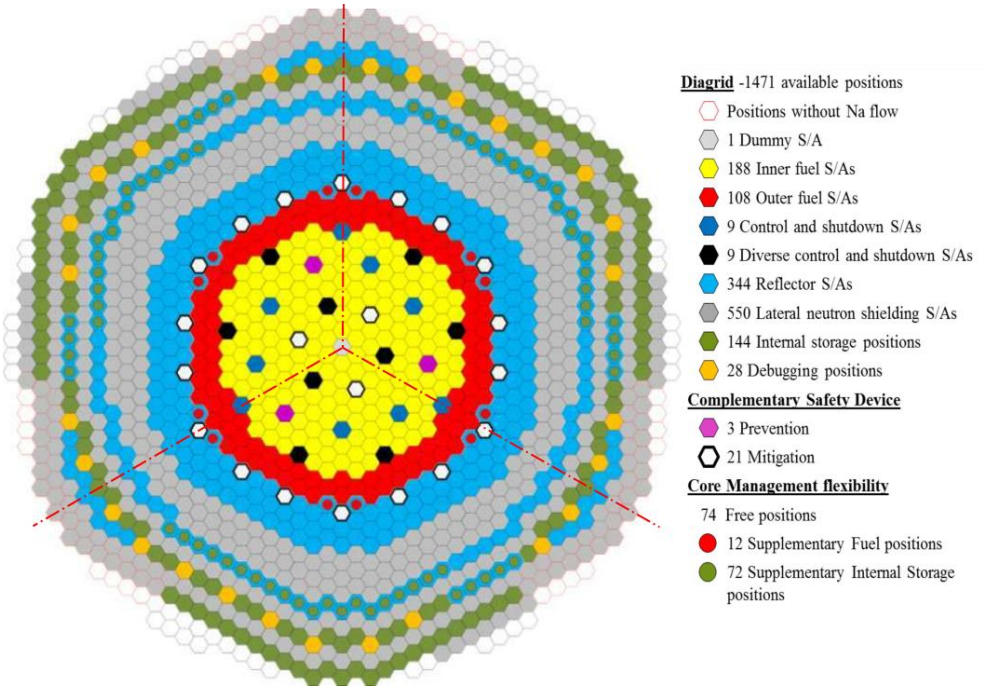

Figure 5-4. Layout of ASTRID core (3-fold rotational symmetry).

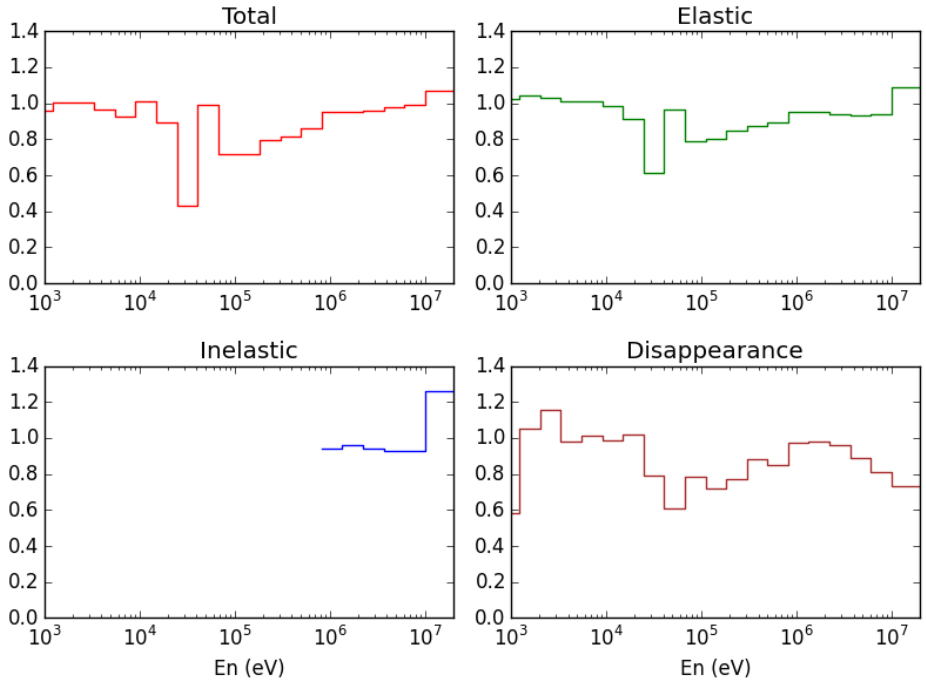

Figure 5-5. Correction coefficients of different (n+^{56}Fe) cross sections for ECCO 33-group full core calculations.

The present work aims to compute the DPA rates for the fuel cladding of the ASTRID inner core, which corresponds to the yellow pointed out in Figure 5-4. The corresponding neutron spectrum from ERANOS-2.3 calculation is shown in Figure 5-3

by the red multigroup structure. The full ASTRID core calculation is performed to compute the ECCO 33-group neutron spectrum and the self-shielding corrected cross sections. Figure 5-5 illustrates the 33-group correction coefficients for the total, elastic scattering, total inelastic scattering, and disappearance cross sections. Detailed explanations are given in our published article [116].

The DPA rate and self-shielded DPA rate at each energy group and their difference (and ratio) are shown in Figure 5-6 for the aforementioned four reactions. Figure 5-6 shows that the self-shielding between 25 keV and 6 MeV is most important in DPA calculations. Out of this band, the self-shielding corrections of cross sections and DPA calculations are weak due to few resonances and low neutron flux (which leads to a very small contribution to total DPA, as shown in Figure 5-6(a)), respectively.

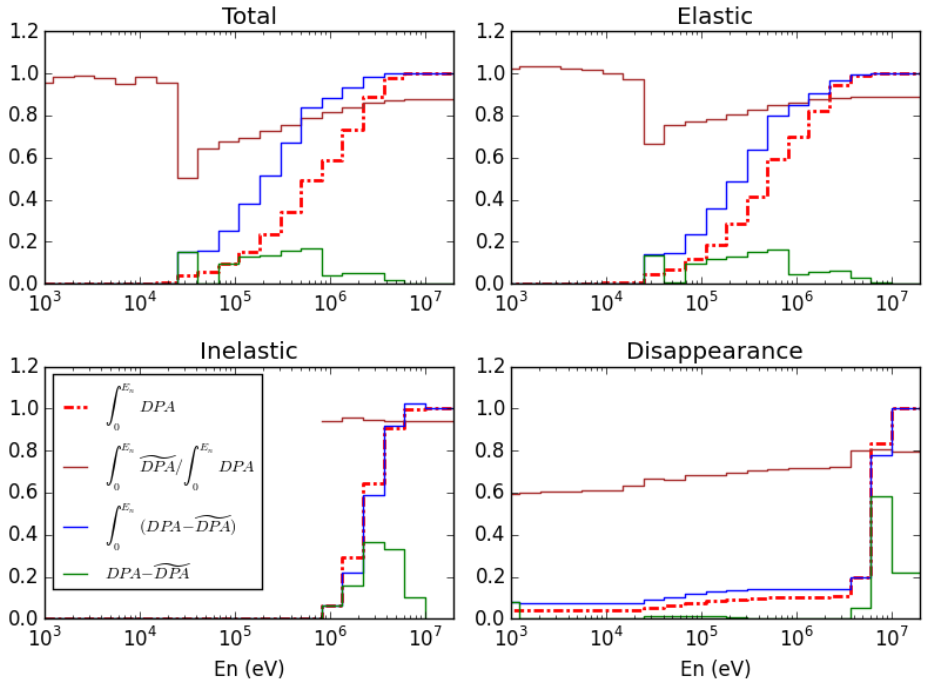

Figure 5-6. Self-shielding effects with 33-group energy structure. DPA stands for the relative DPA rate without self-shielding treatment of cross sections. $\widetilde{DPA}$ refers to the self-shielding corrected DPA rate. $DPA - \widetilde{DPA}$ represents the reduction of DPA due to self-shielding, normalized by its integration over the whole energy range.

Figure 5-7 illustrates the DPA rates in the fuel cladding in the ASTRID inner core without and with the self-shielding corrections of multigroup DPA cross sections (In fact, the self-shielding correction presented here is the total correction of both the self-shielding correction and the correction owing to the use of a general weighting function for computing infinite dilution cross section, more details are given in Ref. [116]). The yellow bars point out the negative corrections on DPA calculations taking the corrections of cross sections into account. It is shown that the DPA computed with total

cross sections is less than the sum of three partial values after the self-shielding correction because of the different self-shielding corrections on different cross sections. 11% relative elastic scattering induced DPA rate is reduced by taking the self-shielding into account. Because inelastic scattering channels are closed below the minimum threshold energy of 862 keV, the self-shielding corrections in the resonance region below 862 keV have no influence on DPA induced by inelastic scatterings. Therefore, the relative reduction of inelastic scattering is less important than the one of elastic scattering. The self-shielding effect on the disappearance reactions induced DPA is important, but its contribution to total DPA is negligible. 10% total DPA is reduced due to the self-shielding treatment in ECCO 33-group full core calculations. The self-shielding corrected DPA rate is 25 DPA/year, of which 81.9%, 18.0%, and 0.1% are induced by elastic scattering, inelastic scatterings, and disappearance reactions, respectively. It represents a 10.4% reduction vs unshielded calculation. Therefore, improper shielding calculations tend to overestimate DPA rates in the core structural materials.

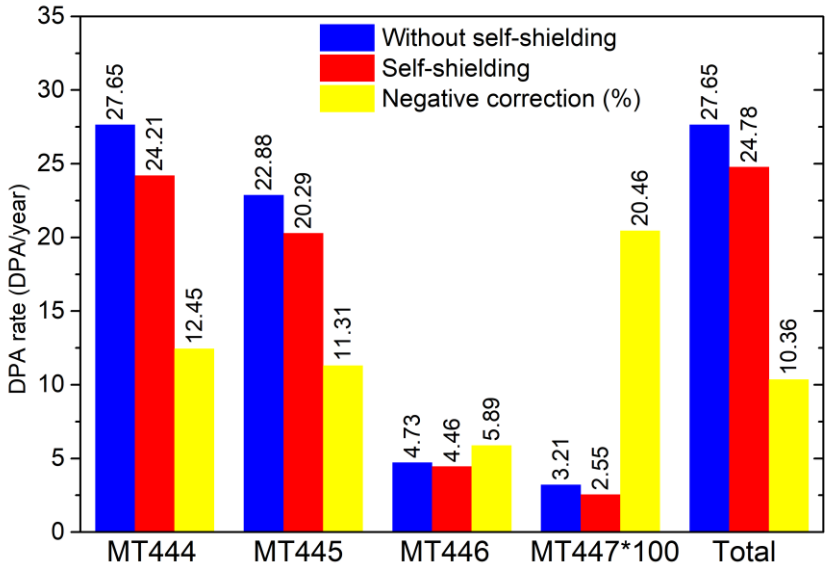

Figure 5-7. DPA rates (in DPA/year) in the fuel cladding in ASTRID inner core computed with ECCO 33-group full core calculations. DPA rate induced by reactions other than MT448 is 0.0098 DPA/year.

5.3 DPA rate calculation by generating PKA spectra

The above two subsections show the methods for calculating DPA rates by folding damage cross sections and neutron flux spectrum. This method is widely used in nuclear engineering because the DPA rate can be directly calculated once the neutron transport calculations are performed. It can be implemented in neutron transport codes so that the DPA rates can be calculated as usual nuclear reaction rates. One shortcoming of this

method is that the damage cross sections are always based on a specific DPA model, whereas no model can perfectly describe the DPA as a function of PKA energy for the time-being [99].

In order to perform accurate DPA rate calculations with advanced models or simulation results, the generation of PKA spectra for a given neutron flux spectrum is preferred. Once the PKA spectra are calculated, the DPA rates can be deduced using any DPA models, in which DPA is an explicit function of PKA energy. Some codes have been developed for this objective, such as SPECTER (ANL, US) [113], DART (CEA, France) [114], and SPECTRA-PKA (UKAEA, UK) [115]. These codes convert neutron spectra into PKA spectra using the neutron-induced ENDF [66] and/or multi-group nuclear data calculated by NJOY [87].

Section 4.3 summarizes the formulae for calculating the PKA energy as a function of different variables for various nuclear reactions. The generation of PKA spectrum χ for a specific neutron spectrum $\phi(E)$ can be performed by:

$$\chi\left(\left[E_{PKA,i}, E_{PKA,i+1}\right]\right) = \sum_j \int_E \int_X \sigma_j(E) f_j(E,X) \phi(E) \delta_{\left[E_{PKA,i}, E_{PKA,i+1}\right]}\left(E_R(E,X)\right) dX dE \tag{5-12}$$

where j represents reaction type, E is the incident energy, X contains all other variables (e.g., $X = \mu$ for discrete reactions and $X = (E', \mu)$ for continuum reactions), the variables E and X in the integrals are restricted by the Delta function $\delta_{\left[E_{PKA,i}, E_{PKA,i+1}\right]}\left(E_R(E,X)\right)$, which is defined by:

$$\delta_{\left[E_{PKA,i}, E_{PKA,i+1}\right]}\left(E_R(E,X)\right) = \begin{cases} 1, & E_{PKA,i} < E_R(E,X) \leq E_{PKA,i+1} \\ 0, & \text{otherwise} \end{cases} \tag{5-13}$$

In most codes, multigroup cross sections rather than pointwise cross sections are used for computing PKA spectra. Therefore, the integration over E becomes a summation on energy groups. SPECTRA-PKA directly uses the recoil matrix $m^j_{ii,ir}$ calculated from a modified-GROUPR module of NJOY, where *j* represents the reaction type and *ii* and *ir* respectively refer to the group numbers of the incident energy and the recoil energy [115].

For the neutron flux spectrum at the inner surface of RPV in a French 900 MWe PWR shown in Figure 5-8, the most important recoil spectra based on ^{56}Fe are shown in Figure 5-9 (calculated by SPECTRA-PKA calculations based on TENDL-2015 nuclear data library [123]). It is shown again that neutron scattering reactions are the major reactions inducing primary radiation damage in a PWR RPV. The 0.55 keV minimum ^{57}Fe recoil energy is equal to the photon kick (because the minimum neutron kick is smaller than 0.5 meV for a thermal neutron).

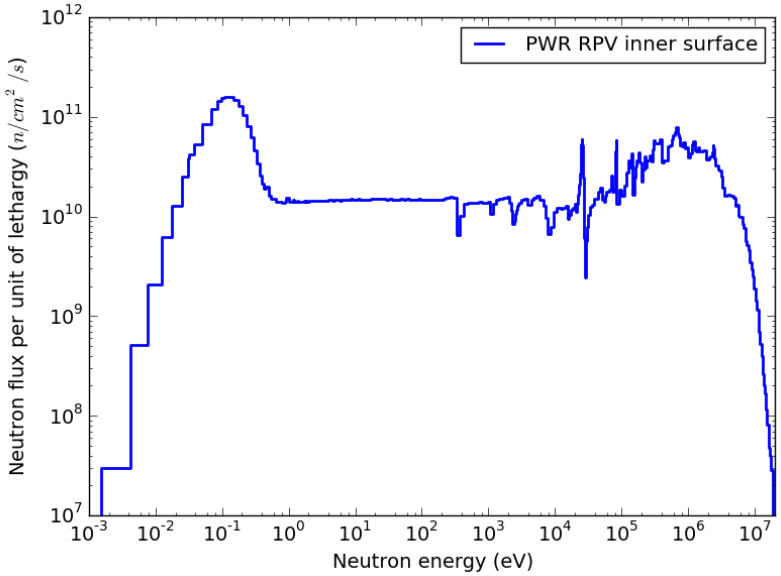

Figure 5-8. Neutron flux spectrum at the inner surface of a French 900 MWe PWR RPV [64].

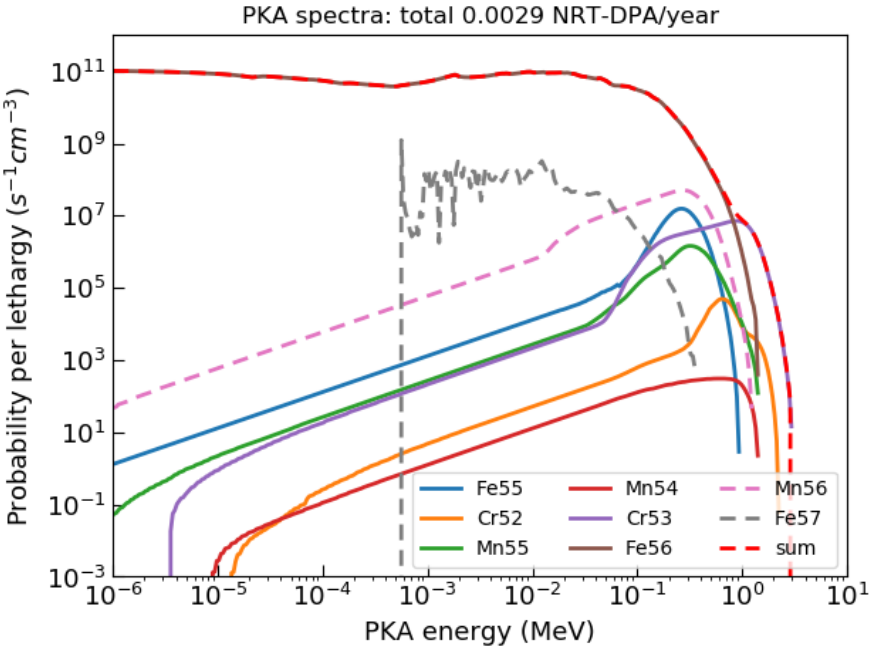

Figure 5-9. PKA spectra of 100% ^{56}Fe material using neutron flux shown in Figure 5-8. SPECTRA-PKA calculations based on TENDL-2015.

It should be noted that the use of NRT or ARC formula for computing damage cross section from nuclear data and for calculating DPA rates using PKA spectra are all approximate calculations. The current NRT formula is based on Lindhard's numerical results from monatomic materials. For a more rigorous calculation, one should solve Lindhard's integral equations. This method is employed in DART [114] (beware, though: DPA calculated by DART is from Lindhard's equations rather than the NRT

formula).

Current codes for calculating PKA spectra from a neutron spectrum are all based on a specific ENDF library and/or a deduced Pointwise ENDF (PENDF) database. However, the self-shielding effect is not taken into account, whereas the self-shielding correction is not negligible for computing total DPA rates (c.f. Section 5.2 [116]). Since the self-shielding correction varies from one reaction to another, it is impossible to simply correct the neutron flux spectrum to perform PKA spectra calculations by considering the self-shielding effect. Thereby, utilization of self-shielding corrected multigroup cross sections (c.f. Section 5.2: correction owing to the weighting function and self-shielding correction) rather than infinite dilution multigroup cross sections calculated with a general weighting function is more physical and should be preferred for considering the self-shielding correction on PKA spectra calculations.

5.4 Fission products-induced DPA in fuel cladding [149]

Since the fuel cladding can be directly irradiated by Fission Products (FPs), the FPs-induced DPA should be important for determining the operating lifetime of fuel assembly in SFRs. Because heavy ions generally have small ranges in materials, FPs-induced damage should be found only near the inner surface of the cladding, where fuel pellets and cladding are in contact and Fuel-Cladding Chemical Interaction (FCCI) [150] may occur. In this region, the irradiation damage may be not as important as the FCCI. However, it is still of interest to investigate the FPs-induced irradiation damage in the fuel cladding because the DPA in the fuel cladding of SFRs is an important quantity "beyond" the concept of atomic displacements. At least, it is important to quantitatively compare the current "DPA level" used in SFRs and the "real" number of DPA. This subsection studies the FPs-induced damage in the fuel cladding of FRs. The investigated material is Fe-14Cr Oxide Dispersion-Strengthened (ODS) alloy, which is developed by CEA [21]

5.4.1 Methodology

This subsection presents the methods and the hypotheses for computing the number of atomic displacements in the fuel cladding induced by the irradiation of FPs. The methods proposed in this subsection and the corresponding numerical results given in Sections 5.4.2.1 and 5.4.2.2 are general for any type of nuclear reactor with UO_2 fuel and Fe-14Cr cladding. The numerical results shown in Section 5.4.2.3 are mainly for the ASTRID inner core but the proposed methods are not restricted for FR applications.

5.4.1.1 Description of the model

Figure 5-10 shows the cross-section view of a fuel rod. The dotted curve in the fuel pellet illustrates the outermost position where FPs can reach the cladding inner surface, whereas the dotted curve in the fuel cladding points out the deepest position where FPs

can propagate. The right figure in Figure 5-10 is the zoom of the region where the FPs have contributions to atomic displacements. FPs produced within the dotted curve-enclosed region in the fuel have no contribution to the atomic displacements for the cladding. The boundary of this region depends on FPs and is determined by SRIM-2013 using 30 000 ions QC. The QC option is chosen because it is much faster than the FC simulation and we focus mainly on the spatial migration range of ions.

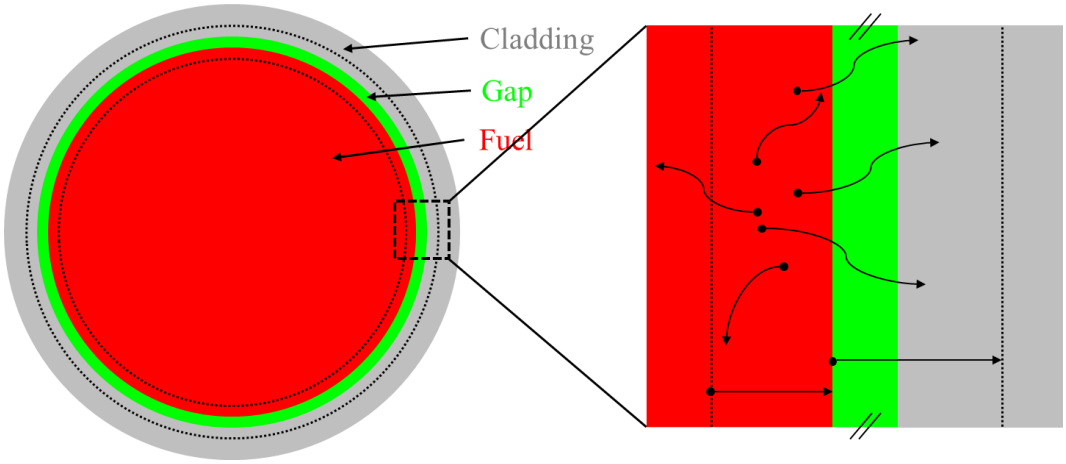

Figure 5-10. Schematic of FPs transport near the periphery of the fuel pellet. The dotted curve in the fuel pellet illustrates the outermost position where FPs can reach the inner surface of cladding, whereas the dotted curve in the fuel cladding points out the deepest position where FPs can propagate.

Since the gap is filled with gas, it is treated as void in the present work. Therefore, for ion transport simulations, it is equivalent to the case that the fuel pellet is directly enclosed by the fuel cladding. Because FPs have limited depth of penetration in the fuel cladding (illustrated by the dotted curve in Figure 5-10), the FPs-induced atomic displacements are only limited in the accessible region. Since both the range of ions and the number of atomic displacements should be determined, the present work uses 3000 ions full cascade simulations to determine the distribution of atomic displacements in the cladding.

In general, a nuclear fission reaction produces two FPs and ν (~ 2.4 for ^{235}U) neutrons. The fission reaction of a heavy nucleus X, e.g., ^{235}U and ^{239}Pu, can be expressed by:

$$\mathrm{n} + \mathrm{X} \rightarrow \mathrm{FP}_h + \mathrm{FP}_l + \nu\mathrm{n} \qquad (5\text{-}14)$$

where the subscript h and l respectively represent the heavy and the light FPs. Different to most neutron-induced reactions, there are hundreds of FPs rather than a few determined products of other reactions. Therefore, the FPs-induced damage rate should be calculated by:

$$v_{total} = \sum_i Y_i \int_r \int_\Omega \int_{E_{k,i}} v_{FP_i}(E_{k,i}, \Omega, r)\, dE_{k,i} d\Omega dr \qquad (5\text{-}15)$$

where $E_{k,i}$, Ω, r, and Y_i respectively represent the kinetic energy, emitted angle, emitted position, and fission yield of each specific FP FP_i.

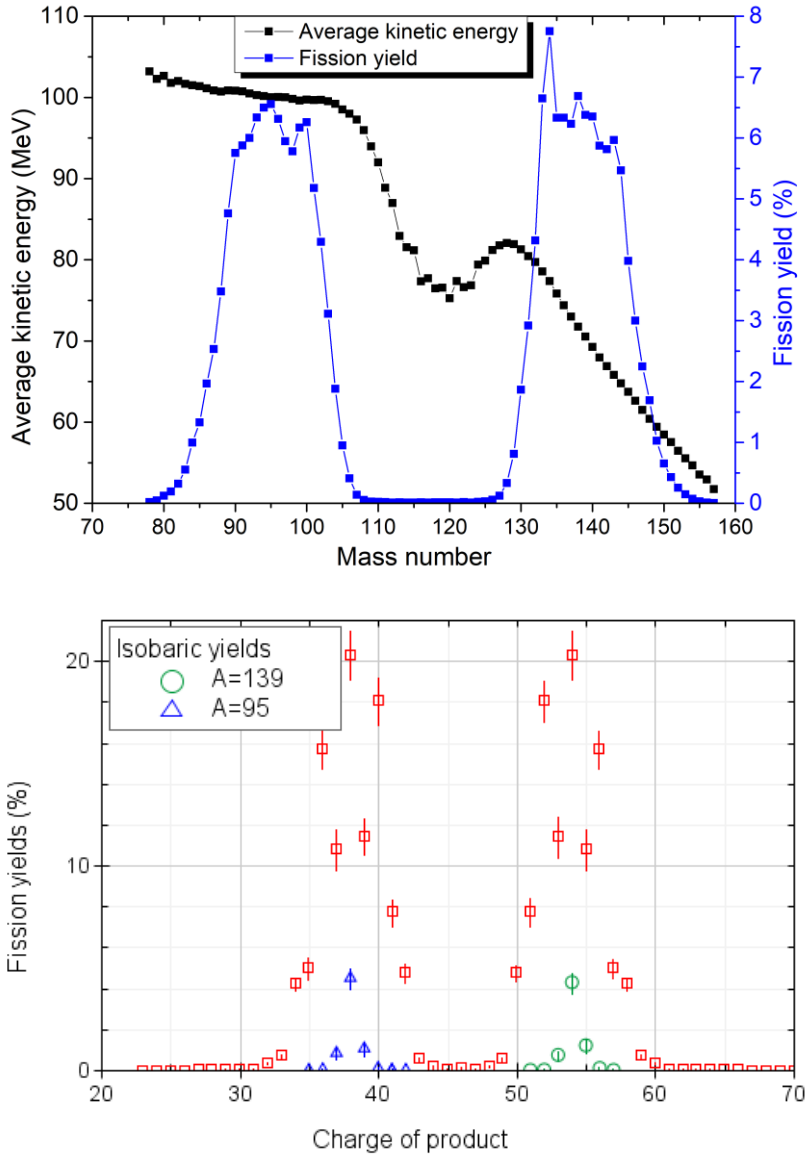

Figure 5-11. JEFF-3.3 fission yields on atomic mass and the FIFRELIN average kinematic energy of FPs (upper) and the JEFF-3.3 charge yields (lower). The red squares, blue triangles, and green circles in the lower figure represent the total charge yields, the charge yields for A = 95 and 139, respectively.

The main fissionable nuclei in thermal reactors and FRs are ^{235}U and ^{239}Pu, respectively. Because the relative fission yields (on atomic mass, charge, and energy) of ^{235}U and ^{239}Pu are not so different and the present work provides an approximate estimate of FPs-induced damage in the cladding, all fission reactions are approximately treated as the fission of ^{235}U here. In addition, the nuclear fuel is assumed to be a pure

UO_2 when simulating the penetration and slowing down of FPs in the fuel for calculating the FPs-induced DPA rates in the fuel cladding. The simulation results are thus useful for both FRs and thermal reactors with Fe-14Cr cladding.

Figure 5-11 shows the fission yields for ^{235}U of JEFF-3.3 [89]. The average kinetic energies of FPs computed with FIFRELIN [151] are shown together with fission mass yields in Figure 5-11. The largest fission yields correspond to A = 95 and A = 139 for light and heavy FPs, respectively. A = 139 is chosen for heavy FP rather than the peak value A = 134 because the former is more representative of heavy FP (i.e. second hump of fission yield in Figure 5-11). As shown in the lower subplot of Figure 5-11, the most probable atomic numbers for the light and the heavy FPs are respectively Z = 38 (Sr) and Z = 54 (Xe). For the sake of simplification, the present work supposes that the FPs are 100% ^{95}Sr and ^{139}Xe, the most probable light and heavy FPs. The corresponding mean kinetic energies are respectively 100 MeV and 70 MeV. It is noteworthy that even if ^{95}Sr and ^{139}Xe are beta decay unstable nuclei, the corresponding 23.9 s and 39.7 s half-lives are relatively large when compared with atomic displacement cascade (about several tens picoseconds [99]).

5.4.1.2 Estimate of fission products-induced atomic displacements in the cladding

Table 5-1 gives the chemical compositions of Fe-14Cr ODS alloy developed by CEA [21]. Since the FPs-induced irradiation damage cannot be simply calculated as neutron-induced damage, SRIM-2013 simulation is used in the present work. To accelerate the convergence of Monte Carlo simulations, only Fe, Cr, and W in Fe-14Cr are considered for SRIM calculations. The threshold displacement energies used in the present work are given in Table 5-2. Because the FPs have quite limited ranges in the fuel and cladding, their contributions to atomic displacements in the cladding depend on their initial positions and angular distributions. As the two cases of incident ^{139}Xe shown in Figure 5-12, different initial positions lead to different ranges and different numbers of atomic displacements in the cladding.

Table 5-1. Chemical compositions (in wt%) of Fe-14Cr ODS alloy [21].

Cr	W	Mn	Ni	Si	Ti	Y_2O_3
14	1	0.3	0.15	0.3	0.3	0.3

Table 5-2. Threshold atomic displacement energy E_d.

Element	U	O	Fe	Cr	W
E_d (eV)	40	20	40	40	90
Ref.	[94]	[94]	[70, 84]	[84]	[84, 90]

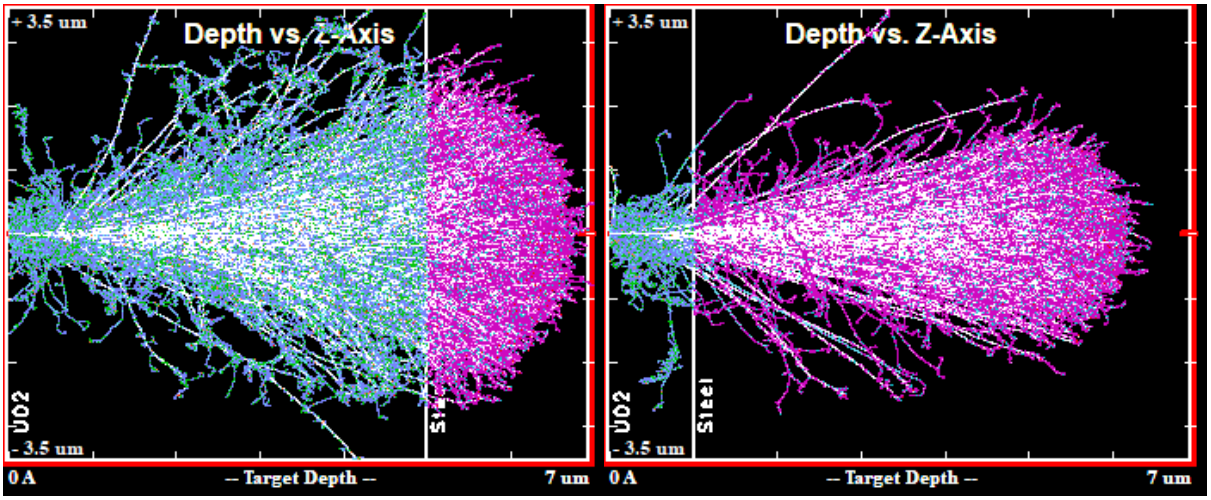

Figure 5-12. SRIM-2013 full cascade simulation of perpendicularly injected 70 MeV ^{139}Xe into 5 μm (left) and 1 μm (right) UO_2 and subsequent Fe-14Cr. Green, cyan, purple, blue, and pink points respectively stand for the displaced U, O, Fe, Cr, and W atoms.

Figure 5-13 illustrates a FP produced at the depth of d_{FP} in the fuel and emitted with an angle θ towards the fuel cladding. Because a SRIM-2013 full cascade simulation with 3000 ions takes about 10 hours for 100 MeV ^{95}Sr and 15 hours for 70 MeV ^{139}Xe in an i5-7200U CPU, the computation burden is too heavy to simulate both the position-dependence and angular distributions. In order to avoid too many simulations to estimate the role of FPs on the irradiation damage in cladding, the present work assumes that:

(i) All light and heavy FPs are ^{95}Sr and ^{139}Xe, respectively.
(ii) Kinetic energies of FPs are 100 MeV and 70 MeV for ^{95}Sr and ^{139}Xe, respectively.
(iii) The gap between the fuel and cladding is void.
(iv) FPs are isotropically emitted in the fuel.
(v) For FPs emitted with the angle towards the cladding $\theta \in [\theta_1,\ \theta_2]$, where θ_1 and θ_2 are angles simulated by SRIM, the induced atomic displacements are supposed to be the same as $\theta = \theta_1$ (or $\theta = \theta_2$ for estimating the lower limit).
(vi) For atomic displacement in the cladding induced by FPs produced at depth $d_{\mathrm{FP}} \in [d_1,\ d_2]$, where d_1 and d_2 are depths simulated by SRIM, we directly take the distribution obtained at the depth $d = d_1$ (or $d = d_2$ for estimating the lower limit).

Assumptions (i) and (ii) should be a good approximation for our studies. It is noted that the default SRIM effective charge of ion Z_{eff} (Z_{eff}^2 is proportional to the ratio of the stopping power of the ion to that of proton [152]) is used, whereas the average charge of FP is 20+. (iii) is reasonable because of the low atomic concentration in the gap. (iv) is true in FR core where the local neutron flux is quasi-homogeneous and

isotropic. (v) overestimates (underestimates, resp.) the atomic displacement because FPs emitted with angle $\theta \in [\theta_1,\ \theta_2]$ generally induce less (more, resp.) vacancies than that with $\theta = \theta_1$ ($\theta = \theta_2$, resp.). (vi) also overestimates (underestimates, resp.) the atomic displacement because the irradiation damage reduces with the thickness of fuel where the FPs should pass through. The histogram distribution assumption is used for (v) and (vi) to conservatively estimate the real vacancies induced by FPs. Consequently, the six assumptions can give a reasonable upper limit (or lower limit) for the number of atomic displacements in the fuel cladding.

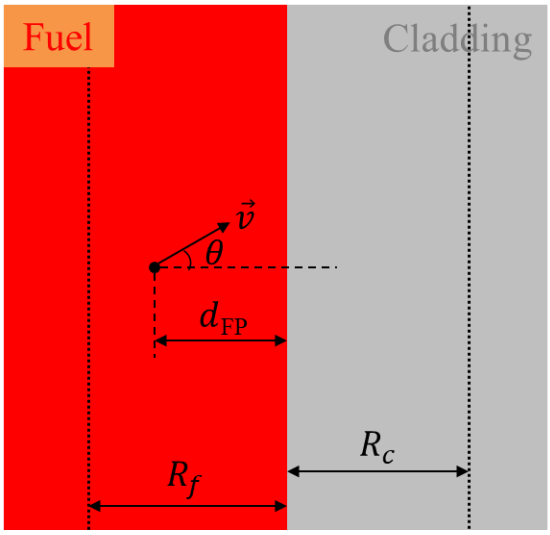

Figure 5-13. Schematic of a FP produced in the depth of d_{FP} in the fuel and emitted with an angle θ towards the fuel cladding.

The isotropic angular distribution (i.e. assumption (iv)) of produced FPs implies:

$$d\Omega = \sin\theta\, d\theta d\varphi = -2\pi d\mu \tag{5-16}$$

where Ω is the solid angle, θ is the colatitude angle, φ is the longitude, and $\mu = \cos\theta$. Consequently, the isotropic angular distribution leads to equiprobable distribution on μ from -1 to 1. Moreover, the probability density for the variable μ ($p(\mu) \equiv p$) satisfies:

$$\int_{-1}^{1} p(\mu) d\mu = 2p = 1 \tag{5-17}$$

Therefore, the probability density for the distribution of μ is $p(\mu) = 1/2$.

For a specific FP produced at depth $d_{\mathrm{FP}} \in [d_j,\ d_{j+1}]$, the angle-integrated number of atomic vacancies is computed by:

$$v(d_{\mathrm{FP}}) = \int_{-1}^{1} v(d_{\mathrm{FP}}, \mu)\, p(\mu) d\mu = \frac{1}{2}\int_{-1}^{1} v(d_{\mathrm{FP}}, \mu)\, d\mu \tag{5-18}$$

Therefore, assumptions (v) and (vi) imply that the upper limit of the FPs-induced atomic vacancies in the fuel cladding is:

$$\bar{v}(d_{\mathrm{FP}}) = \frac{1}{2}\sum_{i>0}\int_{\mu_{i-1}}^{\mu_i} d\mu\, v(d_j, \mu_i) = \frac{1}{2}\sum_{i>0}(\mu_i - \mu_{i-1}) v(d_j, \mu_i) \tag{5-19}$$

where $(\mu_1, \mu_2, \mu_3, \cdots)$ are cosines of the simulated angles and $\mu_0 \equiv \mu_c$. $\mu_c = \cos\theta_c$ is the cosine of the maximum angle that the FP can leave the fuel. As the schematic illustrated in Figure 5-14, the maximum angle θ_c is determined by:

$$\mu_c \equiv \cos\theta_c = d_{\mathrm{FP}}/R_f \tag{5-20}$$

where R_f is the maximum range of the FP in fuel.

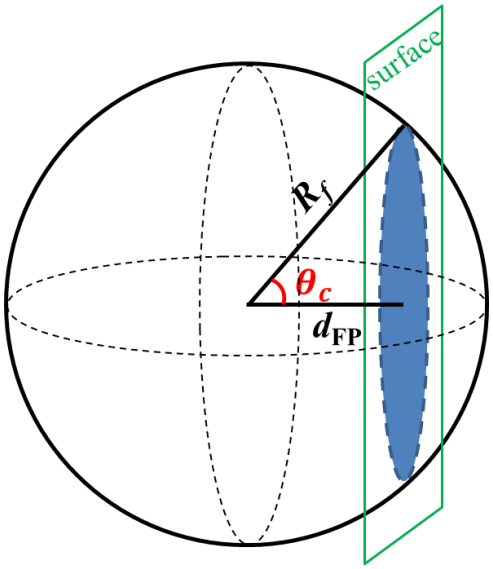

Figure 5-14. Possible angular directions that a FP produced at a distance d_{FP} to the surface of the fuel pellet can leave the fuel. The sphere determines the boundary of the migration of a FP. The plan (cylindric surface of which the radius is much large than R_f) is the surface of the fuel pellet.

On the other hand, the expectation of the vacancies (i.e. volume-averaged vacancies) in the fuel cladding induced by a FP is calculated by:

$$v \equiv \frac{\int v(d_{\mathrm{FP}})dV}{\int dV} = \frac{1}{\pi R^2}\int_0^R v(d_{\mathrm{FP}})2\pi(R - d_{\mathrm{FP}})dd_{\mathrm{FP}} \tag{5-21}$$

where R is the radius of the fuel pellet. Supposing the ranges of FPs are largely smaller than the radius of fuel pellet (i.e. $R_f \ll R$), one can deduce that:

$$v = \frac{2}{R}\int_0^{R_f} v(d_{\mathrm{FP}})dd_{\mathrm{FP}} \tag{5-22}$$

Consequently, assumption (vi) implies that the vacancies in the fuel cladding are overestimated by:

$$\bar{v} = \frac{2}{R}\sum_j (d_{j+1} - d_j)\bar{v}(d_j) \tag{5-23}$$

where $d_{jmax} \equiv R_f$. Inserting Eq. (5-19) into Eq. (5-23), one can deduce that the upper limit of the vacancies in the fuel cladding induced by a specific FP is calculated by:

$$\bar{v} = \frac{1}{R}\sum_j (d_{j+1} - d_j)\sum_{i>0}(\mu_i - \mu_{i-1})v(d_j, \mu_i) \tag{5-24}$$

Using the same reasoning, the lower limit of the vacancies produced by FPs can be determined by:

$$\underline{\nu} = \frac{1}{R}\sum_j \left(d_{j+1} - d_j\right) \sum_{i>0} (\mu_i - \mu_{i-1}) \nu\left(d_{j+1}, \mu_{i-1}\right) \quad (5\text{-}25)$$

Since the FPs-induced damage in the cladding for $\theta = \theta_c$ is quasi-null, it is neglected in the present work to reduce the cases of simulations. Moreover, this additional assumption leads to a smaller value of the lower limit $\underline{\nu}$. The number of atomic displacements induced by FPs is thus included in $[\underline{\nu}, \bar{\nu}]$. For simplification, the quantities associated with the calculations of $\bar{\nu}$ ($\underline{\nu}$ resp.) are called maximum (minimum resp.) estimate and noted by the same symbol $\bar{\nu}$ ($\underline{\nu}$ resp.).

It is noteworthy that the inner radius of the cladding R_{ic} is a little larger than the fuel diameter R. On the other hand, $R_f \ll R$ and $R_c \ll R_{ic}$ for FPs (can be verified in Section 5.4.2.1). Therefore, if one uses the simulation that the fuel is directly enclosed by the cladding, the atomic displacement should be corrected by:

$$\nu\left(d_j, \mu_i\right) = \frac{R}{R_{ic}} \nu_{\text{simu}}\left(d_j, \mu_i\right) \quad (5\text{-}26)$$

One has a numerical approach $R_{ic}/R = 1.03$ deduced from various SFRs. This correction is used in the present work.

In the present work, the SRIM-2013 full cascade simulations are performed every 1 μm for the depth d_{FP} from 0 to d_{jmax-1}. Each 1/6 of μ from 1 to μ_c are simulated for the angular distributions. One can do simulations in finer meshes so that the computed lower and upper limits are closer to the real value. It is always the choice between accuracy and computation burden. The proposed criterion is whether the difference between $\bar{\nu}$ and $\underline{\nu}$ is smaller than the acceptable accuracy.

5.4.2 Numerical results

5.4.2.1 Ranges of fission products in fuel and cladding

In order to intuitively show the ion distributions in materials, Figure 5-15 illustrates the 3D ion distribution of 100 MeV ^{95}Sr into UO_2. Again, we remark that the effective charge in SRIM is used, whereas the average charge of FPs is 20+. The averaged migration range is 8.43 μm and the maximum depth (i.e. R_f) is 9.90 μm. Consequently, light FP produced in UO_2 fuel deeper than 9.90 μm does not influence the damage calculation of the fuel cladding. The ranges and maximum depths of 100 MeV ^{95}Sr and 70 MeV ^{139}Xe in both fuel and cladding are summarized in Table 5-3. For the sake of comparison and verification, Table 5-3 also gives the data obtained with 50 000 ions full cascade simulations with Iradina code [101]. One can find that SRIM-2013 and Iradina give similar data on the ranges and the maximum depths of penetration (R_f and R_c).

According to the values of R_f summarized in Table 5-3, the initial positions for the simulations of 100 MeV ^{95}Sr and 70 MeV ^{139}Xe are restrained in the regions of which the distances to the surface of fuel are smaller than 9.9 μm and 7.8 μm, respectively. In addition, these data verify the assumptions that $R_f \ll R$ and $R_c \ll R_{ic}$ given in Section 5.4.1.

Table 5-3. SRIM-2013 simulation of ^{95}Sr and ^{139}Xe maximum depths into UO_2 fuel and Fe-14Cr cladding.

FP	Energy	Fuel (QC)		Cladding (FC)	
		Range (μm)	R_f (μm)	Range (μm)	R_c (μm)
^{95}Sr	100 MeV	8.43 (8.31)[a]	9.90 (9.96)	7.17 (7.06)	7.95 (7.85)
^{139}Xe	70 MeV	6.07 (5.78)	7.74 (7.76)	5.30 (5.26)	6.35 (6.25)

[a] Values in parenthesis are from Iradina 50 000 ions full cascade simulations

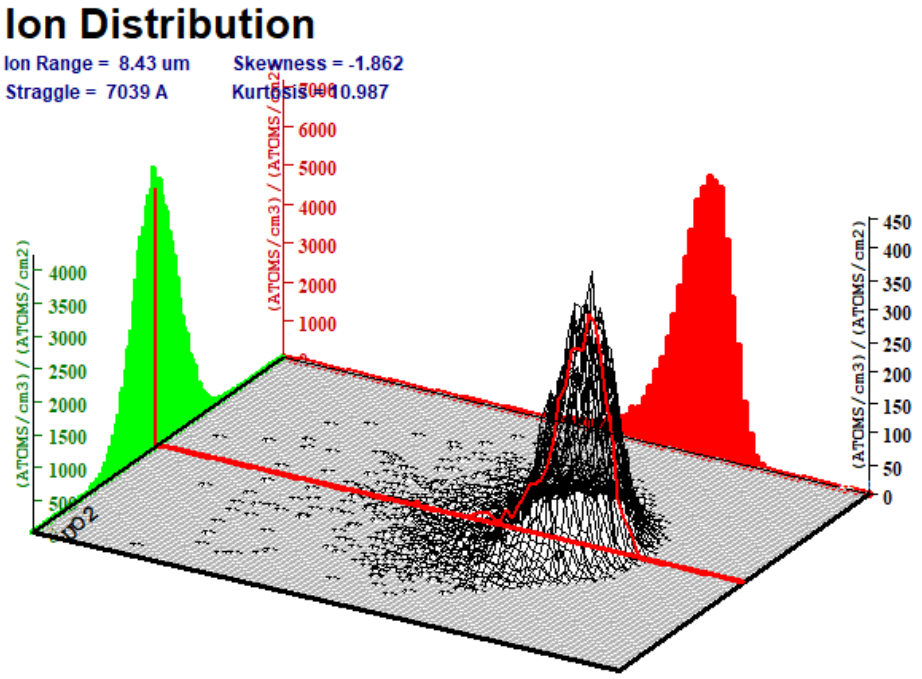

Figure 5-15. 3D ion distribution of 100 MeV ^{95}Sr into UO_2 (SRIM-2013 QC).

5.4.2.2 Atomic displacements induced by fission products

Figure 5-16 shows the distributions of vacancies in Fe-14Cr with SRIM-2013 full cascade simulations for 70 MeV ^{139}Xe (upper) and 100 MeV ^{95}Sr (lower) from different depths in UO_2 fuel with emitted angle $\theta = 0$. It is observed that the peak values of the atomic displacements are not so sensitive to the initial position of FPs for d_{FP} smaller than the range. In the case where d_{FP} is larger than the range, the peak value quickly decreases with the depth in the fuel due to the decrease in the total number of ions that

can reach the cladding. Consequently, the consideration of FPs only with d_{FP} smaller than the range could also be a good approximation.

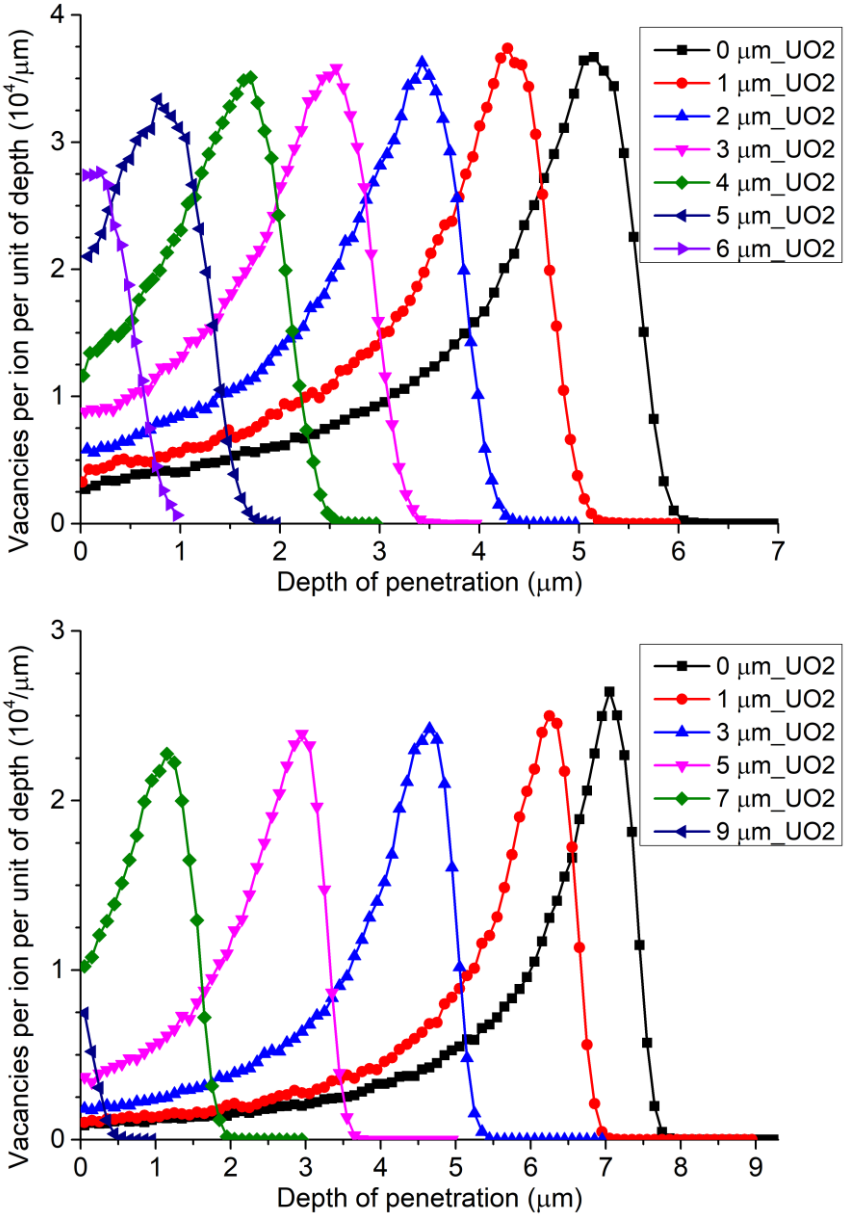

Figure 5-16. Distribution of vacancies in Fe-14Cr with SRIM full cascade simulations for 70 MeV ^{139}Xe (upper) and 100 MeV ^{95}Sr (lower) from different deep UO_2 fuel with $\theta = 0$.

Figure 5-17 illustrates an example of the angular dependence of the atomic displacements in the cladding induced by FPs. Figure 5-17 shows also the averages for the upper limit $\bar{v}$ and lower limit $\underline{v}$, noted by Max. and Min., respectively, for $d_{\mathrm{FP}} = 0$ and $d_{\mathrm{FP}} = 3$ μm. From Figure 5-17, one can find the 1/6 division of μ can give a reasonable angle-averaged value. The only problem shown Figure 5-17(a) is that the atomic displacements at depth smaller than the position of the peak for $\mu = 1/6$ (which is about 1 μm) are unrealistically small when compared with data at depth > 1 μm.

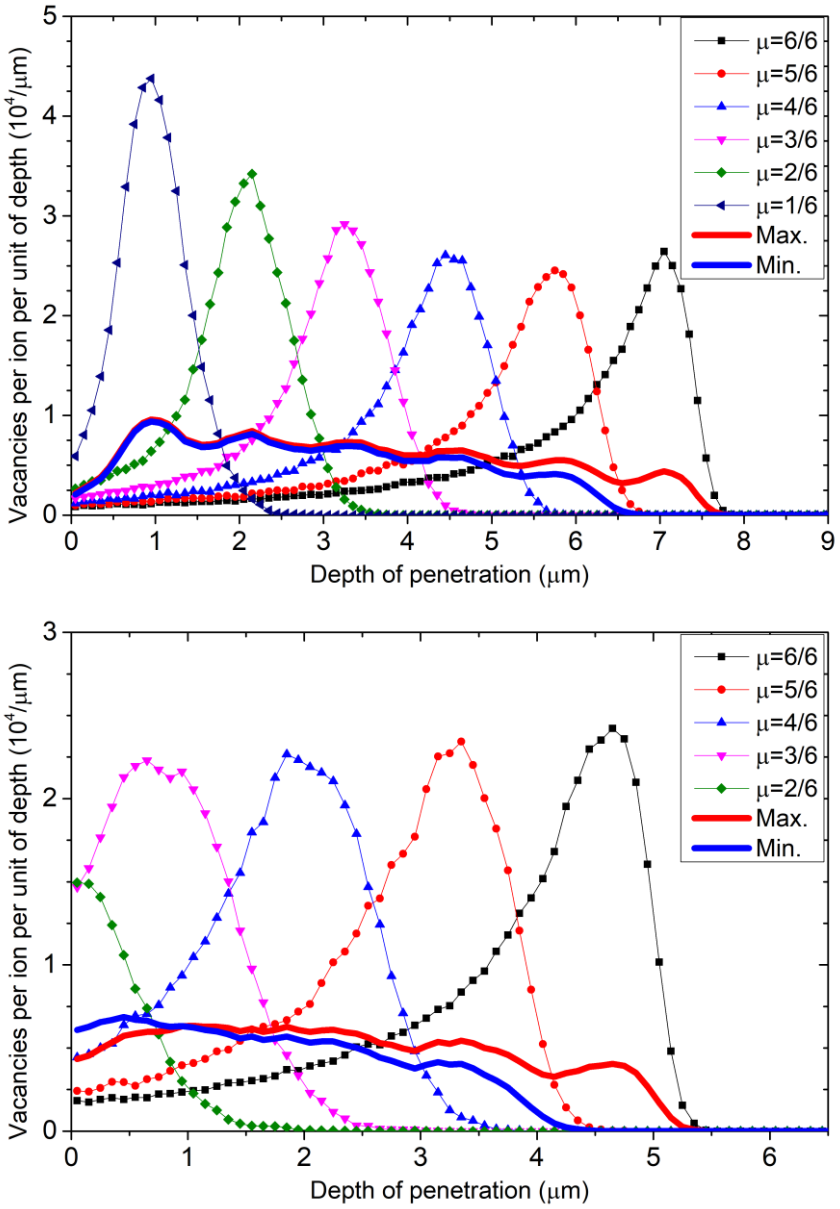

Figure 5-17. Distribution of vacancies in Fe-14Cr induced by 100 MeV ^{95}Sr from the surface of Fe-14Cr (upper) and 3 μm deep UO_2 (lower) with different incident angles and corresponding maximum and minimum averages.

For the upper limit, because the results for $\mu = 1/6$ are used for $\mu \leq 1/6$, the expectation of atomic displacements is smaller than the real case at depth smaller than the peak-position of $\mu = 1/6$. For the lower limit, because the atomic displacements are supposed to be null for $\mu < 1/6$, the same problem is also found as the upper limit. However, this unrealistically small estimate is much less important for $d_{\mathrm{FP}} > 0$ than for $d_{\mathrm{FP}} = 0$ (shown in Figure 5-17(a)) because

(i) $k_s/6 - \mu_c \equiv \min_{k\in\mathbb{N},(k/6-\mu_c)>0}(k/6 - \mu_c) < 1/6$, which implies the probability that the cosine of emission angle included in $[\mu_c, k_s/6]$ (i.e. $k_s/6 - \mu_c$) is

smaller than 1/6 for $d_{\mathrm{FP}} > 0$;

(ii) for a larger emission angle θ, the larger mean free path of ion in the fuel leads to fewer atomic displacements in the cladding.

For the second reason, one can imagine that if μ is very close to μ_c, even though the atomic displacements are quite important near the surface of cladding, its contribution to the expectation or angle-average is quite negligible. It is more obvious if FPs are produced at a deeper position. This reasoning can be verified by Figure 5-17(b), which illustrates the results for 100 MeV ^{95}Sr from 3 μm deep UO_2. Consequently, the approximations using 1/6 division of μ can give a reasonable estimate of FPs-induced atomic displacements in the sense of vacancy attenuation in the cladding.

Since the results shown in Sections 5.4.2.1 and 5.4.2.2 are for FPs emitted from UO_2 into Fe-14Cr cladding without adding any constraint on neutron flux spectrum, it is noteworthy that the corresponding conclusions are the same for Fe-14Cr cladding used in other reactor types.

5.4.2.3 Comparison with neutron-induced damage in cladding

The operating lifetime of fuel assembly in SFRs is mainly determined by the DPA level (~ 200 DPA [18] based on the NRT formula [80]). The current status for determining the lifetime is based on the neutron-induced DPA. On the other hand, the present studies show that the FPs can induce irradiation damage in the cladding from the inner surface up to the first microns. Therefore, it is of interest to compare the neutron-induced DPA rate and the FPs-induced one. In a nuclear reactor, the FPs-induced damage rate per unit of depth R_D in the cladding is computed by:

$$R_D \equiv \frac{V_{fuel} R_{V,fission}}{N_{V,cladding}} \frac{\partial \nu}{\partial V_{cladding}} = \frac{\pi R^2 R_{V,fission}}{2\pi R_{ic} N_{V,cladding}} \frac{\partial \nu}{\partial x} = \frac{R R_{V,fission}}{2 R_{ic} N_{V,cladding}} \frac{R \partial \nu}{\partial x} \quad (5\text{-}27)$$

where ν is the angle-integrated number of atomic displacements obtained by simulations, $R_{V,fission} = \sum_{i \in fuel} \sigma_{f,i} \phi N_{V,i}$ is the volumetric fission reaction rate, and $N_{V,cladding}$ is the atomic concentration of the cladding. $\partial \nu / \partial x$ is the so-called vacancies per ion per unit of depth that can be directly deduced with SRIM calculations. In the present work, $\nu = \bar{\nu}$ and $\nu = \underline{\nu}$ for maximum and minimum estimates, respectively. For SFRs, we remark again that $R_{ic}/R = 1.03$. Figure 5-18 shows the quantity $R\partial\bar{\nu}/\partial x$ for 70 MeV ^{139}Xe and 100 MeV ^{95}Sr. Moreover, Figure 5-18 points out both the maximum estimate $R\partial\bar{\nu}/\partial x$ (noted by Max.) and minimum estimate $R\partial\underline{\nu}/\partial x$ (noted by Min.) for the total FPs-induced damage.

In order to quantitatively compare the neutron-induced DPA rate with FPs-induced damage rate, the present work takes the example of the ASTRID reactor. Using the total

fission rate $R_{V,fission}$ of the ASTRID inner core from ERANOS [153, 154] calculation (with self-shielding correction), one obtains $RR_{V,fission}/2R_{ic}N_{V,cladding} = 6.40 \times 10^{-11}\ \mathrm{s}^{-1} = 2.02 \times 10^{-3}\ \mathrm{year}^{-1}$.

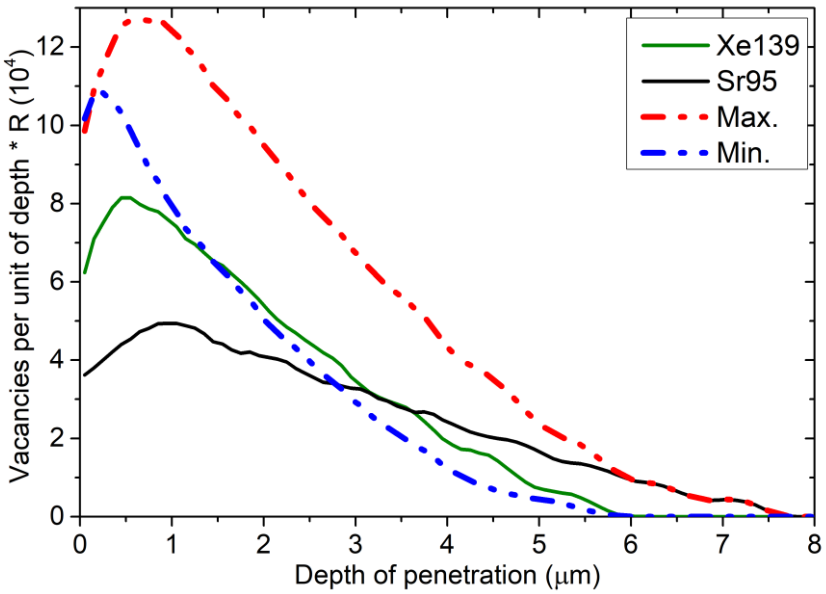

Figure 5-18. Integrated vacancies $R\partial\bar{v}/\partial x$ in Fe-14Cr induced by 70 MeV ^{139}Xe and 100 MeV ^{95}Sr and the corresponding maximum and minimum estimates.

Since the number of vacancies from SRIM full cascade simulations is almost two times that of the NRT formula [106–108], one uses $\hat{R}_D = R_D/2$ to compare with the NRT-based neutron-induced damage rate. The peaks of Max and Min shown in Figure 5-18 lead to $\hat{R}_D = 128$ DPA/year and $\hat{R}_D = 109$ DPA/year, respectively. These values are much larger than the neutron-induced one, which is about 25 DPA/year [116]. It is observed that $\hat{R}_D$ is larger than the neutron-induced damage rate when the depth is smaller than 5.0 μm (3.2 μm, resp.) according to the maximum estimate $\bar{v}$ (minimum estimate $\underline{v}$ resp.). The depths corresponding to 1/10 of the neutron-induced damage rate are 7.4 μm and 5.4 μm, respectively.

Table 5-4 shows the average damage rate from the inner surface to different depths of penetration in Fe-14Cr cladding. The average FPs-induced damage rates in the whole irradiated region, i.e. 0 - 7.9 μm, are about 54 and 30 NRT-DPA/year with the maximum and minimum estimates, respectively. The corresponding averaged value in the first 10 μm are respectively 43 and 23 NRT-DPA/year. One may use the mean value $v = (\underline{v} + \bar{v})/2$ to roughly determine the average FPs-induced damage rate. Consequently, the averaged FPs-induced damage in the first 10 μm (≈ 33 NRT-DPA/year) is slightly larger than the neutron-induced one. The ratio of FPs-induced damage to the neutron-induced one in the whole region or investigated region of Fe-14Cr cladding is

approximately equal to $13.4\ \mu m/t_c$, where $t_c > 7.9\ \mu m$ is the thickness of cladding or the investigated region starting from the inner surface. However, it is noteworthy that only the peak values or the average values shown in Table 5-4 are significant for studying the FPs-induced irradiation damage in the cladding.

Table 5-4. Average FPs-induced damage rates (DPA/year)[a] in different intervals.

Interval[b]	Peak	[0, 5.3]	[0, 7.1]	[0, 6.3]	[0, 7.9]	[0, 10]
Max.	128	77.6	60.4	67.4	54.5	43.0
Min.	109	44.0	33.0	37.1	29.6	23.4

[a] SRIM full cascade simulations-based data divided by 2 for roughly converting to NRT-DPA

[b] Unit is in μm; 5.3, 7.1, 6.3, and 7.9 μm are respectively the ranges of ^{139}Xe, ^{95}Sr and the maximum penetrations of ^{139}Xe, ^{95}Sr in Fe-14Cr.

Because the FPs-induced damage is much more important than the neutron-induced damage in the first few microns cladding facing the fuel pellet, subsequent questions should be discussed. (i) Should we pay more attention to the FPs-induced radiation damage in the innermost few microns of the fuel cladding? (ii) The FPs-induced damage should be taken into account for the determination of the operating lifetime of fuel assemblies in SFRs? The second one could be important for SFRs. At least, it gives a quantitative comparison between the current "DPA level" used in SFRs and the "real" number of DPA.

5.4.3 Summary of fission product-induced radiation damage

This section investigates the FPs-induced atomic displacements in the Fe-14Cr fuel cladding. Four basic assumptions are proposed to simplify the simulations. Except for the treatment of the fuel-cladding gap, three degrees of freedom are reduced using the corresponding assumptions, including the yields of FPs, energy distribution and angular distribution of each FP. In addition to the four basic assumptions, two approximations are proposed to obtain the upper and lower limits of atomic displacements in the cladding so that the cases of simulations can be largely reduced.

SRIM-2013 quick calculations (full cascade simulations, resp.) show that the maximum penetrations of 100 MeV ^{95}Sr (i.e. light FP) and 70 MeV ^{139}Xe (i.e. heavy FP) in UO_2 fuel (Fe-14Cr cladding, resp.) are respectively 9.9 μm and 7.7 μm (7.9 μm and 6.3 μm, resp.). These data are verified with Iradina full cascade simulations. Consequently, the efficient fuel region where FPs can displace atoms in the cladding and the irradiated cladding region by FPs are quite small. Simulations restrained in the efficient regions using 1 μm division of depth in the fuel and 1/6 division of the cosine of emission angle gives reasonable upper and lower limits of the number of FPs-induced atomic displacements in the cladding.

Compared with 25 NRT-DPA/year neutron-induced irradiation damage in the cladding of ASTRID inner core, the FPs-induced maximum damage rate is about 5 times larger. Along with the depth in the cladding, the FPs-induced damage rate is larger than the neutron-induced one at depth smaller than 5.0 μm (3.2 μm, resp.) using the maximum estimate (minimum estimate, resp.) and lower than 1/10 of the neutron-induced DPA deeper than 7.4 μm (5.4 μm, resp.). Therefore, the question of whether the FPs-induced damage should be taken into account in the cladding of SFRs needs to be discussed.

6 Methods for uncertainty propagation

Owing to limited experimental data, theoretical calculation based on several optimized models is the main method to predict the characteristics of a physical quantity. Since no model is perfect, the uncertainty of model calculations should be estimated for determining the confidence interval of theoretical prediction. This kind of uncertainty can be from model defects and poor model parameters.

We showed the model defects of the optical model for calculating the total cross section of ^{56}Fe below 6 MeV: the optical model cannot produce the fluctuations of experimental data (c.f. Figure 2-3 and Refs. [34, 42, 44, 45, 155]). For DPA models, even with the MD-based ARC-DPA model, it cannot predict the performance of several monatomic materials at high PKA energies (e.g., MD data for Au and Pt [99], and W [99, 156]; BCA data for Fe [157]). The model defects show that some improved models should be developed to perform more accurate calculations. The development of new models is a long-term work and is not included in the framework of this Ph.D project.

Assuming the availability of a theoretical model, one can adjust parameters in phenomenological models to get calculated results as close as possible to experimental measurements. At the same time, biases are usually observed between parameters-based calculations and experimental data. These biases are from: discrepancy and dispersion among experimental data, locally optimized model parameters, and model defects. In practice, model defects are not considered if the theoretical calculations and experimental data are globally in good agreement within several σ uncertainties. Then, after the selection of reliable experimental data, one can determine the optimized parameters and the corresponding covariance matrix using measured data (i.e. physical constraints). The covariance matrix is essential to propagate uncertainties of model parameters to subsequent quantities.

This section briefly presents the methods for uncertainty propagation from model parameters. Section 6.1 shows the determination of covariance matrix among model parameters using physical constraints. Section 6.2 summarizes the methods for uncertainty propagation, including the sensitivity-based analytical calculation and the Total Monte Carlo (TMC) sampling technique.

6.1 Covariance between model parameters

The Bayes' theorem implicates that the posterior probability density is proportional to the product of prior probability density and the likelihood:

$$p(\vec{x}|\vec{E},U) = \frac{p(\vec{E}|\vec{x},U)p(\vec{x},U)}{\int p(\vec{E}|\vec{x},U)p(\vec{x},U)d\vec{x}} \tag{6-1}$$

where vector $\vec{x}$ represents the parameters in physical models, $\vec{E}$ denotes the

experimental data, and U refers to the prior information. Under the hypothesis of Gaussian distribution for the probability density of $\vec{x}$ and $\vec{E}$, one obtains:

$$p(\vec{x}, U) = e^{-\frac{1}{2}(\vec{x}-\vec{x}_0)^T M_x^{-1}(\vec{x}-\vec{x}_0)} \tag{6-2}$$

$$p(\vec{E}|\vec{x}, U) = e^{-\frac{1}{2}(\vec{C}-\vec{E})^T M_E^{-1}(\vec{C}-\vec{E})} \tag{6-3}$$

where $\vec{x}_0$ represents the vector containing prior values, $\vec{C}$ and $\vec{E}$ denote the calculated and experimental data, respectively. M_x (M_E resp.) stands for the covariance matrix of $\vec{x}$ ($\vec{E}$ resp.). Using the above Gaussian distribution-based probability densities, one has:

$$p(\vec{x}|\vec{E}, U) \propto e^{-\frac{1}{2}\left[(\vec{x}-\vec{x}_0)^T M_x^{-1}(\vec{x}-\vec{x}_0)+(\vec{C}-\vec{E})^T M_E^{-1}(\vec{C}-\vec{E})\right]} \tag{6-4}$$

The maximization of the posterior probability density is thus equivalent to the minimization of the Generalized Least Square (GLS) cost function χ^2_{GLS}:

$$\chi^2_{GLS} = (\vec{x} - \vec{x}_0)^T M_x^{-1}(\vec{x} - \vec{x}_0) + \left(\vec{C} - \vec{E}\right)^T M_E^{-1}\left(\vec{C} - \vec{E}\right) \tag{6-5}$$

The Gauss-Newton scheme (known as Newton method for one-dimension solution) is used to find the minimum of the GLS cost function by iteration in CONRAD [158, 159]. The criterion of the convergence judgment is the relative variation of χ^2_{GLS} . Posterior $\vec{x}$ and M_x are determined in the fitting procedure by iteration.

All physical parameters and the covariances between different parameters are determined to mimic experimental data of nuclear cross sections and other measured data. The parameters are mainly divided into two sets in CONRAD, physics parameters and nuisance parameters [160]. The formers are directly involved to optimize calculated results, while the latters are not directly used but fundamental for assessing reliable physical models. For example, the nuisance parameters contain systematical uncertainties that avoid unrealistically small uncertainties by fitting parameters according to measured data (these uncertainties are propagated to final uncertainty, called as marginalization [161]). The complete covariance matrix used to propagate uncertainties is thus [160]:

$$\Sigma = \begin{pmatrix} \Sigma_{11} & \Sigma_{12} \\ \Sigma_{21} & \Sigma_{22} \end{pmatrix} \tag{6-6}$$

where

$$\begin{cases} \Sigma_{11} = & M_x + (G_x^T G_x)^{-1} G_x^T G_\theta M_\theta G_\theta^T G_x (G_x^T G_x)^{-1} \\ \Sigma_{12} = & -(G_x^T G_x)^{-1} G_x^T G_\theta M_\theta \\ \Sigma_{21} = & \Sigma_{12}^T \\ \Sigma_{22} = & M_\theta \end{cases} \tag{6-7}$$

where M_x and M_θ are respectively covariance matrices of physics parameters $\vec{x} =$

$(x_1, x_2, \cdots, x_n)^T$ and nuisance parameters $\vec{\theta} = (\theta_1, \theta_2, \cdots, \theta_m)^T$, G_x and G_θ are differential operators. For a quantity $\vec{c} = (c_1, c_2, \cdots, c_k)^T$, the differential operators are computed by:

$$G_x = \begin{pmatrix} \frac{\partial c_1}{\partial x_1} & \cdots & \frac{\partial c_1}{\partial x_n} \\ \vdots & \ddots & \vdots \\ \frac{\partial c_k}{\partial x_1} & \cdots & \frac{\partial c_k}{\partial x_n} \end{pmatrix} \tag{6-8}$$

$$G_\theta = \begin{pmatrix} \frac{\partial c_1}{\partial \theta_1} & \cdots & \frac{\partial c_1}{\partial \theta_m} \\ \vdots & \ddots & \vdots \\ \frac{\partial c_k}{\partial \theta_1} & \cdots & \frac{\partial c_k}{\partial \theta_m} \end{pmatrix} \tag{6-9}$$

Table 6-1 gives the optimized parameters and the corresponding covariance matrix of n+^{56}Fe reaction OMP from CONRAD optimization and marginalization against experimental data of cross sections from EXFOR. Some nuclear cross sections and uncertainties calculated with data given in Table 6-1 are shown in Figure 2-3 and Figure 2-4 in comparison with experimental data.

Table 6-1. OMP parameters and the corresponding uncertainty (1σ) and correlation matrix for n+^{56}Fe reaction [42]*.

Parameter	A_{S0} (MeV)	V_{HF} (MeV)	a_0 (fm)	r (fm)	T(^{56}Fe) (MeV)
Value	15.126	92.627	0.6032	1.224	1.352
Uncertainty	1.966	9.554	0.0551	0.019	0.118
Correlation matrix	1.000	-0.486	-0.851	0.325	0.487
		1.000	0.312	-0.808	0.104
			1.000	-0.307	-0.575
				1.000	-0.414
					1.000

* Details of the OMP parameters:

- $A_S = A_{S0} - 1.8 \times 10^{-2} A$ (MeV) is the depth of the surface imaginary potential;
- V_{HF} is the constant in Hartree-Fock potential, see Eq. (7) in Ref. [37];
- $a = a_0 + 5 \times 10^{-9} A^3$ (fm) is the diffusiveness in Woods-Saxon form;
- $R = rA^{1/3}$ is the radius in Woods-Saxon form;
- T(^{56}Fe) is the "temperature" of ^{56}Fe in the constant temperature model of level density.

6.2 Uncertainty propagation

6.2.1 Analytical method

Using the covariance matrix Σ, one can propagate uncertainties by analytical

calculation using the so-called sandwich formula:

$$\mathrm{Cov} = S\Sigma S^T \tag{6-10}$$

where S is the matrix containing sensitivities:

$$S = \begin{pmatrix} \frac{\partial c_1/c_1}{\partial x_1/x_1} & \cdots & \frac{\partial c_1/c_1}{\partial x_n/x_n} & \frac{\partial c_1/c_1}{\partial \theta_1/\theta_1} & \cdots & \frac{\partial c_1/c_1}{\partial \theta_m/\theta_m} \\ \vdots & \ddots & \vdots & \vdots & \ddots & \vdots \\ \frac{\partial c_k/c_k}{\partial x_1/x_1} & \cdots & \frac{\partial c_k/c_k}{\partial x_n/x_n} & \frac{\partial c_k/c_k}{\partial \theta_1/\theta_1} & \cdots & \frac{\partial c_{k/c_k}}{\partial \theta_m/\theta_m} \end{pmatrix} \tag{6-11}$$

In the case where no nuisance parameter is considered, the covariance matrix is directly obtained by the well-known formula SM_xS^T. It should be noted that if the covariance matrix Σ contains the absolute values of covariances, elements in S matrix are partial derivations, the obtained covariance matrix Cov is absolute; if Σ contains the relative values of covariances, elements in S are sensitivities, the corresponding covariance Cov is also a relative matrix. Figure 6-1 shows an example of correlation matrices among absolute Legendre coefficients for ^{56}Fe neutron elastic scattering with parameters and covariance matrix given in Table 6-1. More results and discussion on the correlations between differential and angle-integrated cross sections can be found in our previous work [155].

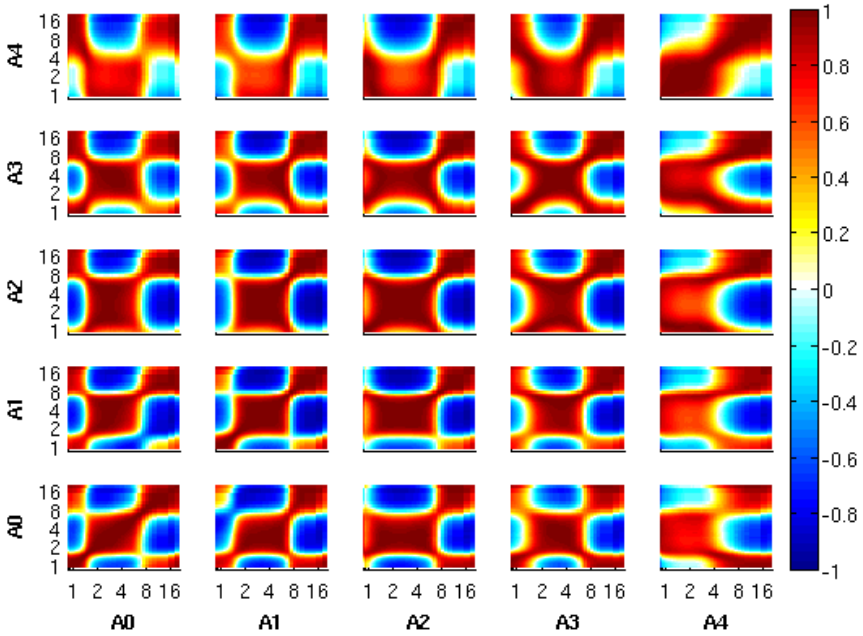

Figure 6-1. Correlation between different orders of Legendre polynomials coefficients for ^{56}Fe neutron elastic scattering (calculated by CONRAD) [34].

6.2.1.1 Remark on sensitivities to DPA model parameters

For an implicit relation between quantity and parameters, one should calculate the sensitivities by the direct perturbation. For explicit DPA models, analytical expressions

are recommended for accurate calculation and reducing computation time. For PKA energy or damage energy above $2.5E_d$ (i.e. $2E_d/0.8$ in the typical expression), one has:

$$\nu_{NRT} = E_{PKA}/[1 + k_L(A\varepsilon^{1/6} + B\varepsilon^{3/4} + C\varepsilon)]/2.5E_d \tag{6-12}$$

It is noted that the "parameters" *A*, *B*, and *C* in NRT model are not exactly physical parameters. The partial derivations of ν_{NRT} to model parameters are analytically determined as:

$$\begin{pmatrix} \partial\nu_{NRT}/\partial A \\ \partial\nu_{NRT}/\partial B \\ \partial\nu_{NRT}/\partial C \\ \partial\nu_{NRT}/\partial E_d \end{pmatrix} = \begin{pmatrix} -2.5E_d k_L (E_{PKA}/E_L)^{1/6} \nu_{NRT}^2/E_{PKA} \\ -2.5E_d k_L (E_{PKA}/E_L)^{3/4} \nu_{NRT}^2/E_{PKA} \\ -2.5E_d k_L \nu_{NRT}^2/E_L \\ -\nu_{NRT}/E_d \end{pmatrix} \tag{6-13}$$

Similarly, above $2.5E_d$, the ARC-DPA can be formed by:

$$\nu_{ARC} = \nu_{NRT} \times \xi_{ARC} \tag{6-14}$$

where

$$\xi_{ARC} = (1 - c_{ARC}) \times \nu_{NRT}^{b_{ARC}} + c_{ARC} \tag{6-15}$$

The partial derivations are thus:

$$\begin{pmatrix} \partial\nu_{ARC}/\partial A \\ \partial\nu_{ARC}/\partial B \\ \partial\nu_{ARC}/\partial C \\ \partial\nu_{ARC}/\partial E_d \\ \partial\nu_{ARC}/\partial b_{ARC} \\ \partial\nu_{ARC}/\partial c_{ARC} \end{pmatrix} = \begin{pmatrix} -2.5E_d k_L \varepsilon^{1/6} \nu_{NRT}^2/E_{PKA} \times \left[\xi_{ARC} + (1 - c_{ARC}) b_{ARC} \nu_{NRT}^{b_{ARC}}\right] \\ -2.5E_d k_L \varepsilon^{3/4} \nu_{NRT}^2/E_{PKA} \times \left[\xi_{ARC} + (1 - c_{ARC}) b_{ARC} \nu_{NRT}^{b_{ARC}}\right] \\ -2.5E_d k_L \nu_{NRT}^2/E_L \times \left[\xi_{ARC} + (1 - c_{ARC}) b_{ARC} \nu_{NRT}^{b_{ARC}}\right] \\ -\nu_{NRT}/E_d \times \left[\xi_{ARC} + (1 - c_{ARC}) b_{ARC} \nu_{NRT}^{b_{ARC}}\right] \\ (1 - c_{ARC}) ln(\nu_{NRT}) \nu_{NRT}^{b_{ARC}+1} \\ \nu_{NRT} \times \left(1 - \nu_{NRT}^{b_{ARC}}\right) \end{pmatrix} \tag{6-16}$$

where $\varepsilon = E_{PKA}/E_L$ is defined in Lindhard's damage energy (c.f. Section 3.3). The sensitivities for the CB-DPA are:

$$\begin{pmatrix} \partial\nu_{CB}/\partial A \\ \partial\nu_{CB}/\partial B \\ \partial\nu_{CB}/\partial C \\ \partial\nu_{CB}/\partial E_d \end{pmatrix} = \begin{pmatrix} -2.5E_d k_L (E_{PKA}/E_L)^{1/6} \nu_{NRT}^2/E_{PKA} \times \left[\xi_{CB} - \frac{\beta\nu_{NRT}}{(1+\beta\nu_{NRT})^2}\right] \\ -2.5E_d k_L (E_{PKA}/E_L)^{3/4} \nu_{NRT}^2/E_{PKA} \times \left[\xi_{CB} - \frac{\beta\nu_{NRT}}{(1+\beta\nu_{NRT})^2}\right] \\ -2.5E_d k_L \nu_{NRT}^2/E_L \times \left[\xi_{CB} - \frac{\beta\nu_{NRT}}{(1+\beta\nu_{NRT})^2}\right] \\ -\nu_{NRT}/E_d \times \left[\xi_{CB} - \frac{\beta\nu_{NRT}}{(1+\beta\nu_{NRT})^2}\right] \end{pmatrix} \tag{6-17}$$

This kind of analytical partial derivations can be determined for any implicit DPA model, such as Sigmund's formula [162] and our recent phenomenological proposition [106]. These analytical expressions are implemented in CONRAD for simplifying calculations (direct perturbation calculation of sensitivities to DPA models is also

available in CONRAD).

Figure 6-2 illustrates the sensitivities of damage cross section to the parameters of the 7th to 11th resonances (from JEFF-3.1.1) and the "DPA parameters" for n+^{56}Fe elastic scattering [34]. In general, the damage cross sections are sensitive to resonance parameters only close to resonances. For incident energy below 1 keV, the damage cross section is quite sensitive to E_d but is not sensitive to other parameters in the standard NRT model because the damage depends only on E_d for damage energy $E_a < 2.5E_d$. The sensitivity of radiation damage cross section to A is almost 0.2 for neutron energy in [5 keV, 100 keV], while the damage cross section is not sensitive to E_d nor to the other two parameters in the NRT model for incident neutron energy up to 100 keV.

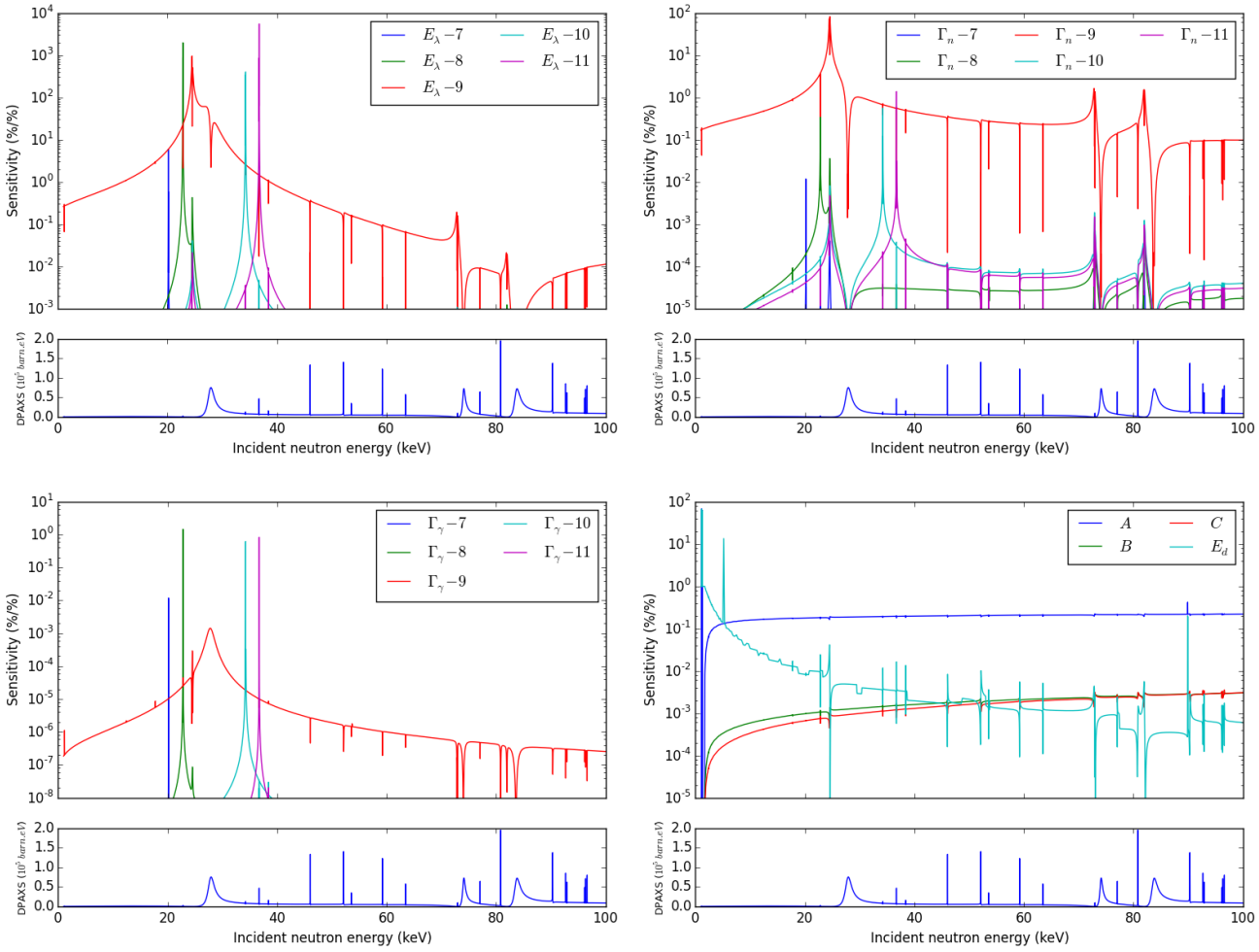

Figure 6-2. Sensitivity of (n+^{56}Fe) damage cross section to resonance parameters and DPA model parameters [34].

6.2.1.2 Uncertainty propagation from nuclear model parameters to k_{eff}

Here we show two examples of uncertainty propagation from n+^{56}Fe nuclear reaction model parameters given in Table 6-1 to the effective multiplication factor k_{eff} in two numerical benchmarks. A thermal reactor benchmark is a homogenized PERLE

experiment [163–165] (reactor core is homogenized). The geometry of the homogenized PERLE benchmark is shown in Figure 6-3 along with the standard PERLE experiment. The use of a homogenized core and a simplified heavy reflector is to reduce the computation burden. A fast reactor benchmark is a homogenized SFR with a SS reflector and shown in Figure 6-4.

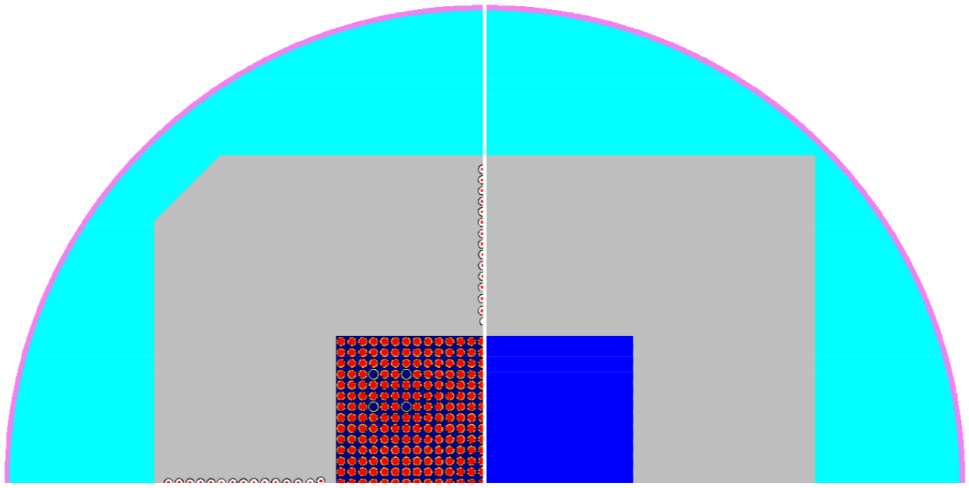

Figure 6-3. ¼ view of the PERLE experiment (left) and the homogenized benchmark (right).

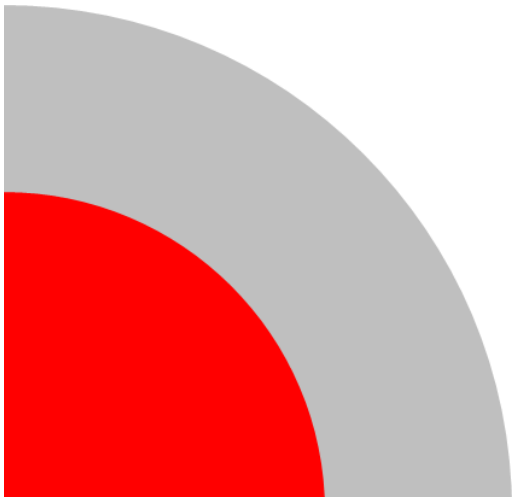

Figure 6-4. ¼ view of the fast benchmark.

In current evaluations, cross Sections (XS) and Angular Distributions (AD) are generally uncorrelated. However, they are correlated by nuclear models (e.g., Figure 6-1). It is thus of interest to propagate the correlation between XS and AD to the uncertainty of such integral quantity k_{eff}, whereas the synergistic effect of XS and AD is rarely investigated in most studies. It is notably that XS or AD is not a simple quantity as a physical parameter, so that the correlation between AD and XS is a general indicator to evaluate the synergy of the two quantities for k_{eff}. The physical correlations between various AD and XS of neutron elastic scattering on ^{56}Fe are as the examples

shown in Figure 6-1.

The neutronic calculations of k_{eff} are performed with the LAST stochastic neutron transport code, which is developed in our laboratory. JEFF-3.1.1 library and the AD and XS of ^{56}Fe above 850 keV calculated with OMP parameters given in Table 6-1 are used. The statistical uncertainties of Monte Carlo simulations are controlled by 2 pcm on k_{eff}. The direct LAST calculation shows k_{eff} = 0.955846 (± 2 pcm). The sensitivities of k_{eff} to parameters are calculated by perturbating $\pm 1\sigma$ uncertainty. The sensitivities of k_{eff} to the OMP parameters by perturbating only the AD, only the XS, and both the AD and XS are summarized in Table 6-2. The corresponding statistical uncertainties (not given in the table) are deduced from $2\sqrt{2}$ pcm uncertainty on k_{eff}.

Table 6-2. Sensitivity of k_{eff} to the OMP parameters (pcm/%) for the two benchmarks.

Benchmark	Perturbation	A_{S0}	V_{HF}	a_0	r	T(^{56}Fe)
Thermal	AD	-0.8614	4.3501	-0.2663	2.9006	-0.0047
	XS	-1.5245	-5.5591	5.8856	-13.5813	-0.3054
	AD+XS	-1.2583	-5.8025	5.8469	-15.6988	-0.1192
Fast	AD	-1.3157	9.1580	0.0502	7.1720	-0.1918
	XS	1.3672	-8.6868	0.0042	22.9990	-11.5669
	AD+XS	-1.2182	2.0931	0.2433	-28.7513	-2.6096

Because the homogenized PERLE benchmark is only a specific case and is far from critical condition, in addition to the absolute uncertainty of k_{eff} (Δk_{eff}), we also calculate the relative uncertainty of k_{eff} ($\Delta k_{eff}/k_{eff}$), and the uncertainty of the reactivity ($\Delta\rho$). The reactivity is defined as:

$$\rho = \frac{k_{eff}-1}{k_{eff}} \tag{6-18}$$

So that the uncertainty of reactivity is deduced by:

$$\Delta\rho = \frac{\Delta k_{eff}}{{k_{eff}}^2} \tag{6-19}$$

The uncertainties concerning k_{eff} from the OMP parameters and the correlation between AD and XS for k_{eff} calculation are given in Table 6-3. The statistical errors are obtained by 50 000 samplings of $2\sqrt{2}$ pcm uncertainty for the deduced difference on k_{eff}, i.e. $dk_{eff,i} = k_{eff}(p_i + \sigma_i) - k_{eff}(p_i - \sigma_i)$.

Table 6-3 shows that the uncertainty from the AD is not negligible when compared with that from the XS. Therefore, the uncertainty of reactivity by propagating only the uncertainties of XS is not well estimated. The correlations between AD and XS of ^{56}Fe for neutron energies above 850 keV are respectively -0.3924±0.0454 in the thermal

benchmark and -1.0243±0.0165 in the fast benchmark. These values show that the consideration of correlations between AD and XS is important for determining the total uncertainties for neutronic calculations. Similarly, a complete correlation matrix between AD and XS is mandatory for uncertainty propagation to DPA rate. It is the reason why the n+^{56}Fe model calculation is used in the following uncertainty propagation for DPA rate.

Table 6-3. Uncertainty (in pcm) concerning k_{eff} from the OMP parameters and the correlation between AD and XS deduced from k_{eff}.

Benchmark	Perturbation	Δk_{eff}	$\Delta k_{eff}/k_{eff}$	$\Delta\rho$
Thermal	AD	46.8±2.0	49.0±2.1	51.2±2.2
	XS	70.8±1.7	74.1±1.8	77.5±1.9
	AD+XS	67.9±1.7	71.0±1.7	74.3±1.8
	Correlation		-0.3924±0.0454	
Fast	AD	95.7±2.0	94.1±2.0	92.5±2.0
	XS	172.7±1.9	169.9±1.9	167.1±1.9
	AD+XS	71.7±2.2	70.5±2.2	69.3±2.2
	Correlation		-1.0243±0.0165 [a]	

[a] The correlation is slightly smaller than -1. This may be due to the numerical calculations and/or the change of neutron spectrum between different simulations.

6.2.2 Total Monte Carlo technique

The TMC technique is widely used to estimate propagated uncertainties via numerous stochastic samplings on model parameters. For a variable x follows the normal distribution $\mathcal{N}(\mu,\sigma^2)$ (noted by $x \hookrightarrow \mathcal{N}(\mu,\sigma^2)$), the expectation of a subsequent physical quantity $f(x)$ (noted by $E(f)$) and the corresponding variance (denoted as $\sigma(f)$) are determined by:

$$E(f) = \frac{1}{N}\sum_{i=1}^{N} f(x_i) \tag{6-20}$$

$$\sigma(f) = \sqrt{\frac{1}{N-1}\sum_{i=1}^{N}[f(x_i) - E(f)]^2} \tag{6-21}$$

where $(x_i)_{i=1:N}$ are random values of N samplings from $\mathcal{N}(\mu,\sigma^2)$. By definition, the covariance between f and another arbitrary quantity g is determined by:

$$\mathrm{Cov}(f,g) = \frac{1}{N}\sum_{i=1}^{N}\big(f(x_i) - E(f)\big)(g(x_i) - E(g)) \tag{6-22}$$

where $E(g)$ is the expectation of g computed with N samplings.

For a multivariable system, one can repeat the above sampling for each variable (so-called as the one-step-at-a-time (OAT) method) if there is no correlation between

different variables. In general, different variables are correlated. In this case, we should calculate a lower triangular matrix L for the covariance matrix M of the parameters using Cholesky decomposition:

$$M = LL^T \tag{6-23}$$

For a n-variable vector $\vec{x} = (x_1, x_2, \cdots, x_n)^T$ with expectation value $\vec{\mu} = (\mu_1, \mu_2, \cdots, \mu_n)^T$ and standard deviation $\vec{\sigma} = (\sigma_1, \sigma_2, \cdots, \sigma_n)^T$, it can be expressed by:

$$\vec{x} = L\vec{y} \tag{6-24}$$

where

$$\vec{y} = \begin{pmatrix} \mu_1 + \sigma_1 t_1 \\ \mu_2 + \sigma_2 t_2 \\ \vdots \\ \mu_n + \sigma_n t_n \end{pmatrix} \tag{6-25}$$

where $\vec{t} = (t_1, t_2, \cdots, t_n)^T$ are n independent random values from $\mathcal{N}(0,1)$ (i.e., $\forall k \in \{1,2,\cdots,n\}, t_k \hookrightarrow \mathcal{N}(0,1)$).

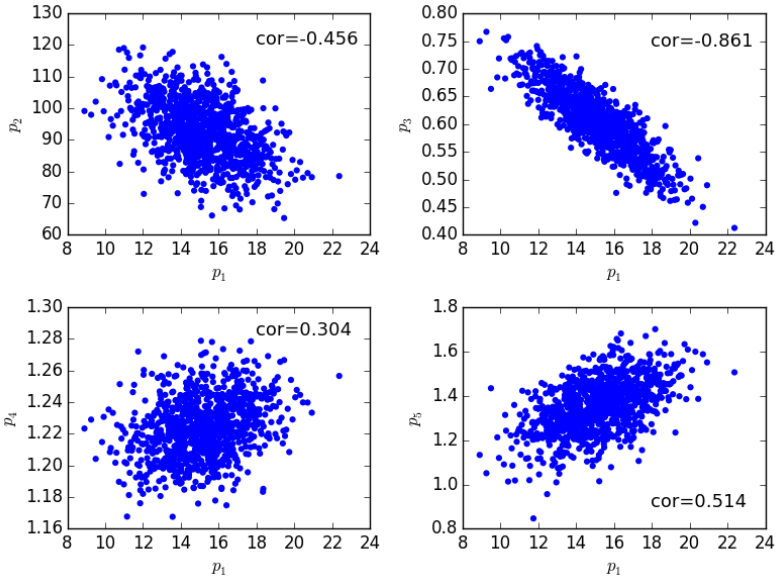

Figure 6-5. 2000 samples LHS of the five OMP parameters for n+^{56}Fe reaction given in Table 6-1: p_i (i = 2,3,4,5) vs. p_1.

Figure 6-5 shows the Latin Hypercube Sampling [166, 167] (LHS)-based 2000 samplings of the five OMP parameters given in Table 6-1. For simplifying, the parameters in Table 6-1 are orderly denoted by p_1 to p_5 in this subsection. Figure 6-6 shows the Gaussian fittings of the first four sampled parameters as shown in Figure 6-5. Table 6-4 shows the sampled parameters along with the corresponding uncertainties and correlations. Compared with normal random sampling, the LHS improves the quality of goodness of sampled variables. However, we remark that the LHS does not

improve the correlation between different variables when compared with simple random sampling.

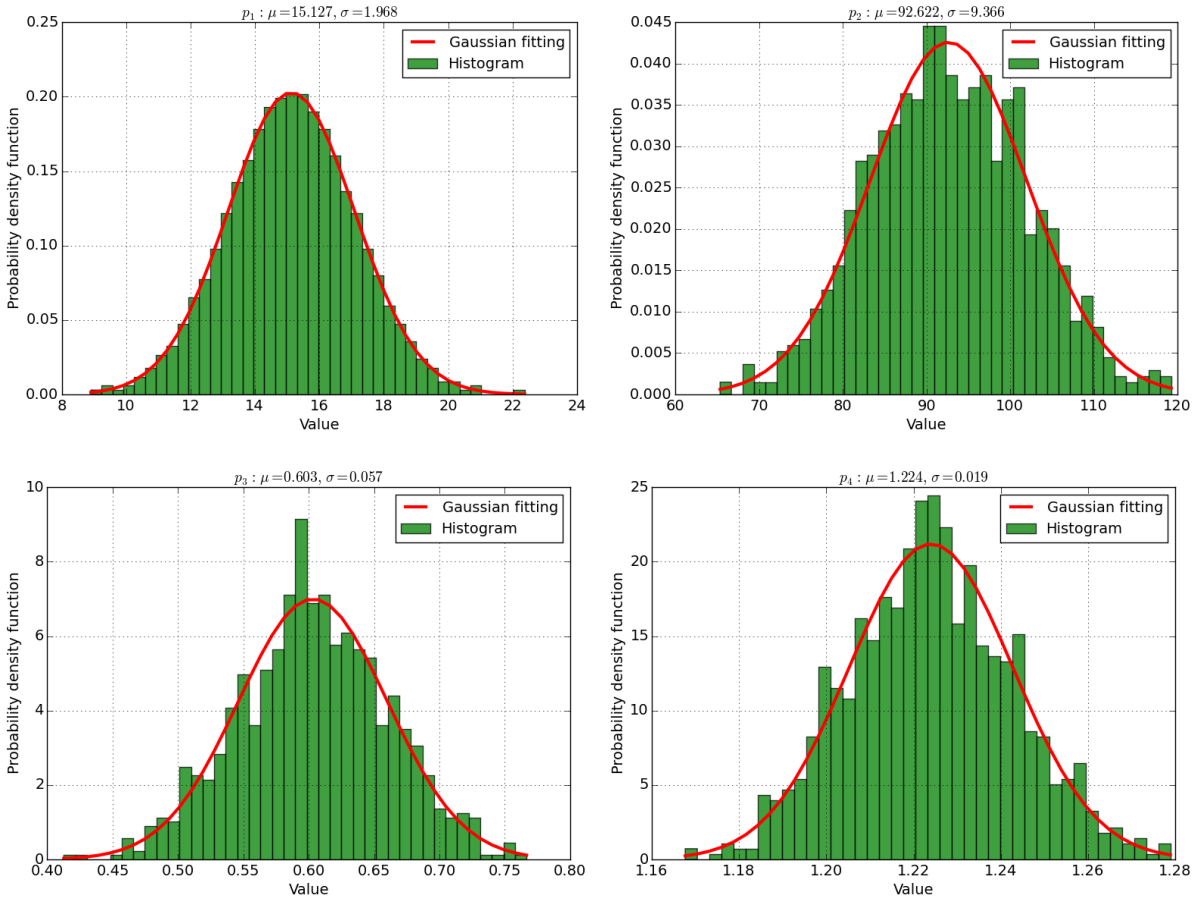

Figure 6-6. 2000 samples LHS of the first four correlated OMP parameters for n+^{56}Fe reaction given in Table 6-1.

Table 6-4. 2000 samples LHS of the OMP parameters given in Table 6-1.

Parameter	A_{S0}	V_{HF}	a_0	r	$T(^{56}Fe)$
Value	15.127	92.622	0.603	1.224	1.352
Uncertainty	1.968	9.366	0.057	0.019	0.119
Correlation matrix	1.000	-0.456	-0.861	0.304	0.514
		1.000	0.286	-0.804	0.128
			1.000	-0.293	-0.581
				1.000	-0.429
					1.000

With N samplings of $\vec{t} = (t_1, t_2, \cdots, t_n)^T \hookrightarrow \left(\mathcal{N}(0,1), \mathcal{N}(0,1), \cdots, \mathcal{N}(0,1)\right)^T$, the expectation and the corresponding uncertainty of the quantity f are determined by:

$$E(f) = \frac{1}{N}\sum_{i=1}^{N} f(\vec{x}_i) \qquad (6\text{-}26)$$

$$\sigma(f) = \sqrt{\frac{1}{N-1}\sum_{i=1}^{N}[f(\vec{x}_i) - E(f)]^2} \tag{6-27}$$

where $\vec{x}_i = L\left(\vec{\mu} + \mathrm{diag}(\sigma_1, \sigma_2, \cdots, \sigma_n)\vec{t}_i\right)$. The covariance between f and an arbitrary quantity g is determined by:

$$\mathrm{Cov}(f, g) = \frac{1}{N}\sum_{i=1}^{N}\left(f(\vec{x}_i) - E(f)\right)(g(\vec{x}_i) - E(g)) \tag{6-28}$$

It is noted that the examples and notations shown in this subsection are all based on the normal distribution, but the methods are general for all other distributions of variables. In nuclear data evaluation, all variables are supposed to follow normal distributions by default. The agreement of uncertainty propagation between the analytical approach and the Monte Carlo method is numerically verified in most studies, such as the resonance parameters shown in Ref. [159] and the neutronic quantities shown in Ref. [168]. This conclusion is based on the validation of the first-order approximation of sensitivities to model parameters in the analytical approach and the well-reproduced correlations among parameters stochastic method (e.g., Table 6-4 vs Table 6-1).

7 Uncertainty assessment of damage rate in a PWR vessel

In this section, an example of uncertainty assessment of DPA rate in the RPV of a simplified PWR mock-up is showed and discussed. The uncertainty of calculated DPA rate is from: nuclear data, DPA model, and neutronic simulations. All aforementioned model defects are not detailedly treated in this section. Nowadays, modern neutronic codes allow very accurate calculations. The small numerical bias (and the controllable statistical uncertainty for stochastic methods) from neutronic simulations is thus not specially investigated here.

The total uncertainty propagated from nuclear data includes the nuclear data-induced uncertainty of the neutron flux spectrum and the uncertainty of damage cross section (i.e. reaction rates and recoil energy distributions of the isotopes in the considered materials). The uncertainty of neutron flux come from all types of nuclear data for all isotopes present in the reactor. Detailed uncertainty assessment of fast neutron flux in a PWR RPV can be found in the Ph.D thesis of Laura Clouvel (CEA/DANS) [169]. The uncertainties of fast neutron flux in a simplified PWR vessel from the Prompt Fission Neutron Spectra (PFNS) are quantified by Léonie Berge (CEA/CAD) [170]. Section 7.1 estimates the uncertainty of DPA rate in a PWR RPV propagated from the neutron flux.

In addition to the neutron flux, uncertainties of nuclear data also contribute to the uncertainty of nuclear reaction rates (nuclear cross section times neutron flux) and the recoil energy distributions. These uncertainties are included in the damage or DPA cross sections. Section 7.2 briefly shows the uncertainty propagated from nuclear data, mainly from nuclear model parameters, to DPA rate. The numerical results are based on n+^{56}Fe reactions.

Section 7.3 focuses on the uncertainty estimates of DPA rate due to the DPA model. Here, the uncertainty of DPA model is actually the uncertainties from DPA model parameters. The relative uncertainty is supposed to be not sensitive to DPA model defects (this assumption is somewhat validated by comparing the results based on the NRT and ARC models). More details are given in Section 7.3. Section 7.4 shows the total uncertainty of DPA rate based on the above partial decompositions. The biases of DPA rate calculation introduced by model defects are briefly discussed in Section 7.5.

7.1 Uncertainty from prompt fission neutron spectrum

This section focuses on the uncertainty propagation from neutron flux to DPA rate. ^{235}U PFNS-induced uncertainty of neutron flux in the RPV of a simplified PWR mock-up was thoroughly studied by Berge using the importance function calculated by Green functions via Tripoli-4® simulations [170]. Because the method for propagating uncertainty from neutron flux to DPA rate is independent on covariance matrix of

neutron flux, the present work directly uses the covariance matrices of neutron flux obtained by Berge during her Ph.D studies for numerical calculations. The geometry of the studied PWR is shown in Figure 7-1. The neutron flux obtained in Tripoli-4® simulations is the average flux from the inner to the outer surface of the RPV in a selected volume (vol. 13 in Figure 7-1). Assuming the exponential law for the attenuation of neutron-induced DPA rate in the RPV, the average DPA rate is equal to [171]:

$$\overline{DPA} = \frac{DPA_0}{t\Sigma^{DPA}}\left(1 - e^{-t\Sigma^{DPA}}\right) \quad (7\text{-}1)$$

where DPA_0 is the DPA rate at the inner surface of RPV, t is the thickness of the RPV, and Σ^{DPA} is an equivalent "macroscopic DPA cross section" [171]. In the case where $e^{-t\Sigma^{DPA}} \ll 1$, the average DPA rate is proportional to the DPA rate at the inner surface.

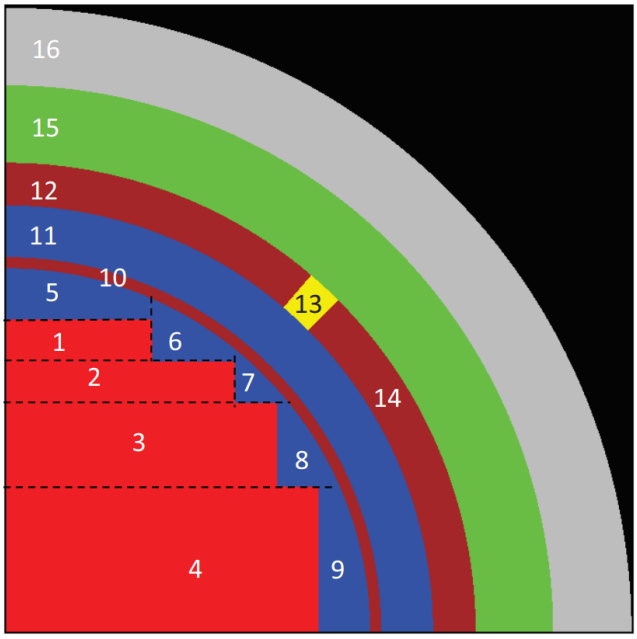

Figure 7-1. ¼ view of a simplified PWR model for performing neutronic calculations [170]. The red part (i.e. vols. 1-4) is the reactor core; a steel envelope (i.e. vol. 10) divides the hot water (i.e. vols. 5-9) and cold water (i.e. vol. 11); the neutron flux in the RPV (i.e. vols. 12-14) is based on the score in vol. 13; the RPV is surrounded by a layer of air (i.e. vol. 15, treated as void in stochastic simulation) and the primary concrete (i.e. vol. 16).

The neutron flux and the corresponding uncertainty propagated from ^{235}U PFNS of ENDF/B-VII.1 library [172] are shown in Figure 7-2 with the normalization factor of the maximum multigroup neutron flux [170]. The relative accumulated DPA rates are shown along with the neutron flux in Figure 7-2. It shows that almost 80% of the DPA is induced by neutron with energies above 1 MeV. The actual percentage is smaller because Ref. [170] considers only neutrons above 0.1 MeV. Nevertheless, this neutron

flux implies $K \equiv \mathrm{DPA}_{\mathrm{NRT}}/\phi_{>0.5\mathrm{MeV}} = 9.7 \times 10^2$ barn, which is close to the value of $K \approx 9.5 \times 10^2$ barn for the RPVs of several reactors shown in Ref. [173].

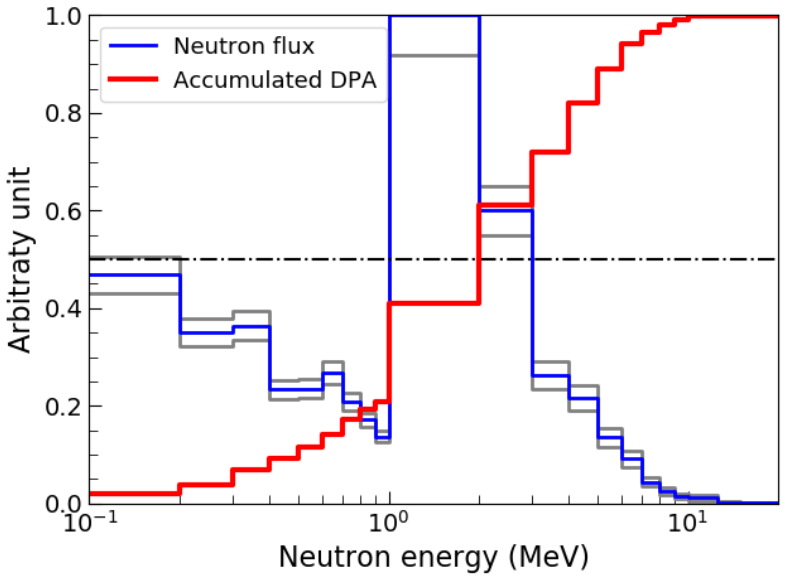

Figure 7-2. Normalized neutron flux and the corresponding uncertainty (in gray) from ENDF/B-VII.1 calculations [170] along with the accumulated DPA rate in the RPV.

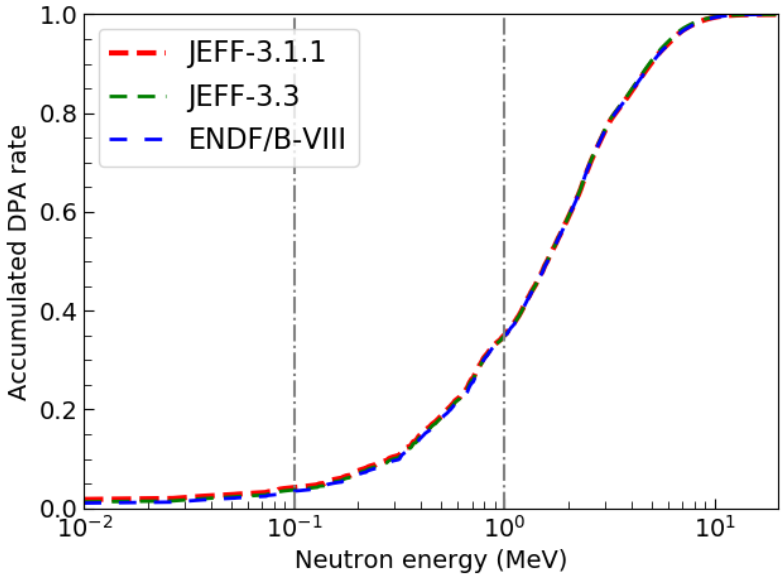

Figure 7-3. Accumulated DPA rate at the RPV inner surface of a 900 MWe PWR. The normalized DPA rates are computed with the JEFF-3.1.1, JEFF-3.3, and ENDF/B-VIII.0-based damage cross sections.

The neutron flux at the RPV inner surface of a French 900 MWe PWR (c.f. Figure 5-8 and Ref. [64]) implies 65% and 4% contributions of neutrons with energies above 1 MeV and below 0.1 MeV, respectively (see Figure 7-3). The different percentages of fast neutron-induced DPA rate between the simplified PWR and the more realistic

model can be due to the different considered volumes (from inner to outer surface vs at the inner surface) and the different multigroup approximations (21-group from 0.1 to 20 MeV vs Tripoli 315-group). Therefore, the uncertainty of DPA rate calculated from the simplified PWR shown in Figure 7-1 is not strictly equal to the one at the RPV inner surface of an industrial PWR. Nevertheless, it provides a reasonable estimate for the uncertainty of DPA rate calculation. Moreover, using the same methodologies presented in this thesis, one can perform more accurate calculations for any specific reactor, not limited to a PWR vessel.

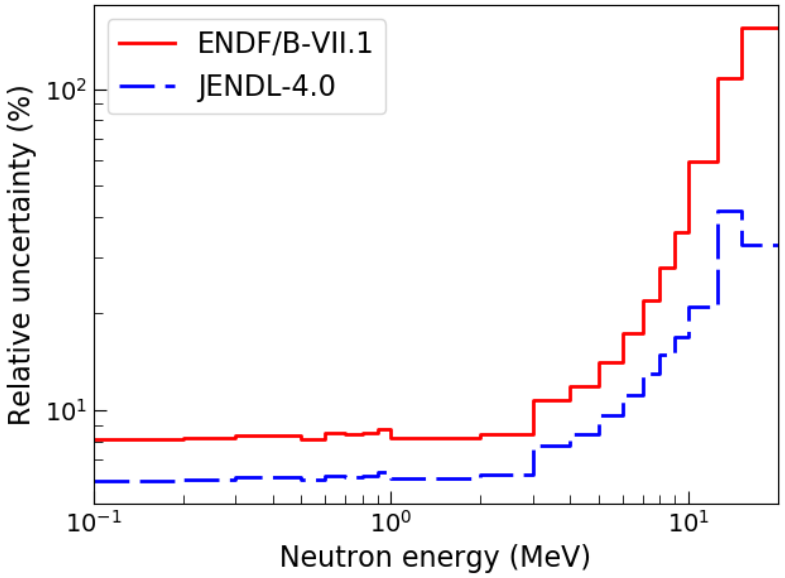

Figure 7-4. Relative uncertainties of neutron flux calculated with PFNS of ENDF/B-VII.1 and JENDL-4.0 [170].

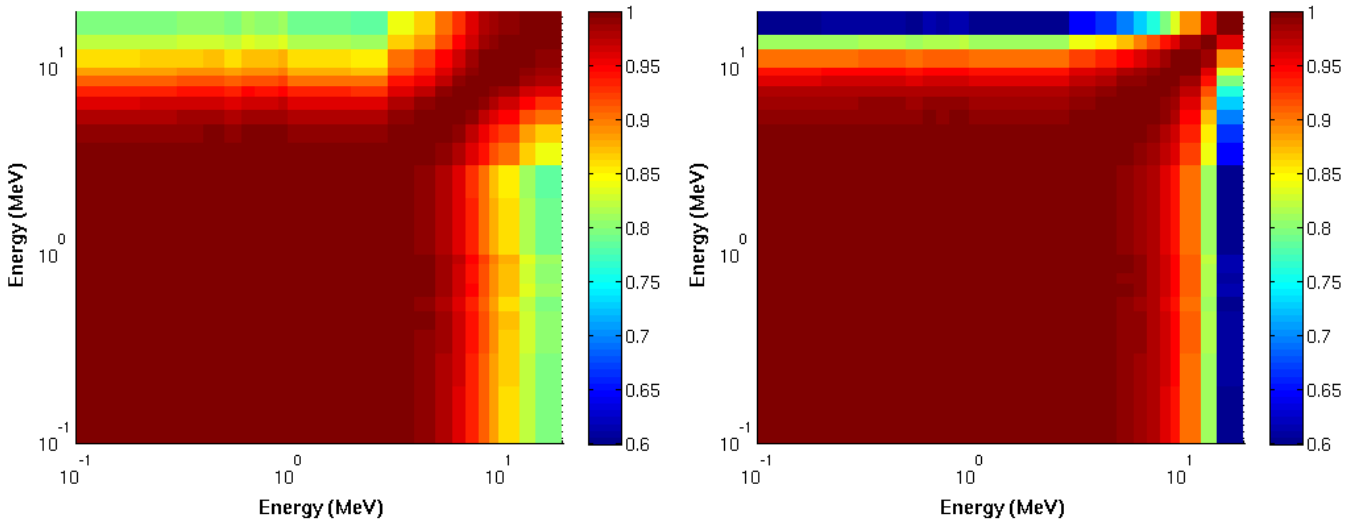

Figure 7-5. Correlation matrices of neutron flux calculated with PFNS of ENDF/B-VII.1 (left) and JENDL-4.0 (right) [170].

Figure 7-4 and Figure 7-5 respectively show the relative uncertainties and the

correlation matrices of the neutron flux in the RPV calculated with the ^{235}U PFNS of ENDF/B-VII.1 [172] and JENDL-4.0 [174]. The PFNS of ENDF/B-VII.1 leads to higher uncertainties of neutron flux in the RPV than that of JENDL-4.0. It is remarkable that the correlations of neutron flux in the RPV shown in Figure 7-5 are all positive. This is a consequence from the uncertainty propagation via importance functions: almost only emitted neutrons with energies > 2 MeV can propagate to the RPV (see Figure A-3) and the correlations of ^{235}U PFNS are all positive (or slightly negative between [1, 2] MeV and [8, 20] MeV for ENDF/B-VII.1) (see Figure A-2).

7.1.1 Analytical method via damage cross sections

To propagate the uncertainty of neutron flux to total DPA rate, analytical sensitivity and the "sandwich" formula are used here. Without considering the self-shielding correction, the total DPA rate is calculated by (c.f. Section 5.1):

$$\tau_{DPA} = \frac{0.8}{2E_d}\sum_k \sigma_{D,k}\phi_k \tag{7-2}$$

Consequently, the sensitivity of DPA rate to the k-th group neutron flux ϕ_k is:

$$\partial\tau_{DPA}/\partial\phi_k = \frac{0.8}{2E_d} \times \sigma_{D,k} \tag{7-3}$$

where the multigroup damage cross section is calculated with NJOY HEATR module and GROUPR module, or from CONRAD calculation. The analytical partial derivations and the covariance matrix (combining Figure 7-4 and Figure 7-5) are used to compute the uncertainty of DPA rate propagated from the covariance matrix neutron flux.

Table 7-1. Relative uncertainty of total NRT-DPA rate (and ARC-DPA rate in the last row) propagated from different covariance matrices of ^{235}U PFNS with and without considering the correlation matrix of neutron flux (i.e. Figure 7-5)[a].

PFNS	ENDF/B-VII.1		JENDL-4.0	
Correlation of ϕ	Without	Figure 7-5(a)	Without	Figure 7-5(b)
JENDL-4.0[b]	3.4%	11.1%	2.4%	7.6%
TENDL-2015	3.3%	10.7%	2.4%	7.4%
CONRAD	3.4%	10.7%	2.5%	7.4%
CONRAD-ARC	3.3%	10.8%	2.4%	7.4%

[a] Correlations of PFNS are always considered. The only difference is whether the correlations of neutron flux spectrum are considered.

[b] Nuclear data for computing total damage cross section of ^{56}Fe.

The relative uncertainties of DPA rates propagated from the ^{235}U PFNS of the two libraries with and without considering the correlation matrix of neutron flux shown in

Figure 7-5 are tabulated in Table 7-1. As expected, the uncertainty of DPA rate from the PFNS of ENDF/B-VII.1 is larger than from JENDL-4.0 library-based calculation owing to the higher uncertainty of the neutron flux spectrum. For both libraries, the positive correlations result in the increase in DPA uncertainties (by a factor of 3) because the sensitivities of total DPA rate to neutron spectra (i.e. multigroup DPA cross section) are all positive. Therefore, the correlation matrix of neutron flux from neutronic calculations is important for estimating the uncertainty of total DPA rate. It is found that the relative uncertainties of ARC-DPA rate are quite close to those of the NRT-DPA. The explanations are given in Section 7.1.2.

7.1.2 Stochastic method via PKA spectrum

As explained in Section 5, for a given neutron flux, the DPA rate can be calculated by folding the neutron flux with damage cross section or by generating PKA spectra. PKA spectrum is an implicit function of neutron flux spectrum, uncertainty propagation to PKA spectrum requires the numerical calculation of sensitivities or the TMC method. Because the analytical method is already used to determine the uncertainty using damage cross section and the stochastic method is more complicated, the TMC technique is used in this subsection to determine the covariance matrix of PKA spectrum. The results shown in this subsection are all based on the neutron flux from the ENDF/B-VII.1 PFNS.

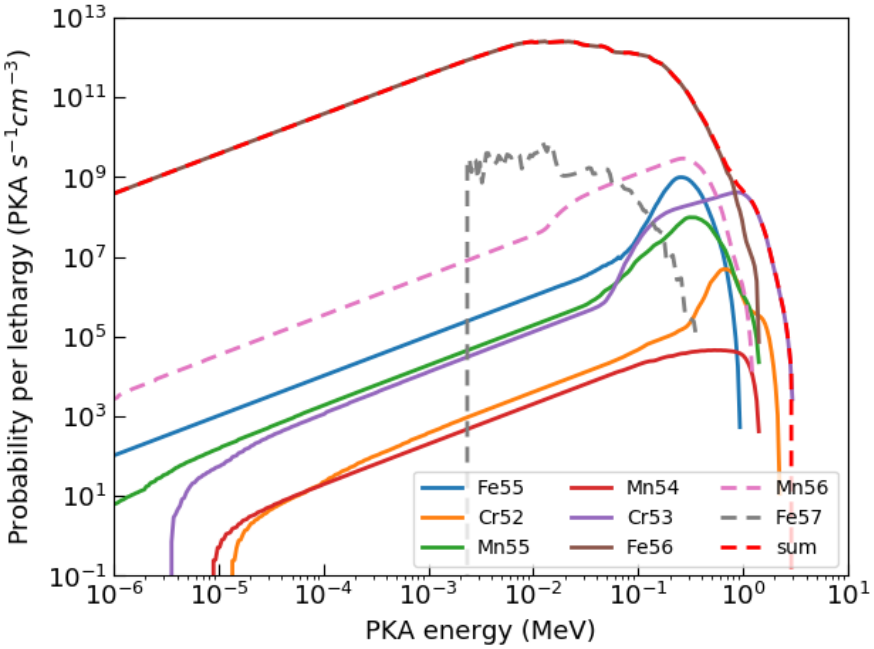

Figure 7-6. PKA spectra of ^{56}Fe material using neutron flux shown in Figure 7-3. SPECTRA-PKA calculations based on TENDL-2015.

Figure 7-6 shows the PKA spectra calculated with SPECTRA-PKA calculations

using TENDL-2015 nuclear data library. As analyzed in Section 5.3, ^{56}Fe PKA is predominant and the contribution of ^{53}Cr PKA becomes important at high PKA energy. The shift of the minimum ^{57}Fe recoil energy compared with Figure 5-9 is due to the 1.77 keV minimum neutron kick by a 0.1 MeV neutron. For the sake of simplification, this subsection focuses directly on the total PKA spectrum, i.e., the sum of all PKA spectra excluding the light nuclei such as H and He isotopes. Figure 7-7 shows the accumulated DPA rates (normalized by the corresponding total DPA rates) versus PKA energy for both NRT and ARC models based on the PKA spectrum shown in Figure 7-6 ($\tau_{ARC}/\tau_{NRT} = 0.315$). Assuming the validation of the athermal recombination efficiency for damage energy > 75 keV proposed by Konobeyev-Fischer-Simakov (KFS) [157], the current ARC model defect results in a -7.8% bias (i.e. $\tau_{KFS} = 1.078\tau_{ARC}$).

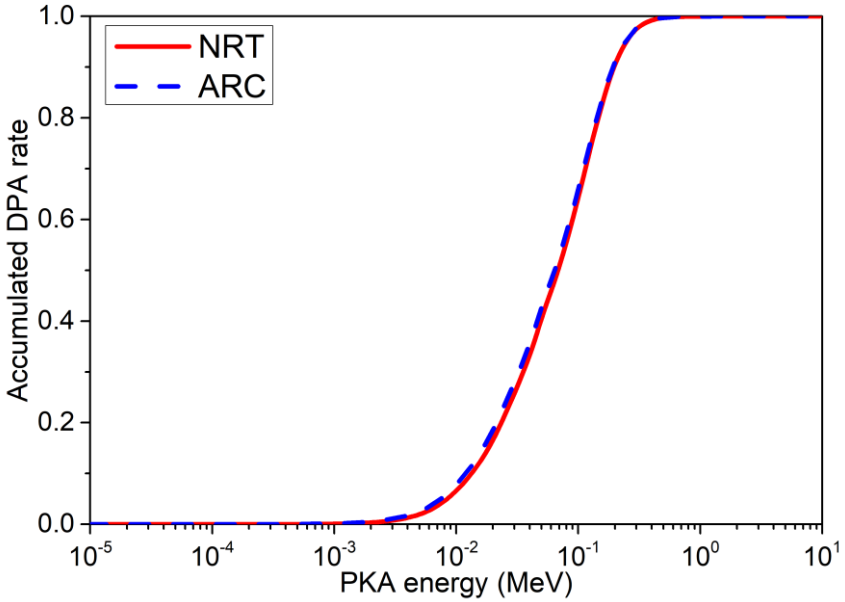

Figure 7-7. Accumulated DPA rate versus PKA energy for NRT and ARC models.

Sampling a correlated multivariable requires a positive-definite covariance matrix. Unfortunately, it is not the case for the covariance of neutron flux determined with the ENDF/B-VII.1 PFNS. Therefore, the algorithm in Appendix A2 is used to make a non-positive-definite covariance matrix be positive-definite. For the presently considered neutron flux, the covariance matrix becomes positive-definite after only 1 iteration. The maximum relative change of matrix elements is 0.009%.

Figure 7-8 illustrates the 5000 LHS TMC calculations of the PKA spectrum using SPECTRA-PKA and TENDL-2015. The original spectrum shown in Figure 7-6, the TMC averages and the corresponding uncertainties with and without considering the correlation matrix of neutron flux are shown together in each plot. The agreement between the original PKA spectrum and the two averaged spectra from TMC samplings

confirms the convergence of stochastic sampling of neutron flux. The relative uncertainties are shown and compared in Figure 7-9. In Figure 7-9, the ratios between the two considerations (0.32 below 10 keV PKA energy and larger above 100 keV PKA energy) are globally in good agreement with the data shown in Table 7-1, which shows the ratio of 0.31 for the uncertainties calculated without and with considering the correlations of neutron flux.

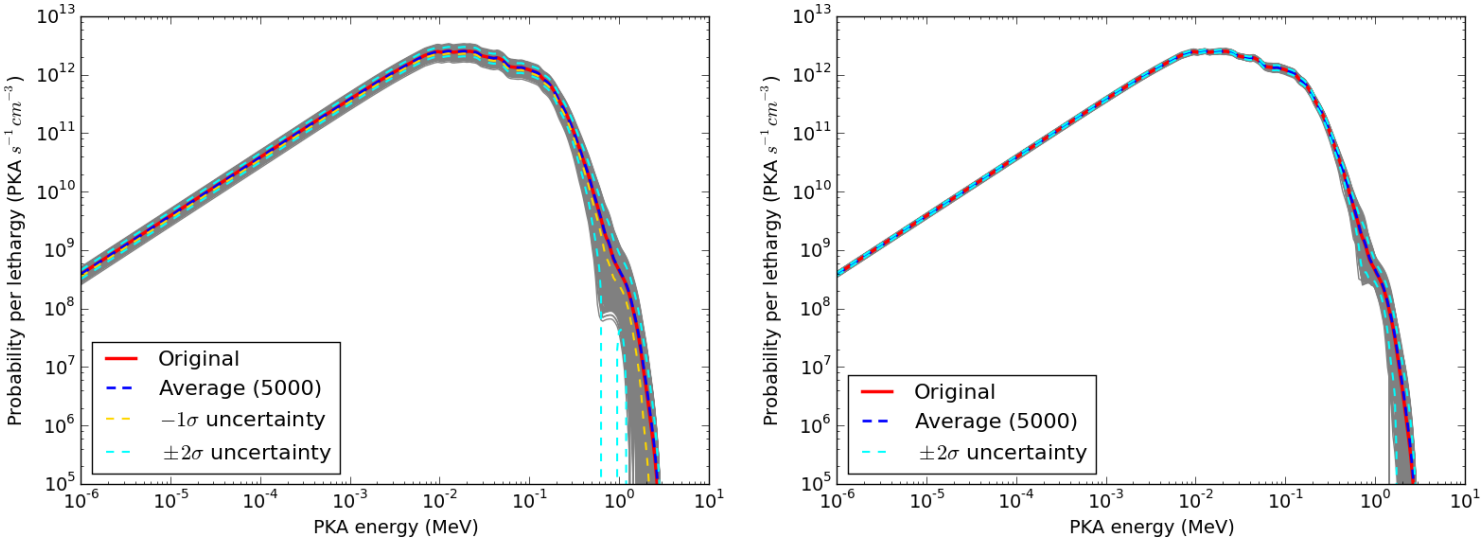

Figure 7-8. PKA spectra calculated with (left) and without (right) considering the correlation matrix of neutron flux spectrum. 5000 LHS TMC calculations.

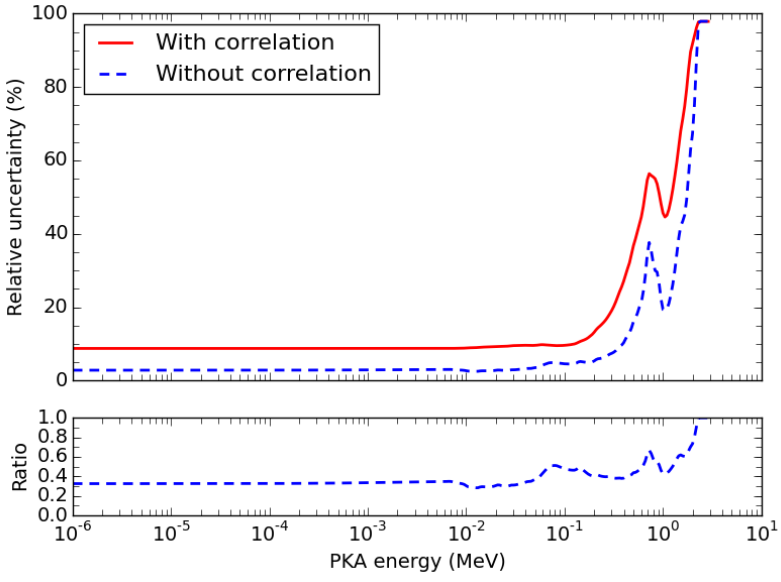

Figure 7-9. Relative uncertainties of PKA spectra shown in Figure 7-8.

Figure 7-10 shows the correlation matrices of the PKA spectra shown in Figure 7-8 with 5000 LHS samplings. Because the correlations of multigroup neutron flux are

always positive and the PKA spectrum increases with increasing neutron flux (i.e. more neutrons → more PKAs), the consideration of correlation matrix of neutron flux leads to a more correlated PKA spectrum. Because the elements of the two correlation matrices shown in Figure 7-10 are all positive, the uncertainties of total DPA rates calculated with PKA spectra are larger if the correlation matrices of PKA spectra are taken into account.

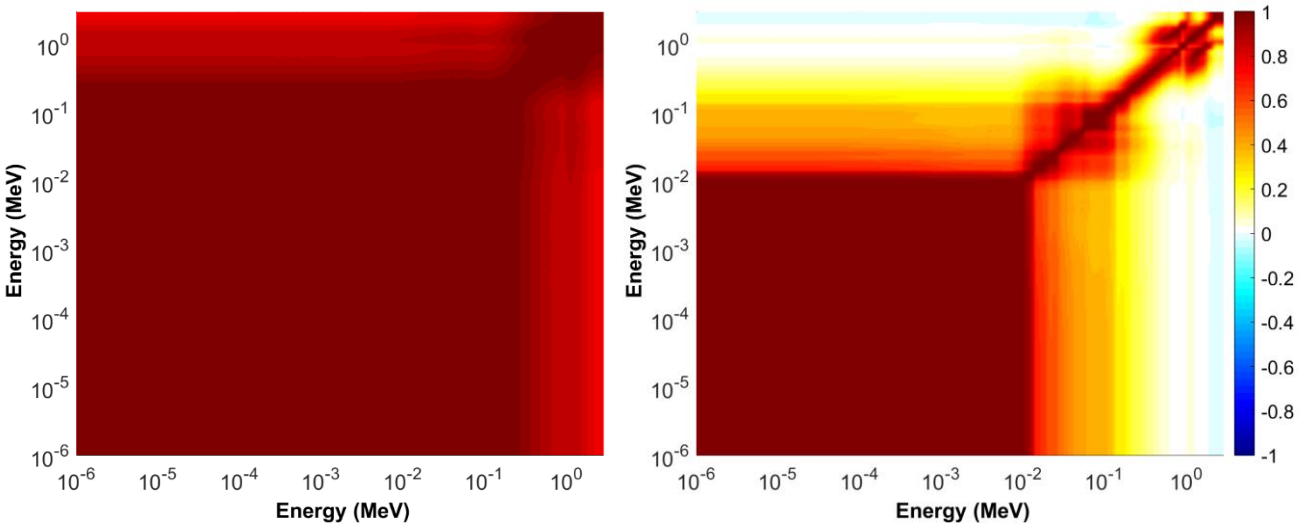

Figure 7-10. Correlation matrices of PKA spectra calculated with (left) and without (right) considering the correlation matrix of neutron flux spectrum. 5000 LHS TMC calculations.

Owing to the fine PKA energy structure ($\log(E^{sup}/E^{inf}) = 0.02$ for each group), the total DPA is calculated using the average energy for each interval of PKA energy. Therefore, the total DPA rate is:

$$\tau_{DPA} = \sum_i \chi(E_{PKA,i}) v(E_{PKA,i}) \quad (7\text{-}4)$$

The sensitivity of total DPA rate to PKA spectrum is thus:

$$\partial \tau_{DPA} / \partial \chi(E_{PKA,i}) = v(E_{PKA,i}) \quad (7\text{-}5)$$

The uncertainty of DPA rate can be simply deduced following the "sandwich" formula using the covariance matrix of PKA spectrum for a specific DPA formula.

Table 7-2 summarizes the relative uncertainties of the total DPA rate (based on NRT and ARC formulae) with and without considering the correlation matrices of neutron flux (i.e. Figure 7-5(a)) and PKA spectrum (i.e. Figure 7-10). For comparison, the results from the direct sum of multigroup PKA rates (equivalent to +1 correlation everywhere) are also presented. The quasi-coincident normalized accumulation curves in Figure 7-7 explain the similar propagated uncertainties of DPA rates from the PKA spectrum based on the NRT and ARC models. Since the correlations of the PKA spectrum shown in Figure 7-10(a) are close to unity, the deduced uncertainty is quite

close to the direct sum calculation. It is noted that the results shown in Table 7-2 are comparable with those in Table 7-1: (3.3% and 10.6%) vs (3.3% and 10.7%) relative uncertainties of the total DPA rate with and without considering the correlations.

Table 7-2. Relative uncertainty of DPA rate from ENDF/B-VII.1 PFNS calculation with and without considering the correlation matrix of neutron flux (i.e. Figure 7-5(a)) and the correlation matrices of PKA spectra (i.e. Figure 7-10).

Correlation of ϕ	Without			Figure 7-5(a)		
Correlation of χ	Without	Figure 7-10(b)	[+1][a]	Without	Figure 7-10(a)	[+1]
Uncertainty NRT	0.5%	3.3%	4.3%	1.2%	10.6%	10.7%
Uncertainty ARC	0.5%	3.3%	4.2%	1.2%	10.6%	10.6%

[a] All elements in the correlation matrix are supposed to be +1. It is equivalent to directly sum uncertainties of DPA rates in all PKA energy groups.

Because the considered neutron flux is autocorrelated at different energies (see Figure 7-5), the correlation matrix of neutron flux is important for propagating uncertainty to DPA rate. For the uncertainty propagated from ^{235}U PFNS via importance function (i.e. Figure 7-5), neglecting the correlation matrix of neutron flux leads to an underestimation of DPA uncertainty (by a factor of 3 for the positive correlations in the 21-group structure considered here) in the RPV. This reasoning also explains the underestimation of the uncertainty of total DPA rate without considering the correlation matrix of PKA spectrum (more than by a factor of 7 for the considered case), because the total DPA rate increases with increasing PKA spectrum and neutron flux. In the presently studied case, the uncertainty from complete consideration of correlation matrices is 21 times larger than the calculation without considering any correlation. It is thus of great importance to take the non-null correlations of both neutron flux and PKA spectrum into account for estimating the uncertainty of DPA.

7.2 Uncertainty from nuclear model parameters

Assuming the availability of current nuclear reaction models, the nuclear data required for computing the radiation damage are correlated by fundamental model parameters. One major advantage of use such model calculation is that the large complete correlation matrix between various quantities is included in a limit number of model parameters [34, 155]. This subsection shows the uncertainty of DPA rate in the RPV of a simplified PWR shown in Section 7.1 propagated from the nuclear model parameters of n+^{56}Fe. The nuclear reaction models are respectively the R-matrix formalism in the RRR and the OM and SM in the continuum region. It is noted again that the model defect is not considered here.

Theoretically, the data in the RRR and those in the continuum region are not correlated because of the independent physical models in the two regions. In practice, the two regions are numerically correlated owing to the physical constraint on the continuity of physical quantities at the boundary. These two regions can be decorrelated only if the continuity across the boundary is systematically ensured, which is not the case for the current phenomenological models.

Because the evaluation of advanced resonance parameters of n+^{56}Fe is still on-going in our laboratory [42, 44, 45] (hopeful to be finished soon), the resonance parameters of JEFF-3.1.1 are used here. The corresponding uncertainties of neutron and gamma widths are not evaluated in JEFF-3.1.1 and are set to be 3% in the present work. Because the resonance energies below 850 keV are generally well determined, the eigenvalues are assumed to be exact (i.e. no uncertainty). Above the upper energy limit of the JEFF-3.1.1 RRR (i.e. 850 keV), the OM and SM calculations shown in Section 2 and Refs. [34, 42] are used. Consequently, the RRR and the continuum region are not correlated in this thesis. The corresponding influence on DPA rate uncertainty calculation is discussed later. The 21-group (the same energy structure as used for the neutron flux) correlation matrix of the NRT-damage cross section is shown in Figure 7-11. The quasi-pointwise correlation matrix is illustrated in Figure A-4 in Appendix A3. It is noted that the covariance matrices propagated from nuclear model parameters are quasi-identical for NRT and ARC models.

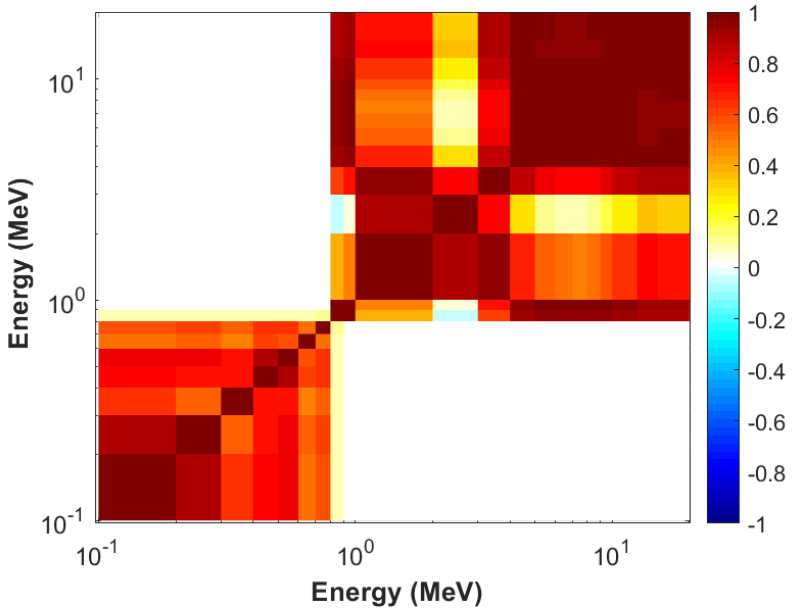

Figure 7-11. 21-group correlation matrix of n+^{56}Fe damage cross section in [0.1, 20] MeV from nuclear reaction model parameters.

The relative uncertainty of n+^{56}Fe damage cross section in the incident energy range of [0.1, 20] MeV from nuclear model parameters is illustrated in Figure 7-12 with

the zoom in the range of [0.1, 0.6] MeV. The relative uncertainties at neutron energies close to the valleys of scattering interferences are relatively large because destructive interference is very sensitive to neutron width so is the damage cross section. However, since the damage cross section close to the resonant energies has a predominant contribution to multigroup data, the uncertainty of the 21-group damage cross section in the RRR is smaller than 2%. This uncertainty should be larger if the resonance self-shielding effect is taken into account due to the decreasing weight of resonant damage cross section (its influence on DPA rate uncertainty is discussed later). The uncertainty in the group [1, 2] MeV is smaller than the minimum uncertainty of the quasi-pointwise damage cross section owing to the non-unit correlations (some are close to 0 and even slightly negative) as shown in Figure A-4 in Appendix A3.

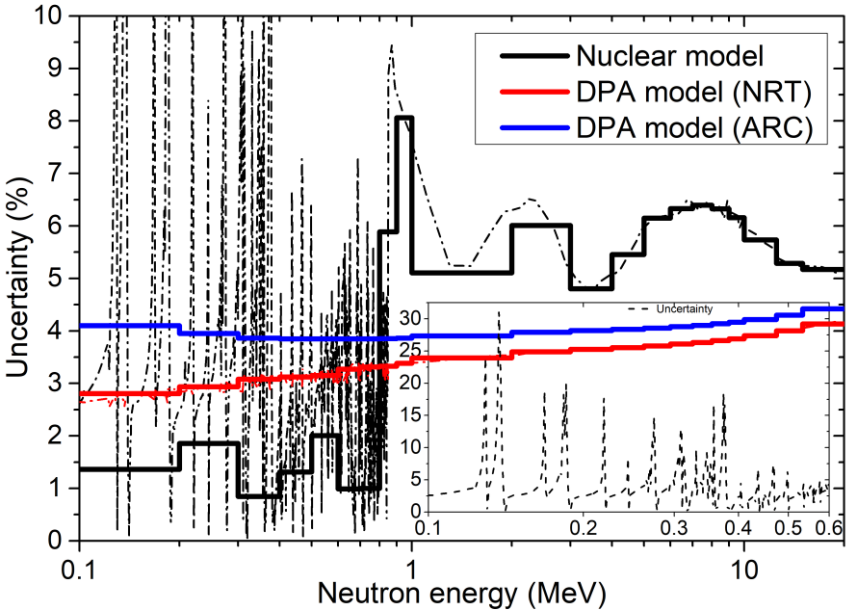

Figure 7-12. Relative uncertainty of n+^{56}Fe damage cross section in [0.1, 20] MeV from nuclear model parameters and DPA models parameters. The histogram plots are performed on the 21-group structure as used for neutron flux. The uncertainties propagated from nuclear model parameters are quasi-identical for the NRT and ARC models so that only the former is shown. The uncertainties propagated from DPA models are used in the following section.

Similar to the sensitivity of DPA rate to the k-th group neutron flux ϕ_k as shown in Section 7.1, its sensitivity to k-th group damage cross section $\sigma_{D,k}$ is:

$$\partial\tau_{DPA}/\partial\sigma_{D,k} = \frac{0.8}{2E_d} \times \phi_k \qquad (7\text{-}6)$$

Using these sensitivities, the uncertainty of DPA rate from the covariance matrix of damage cross section can be directly deduced by the "sandwich" formula. The uncertainties of total DPA rate from nuclear model parameters with and without considering the correlations of damage cross section are given in Table 7-3 (the results

based on the PFNS from ENDF/B-VII.1 and JENDL-4.0 are the same with the shown significant digits). As previously explained, the damage cross section is uncorrelated between the RRR and the continuum region for pure model calculations but practically correlated due to the continuity of physical quantities at the boundary. For estimating the influence of the correlations between the two regions on DPA rate uncertainty calculation, the null correlations shown in Figure 7-11 are replaced by +1 and -1 for extreme considerations.

Table 7-3. Relative uncertainty of total DPA rate from nuclear model parameters with and without considering the correlations of damage cross section.

	Correlation of σ_D	Figure 7-11	Figure 7-11: $0 \rightarrow +1$[b]	Figure 7-11: $0 \rightarrow -1$	Without
NRT	Uncertainty	4.0%	4.2%	3.7%	1.9%
	From < 0.9 MeV[a]	0.23%	-	-	0.17%
ARC	Uncertainty	3.9%	4.1%	3.6%	1.9%
	From < 0.9 MeV	0.25%	-	-	0.17%

[a] 19% of the total DPA rate is induced by neutrons in this energy range.

[b] Figure 7-11: $0 \rightarrow +1$ (or -1) represents that the null correlations in Figure 7-11 are replaced by +1 (or -1) for extreme considerations. The uncertainty propagated for neutron energies below 0.9 MeV is independent of such correlation.

The uncertainties of DPA rate propagated from nuclear reaction models are very close for NRT and ARC models because of the quasi-identical covariance matrices propagated from nuclear reaction model parameters. The two extreme considerations by replacing correlations between the two regions by +1 and -1 imply that the potential deviation of the DPA rate uncertainty propagated from nuclear model parameters is within 0.3% for the present consideration. However, totally neglecting the correlation matrix of damage cross section reduces the uncertainty from nuclear model parameters by a factor of 2. The 2% standard deviation computed with damage cross sections of JEFF-3.1.1 [28], JEFF-3.3 [89], ENDF/B-VIII.0 [65], JENDL-4.0 [174], and TENDL-2019 [123] can be roughly considered as the bias induced by nuclear reaction model defects.

As the data given in Table 7-3, the uncertainty from the damage cross section in the RRR (i.e. < 0.85 MeV) has a negligible contribution to the uncertainty of total DPA rate for the presently studied case. This is a consequence of both the small contribution to DPA rate in this region (19% of the total DPA rate, see Figure 7-4) and the relative small uncertainty of damage cross section (see Figure 7-12). Compared with the uncertainty propagated from the n+^{56}Fe OM parameters, 3% or even 10% relative

uncertainties of neutron and gamma widths do not influence the final uncertainty of DPA rate. Even with the 5% relative uncertainty of nuclear cross section from JEFF-3.1.1 [28, 34], the corresponding < 1% relative uncertainty induced by neutrons in the RRR results in < 4.1% uncertainty of total DPA rate. Therefore, in the RPV of a PWR, the uncertainty of DPA rate due to the nuclear data of n+^{56}Fe reactions is predominated by the covariance matrix in the continuum region. This also verifies that the resonance self-shielding has a limited influence on DPA rate uncertainty calculation.

7.3 Uncertainty from DPA model

If the "systematic uncertainty" of 20% [175] is assumed for different DPA models, about 20% uncertainty of DPA rate from the uncertainty of DPA model is systematically deduced. Because the DPA rate is almost inversely proportional to E_d, the 20% discrepancy among different calculations shown by Simakov [175] is somewhat consistent with our assumption of the 20% uncertainty for E_d (difference between 40 eV [70] and 32 eV [68]) in Ref. [34]. Such a 20% uncertainty gives a quick and simple estimate of DPA calculations.

The present work estimates the uncertainty with more basic and rigorous methods. The uncertainty from DPA models is only from the E_d and the three "parameters A, B, and C" (and additional parameters b_{ARC} and c_{ARC} for ARC-DPA). Because E_d influences the generalized damage energy, the damage energy also depends on E_d. Here, a 20% relative uncertainty for E_d and 12% for A, B, C in the NRT model[①] are used for estimating the uncertainty from the NRT-DPA model.

Figure 7-13 illustrates two schemas for propagating uncertainty of DPA model parameters uncertainty to DPA rate. For DPA model uncertainty propagation, we have to distinguish the generalized damage energy cross section σ_D (or simply called as damage cross section) and the DPA cross section $\sigma_{DPA} = \sigma_D/2.5E_d$ because E_d is an uncertainty source. In the NRT model, because the generalized damage energy (defined in Section 4.4) is quasi-identical to Lindhard damage energy for neutron energy above 0.1 MeV, the uncertainty propagated from E_d is negligible for the damage cross section σ_D. Therefore, the uncertainty of DPA rate can be determined by:

$$\Delta\tau_{DPA} = \sqrt{\Delta(\langle\sigma_D, \phi\rangle)^2 + \Delta E_d^2} \tag{7-7}$$

via the first schema shown in Figure 7-13. Section 7.3.1 shows results for the uncertainty of damage energy rate, i.e. $\langle\sigma_D, \phi\rangle$, which is not sensitive to E_d for the NRT model. However, for the ARC model, because E_d is included in the efficiency function (c.f. Section 3.5), $\langle\sigma_D, \phi\rangle$ depends on E_d. The uncertainty of ARC-DPA rate cannot be

[①] Ref. [176] shows that 12% relative uncertainty of these parameters approximately corresponds with the uncertainty from BCA calculations for iron

directly deduced by Eq. (7-7). Consequently, Section 7.3.2 shows the results and discussion of the DPA rate uncertainties propagated from DPA model parameters via $\langle \sigma_{DPA}, \phi \rangle$ (i.e. the second schema shown in Figure 7-13).

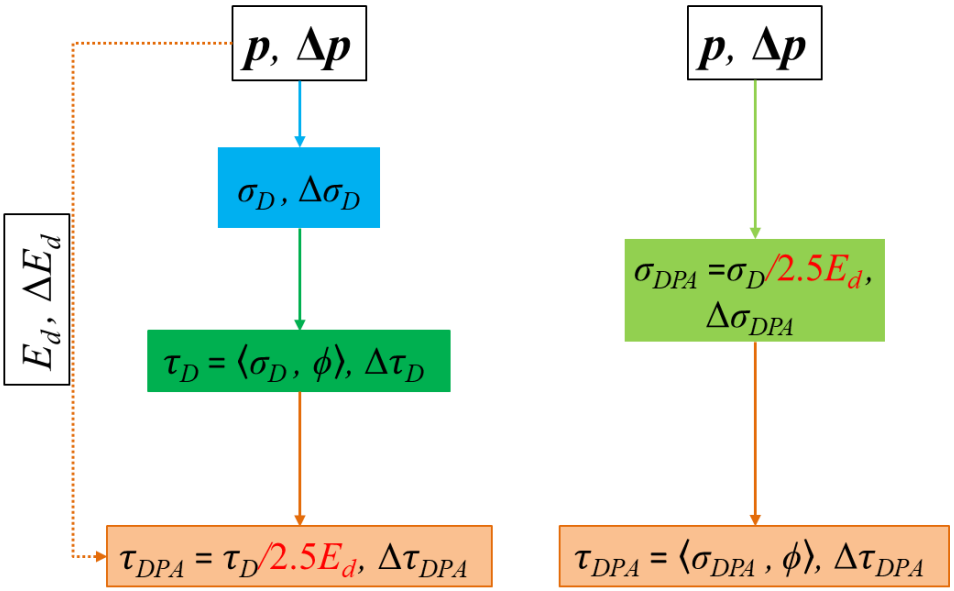

Figure 7-13. Schemas for propagating DPA model parameters uncertainties to DPA rate: via damage energy cross section σ_D (left) vs directly via DPA cross section σ_{DPA} (right). Vector $\boldsymbol{p}$ contains all parameters including E_d, $\Delta\boldsymbol{p}$ is the associated uncertainty vector.

7.3.1 Uncertainty of damage energy rate ‹σ_D, ϕ›

Figure 7-14 shows the correlation matrix of n+^{56}Fe damage cross section in the range of [0.1, 20] MeV propagated from the NRT-DPA model parameters. The correlation matrix for the ARC model is shown in Figure A-5 in Appendix A3. The damage cross section is strongly autocorrelated at different energies because its sensitivity to "parameter A" is almost energy-independent for neutron energy above 40 keV and the "parameter A" has a predominant contribution to the covariance of damage cross section (e.g., sensitivities above 40 keV shown in Figure 6-2). The relative uncertainties of damage cross section propagated from DPA model parameters are included in Figure 7-12 for both NRT and ARC models. The larger relative uncertainty for the ARC model is propagated from E_d (and a small contribution of b_{ARC} and c_{ARC}) via the efficiency function (c.f. Section 3.5), whereas the NRT damage cross section is not sensitive to E_d in the considered region (c.f. Refs. [34, 121]).

Using the same method as described in Section 7.2, the uncertainties of total damage energy rate from DPA model parameters are summarized in Table 7-4 (the results based on the PFNS from ENDF/B-VII.1 and JENDL-4.0 are the same with the significant digits shown in this thesis). The relative uncertainties of damage energy rate

are respectively 3.5% and 1.3% with and without considering the correlations damage cross section for the NRT model. The slightly larger uncertainty of $\langle \sigma_D, \phi \rangle$ for the ARC model is a result of the larger uncertainty of the ARC-damage cross section as shown in Figure 7-12. However, this larger uncertainty of damage energy rate does not directly result in a larger DPA rate uncertainty because of the non-null correlation between σ_D and E_d for the ARC model. Details are presented in in the following section.

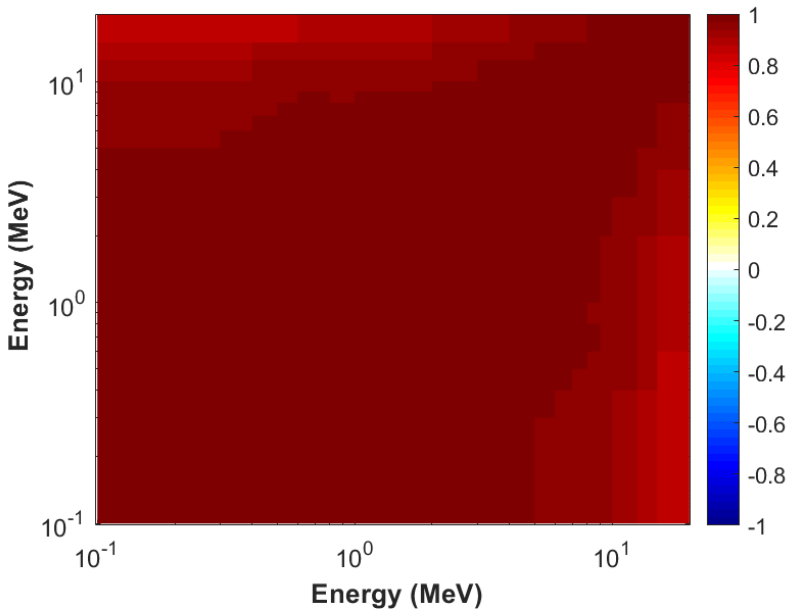

Figure 7-14. 21-group correlation matrix of n+^{56}Fe NRT-damage cross section in [0.1, 20] MeV from DPA model parameters.

Table 7-4. Relative uncertainty of total damage rate from DPA model parameters with and without considering the correlations of damage cross section.

Correlation of σ_D	With (e.g., Figure 7-14)	Without
NRT-DPA	3.5%	1.3%
ARC-DPA	3.9%	1.4%

As previously explained, the uncertainty of $\langle \sigma_D, \phi \rangle$ is almost independent on the uncertainty of E_d for the NRT model. It is noteworthy that even for the ARC model, the damage energy rate uncertainty varies from 3.5% to 3.9% when the uncertainty of E_d is from 5% to 20%. Therefore, for both NRT and ARC models, the uncertainty of $\langle \sigma_D, \phi \rangle$ is not so sensitive to that of E_d. This is another important argument for recommending the use of damage energy cross section σ_D in the case where E_d is not so well determined.

7.3.2 Uncertainty of DPA rate ‹σ_{DPA}, ϕ›

Because σ_D depends on E_d, Eq. (7-7) is not mathematically rigorous for

propagating DPA model parameters uncertainties to DPA rate. Therefore, this section shows the uncertainties of DPA rate directly calculated via $\langle \sigma_{DPA}, \phi \rangle$ (i.e. the second schema shown in Figure 7-13) and compares them with the results obtained via Eq. (7-7). Figure 7-15 shows the relative uncertainty of DPA cross section propagated from DPA model parameters with different uncertainties of the TDE. Contrary to σ_D, σ_{DPA} is very sensitive to E_d. In the case of 5% uncertainty of the TDE (E_d = 41±2 eV for iron [70] is used), the relative uncertainty of ARC-σ_{DPA} is slightly higher than that of the NRT-σ_{DPA} above 4 MeV neutron energy due to the small uncertainty propagated from b_{ARC} and c_{ARC}. In general, the uncertainty of ARC-DPA cross section is smaller. The explanation is given below.

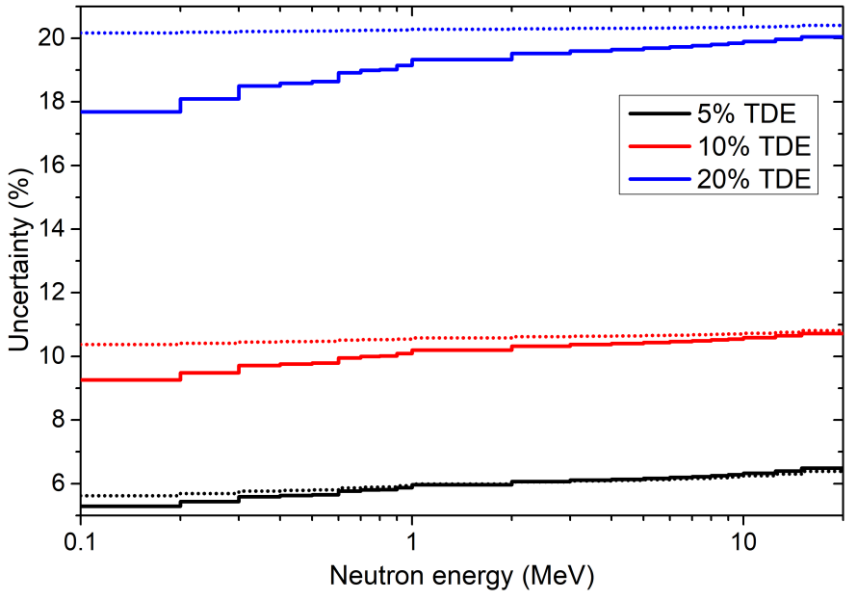

Figure 7-15. Relative uncertainty of n+^{56}Fe DPA cross section in [0.1, 20] MeV propagated from DPA models parameters with different relative uncertainties of the TDE. Solid and dotted curves represent the ARC and NRT models, respectively.

Using the partial derivations obtained in Section 6.2.1.1, for damage energy above 2.5E_d, one obtains:

$$\frac{\frac{\partial \nu_{ARC}}{\partial E_d} \Big/ \frac{\nu_{ARC}}{E_d}}{\frac{\partial \nu_{NRT}}{\partial E_d} \Big/ \frac{\nu_{NRT}}{E_d}} = 1 + b_{ARC} \times \frac{\xi_{ARC} - c_{ARC}}{\xi_{ARC}} \tag{7-8}$$

Because $b_{ARC} < 0$ and $(\xi_{ARC} - c_{ARC}) > 0$, one can conclude that the ARC-DPA is less sensitive to E_d than the NRT-DPA. This explains the smaller uncertainty of the ARC-DPA than that of the NRT-DPA (except that the uncertainty propagated from b_{ARC} and c_{ARC} is more important than $(\Delta_{NRT} - \Delta_{ARC})$ propagated from E_d). In the case where $(\xi_{ARC} - c_{ARC})/\xi_{ARC} \ll 1$, i.e. $\nu_{NRT} \gg [c_{ARC}/(1 - c_{ARC})]^{1/b_{ARC}}$ (= 5 for iron), NRT and ARC have the same sensitivity to E_d, so that their uncertainties propagated from

E_d are equal.

Table 7-5 summarizes the uncertainty of DPA rate, i.e. $\langle \sigma_{DPA}, \phi \rangle = \langle \sigma_D, \phi \rangle / 2.5E_d$, for both NRT and ARC models using 20% uncertainty of E_d. For the NRT model, it is equivalent to the calculation via Eq. (7-7). However, Eq. (7-7) is not applicable for determining the uncertainty of ARC-DPA rate owing to the correlation between E_d and σ_D (because E_d is included in the efficiency function of the ARC model). More precisely, because $\partial \xi_{ARC} / \partial E_d > 0$, $\mathrm{corr}(\sigma_D, 1/E_d) < 0$, which results in a smaller uncertainty than the value deduced by Eq. (7-7).

Table 7-5. Relative uncertainty of total DPA rate from DPA model parameters with and without considering the correlations of damage or DPA cross section.

	Correlation	With	Without
$\langle \sigma_{DPA}, \phi \rangle$ [a]	NRT	20.3%	7.2%
	ARC	19.3%	6.9%
$\langle \sigma_D, \phi \rangle / 2.5E_d$	NRT via Eq. (7-7)	20.3%	20.0%
	ARC via Eq. (7-7)	20.4%	20.0%

[a] Here, the correlations are correlation matrix of σ_{DPA} for the first two rows and that of σ_D for the last two rows.

If the uncertainty is propagated by independent consideration of σ_D and E_d via Eq. (7-7), the uncertainty of E_d is propagated to DPA rate as a systematic uncertainty. In this case, because the strong correlation of DPA cross section induced by E_d is automatically taken into account, the role of correlation due to other DPA model parameters is weakened (see the comparison with and without correlation in the last two rows in Table 7-5). This is also a point supporting the recommendation for using damage cross section σ_D. If the 20% uncertainty (or bias) of E_d is combined for evaluating the uncertainty of DPA rate, the contribution of uncertainty from damage cross section is relatively small for both NRT and ARC models (see Figure 7-15). The role of E_d for uncertainty estimates of DPA rate is further discussed in the following section.

7.4 Total uncertainty of DPA rate

Because the uncertainties propagated from PFNS, nuclear model parameters of n+^{56}Fe, and DPA model parameters are not correlated, the total uncertainty of DPA rate can be simply calculated by:

$$\Delta_{\mathrm{tot}} = \sqrt{\Delta_{\mathrm{PFNS}}^2 + \Delta_{\mathrm{ND}}^2 + \Delta_{\mathrm{DPA}}^2} \quad (7\text{-}9)$$

It is noted again that the covariance matrix of neutron flux used in the present work is

only propagated from the covariance matrix of the PFNS. Other uncertainty sources, e.g., nuclear cross sections and angular distributions of ^{235}U, ^{238}U, ^{1}H, etc., are still not considered here. In a sodium-cooled breed-and-burn core, Ref. [177] shows that the DPA rate uncertainty propagated from nuclear cross sections is only about 2%. It is also is noteworthy that the nuclear data of neutron reactions with isotopes in the RPV influence both the neutron flux and the damage cross section. Therefore, the neutron flux and the damage cross section are correlated. The covariance matrix between them is thus required for computing the uncertainty of DPA rate.

The total uncertainties of the NRT-DPA rate propagated from the ^{235}U PFNS, nuclear model parameters of n+^{56}Fe, and DPA model parameters are summarized in Table 7-6. The total uncertainties of the damage energy rate in the RPV of the investigated PWR are respectively 12% and 9% with the covariance matrices of PFNS from ENDF/B-VII.1 and JENDL-4.0, whereas an underestimation by a factor of 3 is obtained if the correlations of neutron flux and damage cross section are not taken into account.

Table 7-6. Relative total uncertainty of NRT-DPA rate via σ_D with and without considering the correlations in the calculations.

Cov. of PFNS	ENDF/B-VII.1		JENDL-4.0	
Correlation	Complete	Null	Complete	Null
Unc. of $\langle\sigma_D,\phi\rangle$	12.0%	4.1%	9.1%	3.4%
Total unc.-1[a]	23.3%	20.4%	22.0%	20.3%
Total unc.-2[b]	15.6%	10.8%	13.5%	10.6%
Total unc.-3[c]	12.9%	6.4%	10.3%	5.9%

[a] Total uncertainty is the combined value of (i) the total uncertainty of $\langle\sigma_D,\phi\rangle$ and (ii) the additional 20% uncertainty/bias from E_d for computing $\sigma_D \propto \langle\sigma_D,\phi\rangle/E_d$.

[b] Assuming 10% relative uncertainty for E_d. This value corresponds to the weighted average E_d = 39±4 eV, which is obtained from the 11 potentials calculations given in Ref. [70].

[c] Using E_d = 41±2 eV for iron [70].

Table 7-7 shows the same results as those given in Table 7-6 but for the ARC-DPA rate. The uncertainties of the generalized damage energy rate $\langle\sigma_D,\phi\rangle$ for the ARC-DPA are quite close to those for the current standard NRT-DPA. This is a consequence of the predominant contribution of uncertainty from neutron flux. Taking the ENDF/B-VII.1 PFNS case as an example, 10.7% uncertainty is propagated from the covariance matrix of neutron flux, whereas the uncertainty propagated from nuclear reaction and DPA models are respectively 4.0% and 3.5% (3.9% for ARC-DPA).

Table 7-7. Relative total uncertainty of ARC-DPA rate with and without considering the correlations during the calculations.

Cov. of PFNS	ENDF/B-VII.1		JENDL-4.0	
Correlation	Complete	Null	Complete	Null
Unc. of $\langle\sigma_D,\phi\rangle$	12.1%	4.1%	9.3%	3.4%
Total unc.-1	22.5% (23.4%)[a]	7.9% (20.4%)	21.1% (22.0%)	7.5% (20.3%)
Total unc.-2	15.3% (15.7%)	5.3% (10.8%)	13.2% (13.6%)	4.8% (10.6%)
Total unc.-3	12.9% (13.1%)	4.4% (6.4%)	10.3% (10.5%)	3.8% (5.9%)

[a] Values in parenthesis are obtained by Eq. (7-7) via σ_D.

Assuming that correlation matrices are considered in all steps of uncertainty propagation calculations, one can found that the uncertainties of DPA rates propagated via σ_{DPA} covariance matrix are not so different to those computed with σ_D covariance matrix and uncertainty of E_d via Eq. (7-7), even for ARC-DPA rates. This is a direct consequence that $\langle\sigma_D,\phi\rangle$ is not much sensitive to E_d (c.f. Section 7.3.1). Therefore, it is confirmed again that the use of generalized damage energy cross section σ_D for propagating uncertainties to $\langle\sigma_D,\phi\rangle$ is pertinent to quantify the uncertainty of DPA rate for both NRT and ARC models. Furthermore, because the uncertainty of E_d is the predominant source of DPA model parameters uncertainties, σ_{DPA} is strongly autocorrelated at different neutron energies (see Figure A-6 and the descriptions in Appendix A4). This implies that using Eq. (7-7) gives DPA rate uncertainty closer to the exact value than directly using the uncertainty of σ_{DPA} if the complete correlation matrix of σ_{DPA} propagated from DPA model is not available.

Compared with the large uncertainty of 20% for E_d, the contribution of the uncertainties from nuclear data and DPA model is less important for both NRT and ARC models. However, if the relative uncertainty for E_d is reduced to 10%, the contribution from other uncertainty sources is considerable. Using the value of 41±2 eV obtained in Ref. [70], the uncertainty from E_d has a negligible contribution to total uncertainty. Therefore, the best choice or the recommendation for estimating the uncertainty of DPA rate calculation should be the determination of the uncertainty of damage energy rate $\langle\sigma_D,\phi\rangle$, then the combined total uncertainty is calculated for each reasonable uncertainty of E_d via Eq. (7-7). Certainly, regardless of the complexity and the time-intensive calculation, the *ab initio* uncertainty propagation as shown in this section gives a more accurate DPA rate uncertainty for each specific value and uncertainty of E_d.

7.5 Discussion on additional biases induced by model defects

In addition to uncertainties propagated from different sources, the model defects

result in calculation biases. Section 7.1 shows the DPA rate uncertainty propagated from neutron flux (deduced from ^{235}U PFNS). It should be noted that the bias of calculated neutron flux, mainly due to nuclear data, leads to an additional bias of the calculated DPA rate. Taking the fast neutron flux in the vessel model of the FLUOLE-2 experiment [178] as an example, 1% to 3% calculation-measure biases are observed [179], even though these discrepancies are within the calculated uncertainties.

The 2% standard deviation of DPA rate calculated with different nuclear data libraries can be considered as an approximate bias due to evaluated nuclear reaction data. It is noteworthy that the nuclear reaction model defects are already taken into account in the evaluated libraries. The 2% bias is propagated from the discrepancy among different methods for treating nuclear reaction model defects. If one directly compares the model calculations by CONRAD and the damage cross sections computed from evaluated libraries, a +16% bias is obtained (i.e. $\tau_{\mathrm{Model}} = 1.16\tau_{\mathrm{ENDF}}$) (the explanations of such bias are given in Ref. [34]). However, since most of the current DPA rate calculations are based on an evaluated nuclear data library, a 2% bias due to nuclear data is a reasonable approximation for DPA rate calculation of iron in a PWR vessel.

As for the DPA model defects, a 20% bias/uncertainty of E_d is enough to include the discrepancies among different MD simulations data (as shown in Figure 4 of Ref. [175]). If we only compare DPA model calculations without considering the spread among MD simulations, the current ARC-DPA formula results in a -8% bias when compared with the efficiency function proposed by Konobeyev-Fischer-Simakov [157]:

$$\xi_{KFS}(E_a) = \begin{cases} \xi_{ARC}(E_a), & E_a < 75\ \mathrm{keV} \\ 7.04 \times 10^{-4} E_a^{1/4} - 0.0195 E_a^{-1/4} + 0.422, & E_a \geq 75\ \mathrm{keV} \end{cases} \quad (7\text{-}10)$$

where the unit of E_a in the second row is MeV in this equation. Consequently, compared with the calculation using an ENDF and the efficiency ξ_{KFS}, the CONARD pure nuclear models and the current ARC-DPA model calculation leads to a +8% bias (i.e. $\tau_{\mathrm{CONRAD+ARC}} = 1.08\tau_{\mathrm{ENDF+KFS}}$), whereas an ENDF and the current ARC model calculation results in a -8% bias (i.e. $\tau_{\mathrm{ENDF+ARC}} = 0.92\tau_{\mathrm{ENDF+KFS}}$).

It is noted that ξ_{ARC} or ξ_{KFS} is not strictly validated against experimental data, even though the KIT p+Fe DPA cross section (based on ξ_{KFS} and the KIT p+Fe nuclear data) are in good agreement with experimental data for proton energies from 1 keV up to 3 GeV [180]. The DPA model defect is still questionable. If one compares ARC and NRT models, $\tau_{ARC}/\tau_{NRT} = 0.315$ implies +68% bias induced by the NRT model. However, it should be kept in mind that the NRT and the ARC are more like two different models that the athermal recombination is not considered for the former. In general, more experimental data are required for quantifying the DPA model defects, especially for

elements of which large discrepancies are observed between different MD simulations. Assuming that the discrepancy between ξ_{ARC} and ξ_{KFS} gives a reasonable estimate of DPA model defect, the bias of DPA rate calculation is mainly from the DPA model defect if the current evaluated nuclear data are used.

8 Conclusions and prospects

8.1 Conclusions

The main objective of this thesis is to develop and improve the methodologies for accurately computing the neutron irradiation-induced displacement damage and the corresponding uncertainty. The research covers nuclear models for evaluating nuclear reaction data, primary damage models for estimating the number of atomic displacements from the kinetic energy of a PKA, physical and numerical theories for calculating damage cross section using nuclear data and DPA models, methods for computing DPA rate using neutron flux from neutron transport simulations, and strategies for propagating uncertainties to final DPA estimate.

After a brief review on nuclear reaction models and primary radiation damage models, we propose complete methods for calculating damage cross section from different nuclear reactions. An improved interpolation is proposed and recommended to correctly reproduce the peak value of energy-angular distribution from tabulated data. The recoil energies from neutron-induced reactions are systematically summarized with the estimation of the relativistic effect and thermal vibration of the target based on fundamental equations. Particularly, a new method for computing the recoil energy from charged particle emission reactions is proposed by considering the quantum tunneling and Coulomb barrier. Improved methods are developed for ensuring numerical integration and verifying the accuracy of numerical calculation. The calculations of damage cross section from neutron radiative capture reaction and N-body reactions are also thoroughly analyzed and discussed.

In addition to the neutron irradiation-induced displacement damage, the electron, positron, and photon-induced irradiation damage can be important in certain applications, e.g., in the RPV of a BWR. The DPA cross sections induced by these light particles are also investigated in this thesis. Furthermore, because beta decay is a three-body reaction, a detailed method for estimating beta decay-induced damage is proposed. The thorough discussion on the calculation of damage cross section for polyatomic materials is also presented. It is noteworthy that the damage cross section of a polyatomic material cannot be simply deduced from that of each isotope as the nuclear cross section.

For neutron irradiation-induced damage rate calculation in an irradiation environment, two methods can be used. The first one is by folding neutron flux and damage cross section. This method is also widely used in most of current applications because it can be a direct response function from neutron transport simulations. However, the self-shielding correction on multigroup damage cross section should be considered, whereas it is not automatically treated in neutron transport codes. In the

ASTRID inner core, the self-shielded ECCO 33-group damage cross section leads to about 10% reduction of total DPA rate when compared with infinite dilution ECCO 33-group damage cross section. The second method is to convert neutron flux into PKA spectra. This method can be more easily used to combine with new DPA models. Nevertheless, current calculations of PKA spectrum are based on infinite dilution cross sections, so that the correction of multigroup cross section in a specific case is still not considered.

Compared with the neutron-induced irradiation damage, less attention has been paid to the irradiation of fuel cladding induced by FPs. Therefore, we propose a general method for computing FPs-induced displacement damage by BCA or MD simulations. It is shown that the maximum penetration of FPs in the Fe-14Cr ODS cladding is less than 10 μm. However, the peak value of the FPs-induced damage rate (based on SRIM full cascade simulations, the final rate is divided by a factor of 2 for roughly converting to NRT-DPA) can be 4 to 5 times larger than the neutron-induced one in ASTRID inner core cladding. Because the DPA level is a main criterion for determining the operating lifetime of an assembly in SFRs, the question of whether the FPs-induced damage should be taken into account in the cladding of SFRs needs to be discussed.

In order to estimate the uncertainty of calculated DPA rate, we show the results in the RPV of a simplified PWR as an example. The covariance matrices of ^{235}U PFNS from ENDF/B-VII.1 and JENDL-4.0 respectively lead to 11% and 7% relative uncertainty of total DPA rate. If the correlations of the neutron flux are neglected, the uncertainties are strongly underestimated to 3% and 2%, respectively. These results are consistent between the analytical calculation (i.e. based on sensitivity) with damage cross section and the TMC calculation via PKA spectrum by sampling neutron flux. It is noteworthy that the uncertainty from complete consideration of correlation matrices of neutron flux and PKA spectrum is 21 times larger than the calculation without considering any correlation. The correlations are thus of great importance for estimating the uncertainty of DPA rate.

The uncertainties of n+^{56}Fe nuclear model parameters rise to 4% uncertainty on total DPA. It is noteworthy that the uncertainties in the RRR have a little influence on the uncertainty of DPA rate calculation for the RPV. The uncertainty propagated from NRT-DPA model parameters is about 3.5% (without considering the bias induced by the TDE). The total uncertainties of damage rate are respectively 12% and 9% based on the ^{235}U PFNS from ENDF/VII.1 and JENDL-4.0, whereas neglecting the correlations of damage cross section and neutron flux implies to an underestimation by a factor of 3. This uncertainty should then be combined with the uncertainty of the TDE (can be from 5% [70] up to 20% [34] for iron) to determine the total uncertainty of DPA rate.

8.2 Prospects

As explained in Ref. [34], the models defect is one of the main challenges for irradiation damage calculations. More efforts are required for improving model-based calculations. For nuclear data, accurate and inherent coherent evaluations with complete covariance matrices are expected. As for DPA models, more and more R&D efforts have been carried out. However, more accurate experimental data are required to validate theoretical models because most MD simulations are still based on semi-empirical interatomic potentials. With improved theoretical models and model parameters, one could calculate the damage cross section and its covariance matrix from model parameters by step calculation in the CONRAD code [34].

The Jules Horowitz Reactor (JHR) material test reactor under construction in CEA Cadarache will be helpful to validate the neutron irradiation DPA calculations. In order to avoid as much as possible that atoms displaced to previously produced atomic vacancies, the total irradiation level should be controlled by a small value of DPA. For a particular emphasis on the neutron irradiation of the RPV, $K \equiv \mathrm{DPA}_{\mathrm{NRT}}/\phi_{>0.5\mathrm{MeV}} \approx 9.5 \times 10^2$ barn is proposed as an additional criterion of neutron flux for the experimental design [173].

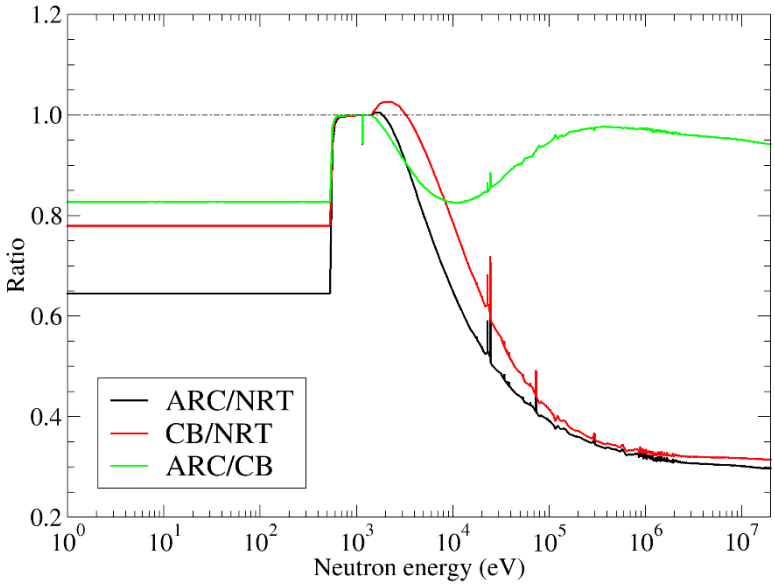

Figure 8-1. Comparison of different damage cross sections based on JEFF-3.3 n+^{56}Fe.

For validating DPA models, as the examples shown in Figure 8-1, one may design several samples by filtering neutrons below 2 MeV or even higher to determine the asymptotic value of the efficiency compared with NRT for iron. However, considering the increase in the efficiency for PKA energy above ~0.1 MeV [157], neutron flux with energy around 2 MeV (→ 0.14 MeV maximum recoil energy from neutron elastic scattering) could be used. Different neutron flux with predominant contributions to DPA

in the range of [2 keV, 100 keV] can validate different efficiency functions. Using the current version of CONRAD [34], one can adjust DPA model parameters (and nuclear model parameters if necessary) according to integral experimental data on DPA irradiated in the JHR.

For fusion applications, because the neutrons with energies above 10 MeV are an important source of irradiation, the PKA energies (e.g., Figure 4-12) include the increasing region of the efficiency shown in Ref. [157], and improved DPA models should be used. In addition, because N-body emission channels are generally open at such energies, complete and accurate recoil data should be given, as explained in Section 4.4.3.

In addition to the accurate calculation of DPA rate, a more accurate uncertainty estimate is also important. Firstly, for the neutron flux, its covariance matrix should be propagated from all uncertainty sources, such as the work of Clouvel [169]. Then the correlation matrix between neutron flux and damage cross section is also mandatory for a proper estimation of the uncertainties. This accurate uncertainty estimation requires a large number of sensitivity calculations and is not performed in current applications. To reduce the workloads, one may use a conservative upper bound as:

$$\Delta_{\mathrm{tot}} \leq \Delta_{\mathrm{Flux}} + \Delta_{\sigma_{\mathrm{DPA}}} \tag{8-1}$$

Last but not least, current regulations concerning neutron irradiation damage are based on the NRT-DPA or fast neutron fluence [181]. Because the ARC model is more realistic than the NRT model, it should be used with accurate parameters in future applications. As for the use of fast neutron fluence, even though neutron flux > 0.5 MeV is shown more representative than that > 1 MeV for the attenuation of DPA in stainless steels, it is hard to find a threshold that DPA and fast neutron flux can be explicitly correlated [171, 173]. Therefore, the measure of neutron irradiation damage is still a challenge for nuclear R&D.

Appendix

A1 Differential cross section of hard-spheres elastic scattering

Figure A-1 illustrates the schematic for hard-sphere elastic scattering in the CM frame. For incident energy of E, Eq. (4-24) shows that the recoil energy T is:

$$T = \frac{1}{2}E(1-\cos\theta) \tag{A-1}$$

On the other hand, the symmetry in the CM frame implies $\theta = 2\varphi$, where φ satisfies:

$$\cos\varphi = \frac{P}{2R} \tag{A-2}$$

where P is the impact parameter and R is the radius of the hard-sphere. Using the equality $\cos 2\varphi = 2\cos^2\varphi - 1$, one obtains:

$$T = E(1-\cos^2\varphi) = E\left[1-\left(\frac{P}{2R}\right)^2\right] \tag{A-3}$$

Therefore,

$$dT = -\frac{E}{2R^2}PdP \tag{A-4}$$

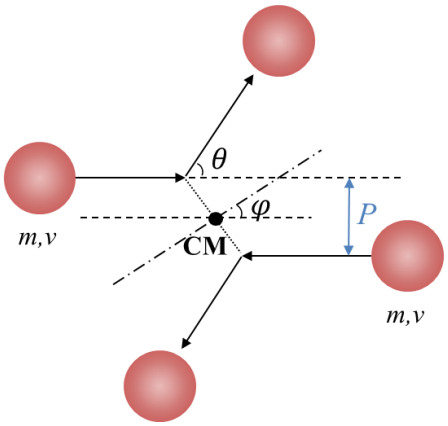

Figure A-1. Schematic for hard-spheres elastic scattering in the CM frame.

Let denote $\sigma(E,T)$ the normalized differential cross section. One has:

$$\sigma(E,T)dT = -\frac{2\pi PdP}{\int_0^{2R} 2\pi PdP} \tag{A-5}$$

The negative symbol is because the T decreases with the increase in the impact parameter P. Consequently, the differential cross section is:

$$\sigma(E,T) = \frac{PdP}{2R^2dT} = \frac{1}{E} \tag{A-6}$$

A2 Complementary data for explaining the positive correlations of neutron flux used in Section 7 [170]

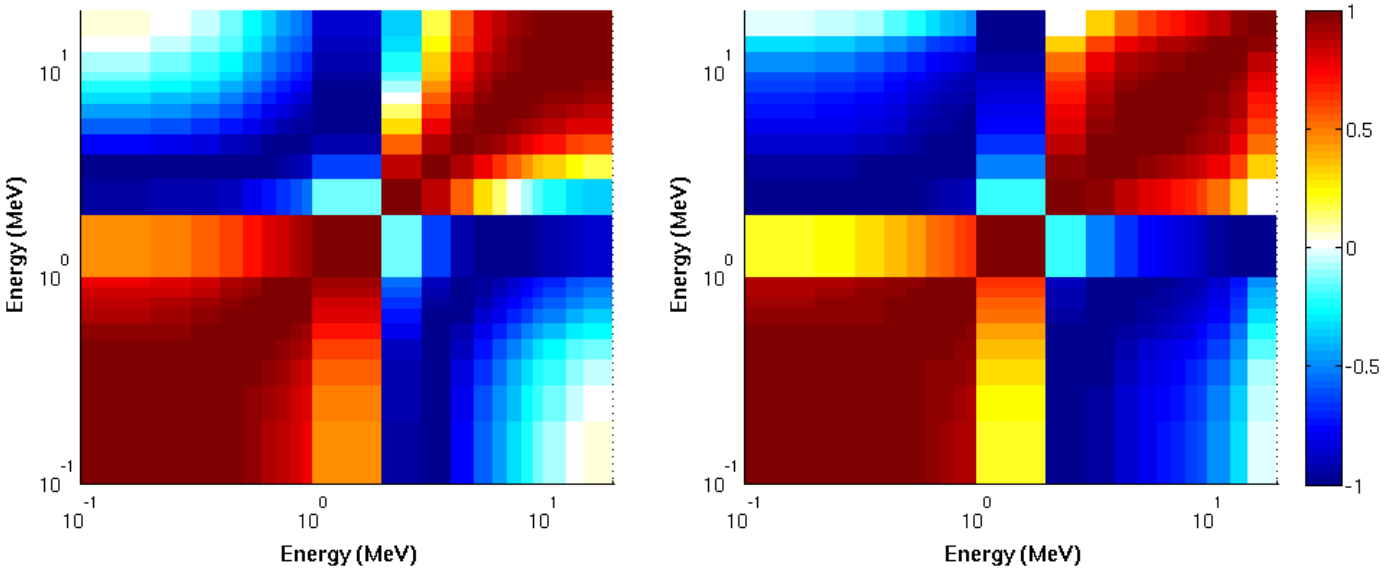

Figure A-2. Correlation matrices of ^{235}U PFNS from different evaluations: ENDF/B-VII.1 (left) and JENDL-4.0 (right).

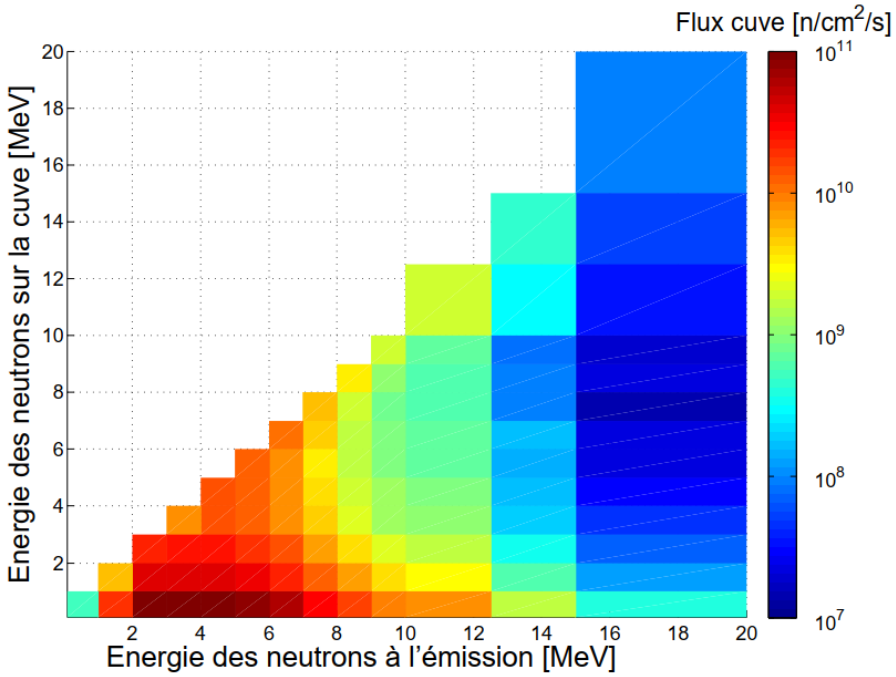

Figure A-3. Neutron flux in the RPV propagated from ^{235}U PFNS (calculations are based on the Madland-Nix PFNS). The abscissa is the energy of the emitted neutron (i.e. energy in the ^{235}U PFNS), the ordinate is the energy for neutron propagated to the RPV.

A3 Algorithm to make a covariance matrix be positive-definite

An algorithm to make a non-positive-definite covariance matrix M be positive-definite. This algorithm was also implemented in CONRAD by Pascal Archier.

```
niter = 5000;           //can be an any user-defined maximum value
of iteration
notPosDef = true;
factor = 2;
it = 0;
while (notPosDef && it < niter)
      it = it + 1;
      for i = 1:size(M,1)
            factor1 = 1 + rand(1)*1e-4;
            M(i,i) = M(i,i)*factor1;
            factor = min(factor, factor1);
      end;
      if min(eig(M)) > 0;
            notPosDef = false;
      end;
 end;
 M = M/factor;
```

A4 Complementary correlation matrices

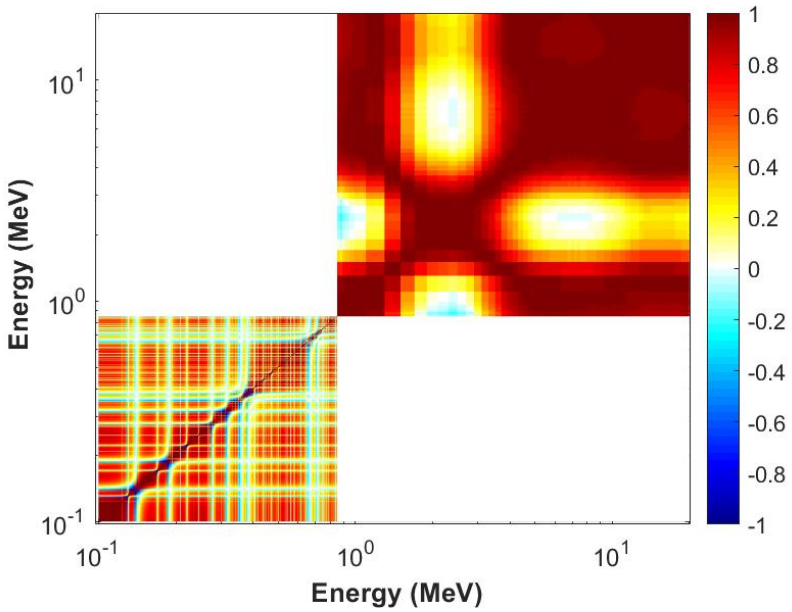

Figure A-4. Correlation matrix of n+^{56}Fe damage cross section in [0.1, 20] MeV from nuclear reaction model parameters. The two clusters in the continuum region correspond to the two humps of uncertainty shown in Figure 7-12.

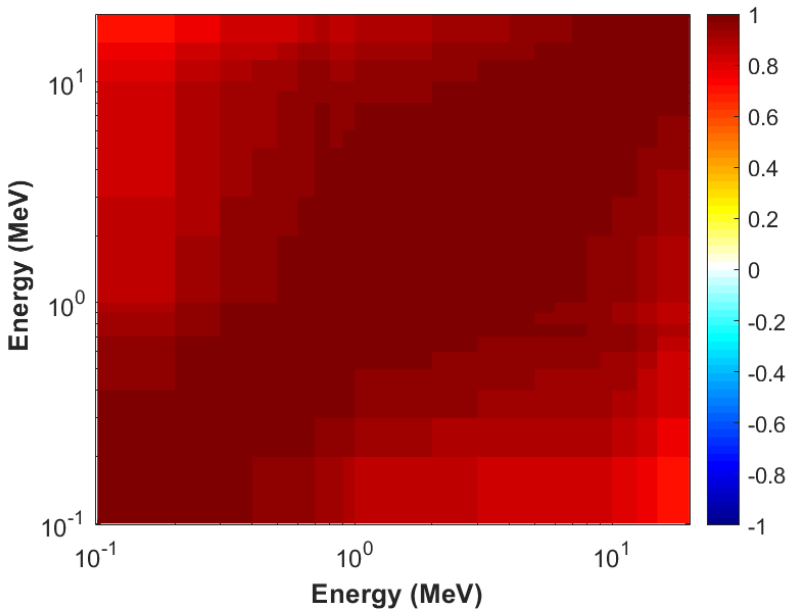

Figure A-5. 21-group correlation matrix of n+^{56}Fe damage cross section in [0.1, 20] MeV from ARC-DPA model parameters.

Figure A-6 shows the correlation matrix of n+^{56}Fe DPA cross section propagated from DPA model parameters for both the NRT and ARC models by assuming E_d = 41±2 eV. The correlations are closer to +1 for 10% and 20% uncertainties of E_d.

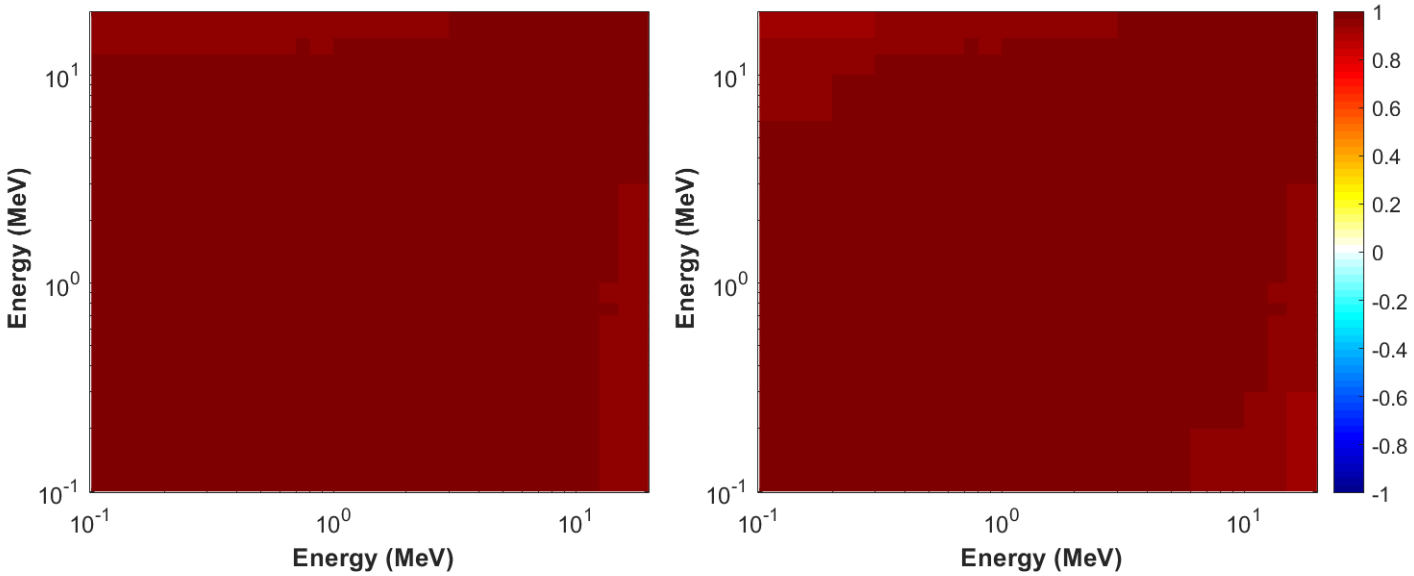

Figure A-6. 21-group correlation matrix of n+^{56}Fe DPA cross section in [0.1, 20] MeV propagated from DPA model parameters by assuming E_d = 41±2 eV: NRT (left, min=0.940) and ARC (right, min=0.924) models.

A5 List of publications

Journal articles:

1. **S. Chen**, P. Tamagno, D. Bernard *et al.*, "From nuclear physics to displacement damage calculation and uncertainty propagation in CONRAD," *Results in Physics*, vol. 17, 103023, 2020
2. **S. Chen** and D. Bernard, "On the calculation of atomic displacements using damage energy," *Results in Physics*, vol. 16, 102835, 2020
3. **S. Chen** and D. Bernard, "Radiation damage calculations for charged particle emission nuclear reactions," *Chinese Journal of Physics*, vol. 66, pp. 135–149, 2020
4. **S. Chen** and D. Bernard, "Contribution of fission products to displacement damage in fast reactor fuel cladding," *Annals of Nuclear Energy*, vol. 145, 107603, 2020
5. **S. Chen**, D. Bernard, and P. Blaise, "Attenuation of neutron and photon-induced irradiation damage in pressurized water reactor pressure vessels," *Annals of Nuclear Energy*, vol. 145, 107601, 2020
6. **S. Chen** and D. Bernard, "On the beta decay-induced radiation damage," *Nuclear Instruments and Methods in Physics Research Section B*, vol. 467, pp. 58–64, 2020
7. **S. Chen** and D. Bernard, "Relativistic effect on two-body reaction inducing atomic displacement," *Journal of Nuclear Materials*, vol. 522, pp. 236–245, 2019
8. **S. Chen** and D. Bernard, "Application of special relativity in damage calculations," *Nuclear Instruments and Methods in Physics Research Section B,* vol. 440, pp. 107–113, 2019
9. **S. Chen**, D. Bernard, and L. Buiron, "Study on the self-shielding and temperature influences on the neutron irradiation damage calculations in reactors," *Nuclear Engineering and Design*, vol. 346, pp. 85–96, 2019
10. **S. Chen**, D. Bernard, and C. De Saint Jean, "Calculation and analysis of gamma-induced irradiation damage cross section," *Nuclear Instruments and Methods in Physics Research Section B*, vol. 447, pp. 8–21, 2019
11. **S. Chen**, D. Bernard, P. Tamagno *et al.*, "Calculation and verification of neutron irradiation damage with differential cross sections," *Nuclear Instruments and Methods in Physics Research Section B*, vol. 456, pp. 120–132, 2019
12. **S. Chen** and D. Bernard, "Attenuation of atomic displacement damage in the heavy reflector of the PERLE experiment," *Nuclear Engineering and Design*, vol. 353, 110205, 2019

Conference papers:

13. **S. Chen**, D. Bernard, C. De Saint Jean, "Relativistic Effect on Atomic Displacement Damage for Two-Body Inducing Discrete Reactions," *EPJ Web of Conferences*, vol. 239, 08004, 2020
14. **S. Chen**, D. Bernard, J. Tommasi, and C. De Saint Jean, "Improved Model for Atomic Displacement Calculation," *EPJ Web of Conferences*, vol. 239, 08003, 2020
15. M. Diakaki, **S. Chen**, G. Noguere, *et al.*, "Evaluation of neutron induced reactions on ^{56}Fe with CONRAD," *EPJ Web of Conferences*, vol. 239, 11005, 2020

16. **S. Chen**, D. Bernard, P. Archier, *et al.*, “Covariance Matrices for Differential and Angle-Integrated Neutron-Induced Elastic and Inelastic Scattering Cross Sections of ^{56}Fe,” *EPJ Web of Conferences*, vol. 211, 07002, 2019
17. M. Diakaki, **S. Chen**, G. Noguere, *et al.*, “Status of the evaluation of n+^{56}Fe reaction data and experimental validation,” in Consultants’ Meeting on INDEN, IAEA, 2019
18. M. Diakaki, **S. Chen**, P. Tamagno, and D. Bernard, “Evaluation of n+^{56}Fe Reaction Data (+Covariances) and Experimental Validation,” in Consultants’ Meeting on INDEN, IAEA, 2018

References

[1] International Energy Agency, "Electricity Statistics - 2017." https://www.iea.org/statistics/electricity/.

[2] International Energy Agency, "Total primary energy supply by fuel, 1971 and 2017 – Charts – Data & Statistics." https://www.iea.org/data-and-statistics/charts/total-primary-energy-supply-by-fuel-1971-and-2017.

[3] N. R. Brown, A. Aronson, M. Todosow, *et al.*, "Neutronic performance of uranium nitride composite fuels in a PWR," *Nucl. Eng. Des.*, vol. 275, pp. 393–407, Aug. 2014, doi: 10.1016/j.nucengdes.2014.04.040.

[4] N. R. Brown, M. Todosow, and A. Cuadra, "Screening of advanced cladding materials and UN–U_3Si_5 fuel," *J. Nucl. Mater.*, vol. 462, pp. 26–42, 2015, doi: 10.1016/j.jnucmat.2015.03.016.

[5] S. Chen and C. Yuan, "Neutronic Analysis on Potential Accident Tolerant Fuel-Cladding Combination U_3Si_2-FeCrAl," *Sci. Technol. Nucl. Install.*, vol. 2017, p. 3146985, 2017, doi: 10.1155/2017/3146985.

[6] S. Chen, C. Yuan, and D. Guo, "Radial distributions of power and isotopic concentrations in candidate accident tolerant fuel U_3Si_2 and UO_2/U_3Si_2 fuel pins with FeCrAl cladding," *Ann. Nucl. Energy*, vol. 124, pp. 460–471, Feb. 2019, doi: 10.1016/j.anucene.2018.10.025.

[7] S. Chen and C. Yuan, "Minor Actinides transmutation in candidate accident tolerant fuel-claddings U_3Si_2-FeCrAl and U_3Si_2-SiC," *Ann. Nucl. Energy*, vol. 127, pp. 204–214, May 2019, doi: 10.1016/j.anucene.2018.12.003.

[8] W. Li and K. Shirvan, "U_3Si_2-SiC fuel performance analysis in BISON during normal operation," *Ann. Nucl. Energy*, vol. 132, pp. 34–45, Oct. 2019, doi: 10.1016/j.anucene.2019.04.021.

[9] X. Wu, T. Kozlowski, and J. D. Hales, "Neutronics and fuel performance evaluation of accident tolerant FeCrAl cladding under normal operation conditions," *Ann. Nucl. Energy*, vol. 85, pp. 763–775, Nov. 2015, doi: 10.1016/j.anucene.2015.06.032.

[10] K. A. Terrani, B. A. Pint, Y.-J. Kim, *et al.*, "Uniform corrosion of FeCrAl alloys in LWR coolant environments," *J. Nucl. Mater.*, vol. 479, pp. 36–47, Oct. 2016, doi: 10.1016/j.jnucmat.2016.06.047.

[11] K. G. Field, M. A. Snead, Y. Yamamoto, *et al.*, "Handbook on the Material Properties of FeCrAl Alloys for Nuclear Power Production Applications," U.S. Department of Energy, ORNL/TM-2017/186 Rev.1, Aug. 2017. https://info.ornl.gov/sites/publications/Files/Pub74128.pdf.

[12] K. A. Gamble, T. Barani, D. Pizzocri, *et al.*, "An investigation of FeCrAl cladding behavior under normal operating and loss of coolant conditions," *J. Nucl. Mater.*, vol. 491, pp. 55–66, Aug. 2017, doi: 10.1016/j.jnucmat.2017.04.039.

[13] K. A. Unocic, Y. Yamamoto, and B. A. Pint, "Effect of Al and Cr Content on Air and Steam Oxidation of FeCrAl Alloys and Commercial APMT Alloy," *Oxid. Met.*, vol. 87, no. 3, pp. 431–441, Apr. 2017, doi: 10.1007/s11085-017-9745-1.

[14] S. Dryepondt, K. A. Unocic, D. T. Hoelzer, *et al.*, "Development of low-Cr ODS FeCrAl alloys for accident-tolerant fuel cladding," *J. Nucl. Mater.*, vol. 501, pp. 59–71, Apr. 2018, doi: 10.1016/j.jnucmat.2017.12.035.

[15] S. Chen and C. Yuan, "Neutronic study of UO_2-BeO fuel with various claddings," *Nucl. Mater. Energy*, vol. 22, p. 100728, Jan. 2020, doi: 10.1016/j.nme.2020.100728.

[16] S. Chen, X. He, and C. Yuan, “Recent studies on potential accident-tolerant fuel-cladding systems in light water reactors,” *Nucl. Sci. Tech.*, vol. 31, no. 3, p. 32, Mar. 2020, doi: 10.1007/s41365-020-0741-9.
[17] MS. Chenaud, N. Devictor, G. Mignot, *et al.*, “Status of the ASTRID core at the end of the pre-conceptual design phase 1,” *Nucl. Eng. Technol.*, vol. 45, no. 6, pp. 721–730, Nov. 2013, doi: 10.5516/NET.02.2013.519.
[18] P. Yvon and F. Carré, “Structural materials challenges for advanced reactor systems,” *J. Nucl. Mater.*, vol. 385, no. 2, pp. 217–222, Mar. 2009, doi: 10.1016/j.jnucmat.2008.11.026.
[19] H. Ohshima and S. Kubo, “5 - Sodium-cooled fast reactor,” in *Handbook of Generation IV Nuclear Reactors*, Elsevier, 2016, pp. 97–118.
[20] ASTM E693-17, *Standard Practice for Characterizing Neutron Exposures in Iron and Low Alloy Steels in Terms of Displacements Per Atom (DPA)*. West Conshohocken, PA: ASTM International, 2017.
[21] P. Dubuisson, Y. de Carlan, V. Garat, *et al.*, “ODS Ferritic/martensitic alloys for Sodium Fast Reactor fuel pin cladding,” *J. Nucl. Mater.*, vol. 428, no. 1, pp. 6–12, Sep. 2012, doi: 10.1016/j.jnucmat.2011.10.037.
[22] C. Pokor, X. Averty, Y. Bréchet, *et al.*, “Effect of irradiation defects on the work hardening behavior,” *Scr. Mater.*, vol. 50, no. 5, pp. 597–600, Mar. 2004, doi: 10.1016/j.scriptamat.2003.11.029.
[23] G. S. Was, “The Displacement of Atoms,” in *Fundamentals of Radiation Materials Science*, New York, NY: Springer New York, 2017, pp. 77–130.
[24] X. Averty, J.-C. Brachet, J.-P. Pizzanelli, *et al.*, “Tensile properties of austenitic, martensitic, and ferritic steels irradiated at 325°C up to 3.4 dpa in the OSIRIS experimental reactor,” in *Proceedings of the International Symposium Fontevraud IV*, Paris, France, 1998, vol. 1, pp. 293–306.
[25] G. S. Was, J. T. Busby, T. Allen, *et al.*, “Emulation of neutron irradiation effects with protons: validation of principle,” *J. Nucl. Mater.*, vol. 300, no. 2, pp. 198–216, Feb. 2002, doi: 10.1016/S0022-3115(01)00751-6.
[26] N. Waeckel, “Overview on Key Needs, for Operation, Design and Licensing: Fuel and Material Performance under Irradiation,” in *FJOH 2018*, Aix-en-Provence, France, Aug. 2018.
[27] R. E. MacFarlane, D. W. Muir, and F. M. Mann, “Radiation Damage Calculations with NJOY,” *J. Nucl. Mater.*, vol. 123, no. 1–3, pp. 1041–1046, 1984, doi: 10.1016/0022-3115(84)90216-2.
[28] A. Santamarina, D. Bernard, P. Blaise, *et al.*, “The JEFF-3.1.1 Nuclear Data Library,” OECD/NEA, JEFF Report 22, NEA No. 6807, 2009. https://www.oecd-nea.org/dbdata/nds_jefreports/jefreport-22/nea6807-jeff22.pdf.
[29] A. M. Lane and R. G. Thomas, “R-Matrix Theory of Nuclear Reactions,” *Rev. Mod. Phys.*, vol. 30, no. 2, pp. 257–353, Apr. 1958, doi: 10.1103/RevModPhys.30.257.
[30] N. M. Larson, “Updated User’s Guide for Sammy: Multilevel R-Matrix Fits to Neutron Data Using Bayes’ Equations,” Oak Ridge National Laboratory (ORNL), 2008.
[31] G. Breit and E. Wigner, “Capture of Slow Neutrons,” *Phys. Rev.*, vol. 49, p. 519, 1936, doi: 10.1103/PhysRev.49.519.
[32] C. W. Reich and M. S. Moore, “Multilevel Formula for the Fission Process,” *Phys. Rev.*, vol. 111, no. 3, pp. 929–933, Aug. 1958, doi:

10.1103/PhysRev.111.929.
[33] P. Archier, C. De Saint Jean, O. Litaize, *et al.*, "CONRAD Evaluation Code: Development Status and Perspectives," *Nucl. Data Sheets*, vol. 118, pp. 488–490, 2014, doi: 10.1016/j.nds.2014.04.114.
[34] S. Chen, P. Tamagno, D. Bernard, *et al.*, "From nuclear physics to displacement damage calculation and uncertainty propagation in CONRAD," *Results Phys.*, vol. 17, p. 103023, Jun. 2020, doi: 10.1016/j.rinp.2020.103023.
[35] A. Koning and J. Delaroche, "Local and global nucleon optical models from 1 keV to 200 MeV," *Nucl. Phys. A*, vol. 713, no. 3–4, pp. 231–310, Jan. 2003, doi: 10.1016/S0375-9474(02)01321-0.
[36] R. D. Woods and D. S. Saxon, "Diffuse Surface Optical Model for Nucleon-Nuclei Scattering," *Phys. Rev.*, vol. 95, no. 2, pp. 577–578, Jul. 1954, doi: 10.1103/PhysRev.95.577.
[37] B. Morillon and P. Romain, "Dispersive and global spherical optical model with a local energy approximation for the scattering of neutrons by nuclei from 1 keV to 200 MeV," *Phys. Rev. C*, vol. 70, no. 1, p. 014601, Jul. 2004, doi: 10.1103/PhysRevC.70.014601.
[38] C. Mahaux, H. Ngô, and G. R. Satchler, "Causality and the threshold anomaly of the nucleus-nucleus potential," *Nucl. Phys. A*, vol. 449, no. 2, pp. 354–394, Feb. 1986, doi: 10.1016/0375-9474(86)90009-6.
[39] P. Romain and J. P. Delaroche, "A dispersive coupled channels analysis of nucleon scattering from ^{181}Ta and ^{182,184,186}W up to 200 MeV," in *Proceedings of the Specialists' Meeting on the Nucleon Nucleus Optical Model up to 200 MeV*, Bruyères-le-Chatel, France, Nov. 1996, https://www.oecd-nea.org/science/om200/romain.pdf.
[40] R. Capote, M. Herman, P. Obložinský, *et al.*, "RIPL – Reference Input Parameter Library for Calculation of Nuclear Reactions and Nuclear Data Evaluations," *Nucl. Data Sheets*, vol. 110, no. 12, pp. 3107–3214, Dec. 2009, doi: 10.1016/j.nds.2009.10.004.
[41] J. Raynal, "ECIS code, distributed by the NEA DATA Bank," Paris, France, 2003.
[42] M. Diakaki, S. Chen, G. Noguere, *et al.*, "Evaluation of neutron induced reactions on ^{56}Fe with CONRAD," *EPJ Web Conf.*, vol. 239, p. 11005, 2020, doi: 10.1051/epjconf/202023911005.
[43] N. Otuka, E. Dupont, V. Semkova, *et al.*, "Towards a More Complete and Accurate Experimental Nuclear Reaction Data Library (EXFOR): International Collaboration Between Nuclear Reaction Data Centres (NRDC)," *Nucl. Data Sheets*, vol. 120, pp. 272–276, 2014, doi: 10.1016/j.nds.2014.07.065.
[44] M. Diakaki, S. Chen, G. Noguere, *et al.*, "Status of the evaluation of n + ^{56}Fe reaction data and experimental validation," presented at the Consultants' Meeting on INDEN - International Nuclear Data Evaluation Network - on the Evaluated Nuclear Data of the Structural Materials, IAEA, Vienna, Dec. 2019, https://www-nds.iaea.org/index-meeting-crp/CM-INDEN-IV-2019/docs/Diakaki_INDEN_2019.pdf.
[45] M. Diakaki, S. Chen, P. Tamagno, *et al.*, "Evaluation of n + ^{56}Fe Reaction Data (+Covariances) and Experimental Validation," presented at the Consultants' Meeting on INDEN - International Nuclear Data Evaluation Network - on the Evaluated Nuclear Data of the Structural Materials, IAEA, Vienna, Nov. 2018, https://www-nds.iaea.org/index-meeting-crp/CM-INDEN-III-2018/docs/Bernard_INDEN.pdf.

[46] W. Hauser and H. Feshbach, “The inelastic scattering of neutrons,” *Phys. Rev.*, vol. 87, no. 2, p. 366, 1952, doi: 10.1103/PhysRev.87.366.
[47] A. M. Lane and J. E. Lynn, “Fast Neutron Capture below 1 MeV: The Cross Sections for238U and232Th,” *Proc. Phys. Soc. Sect. A*, vol. 70, no. 8, pp. 557–570, Aug. 1957, doi: 10.1088/0370-1298/70/8/301.
[48] L. Dresner, in *Proceedings of the International Conference on Neutron Reactions with the Nucleus*, Columbia Univ., 1957, vol. Report CU-157 (1957), p. 71.
[49] S. Hilaire, Ch. Lagrange, and A. J. Koning, “Comparisons between various width fluctuation correction factors for compound nucleus reactions,” *Ann. Phys.*, vol. 306, no. 2, pp. 209–231, Aug. 2003, doi: 10.1016/S0003-4916(03)00076-9.
[50] J. Kopecky and M. Uhl, “Test of gamma-ray strength functions in nuclear reaction model calculations,” *Phys. Rev. C*, vol. 41, no. 5, pp. 1941–1955, May 1990, doi: 10.1103/PhysRevC.41.1941.
[51] D. M. Brink, “Individual particle and collective aspects of the nuclear photoeffect,” *Nucl. Phys.*, vol. 4, pp. 215–220, 1957, doi: 10.1016/0029-5582(87)90021-6.
[52] P. Axel, “Electric dipole ground-state transition width strength function and 7-MeV photon interactions,” *Phys. Rev.*, vol. 126, no. 2, p. 671, 1962, doi: 10.1103/PhysRev.126.671.
[53] A. Gilbert and A. Cameron, “A composite nuclear-level density formula with shell corrections,” *Can. J. Phys.*, vol. 43, no. 8, pp. 1446–1496, 1965, doi: 10.1139/p65-139.
[54] W. Dilg, W. Schantl, H. Vonach, *et al.*, “Level density parameters for the back-shifted fermi gas model in the mass range 40< A< 250,” *Nucl. Phys. A*, vol. 217, no. 2, pp. 269–298, 1973, doi: 10.1016/0375-9474(73)90196-6.
[55] A. J. Koning, S. Hilaire, and M. C. Duijvestijn, “TALYS-1.0,” in *Proceedings of the International Conference on Nuclear Data for Science and Technology*, Nice, France, Apr. 2007, pp. 211–214.
[56] S. Chen, “DPA number and damage cross section calculations in CONRAD-V2,” CEA Cadarache, SPRC/LEPh (unpublished), Aug. 2020.
[57] J. M. Blatt and L. Biedenharn, “The angular distribution of scattering and reaction cross sections,” *Rev. Mod. Phys.*, vol. 24, no. 4, p. 258, 1952, doi: 10.1103/RevModPhys.24.258.
[58] G. Racah, “Theory of Complex Spectra. I,” *Phys. Rev.*, vol. 61, no. 3–4, pp. 186–197, Feb. 1942, doi: 10.1103/PhysRev.61.186.
[59] G. Racah, “Theory of Complex Spectra. II,” *Phys. Rev.*, vol. 62, no. 9–10, pp. 438–462, Nov. 1942, doi: 10.1103/PhysRev.62.438.
[60] L. C. Biedenharn, J. M. Blatt, and M. E. Rose, “Some Properties of the Racah and Associated Coefficients,” *Rev. Mod. Phys.*, vol. 24, no. 4, pp. 249–257, Oct. 1952, doi: 10.1103/RevModPhys.24.249.
[61] L. Leal, E. Ivanov, G. Noguere, *et al.*, “Resonance parameter and covariance evaluation for ^{16}O up to 6 MeV,” *EPJ Nucl. Sci. Technol.*, vol. 2, p. 43, 2016, doi: 10.1051/epjn/2016036.
[62] C. Kalbach, “Systematics of continuum angular distributions: Extensions to higher energies,” *Phys. Rev. C*, vol. 37, no. 6, pp. 2350–2370, Jun. 1988, doi: 10.1103/PhysRevC.37.2350.
[63] C. Kalbach and F. M. Mann, “Phenomenology of continuum angular distributions. I. Systematics and parametrization,” *Phys. Rev. C*, vol. 23, no. 1, p. 112, 1981, doi: 10.1103/PhysRevC.23.112.

[64] S. Chen, D. Bernard, P. Tamagno, *et al.*, "Calculation and verification of neutron irradiation damage with differential cross sections," *Nucl. Instrum. Methods Phys. Res. Sect. B Beam Interact. Mater. At.*, vol. 456, pp. 120–132, Oct. 2019, doi: 10.1016/j.nimb.2019.07.011.

[65] D. A. Brown, M. B. Chadwick, R. Capote, *et al.*, "ENDF/B-VIII.0: The 8th Major Release of the Nuclear Reaction Data Library with CIELO-project Cross Sections, New Standards and Thermal Scattering Data," *Nucl. Data Sheets*, vol. 148, pp. 1–142, Feb. 2018, doi: 10.1016/j.nds.2018.02.001.

[66] Cross Sections Evaluation Working Group, "ENDF-6 Formats Manual - Data Formats and Procedures for the Evaluated Nuclear Data File ENDF/B-VI and ENDF/B-VII," National Nuclear Data Center, Brookhaven National Laboratory, BNL-90365-2009, Jul. 2010. https://www.oecd-nea.org/dbdata/data/manual-endf/endf102.pdf.

[67] G. W. Hedstrom, "Interpolation of nuclear reaction energy distributions," *J. Nucl. Sci. Technol.*, vol. 54, no. 10, pp. 1095–1117, Oct. 2017, doi: 10.1080/00223131.2017.1345335.

[68] P. Olsson, C. S. Becquart, and C. Domain, "Ab initio threshold displacement energies in iron," *Mater. Res. Lett.*, vol. 4, no. 4, pp. 219–225, Oct. 2016, doi: 10.1080/21663831.2016.1181680.

[69] W. E. King, K. L. Merkle, and M. Meshii, "Threshold energy surface and frenkel pair resistivity for Cu," *J. Nucl. Mater.*, vol. 117, pp. 12–25, Jul. 1983, doi: 10.1016/0022-3115(83)90005-3.

[70] K. Nordlund, J. Wallenius, and L. Malerba, "Molecular dynamics simulations of threshold displacement energies in Fe," *Nucl. Instrum. Methods Phys. Res. Sect. B Beam Interact. Mater. At.*, vol. 246, no. 2, pp. 322–332, May 2006, doi: 10.1016/j.nimb.2006.01.003.

[71] G. H. Kinchin and R. S. Pease, "The Displacement of Atoms in Solids by Radiation," *Rep Prog Phys*, vol. 18, no. 1, pp. 1–51, 1955, doi: 10.1088/0034-4885/18/1/301.

[72] J. Lindhard, V. Nielsen, M. Scharff, *et al.*, "Integral equations governing radiation effects," *Mat Fys Medd Dan Vid Selsk*, vol. 33, no. 10, pp. 1–42, 1963, http://gymarkiv.sdu.dk/MFM/kdvs/mfm%2030-39/mfm-33-10.pdf.

[73] S. Chen and D. Bernard, "Radiation damage calculations for charged particle emission nuclear reactions," *Chin. J. Phys.*, vol. 66, pp. 135–149, Aug. 2020, doi: 10.1016/j.cjph.2020.04.025.

[74] L. H. Thomas, "Calculation of Atomic Fields," *Math. Proc. Camb. Philos. Soc.*, vol. 23, no. 5, pp. 542–548, 1927, doi: 10.1017/S0305004100011683.

[75] E. Fermi, "Statistical method to determine some properties of atoms," *Rend Accad Naz Lincei*, vol. 6, pp. 602–607, 1927, http://ricerca.mat.uniroma3.it/ipparco/pagine/deposito/2011/TF.pdf.

[76] J. Lindhard, V. Nielsen, and M. Scharff, "Approximation Method in Classical Scattering by Screened Coulomb Fields," *Kgl Dan Vidensk Selsk Mat-Fys Medd*, vol. 36, no. 10, pp. 1–32, 1968, http://gymarkiv.sdu.dk/MFM/kdvs/mfm%2030-39/mfm-36-10.pdf.

[77] M. T. Robinson, "The Energy Dependence of Neutron Radiation Damage in Solids," in *Nuclear Fusion Reactors*, 1970, pp. 364–378, https://www.icevirtuallibrary.com/doi/abs/10.1680/nfr.44661.0025.

[78] C. A. Coulter and D. M. Parkin, "Damage energy functions in polyatomic materials," *J. Nucl. Mater.*, vol. 88, no. 2, pp. 249–260, 1980, doi: 10.1016/0022-

3115(80)90280-9.
[79] M. T. Robinson and I. M. Torrens, “Computer simulation of atomic-displacement cascades in solids in the binary-collision approximation,” *Phys. Rev. B*, vol. 9, no. 12, pp. 5008–5024, Jun. 1974, doi: 10.1103/PhysRevB.9.5008.
[80] M. J. Norgett, M. T. Robinson, and I. M. Torrens, “A proposed method of calculating displacement dose rates,” *Nucl. Eng. Des.*, vol. 33, no. 1, pp. 50–54, Aug. 1975, doi: 10.1016/0029-5493(75)90035-7.
[81] S. Chen and D. Bernard, “On the beta decay-induced radiation damage,” *Nucl. Instrum. Methods Phys. Res. Sect. B Beam Interact. Mater. At.*, Mar. 2020, doi: 10.1016/j.nimb.2020.01.017.
[82] R. S. Averback, R. Benedek, and K. L. Merkle, “Ion-irradiation studies of the damage function of copper and silver,” *Phys. Rev. B*, vol. 18, no. 8, p. 4156, 1978, doi: 10.1103/PhysRevB.18.4156.
[83] K. Nordlund, “Modified NRT equations for damage and mixing developed by the OECD NEA primary damage group,” presented at the Primary Radiation Damage: from nuclear reaction to point defects, Vienna, Austria, 2012, pp. 18–24, http://inis.iaea.org/Search/search.aspx?orig_q=RN:44028919.
[84] K. Nordlund, A. E. Sand, F. Granberg, *et al.*, “Primary Radiation Damage in Materials,” OECD/NEA, NEA/NSC/DOC(2015)9, 2015. https://www.oecd-nea.org/science/docs/2015/nsc-doc2015-9.pdf.
[85] K. Nordlund, S. J. Zinkle, A. E. Sand, *et al.*, “Improving atomic displacement and replacement calculations with physically realistic damage models,” *Nat. Commun.*, vol. 9, no. 1, p. 1084, 2018, doi: 10.1038/s41467-018-03415-5.
[86] A. Yu. Konobeyev, U. Fischer, Yu. A. Korovin, *et al.*, “Evaluation of effective threshold displacement energies and other data required for the calculation of advanced atomic displacement cross-sections,” *Nucl. Energy Technol.*, vol. 3, no. 3, pp. 169–175, Sep. 2017, doi: 10.1016/j.nucet.2017.08.007.
[87] R. E. MacFarlane and A. C. Kahler, “Methods for Processing ENDF/B-VII with NJOY,” *Nucl. Data Sheets*, vol. 111, no. 12, pp. 2739–2890, Dec. 2010, doi: 10.1016/j.nds.2010.11.001.
[88] A. Yu. Konobeyev, U. Fischer, and S. P. Simakov, “Neutron displacement cross-sections for materials from Be to U calculated using the arc-dpa concept,” presented at the 13th International Topical Meeting on the Applications of Accelerators (AccApp’17), Quebec, Canada, Aug. 2017, https://www-nds.iaea.org/public/download-endf/DXS/Displacement_XS/DXS.(2017)/Description_of_methods/DXS_AccApp17.pdf.
[89] A. J. M. Plompen, O. Cabellos, C. De Saint Jean, *et al.*, “The joint evaluated fission and fusion nuclear data library, JEFF-3.3,” *Eur. Phys. J. A*, vol. 56, p. 181, Jul. 2020, doi: 10.1140/epja/s10050-020-00141-9.
[90] C. H. M. Broeders and A. Yu. Konobeyev, “Defect production efficiency in metals under neutron irradiation,” *J. Nucl. Mater.*, vol. 328, no. 2, pp. 197–214, Jul. 2004, doi: 10.1016/j.jnucmat.2004.05.002.
[91] S. Chen, D. Bernard, J. Tommasi, *et al.*, “Improved model for atomic displacement calculation,” *EPJ Web Conf.*, vol. 239, p. 08003, 2020, doi: 10.1051/epjconf/202023908003.
[92] K. Nordlund, M. Ghaly, R. S. Averback, *et al.*, “Defect production in collision cascades in elemental semiconductors and fcc metals,” *Phys. Rev. B*, vol. 57, no. 13, pp. 7556–7570, Apr. 1998, doi: 10.1103/PhysRevB.57.7556.

[93] A. De Backer, A. E. Sand, K. Nordlund, *et al.*, "Subcascade formation and defect cluster size scaling in high-energy collision events in metals," *EPL Europhys. Lett.*, vol. 115, no. 2, p. 26001, Jul. 2016, doi: 10.1209/0295-5075/115/26001.
[94] J.-P. Crocombette, L. Van Brutzel, D. Simeone, *et al.*, "Molecular dynamics simulations of high energy cascade in ordered alloys: Defect production and subcascade division," *J. Nucl. Mater.*, vol. 474, pp. 134–142, Jun. 2016, doi: 10.1016/j.jnucmat.2016.03.020.
[95] C. Björkas and K. Nordlund, "Comparative study of cascade damage in Fe simulated with recent potentials," *Nucl. Instrum. Methods Phys. Res. Sect. B Beam Interact. Mater. At.*, vol. 259, no. 2, pp. 853–860, Jun. 2007, doi: 10.1016/j.nimb.2007.03.076.
[96] A. E. Sand and K. Nordlund, "On the lower energy limit of electronic stopping in simulated collision cascades in Ni, Pd and Pt," *J. Nucl. Mater.*, vol. 456, pp. 99–105, Jan. 2015, doi: 10.1016/j.jnucmat.2014.09.029.
[97] P. Jung, "Production of atomic defects in metals," in *Atomic Defects in Metals*, vol. 25, H. Ullmaier, Ed. Berlin/Heidelberg: Springer-Verlag, 1991.
[98] P. Lucasson, "The production of frenkel defects in metals," in *Fundamental aspects of radiation damage in metals*, Oak Ridge National Laboratory, US, Oct. 1975, vol. 1, pp. 42–65.
[99] K. Nordlund, S. J. Zinkle, A. E. Sand, *et al.*, "Primary radiation damage: A review of current understanding and models," *J. Nucl. Mater.*, vol. 512, pp. 450–479, Oct. 2018, doi: 10.1016/j.jnucmat.2018.10.027.
[100] J. F. Ziegler, M. D. Ziegler, and J. P. Biersack, "SRIM – The stopping and range of ions in matter (2010)," *Nucl. Instrum. Methods Phys. Res. Sect. B Beam Interact. Mater. At.*, vol. 268, no. 11, pp. 1818–1823, Jun. 2010, doi: 10.1016/j.nimb.2010.02.091.
[101] C. Borschel and C. Ronning, "Ion beam irradiation of nanostructures – A 3D Monte Carlo simulation code," *Nucl. Instrum. Methods Phys. Res. Sect. B Beam Interact. Mater. At.*, vol. 269, no. 19, pp. 2133–2138, Oct. 2011, doi: 10.1016/j.nimb.2011.07.004.
[102] J.-P. Crocombette and C. Van Wambeke, "Quick calculation of damage for ion irradiation: implementation in Iradina and comparisons to SRIM," *EPJ Nucl. Sci. Technol.*, vol. 5, p. 7, 2019, doi: 10.1051/epjn/2019003.
[103] R. E. Stoller, "1.11 - Primary Radiation Damage Formation," in *Comprehensive Nuclear Materials*, R. J. M. Konings, Ed. Oxford: Elsevier, 2012, pp. 293–332.
[104] J.-P. Crocombette and T. Jourdan, "Cell Molecular Dynamics for Cascades (CMDC): A new tool for cascade simulation," *Nucl. Instrum. Methods Phys. Res. Sect. B Beam Interact. Mater. At.*, vol. 352, pp. 9–13, Jun. 2015, doi: 10.1016/j.nimb.2014.12.009.
[105] C. J. Ortiz, "A combined BCA-MD method with adaptive volume to simulate high-energy atomic-collision cascades in solids under irradiation," *Comput. Mater. Sci.*, vol. 154, pp. 325–334, Nov. 2018, doi: 10.1016/j.commatsci.2018.07.058.
[106] S. Chen and D. Bernard, "On the calculation of atomic displacements using damage energy," *Results Phys.*, vol. 16, p. 102835, Mar. 2020, doi: 10.1016/j.rinp.2019.102835.
[107] R. E. Stoller, M. B. Toloczko, G. S. Was, *et al.*, "On the use of SRIM for computing radiation damage exposure," *Nucl. Instrum. Methods Phys. Res. Sect. B Beam Interact. Mater. At.*, vol. 310, pp. 75–80, Sep. 2013, doi:

10.1016/j.nimb.2013.05.008.
[108] M. I. Bratchenko, V. V. Bryk, S. V. Dyuldya, *et al.*, “Comments on DPA calculation methods for ion beam driven simulation irradiations,” *Вопросы Атомной Науки И Техники*, vol. 2, no. 84, pp. 11–16, 2013, http://dspace.nbuv.gov.ua/handle/123456789/111686.
[109] W. J. Weber and Y. Zhang, “Predicting damage production in monoatomic and multi-elemental targets using stopping and range of ions in matter code: Challenges and recommendations,” *Curr. Opin. Solid State Mater. Sci.*, vol. 23, no. 4, p. 100757, Aug. 2019, doi: 10.1016/j.cossms.2019.06.001.
[110] J. C. Meyer, F. Eder, S. Kurasch, *et al.*, “Accurate Measurement of Electron Beam Induced Displacement Cross Sections for Single-Layer Graphene,” *Phys. Rev. Lett.*, vol. 108, no. 19, p. 196102, May 2012, doi: 10.1103/PhysRevLett.108.196102.
[111] Y. Ma, “A study of point defects in UO_{2+x} and their impact upon fuel properties,” PhD thesis, Université Aix-Marseille, 2017.
[112] M. Alatalo, B. Barbiellini, M. Hakala, *et al.*, “Theoretical and experimental study of positron annihilation with core electrons in solids,” *Phys. Rev. B*, vol. 54, no. 4, pp. 2397–2409, Jul. 1996, doi: 10.1103/PhysRevB.54.2397.
[113] L. R. Greenwood and R. K. Smither, “SPECTER: Neutron damage calculations for materials irradiations,” Argonne National Laboratory, Argonne National Laboratory, ANL/FPP/TM-197, Jan. 1985. https://www-nds.iaea.org/irdf2002/codes/SPECTER.pdf.
[114] L. Lunéville, D. Simeone, and C. Jouanne, “Calculation of radiation damage induced by neutrons in compound materials,” *J. Nucl. Mater.*, vol. 353, no. 1–2, pp. 89–100, Jul. 2006, doi: 10.1016/j.jnucmat.2006.03.006.
[115] M. R. Gilbert, J. Marian, and J.-Ch. Sublet, “Energy spectra of primary knock-on atoms under neutron irradiation,” *J. Nucl. Mater.*, vol. 467, pp. 121–134, Dec. 2015, doi: 10.1016/j.jnucmat.2015.09.023.
[116] S. Chen, D. Bernard, and L. Buiron, “Study on the self-shielding and temperature influences on the neutron irradiation damage calculations in reactors,” *Nucl. Eng. Des.*, vol. 346, pp. 85–96, May 2019, doi: 10.1016/j.nucengdes.2019.03.006.
[117] S. Chen and D. Bernard, “Relativistic effect on two-body reaction inducing atomic displacement,” *J. Nucl. Mater.*, vol. 522, pp. 236–245, Aug. 2019, doi: 10.1016/j.jnucmat.2019.05.020.
[118] S. Chen, D. Bernard, and C. D. S. Jean, “Relativistic effect on atomic displacement damage for two-body inducing discrete reactions,” *EPJ Web Conf.*, vol. 239, p. 08004, 2020, doi: 10.1051/epjconf/202023908004.
[119] W. Yin, T. Zu, L. Cao, *et al.*, “Development and verification of heat production and radiation damage energy production cross section module in the nuclear data processing code NECP-Atlas,” *Ann. Nucl. Energy*, vol. 144, p. 107544, Sep. 2020, doi: 10.1016/j.anucene.2020.107544.
[120] J. Knaster, A. Moeslang, and T. Muroga, “Materials research for fusion,” *Nat. Phys.*, pp. 424–434, May 2016, doi: 10.1038/nphys3735.
[121] D. Bernard, “Estimation of bias and uncertainties for radiation damage calculation (Fission Reactors),” IAEA INDC International Nuclear Data Committee, Nuclear Reaction Data and Uncertainties for Radiation Damage, INDC(NDS)-0719, 2016. https://uu.diva-portal.org/smash/get/diva2:955795/FULLTEXT01.pdf.
[122] R. E. MacFarlane, D. W. Muir, R. M. Boicourt, *et al.*, “The NJOY Nuclear Data

Processing System, Version 2016," Los Alamos National Laboratory (LANL), Los Alamos, NM, United States, LA-UR-17-20093, 2016.
[123] A. J. Koning and D. Rochman, "Modern Nuclear Data Evaluation with the TALYS Code System," *Nucl. Data Sheets*, vol. 113, no. 12, pp. 2841–2934, Dec. 2012, doi: 10.1016/j.nds.2012.11.002.
[124] S. Chen, D. Bernard, and C. De Saint Jean, "Calculation and analysis of gamma-induced irradiation damage cross section," *Nucl. Instrum. Methods Phys. Res. Sect. B Beam Interact. Mater. At.*, vol. 447, pp. 8–21, May 2019, doi: 10.1016/j.nimb.2019.03.035.
[125] N. F. Mott, "The scattering of fast electrons by atomic nuclei," *Proc. R. Soc. A*, vol. 124, no. 794, pp. 425–442, Jun. 1929, doi: 10.1098/rspa.1929.0127.
[126] W. A. McKinley and H. Feshbach, "The Coulomb Scattering of Relativistic Electrons by Nuclei," *Phys. Rev.*, vol. 74, no. 12, pp. 1759–1763, Dec. 1948, doi: 10.1103/PhysRev.74.1759.
[127] O. S. Oen and D. K. Holmes, "Cross Sections for Atomic Displacements in Solids by Gamma Rays," *J. Appl. Phys.*, vol. 30, no. 8, pp. 1289–1295, 1959, doi: 10.1063/1.1735307.
[128] O. Klein and Y. Nishina, "Über die Streuung von Strahlung durch freie Elektronen nach der neuen relativistischen Quantendynamik von Dirac," *Z. Für Phys.*, vol. 52, no. 11, pp. 853–868, Nov. 1929, doi: 10.1007/BF01366453.
[129] H. O. Wyckoff, A. Allisy, R. S. Caswell, *et al.*, "Stopping Powers for Electrons and Positrons," International Commission on Radiation Unit and measurements, MD. 20814, USA, ICRU Report 37, Oct. 1984. https://doi.org/10.1093/jicru/os19.2.Report37.
[130] J. A. Bearden and A. F. Burr, "Reevaluation of X-Ray Atomic Energy Levels," *Rev. Mod. Phys.*, vol. 39, no. 1, pp. 125–142, Jan. 1967, doi: 10.1103/RevModPhys.39.125.
[131] C. M. Davisson and R. D. Evans, "Gamma-Ray Absorption Coefficients," *Rev. Mod. Phys.*, vol. 24, no. 2, pp. 79–107, Apr. 1952, doi: 10.1103/RevModPhys.24.79.
[132] D. E. Alexander, "Defect production considerations for gamma ray irradiation of reactor pressure vessel steels," *J. Nucl. Mater.*, vol. 240, no. 3, pp. 196–204, Feb. 1997, doi: 10.1016/S0022-3115(96)00713-1.
[133] J. Kwon and A. T. Motta, "Gamma displacement cross-sections in various materials," *Ann. Nucl. Energy*, vol. 27, no. 18, pp. 1627–1642, Dec. 2000, doi: 10.1016/S0306-4549(00)00024-4.
[134] K. Fukuya and I. Kimura, "Calculation of Gamma Induced Displacement Cross-sections of Iron Considering Positron Contribution and Using Standard Damage Model," *J. Nucl. Sci. Technol.*, vol. 40, no. 6, pp. 423–428, Jun. 2003, doi: 10.1080/18811248.2003.9715375.
[135] H. Bethe and W. Heitler, "On the stopping of fast particles and on the creation of positive electrons," *Proc R Soc Lond A*, vol. 146, no. 856, pp. 83–112, Aug. 1934, doi: 10.1098/rspa.1934.0140.
[136] H. A. Bethe, "The influence of screening on the creation and stopping of electrons," *Math. Proc. Camb. Philos. Soc.*, vol. 30, no. 4, pp. 524–539, Oct. 1934, doi: 10.1017/S0305004100012779.
[137] R. D. Evans, *The atomic nucleus*. New York: McGraw-Hill, 1955.
[138] E. Brun, F. Damian, C. M. Diop, *et al.*, "TRIPOLI-4®, CEA, EDF and AREVA reference Monte Carlo code," *Ann. Nucl. Energy*, vol. 82, pp. 151–160, Aug.

2015, doi: 10.1016/j.anucene.2014.07.053.
[139] D. E. Cullen, M. H. Chen, J. H. Hubbell, *et al.*, "Tables and graphs of photon-interaction cross sections from 10 eV to 100 GeV derived from the LLNL Evaluated Photon Data Library (EPDL)," Lawrence Livermore National Laboratory, UCRL-50400-Vol.6-Rev.4-Pt.B, Oct. 1989. https://www.osti.gov/biblio/6901928.
[140] S. P. Simakov and U. Fischer, "Displacement damage induced in iron by gammas and neutrons under irradiation in the IFMIF test cell," *J. Nucl. Mater.*, vol. 417, no. 1–3, pp. 1321–1324, Oct. 2011, doi: 10.1016/j.jnucmat.2010.12.175.
[141] M. R. Gilbert and J.-Ch. Sublet, "PKA distributions: Contributions from transmutation products and from radioactive decay," *Nucl. Mater. Energy*, vol. 9, pp. 576–580, Dec. 2016, doi: 10.1016/j.nme.2016.02.006.
[142] E. Fermi, *Nuclear Physics*. University of Chicago Press, 1974.
[143] H. Junde, H. Su, and Y. Dong, "Nuclear Data Sheets for A = 56," *Nucl. Data Sheets*, vol. 112, no. 6, pp. 1513–1645, Jun. 2011, doi: 10.1016/j.nds.2011.04.004.
[144] M. E. Rose and R. K. Osborn, "Nuclear Matrix Elements in Beta Decay," *Phys. Rev.*, vol. 93, no. 6, pp. 1326–1336, Mar. 1954, doi: 10.1103/PhysRev.93.1326.
[145] N. Soppera, M. Bossant, and E. Dupont, "JANIS 4: An Improved Version of the NEA Java-based Nuclear Data Information System," *Nucl. Data Sheets*, vol. 120, pp. 294–296, Jun. 2014, doi: 10.1016/j.nds.2014.07.071.
[146] K. S. Krane and D. Halliday, *Introductory nuclear physics*. New York: John Wiley & Sons, Inc., 1987.
[147] N. M. Ghoniem and S. P. Chou, "Binary collision Monte Carlo simulations of cascades in polyatomic ceramics," *J. Nucl. Mater.*, vol. 155–157, no. Part 2, pp. 1263–1267, Jul. 1988, doi: 10.1016/0022-3115(88)90508-9.
[148] G. Rimpault, P. Ribon, M. Grimstone, *et al.*, "Validation of new sub-group algorithms for resonance self-shielding in heterogeneous structures," Nuclear Energy Agency of the OECD (NEA), Saclay, France, Seminar on NJOY and THEMIS, INIS-XN--305, 1989. http://inis.iaea.org/Search/search.aspx?orig_q=RN:22032416.
[149] S. Chen and D. Bernard, "Contribution of fission products to displacement damage in fast reactor fuel cladding," *Ann. Nucl. Energy*, vol. 145, p. 107603, Sep. 2020, doi: 10.1016/j.anucene.2020.107603.
[150] D. C. Fee and C. E. Johnson, "Fuel-cladding chemical interaction in uranium-plutonium oxide fast reactor fuel pins," *J. Nucl. Mater.*, vol. 96, no. 1, pp. 80–104, Jan. 1981, doi: 10.1016/0022-3115(81)90221-X.
[151] O. Litaize, O. Serot, and L. Berge, "Fission modelling with FIFRELIN," *Eur. Phys. J. A*, vol. 51, p. 177, Dec. 2015, doi: 10.1140/epja/i2015-15177-9.
[152] J. F. Ziegler and J. P. Biersack, "The stopping and range of ions in matter," in *Treatise on Heavy-Ion Science*, Springer, 1985, pp. 93–129.
[153] J. M. Ruggieri, J. Tommasi, J. F. Lebrat, *et al.*, "ERANOS 2.1: International Code System for GEN IV Fast Reactor Analysis," in *Proceedings of ICAPP 06*, Reno, NV USA, Jun. 2006, pp. 2432–2439.
[154] J. Tommasi, J. F. Lebrat, P. Archier, *et al.*, "Status of ERANOS-2 code system validation for sodium fast reactor applications," presented at the PHYSOR 2010, Pittsburgh, Pennsylvania, USA, May 2010.
[155] S. Chen, D. Bernard, P. Archier, *et al.*, "Covariance Matrices for Differential and Angle-Integrated Neutron-Induced Elastic and Inelastic Scattering Cross Sections of ^{56}Fe," *EPJ Web Conf.*, vol. 211, p. 07002, 2019, doi:

10.1051/epjconf/201921107002.
[156] W. Setyawan, G. Nandipati, K. J. Roche, *et al.*, “Displacement cascades and defects annealing in tungsten, Part I: Defect database from molecular dynamics simulations,” *J. Nucl. Mater.*, vol. 462, pp. 329–337, Jul. 2015, doi: 10.1016/j.jnucmat.2014.12.056.
[157] A. Yu. Konobeyev, U. Fischer, and S. P. Simakov, “Improved atomic displacement cross-sections for proton irradiation of aluminium, iron, copper, and tungsten at energies up to 10 GeV,” *Nucl. Instrum. Methods Phys. Res. Sect. B Beam Interact. Mater. At.*, vol. 431, pp. 55–58, Sep. 2018, doi: 10.1016/j.nimb.2018.06.021.
[158] E. Privas, P. Archier, D. Bernard, *et al.*, “Generation of ^{238}U Covariance Matrices by Using the Integral Data Assimilation Technique of the CONRAD Code,” *EPJ Web Conf.*, vol. 106, p. 04015, 2016, doi: 10.1051/epjconf/201610604015.
[159] C. De Saint Jean, P. Archier, E. Privas, *et al.*, “Evaluation of Neutron-induced Cross Sections and their Related Covariances with Physical Constraints,” *Nucl. Data Sheets*, vol. 148, pp. 383–419, Feb. 2018, doi: 10.1016/j.nds.2018.02.010.
[160] G. Noguere, P. Archier, C. De Saint Jean, *et al.*, “Zero Variance Penalty Model for the Generation of Covariance Matrices in Integral Data Assimilation Problems,” *Nucl. Sci. Eng.*, vol. 172, no. 2, pp. 164–179, 2012, doi: 10.13182/NSE11-72.
[161] B. Habert, C. De Saint Jean, G. Noguere, *et al.*, “Retroactive Generation of Covariance Matrix of Nuclear Model Parameters Using Marginalization Techniques,” *Nucl. Sci. Eng.*, vol. 166, no. 3, pp. 276–287, Nov. 2010, doi: 10.13182/NSE09-85.
[162] P. Sigmund, “On the number of atoms displaced by implanted ions or energetic recoil atoms,” *Appl. Phys. Lett.*, vol. 14, no. 3, pp. 114–117, 1969, doi: 10.1063/1.1652730.
[163] A. Santamarina, C. Vaglio, P. Blaise, *et al.*, “The PERLE experiment for the qualification of PWR heavy reflectors,” presented at the PHYSOR2008, Interlaken, Switzerland, Sep. 2008.
[164] C. Vaglio-Gaudard, A. Santamarina, P. Blaise, *et al.*, “Interpretation of PERLE Experiment for the Validation of Iron Nuclear Data Using Monte Carlo Calculations,” *Nucl. Sci. Eng.*, vol. 166, no. 2, pp. 89–106, Oct. 2010, doi: 10.13182/NSE09-91.
[165] S. Ravaux, “Qualification du Calcul de l’Échauffement Photonique dans les Réacteurs Nucléaires,” PhD thesis, Université de Grenoble, 2013.
[166] M. D. McKay, R. J. Beckman, and W. J. Conover, “Comparison of Three Methods for Selecting Values of Input Variables in the Analysis of Output from a Computer Code,” *Technometrics*, vol. 21, no. 2, pp. 239–245, May 1979, doi: 10.1080/00401706.1979.10489755.
[167] M. Stein, “Large Sample Properties of Simulations Using Latin Hypercube Sampling,” *Technometrics*, vol. 29, no. 2, pp. 143–151, 1987, doi: 10.1080/00401706.1987.10488205.
[168] D. Rochman, A. J. Koning, S. C. van der Marck, *et al.*, “Nuclear data uncertainty propagation: Perturbation vs. Monte Carlo,” *Ann. Nucl. Energy*, vol. 38, no. 5, pp. 942–952, May 2011, doi: 10.1016/j.anucene.2011.01.026.
[169] L. Clouvel, “Quantification de l’incertitude du flux neutronique rapide reçu par la cuve d’un réacteur à eau pressurisée,” PhD thesis, Université Paris-Sud, 2019.
[170] L. Berge, “Contribution à la modélisation des spectres de neutrons prompts de

fission. Propagation d'incertitudes sur un calcul de fluence cuve," PhD thesis, Université Grenoble Alpes, 2015.
[171] S. Chen and D. Bernard, "Attenuation of atomic displacement damage in the heavy reflector of the PERLE experiment and application to EPR," *Nucl. Eng. Des.*, vol. 353, p. 110205, Nov. 2019, doi: 10.1016/j.nucengdes.2019.110205.
[172] M. B. Chadwick, M. Herman, P. Obložinský, *et al.*, "ENDF/B-VII.1 Nuclear Data for Science and Technology: Cross Sections, Covariances, Fission Product Yields and Decay Data," *Nucl. Data Sheets*, vol. 112, no. 12, pp. 2887–2996, Dec. 2011, doi: 10.1016/j.nds.2011.11.002.
[173] S. Chen, D. Bernard, and P. Blaise, "Attenuation of neutron and photon-induced irradiation damage in pressurized water reactor pressure vessels," *Ann. Nucl. Energy*, vol. 145, p. 107601, Sep. 2020, doi: 10.1016/j.anucene.2020.107601.
[174] K. Shibata, O. Iwamoto, T. Nakagawa, *et al.*, "JENDL-4.0: A New Library for Nuclear Science and Engineering," *J. Nucl. Sci. Technol.*, vol. 48, no. 1, pp. 1–30, Jan. 2011, doi: 10.1080/18811248.2011.9711675.
[175] S. P. Simakov, U. Fischer, A. J. Koning, *et al.*, "Iron NRT- and arc-displacement cross sections and their covariances," *Nucl. Mater. Energy*, vol. 15, pp. 244–248, May 2018, doi: 10.1016/j.nme.2018.05.006.
[176] A. Y. Konobeyev, U. Fischer, and S. P. Simakov, "Uncertainty assessment for the number of defects calculated using the NRT damage model," Karlsruher Institutfür Technologie, KIT Scientific Working Papers 70, 2017. https://publikationen.bibliothek.kit.edu/1000074095.
[177] C. Keckler, M. Fratoni, and E. Greenspan, "Sensitivity and Uncertainty Analysis of Neutron Spectrum and DPA in a B&B Core," *Nucl. Sci. Eng.*, Feb. 2020, doi: 10.1080/00295639.2020.1715688.
[178] N. Thiollay, J. D. Salvo, C. Sandrin, *et al.*, "FLUOLE-2: An Experiment for PWR Pressure Vessel Surveillance," *EPJ Web Conf.*, vol. 106, p. 02015, 2016, doi: 10.1051/epjconf/201610602015.
[179] N. Thiollay, "Validation de la fluence reçue par la cuve," presented at the Journée Technique SFEN "Poursuivre le fonctionnement des réacteurs nucléaires après 40 ans," Paris, France, Nov. 2019, https://hal-cea.archives-ouvertes.fr/cea-02614139/document.
[180] H. Matsuda, S.-I. Meigo, Y. Iwamoto, *et al.*, "Measurement of displacement cross-sections of copper and iron for proton with kinetic energies in the range 0.4 – 3 GeV," *J. Nucl. Sci. Technol.*, vol. 57, no. 10, pp. 1141–1151, Oct. 2020, doi: 10.1080/00223131.2020.1771453.
[181] ISO 19226:2017, *Nuclear energy — Determination of neutron fluence and displacement per atom (dpa) in reactor vessel and internals*. 2017.

Résumé étendu

Les dommages causés par l'irradiation constituent un défi majeur pour l'industrie nucléaire. Le calcul précis des dommages dans les matériaux nucléaires induits par les particules présentes dans le système (neutrons, mais également photons et particules chargées) ainsi que la quantification précise des incertitudes associées est donc fondamental pour à la fois accroitre la performance du parc électronucléaire actuel, mais également sa sûreté. L'objectif principal de cette thèse s'inscrit dans cette thématique de développer et d'améliorer les méthodologies utilisées pour calculer précisément les dommages induits par l'irradiation neutronique et les incertitudes correspondantes.

L'extension des travaux vers la nouvelle génération de réacteurs permet en outre d'accroitre le caractère prédictif des outils. La recherche menée dans cette thèse couvre les différents modèles nucléaires nécessaires à l'évaluation des données de réaction nucléaire, les modèles de dommages primaires pour estimer le nombre de déplacements atomiques à partir de l'énergie cinétique d'un Primary Knock-on Atom (PKA), les théories physiques et les méthodes numériques associées pour calculer la section efficace des dommages en utilisant les données nucléaires et les modèles de Déplacement par Atome (DPA), les méthodes de calcul du taux de DPA en utilisant les flux de neutrons et photons issus des simulations, et des stratégies de la propagation des incertitudes jusqu'à l'incertitude finale du calcul du DPA.

Après une brève revue des modèles de réactions nucléaires et des modèles de dommages primaires par irradiation, nous proposons des méthodes complètes pour calculer la section efficace des dommages à partir de différentes réactions nucléaires. Une méthode d'interpolation améliorée, appelée « Peak value-based Unit-Base Interpolation » (PUBI) dans la thèse, est proposée et recommandée pour bien reproduire la valeur crête des distributions en énergie et en angle de diffusion à partir de données tabulées. Au niveau de l'irradiation induite par un ion ou PKA, on refait un raisonnement à partir de l'équation de conservation du nombre de déplacements finaux : ce nombre ne doit pas être changé après une collision atomistique. Ceci fournit une explication physique de la différence observée d'un facteur d'environ 2 sur le nombre de déplacements atomiques entre le « Quick Calculation (QC) » et la « Full Cascade simulation (FC) » calculés par des codes de référence tels que SRIM. Une fonction

simple de l'efficacité est proposée dans le cadre de la thèse pour calculer le nombre de DPA en considérant la recombinaison athermique des atomes déplacés sans ajouter de paramètres complémentaires. Cette formule de l'efficacité de la cascade interatomique est validée par rapport à des données expérimentales du Fe, Ni, et Cu.

Les énergies de recul des réactions induites par les neutrons sont systématiquement estimées à partir des équations de la cinématique physique. On montre que le mouvement thermique de la cible n'a presque pas d'impact sur le calcul du DPA, tandis que l'effet relativiste n'est pas négligeable pour des neutrons et protons incidents de haute énergie comme ceux qui produit dans les sources de spallation (la correction sur l'énergie de recul pour des réactions de diffusion est approximativement égale à (E_n/20)% avec l'énergie du neutron ou proton incident E_n en MeV). En particulier, une nouvelle méthode de calcul de l'énergie de recul des réactions d'émission de particules chargées est proposée en considérant l'effet tunnel et la barrière Coulombienne. Le DPA total calculé par cette méthode et celui calculé avec la méthode implémentée dans NJOY présente une légère différence pour la plupart des isotopes dont le DPA est pourtant dominé par des réactions de diffusion, notamment pour le ^{56}Fe et le ^{58}Ni. Cependant, la différence peut être importante pour les noyaux avec des voies d'émission de particules chargées ouvertes à l'énergie thermique, comme le ^{6}Li, le ^{10}B, et le ^{59}Ni.

On montre que la méthode numérique utilisée dans NJOY pour calculer les intégrations sur l'angle d'émission pour la section de dommage ne peut pas garantir la convergence en raison de la discontinuité de l'intégrant. Une méthode améliorée est proposée pour assurer la convergence de l'intégration numérique. Des méthodes complémentaires sont testées pour vérifier la précision des calculs numériques. Les calculs de sections efficaces de dommage issues de la capture radiative des neutrons et des réactions à émissions multiples sont également analysés et discutés en profondeur. Même si les méthodes utilisées dans NJOY pour ces réactions semblent satisfaisantes, des calculs plus précis et plus exacts complexes et dépendent du caractère multistep des émissions seraient nécessaires.

En plus des dommages de déplacement induits par l'irradiation des neutrons, les dommages causés par l'irradiation induite par les électrons, les positrons, et les photons peuvent être importants dans certaines applications, par exemple les DPA induits par les photons dans la cuve d'un réacteur à eau bouillante. Les sections efficaces de DPA induites par ces particules légères sont également étudiées dans cette thèse. En

particulier, nous nous sommes intéressés à la désintégration bêta, qui est une réaction à trois corps : une méthode détaillée pour calculer les dommages induits par la désintégration bêta dans les matériaux est proposée en utilisant les énergies d'excitation du nucléide descendant et les intensités de désexcitation associées.

Une discussion approfondie sur le calcul de la section efficace des dommages pour les matériaux polyatomiques est également présentée. Les analyses sont faites à partir de la définition des sections DPA isotopiques. Il est à noter que la section de dommage d'un matériau polyatomique ne peut pas être simplement déduite par sommation de chaque isotope, comme c'est le cas pour les sections efficaces partielles de réaction nucléaire. Une approximation est proposée pour calculer la section DPA d'un matériau polyatomique en utilisant des simulations atomistiques pour vérifier les hypothèses et déduire certains coefficients, et les sections DPA de chaque isotope, à partir des modèles décrits auparavant.

Pour le calcul du taux de dommages induits par l'irradiation neutronique, deux méthodes peuvent être utilisées. La première consiste à convoluer le flux neutronique à la section efficace de dommage. Cette méthode est également largement utilisée dans la plupart des applications actuelles car elle peut être directement utilisée comme fonction réponse dans les codes de transport des neutrons. Cependant, la correction d'autoprotection sur la section de dommage multi-groupe doit être prise en compte. Dans le cas particulier de la gaine du cœur interne du démonstrateur technologique de 4ème génération ASTRID, on montre que l'autoprotection de la section de dommage en ECCO 33-groupe entraîne une réduction d'environ 10% du taux de DPA par rapport à la section efficace de dommage à dilution infinie.

La deuxième méthode consiste à calculer les spectres PKA. Cette méthode peut être plus facilement utilisée en combinaison avec les nouveaux modèles DPA. Néanmoins, les calculs actuels du spectre PKA sont basés sur des sections efficaces multi-group à dilution infinie et moyennées par une fonction poids générale, de sorte que la correction de la section efficace multi-groupe avec le spectre réaliste dans un cas spécifique n'est toujours pas considérée. Il faut garder en tête la sous-estimation si les sections efficaces à dilution infinie sont utilisées pour calculer les taux de DPA avec n'importe quelle méthode. La recommandation issue de nos travaux est de toujours utiliser les sections autoprotégées.

Par rapport aux dommages causés par l'irradiation induite par les neutrons,

l'irradiation induite par les Produits de Fission (PFs) dans la gaine du combustible a fait l'objet de moins de travaux jusqu'à présent. Par conséquent, nous proposons une méthode générale pour calculer les dommages de déplacement induits par les PFs avec des simulations atomistiques (i.e. via l'approximation de la collision binaire ou des modélisations par dynamique moléculaire). Il est démontré que la pénétration maximale des PFs dans la gaine Fe-14Cr est inférieure à 10 μm. Cependant, la valeur maximale du taux de dommage induit par les PFs (basée sur les simulations FC dans SRIM. On remarque que les résultats venant de SRIM Monte Carlo simulations sont divisés par un facteur 2 pour les convertir approximativement en Norgett-Robinson-Torrens (NRT)-DPA.) peut être 4 à 5 fois plus grande que celle induite par les neutrons dans la gaine du cœur interne d'ASTRID. Étant donné que le niveau de DPA est un critère important pour déterminer la durée de vie opérationnelle d'un assemblage combustible dans les Réacteurs à Neutrons Rapides (RNRs), la question de savoir si les dommages induits par les PFs doivent être pris en compte dans la gaine des RNRs doit être discutée pour les applications dans le futur.

Afin d'estimer l'incertitude du taux de DPA calculé, nous prenons l'exemple de résultats obtenus pour la cuve d'un Réacteur à Eau Pressurisée (REP) simplifié. Les matrices de covariance du spectre des neutrons prompts de fission (Prompt Fission Neutron Spectrum, PFNS) de l'^{235}U venant de ENDF/B-VII.1 et JENDL-4.0 conduisent respectivement à 11% et 7% d'incertitude relative sur le taux de DPA total. Si les corrélations du flux des neutrons sont négligées, les incertitudes sont fortement sous-estimées à 3% et 2% respectivement. Ces résultats sont cohérents avec ceux obtenus avec le calcul analytique (i.e. basé sur la sensibilité et la matrice de covariance) avec la section efficace de dommage et le calcul stochastique (i.e. total Monte Carlo) via le spectre PKA en échantillonnant le flux neutronique. Il est à noter que l'incertitude liée à la prise en compte complète des matrices de corrélation du flux neutronique et du spectre PKA est 21 fois plus importante que le calcul sans tenir compte d'aucune corrélation pour l'exemple montré dans cette thèse. Les corrélations sont donc très importantes pour estimer l'incertitude du taux de DPA.

Les incertitudes des paramètres du modèle nucléaire n+^{56}Fe entraînent une incertitude de 4% sur le taux de DPA. On montre en outre que les incertitudes dans la région de résonances influencent peu l'incertitude du taux de DPA calculé dans la cuve d'un REP. L'incertitude propagée à partir des paramètres du modèle NRT-DPA est

d'environ 3,5%. Basées sur les matrices de covariance du flux de neutron propagées des matrices covariance du PFNS de l'^{235}U de ENDF/B-VII.1 et JENDL-4.0, les incertitudes totales du taux de dommages sont respectivement de 12% et 9%, alors que négliger les corrélations de la section efficace des dommages et du flux neutronique implique une sous-estimation d'un facteur 3. Cette incertitude doit ensuite être combinée quadratiquement avec l'incertitude sur l'énergie du seuil de déplacement atomique (qui peut aller de 5% à 20% pour le fer) pour déterminer l'incertitude finale du taux de DPA.

Enfin, en conclusion et perspective de cette thèse, on liste quelques propositions d'expériences dédiées pour la conception de dispositif d'irradiation de matériaux dans le futur réaction technologique Jules Horowitz (RJH) en cours de construction sur le site du CEA de Cadarache. Ces mesures devraient permettre de vérifier a posteriori les modèles théoriques et asseoir les incertitudes proposées dans le travail de thèse.